75–78–W

TRANSCUTANEOUS MEASUREMENT OF AORTIC BLOOD VELOCITY BY ULTRASOUND A THEORETICAL AND EXPERIMENTAL APPROACH

by

Bjørn A. J. Angelsen

Universitetet i Trondheim
NORGES TEKNISKE HØGSKOLE
Institutt for teknisk kybernetikk

August 1975

The University of Trondheim
THE NORWEGIAN INSTITUTE OF TECHNOLOGY
Division of engineering cybernetics

Trondheim, Norway

UNIVERSITETET I TRONDHEIM
NORGES TEKNISKE HØGSKOLE
INSTITUTT FOR TEKNISK KYBERNETIKK

THE UNIVERSITY OF TRONDHEIM
THE NORWEGIAN INSTITUTE OF TECHNOLOGY
Division of Engineering Cybernetics

RAPPORTNUMMER: 75-78-W

TILGJENGELIGHET: Accessible

RAPPORTENS TITTEL	DATO
TRANSCUTANEOUS MEASUREMENT OF AORTIC BLOOD VELOCITY BY ULTRASOUND A THEORETICAL AND EXPERIMENTAL APPROACH	August 1975
	ANTALL SIDER OG BILAG: 277
SAKSBEARBEIDER / FORF.: Bjørn A.J. Angelsen	ANSV. SIGN.
OPPDRAGSGIVER:	PROSJEKTNUMMER: 480724.5

EKSTRAKT

A pulsed ultrasonic doppler meter capable of transcutaneously measuring blood velocity in the human aorta and the heart has been built and tested, both by laboratory experiments and by in vivo tests.

The scattering of ultrasound from blood has been studied theoretically and the validity of three velocity estimators is shown both theoretically and experimentally.

3 STIKKORD

Ultrasound
Blood velocity
Doppler

ABSTRACT

A pulsed ultrasonic blood velocity meter capable of measuring blood velocity in deep arteries such as the aorta, has been built. The intrument has been tested in laboratory experiments and appears to give accurate estimates of mean velocity. Examples of in vivo measurements are given , but due to the unknown angle between the velocity direction and the ultrasonic beam and difficulties in obtaining uniform illumination of the artery, only relative values can be obtained. A sector scanning method which resolves these problems is discussed and by initial experiments the velocity profile in the aortic arc is obtained.

A theory of the scattering of ultrasound from blood is given. The blood is treated as a continuum and the scattering is caused by stochastic fluctuations in density and compressibility. These are caused by the stochastic fluctuations in the cell concentration. The scattering cross-section is anisotropic and proportional to the frequency in the fourth power. When the cell concentration is so low that interaction between the cells can be neglected, the scattering cross-section will be proportional to the mean cell concentration. When the concentration is raised so that interaction is strong, a decrease from this proportionality is found.

An expression for the received signal in doppler measurements is given. From this expression the relation between the velocity field and signal correlation properties and power spectrum is found. The received signal is Gaussian and all information of the velocity field is therefore contained in second moments, i.e. the auto-correlation function of the rf-signal or equivalent, the auto- and cross-correlation functions of the quadrature components of the rf-signal. For stationary velocity fields the information is equivalently contained in the power spectra.

A new type of mean velocity estimator is given. It is shown that it, together with two earlier proposed estimators, gives a vector weighted average of the velocity field in the observation region. The estimator variance when finite time averaging is used is also calculated and 10 % uncertainty in practical measurements is achieved. There is no significant difference between the estimators.

PREFACE

This work was performed dureing the years 1973-1974 when I held a scholarship at the University of Trondheim, The Norwegian Institute of Technology, Division og Engineering Cybernetics. The work has also been supported by Autronica A/S and Forenede Liv A/S.

During the course of the investigation I have through stimulating discussions received advice and assistance from many people, whom I hereby wish to thank.

Dr. Philos. Rune Aaslid for stimulating discussions and suggestion of the work.

Dr. Alf O. Brubakk for his eager interest and cooperation, showing a remarkable acception of the engineering attitude towards problem solution.

Professor Jens G. Balchen at The Division of Engineering Cybernetics, Trondheim, for his encouragement and advice, especially on using modelling and parameter estimation techniques to determine velocity profiles. I have also been given very good working facilities at his department.

Assistant professor, Dr.Techn. Eivind Hiis Hauge for stimulating discussions and suggestions on the scattering theory.

Assistant professor, Dr. Techn. Kjell A. Ingebriktsen and Lic. Techn. Helge Engan for discussions on ultrasonics and transducers.

My wife, Guri Angelsen, and Marit Eriksen who carefully prepared the drawings.

Kari Hagen for typing the manuscript and patiently performing corrections when better solutions were found.

Tormod Hals for reading the manuscript.

The staff at The Division of Engineering Cybernetics and Mr. Hans Ilstad, Øystein Buer, Kjell Nordseth, Sverre Horntvedt and Magne Strandengen for technical assistance in building apparatus.

Trondheim, August 1975

Bjørn Angelsen

TABLE OF CONTENTS

NOMENCLATURE

$\langle(\cdot)\rangle$, $E\{(\cdot)\}$	ensemble average
$(\tilde{\cdot})$	time average
$(\overline{\cdot})$	space average
$E(\omega) \leftrightarrow e(t)$	Fourier transform pair is symbolized by $\leftrightarrow$
$\mathbb{R}$	set of real numbers
$R_{xy}(t_1,t_2)$	cross correlation function between x and y (pp 236)
$C_{xy}(t_1,t_2)$	cross covariance function between x and y (pp 236)
$\rho_{xy}(t_1,t_2)$	normalized cross correlation function between x and y (pp 121, 123, 160, 161)
$\zeta_{xy}(t_1,t_2)$	normalized cross covariance function between x and y (pp 158, 162)
$G_{xy}(\omega)$	cross power spectrum between x and y (pp 108, 238)
$\delta x = x - \langle x\rangle$	fluctuation of x
	If x and y are complicated expressions, they are separated by a comma to avoid misunderstanding. Finite time estimates are denoted by ˜ or ^.
t, p, τ	time and time lag parameters
$\vec{e}_1, \vec{e}_2, \vec{e}_3$	orthonormal vectors in space
$\vec{r} = x_1\vec{e}_1 + x_2\vec{e}_2 + x_3\vec{e}_3$ $\vec{\xi} = \xi_1\vec{e}_1 + \xi_2\vec{e}_2 + \xi_3\vec{e}_3$ $\vec{\zeta} = \zeta_1\vec{e}_1 + \zeta_2\vec{e}_2 + \zeta_3\vec{e}_3$	position vectors in the space
$\vec{\sigma} = \xi_1\vec{e}_1 + \xi_2\vec{e}_2$	position vector in the plane
f	frequency
ω	angular frequency
λ	wavelength
c	velocity of sound

$\vec{k} = k_1\vec{e}_1 + k_2\vec{e}_2 + k_3\vec{e}_3$	wave vector
$\vec{k}_T$	wave vector of transmitting transducer (pp 101)
$\vec{k}_R$	wave vector of receiving transducer (pp 103)
$\vec{q} = -(\vec{k}_T + \vec{k}_R)$	
$n_T(\vec{r},t)$	total concentration of cells (pp 74)
$n_0(\vec{r},t)$	ensemble average of n_T (pp 74)
$n(\vec{r},t) = n_T(\vec{r},t)-n_0(\vec{r},t)$	fluctuation of n_T (pp74)
$N(\vec{q},\omega)$	Fouriertransform of $n(\vec{r},t)$ (pp 109)
$N(\vec{q},t)$	space Fouriertransform of $n(\vec{r},t)$ (pp 110)
$N_0(\vec{q})$	space Fouriertransform of $n(\vec{r},0)$ (pp 110)
$\vec{j}(\vec{r},t)$	stochastic concentration current of cells (pp 76)
$A(\vec{r},t)$	scalar potential of $\vec{j}(\vec{r},t)$ (pp 77)
$\vec{B}(\vec{r},t)$	vector potential of $\vec{j}(\vec{r},t)$ (pp 77)
D	diffusion constant of cells (pp 76)
μ	mobility of cells (pp 80)
ν	viscosity og blood (pp 80)
$\rho(\vec{r},t)$	density of blood (pp 88)
$\rho_0(\vec{r},t)$	ensemble average of ρ (pp 88)
$\rho_1(\vec{r}.t) = \rho(\vec{r},t)-\rho_0(\vec{r},t)$	fluctuation of ρ (pp 88)
ρ_p	density of plasma (pp 96)
ρ_c	density of cells (pp 96)
$\varkappa(\vec{r},t)$	compressibility of blood (pp 87)
$\varkappa_0(\vec{r},t)$	ensemble average of $\varkappa$ (pp 88)
$\varkappa_1(\vec{r},t) = \varkappa(\vec{r},t)-\varkappa_0(\vec{r},t)$	fluctuation of $\varkappa$ (pp 88)
c_0	mean velocity of sound for blood (pp 89)
$\gamma_\varkappa$	compressibility fluctuation factor (pp 93)
γ_ρ	density fluctuation factor (pp 93)
k	Boltzmann's constant
T	Temperature

$\vec{v}(\vec{r},t)$	velocity field of blood (pp 76)
$\bar{v}$	mean velocity in a tube
$\hat{\vec{v}}$	vector weighted average of velocity field in the observation region (pp 138)
$\tilde{\vec{v}}$	finite time estimate of $\hat{\vec{v}}$ (pp 153)
$\vec{u}(\vec{r},t)$	velocity field of acoustic displacement (pp 87)
$p(\vec{r},t)$	acoustic pressure field (pp 87)
$\hat{p}(\vec{r},t)$	complex envelope pf p (pp 90)
$p_0(\vec{r},t)$	incident acoustic pressure wave (pp 89)
$\hat{p}_0(\vec{r})$	complex amplitude of p_0 (pp 89)
$\hat{p}_s(\vec{r},t)$	complex envelope of scattered wave (pp 91)
$e(t)$	received rf-signal (pp 102)
$\hat{e}(t)$	complex envelope of $e(t)$ (pp 105)
$e_1(t), e_2(t)$	quadrature components of e, the real and the imaginary part of $\hat{e}$. (pp 105)
$\hat{E}_T(\omega)$	finite time Fouriertransform of $\hat{e}$ (pp 107)
$E_1(\omega), E_2(\omega)$	finite time Fouriertransform of e_1 and e_2 (pp 163)
$R(\vec{\xi})$	amplitude weighting function of observation region (pp 103)
$\hat{R}(\vec{q})$	Fouriertransform of R (pp 107)
$\psi(\vec{\xi})$	phase weighting function (pp 103)
$L(\vec{\sigma})$	transition length through the observation region (pp 116)
θ	angle between ultrasonic beam and velocity direction (pp 116)
T_t	transit time through the observation region (pp 115,123)
T_d	period of doppler frequency corresponding to $\bar{v}$ (pp 123)
T	Integration time of averaging filter (pp 165, 237)
$h(\tau)$	impulse response of averaging filter (pp 154)
$h_0(\tau)$	reference filter for scaling (pp 237)
$H(\omega)$	frequency response of averaging filters

$H(x)$	Heavisides unit step function (pp 78)
$\delta(x)$	Dirac's unit impulse function
$\delta_{k\ell}$	Kroenecker's δ

1. INTRODUCTION

1.1. Review of Ultrasound diagnostic methods.

The use of ultrasound for transcutaneous medical diagnoses has been investigated for the past two decades. The methods used may be devided into two major groups

i) Ultrasonic imaging
ii) Ultrasonic blood velocity measurement.

For *imaging* ultrasound has the great advantage over x-ray techniques in that images may be obtained of defects and tissue that is difficult or impossible to obtain by x-rays. In addition the threshold dosis for damage of tissue is very much larger than what is necessary to obtain the image. Because of this ultrasound has become widely used in fields where x-rays has been considered too dangerous, such as diagnosis of the pregnant woman.

The main advantage of using ultrasound in *flowmetry* is that measurements may be performed transcutaneously. In addition calibration is very simple and by a pulsed meter velocity profiles may be obtained. For the last two reasons ultrasonic velocity meters have also been used interoperatively [63].

A. Ultrasonic imaging.

The usual method for ultrasonic imaging is to transmit a short burst of ultrasound into the tissue. The sound is then reflected by changes of the acoustic parameters of the tissue. The reflected signal is picked up by the same transducer as used for transmission, and amplified to get an appropriate signal level for processing.

The simplest way to present the data is to trigger an ordinary y/time scope by the transmitted burst. The intensity of the received signal may thus be displayed versus the time of arrival at the transducer. Let the x-axis time resolution be Δt µsec/div. The conversion factor between the depth in the tissue and the screen divisions will be

$$\frac{\Delta tc}{2} = 0.766 \cdot \Delta t \text{ mm/div} \qquad (1.1)$$

where c is the velocity of sound ($\approx$ 1530 m/s). This method of displaying the data is called *A-scan*. Figure 1.1a shows a typical A-scan of structures in the heart.

M-scan is another way of displaying the data which is analogous to the echosounder technique used in marine applications. A storage screen is used, and the ray is scanned fast vertically (typ. 13.3 μs/div which gives 10 mm/div) and slowly horizontally (typ. seconds pr. frame) at the same time.

The beam starts at the top of the frame at the transmission of each pulse, and is z-axis modulated by the intensity of the received signal. A reflector which has a fixed position then gives a horizontal line on the screen as the beam is moving horizontally.

The distance of the line from the top of the screen gives the depth of the reflector by the conversion factor given in Eq. (1.1). If the depth of the reflector changes with time, the line will be curved, and the instantaneous depth may be read from the display.

M-scan has its most potential area of application in the diagnoses of heart diseases. Figure 1.1b shows a typical M-scan of the left ventricle. The M-scan technique can also be used to measure the diameter of the aorta for estimating the volume flow of blood (see Section 7.3).

In the *B-scan* technique the transducer is mechanically scanned across the skin. The position and direction of the transducer is measured by suitable mechanisms. The coordinates are transferred to the direction and location of a fast linear scan of the electron beam across a storage screen. This scan is analogous to the veritcal motion of the beam in the M-scan technique. By z-axis modulating the beam by the intensity of the reflected signal, an image of the acoustic properties of the tissue may gradually be obtained by slowly scanning the transducer across the skin.

The B-scan technique can be used only with time stationary tissue because of the long time necessary to obtain a picture. Its area of application has been in the visualization of organs in the abdominal region, obsterics diagnoses and diagnoses of the pregnant woman. By synchronizing the display with the ECG signal, images of the heart in a fixed part of the cardiac cycle may be obtained by scanning over many cycles. This is called ultrasonic tomogram.

The main disadvantage of B-scan is the long time required to obtain an image. This has led investigators to construct arrays of transducers so that the scanning may be performed electronically and thereby fast. Two major types of arrays have been constructed

i) Multitransducer arrays
ii) Phase controlled arrays.

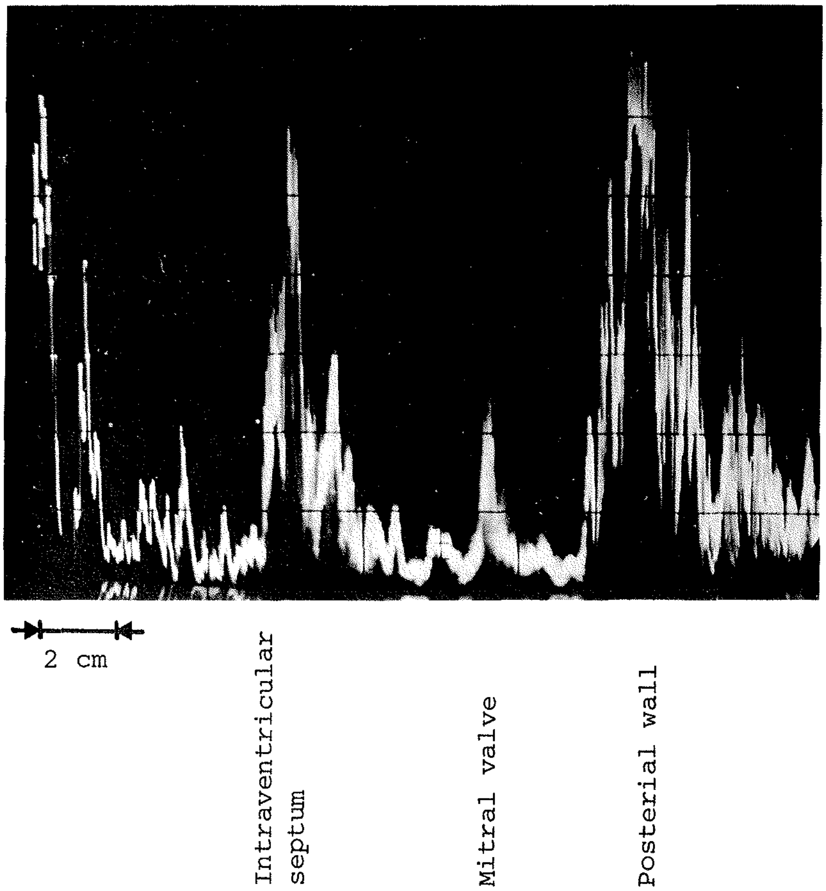

a)

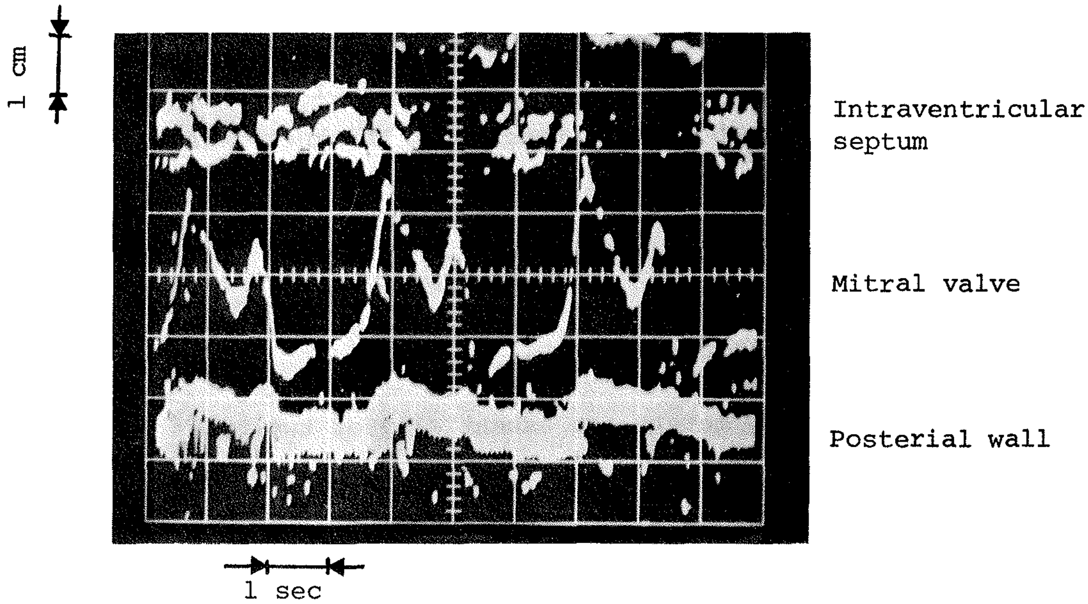

b)

Figure 1.1. *a) Typical A-scan of echos from structures in the heart.*
b) M-scan display of echos from structures in the heart.
The time variable depth of the structures may be observed.

In *multitransducer arrays* a single element or small group of elements of the array is used for transmission and reception in each period of time. By electronic switching, the active elements move along the array analogous to moving the transducer in the B-scan technique. Since the switching may be performed fast, one is enabled to study moving targets. The major application of this technique has been in heart disease diagnoses [2], [3], [9], [10].

In *phase controlled arrays* techniques used in radar and sonar have been applied to medicine. By controlling the phase of each element the direction of energy transmission and sensitivity of reception may be controlled [8]. Thus a sector scan image of the tissue is obtained. The technique requires complex electronics and therefore several investigators try to simplify the signal processing by using ultrasonic surface wave delay lines [11].

A review of the most common used imaging techniques has been given by Wells [12].

The ultrasonic *frequencies* used for imaging are in the range of 1-5 MHz, 2 MHz being the most commonly used. The optimum frequency is determined by two factors, the absorption of the wave in the tissue and the resolution capability. To get low absorption a low frequency is favoured because the absorption increases with increasing frequency. To get a good resolution capability, a high frequency is favoured because the minimum pulse length is inversely proportional to the frequency.

The minimum pulse length is determined by the system bandwidth which is limited by the transducer. The resonance frequency of the transducer is determined by its thickness. Changing the transducer thickness, keeps the relative bandwidth constant, so that the absolute bandwidth increases proportional to the resonance frequency.

B. Ultrasonic flowvelocity meters.

Ultrasonic flowvelocity meters are essentially of two types

i) Transit time meters
ii) Dopplershift meters.

In the first case, the difference in *transit time* between the upstream and downstream direction of an ultrasonic pulse, which crosses the vessel, is measured. This gives an estimate of the mean velocity of flow in the traversed region. The meter has to be used invasively [13].

Dopplermeters measure the dopplershift in frequency of ultrasound scattered by the concentration fluctuations of cells in blood. Of dopplermeters there are essentially three types

i) Continuous wave meteres (CW)
ii) Pulsed wave meters (PW)
iii) Correlation meters.

In the *CW-meter* [14], [17] a continuous ultrasonic beam is emitted towards the vessel by one transducer. The scattered ultrasound is received by another transducer and processed in an appropriate way. CW-velocity meters are commercially available for the measurement of velocity in peripheral vessels.

The *pulsed wave meter* [15], [16], [18] emits short pulses of ultrasound towards the vessel. After the transmission period, the scattered signal is received by the same transducer. Timegating of the received signals gives depth resolution.

By multigating the received signal with short intervals to different channels a simultaneous observation of the velocity at different depths along the beam may be performed [16], [63]. This technique is suitable for measuring velocity profiles in pulsatile flow like in the arteries.

To avoid *range ambiguity*, the reflected signal has to be received before the next pulse is transmitted. For observation of deep vessels a slow pulse rate must be used. On the other hand, to avoid *velocity ambiguity*, the scatterer cannot move more than a quarter of the ultrasonic wavelength in the direction towards or away from the transducer before it is hit by a pulse. Therefore, to measure high velocities a high pulse repetition frequency should be used. These two opposing requirements can be met only when the following inequality holds

$$v \cdot R < \frac{c^2}{8f_0} \tag{2.7}$$

v is the radial velocity component of the scatterer at distance R from the transducer. c is the velocity of ultrasound and f_0 the frequency. A similar limit on the *range velocity product* to avoid ambiguity will always be present when a pulsed beam in some way is used.

To increase the limit of this product, *coded pulses* with varying codes can be used [6]. Depth resolution may also be obained by emitting bandpass filtered noise continuously and performing *correlation* between the received signal and a delayed version of the transmitted signal [7]. By this method two transucers have to be used for transmission and reception. If a single transducer is used, the transmitted signal may be pulsed at a high rate to avoid velocity ambiguity. Range ambiguity is avoided by the correlation technique. Similarily *pseudorandom codes* known from radar and sonar may be used [57]. In the special application with measurement of velocity at a fixed depth, the noise correlation system seems to be the simplest to realize electronically.

Frequencies used for velocity measurements are in the range of 2-10 MHz. The scattering cross section of blood increases with increasing frequency in the fourth power (Chapter 4). Since the absorption increases with increasing frequency too, there is an optimum frequency for measuring velocity at a fixed depth [22]. This has led to a use of 5-10 MHz for peripheral arteries, while a lower frequency of 2-3 MHz has been used for the deeper arteries [21], [65], [66]. For the pulsed meter there is an additional requirement that the condition (2.7) on the range velocity product has to be met. This requires a low frequency of the ultrasound.

By scanning the transducer mechanically or electronically [3], [4], velocity meters may be used to obtain images of the flow cross section.

Besides being used for blood velocity meters, ultrasonic doppler instruments are used for early detection of the motion of the fetal heart [19].

1.2. Aim and content of this work.

The aim of this work was basicly to design an ultrasonic doppler apparatus capable of transcutaneously measuring the velocity of blood in deep arteries such as aorta. Out of this work grew the need for a better theoretical understanding of the ultrasonic scattering process in blood and how velocity could be calculated from the received signal.

Transcutaneous measurement of aortic blood velocity has been reported by MacKay [65] and by Light & al [66] who both use a CW meter. The transducer is situated at the suprasternal notch as shown in Figure 1.2.

Because of the inability of the CW-meter to resolve depth all the bloodflow in the path of the beam is measured. There are several ramifications of aorta in this region, so it is not only the flow in the aorta which is measured.

Light claims to avoid this difficulty by spectrum analyzing the received signal. The branch arteries and veins in this region all have a large angle

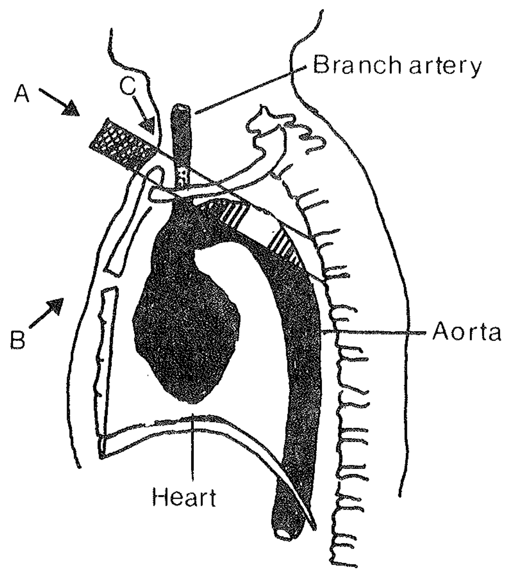

Figure 1.2. Schematic illustration of the measurement of aortic blood velocity. The transducer is placed at the suprasternal notch and points towards the aortic arc. The flow in aorta ascendence may be observed by holding the transducer in the C direction. Aortic blood flow is sometimes observable from the B route.

of inclination to the beam. In addition the flow in some of them will be in the opposite direction to that in the aorta. Flow from this part therefore gives small frequency shifts or a frequency shift different in sign compared to that from the aortic arc, where the beam is almost tangential to the flow direction. Since there are good indications that the flow profile is almost rectangular, the contour of the spectrum should be an estimate of the mean aortic velocity.

Although arguments can be given that this system works, the inability to resolve depth is a severe practical limitation. First of all a depth resolution enables the operator to control what region of flow he is actually measuring.

Second, all the false information is removed from the received signal. In this way a simple mean velocity estimator may be applied instead of the spectrum analysis.

Thirdly, by focusing the beam, the velocity profile may be obtained by either scanning the focus across the vessel lumen or by multigating the return signal when the beam crosses the vessel [63].

We have chosen to build a pulsed wave velocity meter to obtain depth resolution. To get a high limit of the range velocity product, as low a frequency of the ultrasound as possible should be used, Eq. (2.7). Since the scattering cross section of blood is proportional to the frequency in the fourth power, the lower limit of the frequency is determined by requirements on the signal to noise ratio.

Several frequencies were tried and 2 MHz seems to be the best choise from several practical reasons. A S/N ratio of 20 dB is obtained in most cases, and S/N ratio of 30 dB has been observed. We use two pulse repetition frequencies, 6.5 kHz and 9.75 kHz. The 9.75 kHz frequency gives a maximum measureable velocity of 1.7 m/s and a maximum range of 7.3 cm. The 6.5 kHz frequency gives a maximum velocity of 1.1 m/s and a maximum range of 11 cm.

The only practical situation where the velocity limit has been violated is by aortic stenoses, where velocities up to 5 m/s has been measured. To observe such velocities a continuous wave instrument may be used since the high velocities exist only in the region of the stenosis. The location of the stenosis may be observed by the pulsed meter.

Although the doppler velocity meter has been ivestigated for the past decade, little theoretical or experimental work has been done to study the scattering process, and thereby the functioning of velocity estimators based on the received signal. The only experimental study of the scattering process to date seems to be that of Reid & al. [44].

Their conclusion that the red cells may be considered as stochastically independent scatterers in the concentration range of 7-40 % seems unlikely, both from experiments we have performed and from physical reasoning based on the mean distance between the cells compared to their size.

Flax & al.[48] was the first to take a step towards a theoretical description of the velocity meter, basing their assumptions on the work of Reid & al. Although their approach was very simple, they, using the results of Rice [20], showed some properties of the zero counting detector which proves to hold for the more detailed model of scattering presented in this work.

A more detailed model of the scattering process is given by Brody [45]. He too bases his model on the assumption of stochastically independent scatterers set forth in the paper of Reid & al. He also considers timesteady velocity fields only.

We felt that the assumption of independent scatterers was not valid, and we therefore undertook a study of the scattering process based on a model which takes the interaction between cells into account. Insdtead of calculating the scattered field by the sum of the contribution from individual cells, we treat the scattering to be caused by fluctuations in the acoustic parameters of a continuum. This simplifies the calculations as long as the correlation length of the fluctuations are small compared to the wavelength. We are also able to handle nonstationary velocities, and the validity of estimators are shown for arbitrary timevarying velocity fields. The theory is given in Chapter 4 and 5.

It turns out that the interaction between the cells introduces little principal change of the results as long as the ultrasonic wavelength is large compared to the correlation length for the fluctuations. The results of Flax and Brody are not severely degraded, except that the scattered intencity will decrease from the proportional dependency of the cell concentration, n_0, when interaction between the cells occur.

Reliable calculations of the blood velocity from the received signal has been a problem since the earliest experiments of Satomura [14] and Franklin & al. [17]. The zero counting detector in various forms has been the most frequently used estimator for the velocity. Early experimental evidence and the theoretical work of Flax & al has shown that this estimator has to be calibrated after the velocity profile.

Many workers therefore have felt that a full spectrum analysis was the best way to treat the information [21], [65], [66]. This, however, requires complex instrumentation and gives the user an overflow of data since in most applications it is only the mean velocity across the vessel lumen which is interesting. A spectral analysis, however, may reveal the type of flow, laminar, turbulent, etc.

Until recently there has existed no satisfactory solution of this problem. In his Ph.D. thesis, Brody suggests an estimator that calculates the mean velocity in the region observed by the instrument. The estimator may be realized by analogue components. Independently Arts and Roevros [70] have proposed an estimator which is approximately equal to that given by Brody. From our theory of the ultrasonic scattering, we show that these estimators give a vector weighted average of the velocity field across the region of observation, Chapter 5.

The estimators of Brody and Arts and Roevros have the disadvantage that they use ordinary multiplcation and division. With commercially available components it is difficult to obtain these functions with sufficient long time stability to an economical price. In our search for a better solution we have developed an estimator which uses sgn-multiplication* instead of ordinary multiplication. By this, far better long time stability is obtained. The necessary trimming components are also fewer and the estimator proves to have a smaller variance. The validity of the estimator is proved theoretically from our model of the scattering process. (See Section 5.2).

The zero crossing detector has got its renesance with the invention of the pulsed wave meter. By timegating of the received signal and focusing the ultrasonic beam, the region of observation can be made so small that the velocity field is essentially constant within this region. In this case the spectrum of the received signal is so narrow that the zero counting detector works well. We do not consider this type of estimator here since we feel that the results given by Flax & al. are satisfactory. His assumption of the powerspectrum of the received signal follows from approximations of our theory.

A schematic description of the functioning of dopplermeters are given in Chapter 2. This is done to form a basis for the understanding of the rest of this work. A more detailed description of our instrument is found in Chapter 7 together with experimental studies on its functioning. In vitro measurements of the mean velocity of a steady and pulsatile flow, velocity profiles of steady flow and an experimental study and comparison between the Arts velocity estimator and our new estimator are given. Some results of in vivo measurements of blood velocity in aorta are also given in this chapter.

The aortic diameter is measured by the ordinary M-scan technique. By measuring the mean velocity across the vessel with our instrument, the volume flow of blood may be estimated. One essential difficulty in doing this is that the angle of inclination between the ultrasonic beam and the flow direction is not known. This angle seems to be quite large for the ascending aorta. To avoid this difficulty Aaslid [23] has suggested to use a focused transducer to get a small observation region, and then scan this region across the arterial lumen. By suitable techniques the lumen area seen along the ultrasonic beam may be obtained. Multiplicating this area with the component of the mean velocity measured (along the ultrasonic beam) the volume flow of blood is obtained, without knowing the angle of incidence between the beam and the flow direction. A mechanical sectorscanning system has therefore been built. There has not yet been time to use this system for cardiac output measurements, but an example of vessel-visualization is given in Chapter 7.

---

* For def. of sgn multiplication see Section 5.2.

The functioning of the transducer is described in Chapter 3. We use ceramic transducer discs of a lead-zirconate-titanate composite, operating at resonance in the thickness mode. The bandwidth of the transducers is limited and this sets a limit on the shortest pulse that may be transmitted and received. The length of the observation region along the ultrasonic beam is $ct_p/2$, where c is the wave velocity and t_p the duration of the pulse. To get a good longitudinal resolution of the system, a large bandwidth of the transducer is desired. This may be achieved by either backing the transducer with high acoustic impedance, absorbing backing or using acoustical matching layers to raise the acoustic load impedance seen from the transducer face.

The first method introduces losses in the transducer which is a severe drawback in our application where the received signal power is low. We have therefore studied the effect of matching the transducer to the load both theoretically and experimentally (Section 3.4). A large increase in the transducer bandwidth is obtained without introducing losses in the transducer.

2. DOPPLER VELOCITY METERS

To form a basis of the understanding of the rest of this work we give a schematic description of ultrasonic velocity meters. We start with the continuous wave meter and then describe the modifications for pulsed wave meters and correlation meters. More detailed descriptions of our instrument is given in Chapter 7. Signal to noise power ratios are compared for the instruments.

2.1. Continuous wave meter (CW) [14], [17].

Measurement of blood velocity by a CW meter was first reported by Satomura [14] and has since then been investigated by numerous workers. A block diagram of the meter is shown in Figure 2.1.

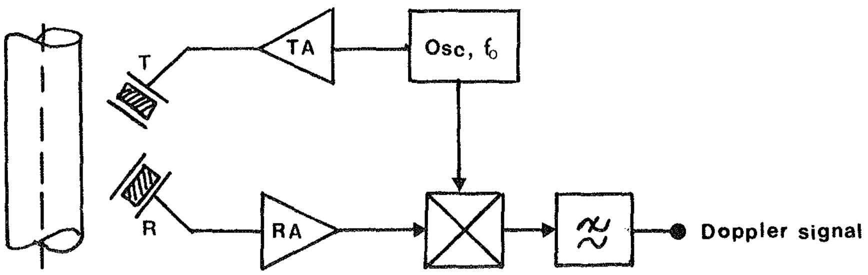

Figure 2.1. Schematic CW dopplermeter.

The oscillator generates a continuous signal of single frequency f_o. This signal is transmitted by the transducer T. The ultrasound is scattered from fluctuations in the concentration of cells. The scattered wave is picked up by the transducer R and passes through a receiving amplifier RA before it is analyzed.

A typical transducer vessel configuration is shown in Figure 2.2. The acoustic beams when the transducers are excited separately are shown schematically. By reciprocity the pattern of sensitivity of the receiving transducer will be the same as the field pattern during emission (Section 4.3C).

In most cases of application the vessel is in the nearfield of the transducers. For transducers that are small compared to the wavelength, the field in this part has a very complex dependency on space (Section 3.1). If, however, the transducers are large compared to the wavelength, the near field may be approximated by plane waves.

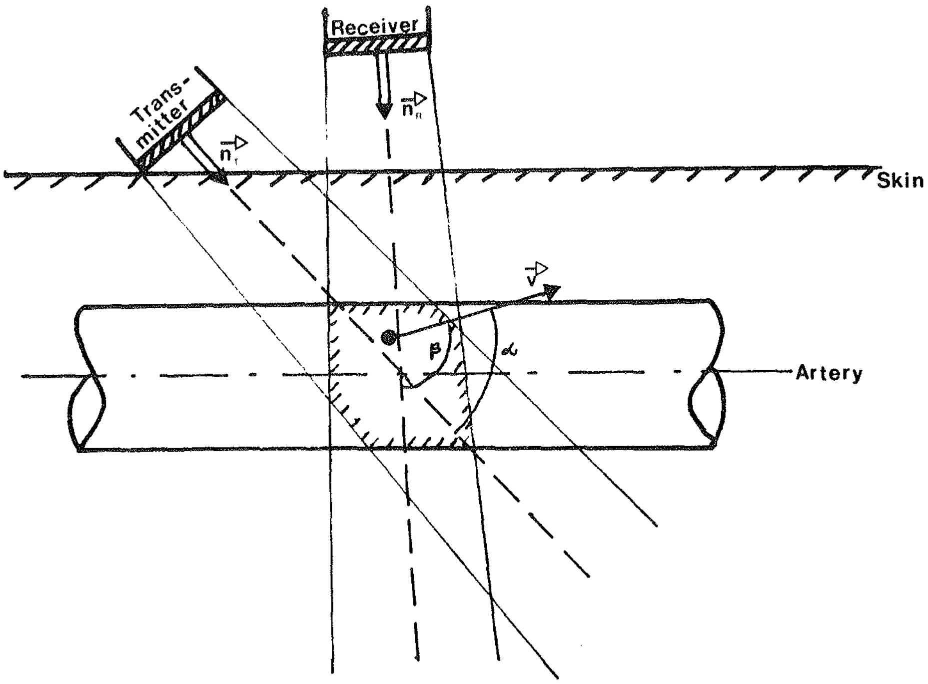

Figure 2.2. Schematic representation of the vessel and transducers for transcutaneous blood velocity measurement. $\vec{n}_T$ *and* $\vec{n}_R$ *are the unit normal vectors to the transducer faces.*

The foldover between the transmitting and the receiving transducer field patterns determines the region of the artery that is observed. This region is shadowed in Figure 2.2. Asuming large transducers so that the plane wave approximation may be performed, a scatterer which traverses this region with velocity $\vec{v}$ gives a burst of oscillations out of the receiving transducer with mean frequency (Section 5.1C)

$$f = f_0[1 - \frac{v}{c}(\cos\alpha + \cos\beta)] = f_0[1 - \frac{1}{c}\vec{v}(\vec{n}_T + \vec{n}_R)] \tag{2.1}$$

c is the velocity of sound.

This expression is actually valid only when $v/c \ll 1$, which is true in our case where $c \approx 1500$ m/s and $v \approx 1$ m/s. Because of the finite transit time of the scatterer through the observation region, the received signal actually has a distribution of frequencies around f (see Section 5.1C).

The *doppler frequency* f_d is defined by

$$f_d = f - f_0 = -\frac{f_0}{c}\vec{v}(\vec{n}_T + \vec{n}_R) \tag{2.2}$$

A scatterer moving towards $\vec{n}_T + \vec{n}_R$ gives a *positive* doppler frequency, while a scatterer with a velocity component along $\vec{n}_T + \vec{n}_R$ gives a *negative* doppler frequency. It is therefore convenient to define *positive direction of velocity* towards $\vec{n}_T + \vec{n}_R$.

For transducers that are not large compared to the wave length, the spectrum will be additionally broadened, while the mean frequency will be the same (see Section 5.1E).

In the practical situation the received signal will be the sum from many scatterers. It will consist of the carrier frequency f_0 which is reflected from stationary targets together with a sideband reflected from moving targets.

To get better frequency resolution in the processing, the signal spectrum is shifted to lower frequencies by a synchronous demodulator. This is essentially a multiplicator where the signal is multiplied with a reference signal of fixed frequency, f_r, and lowpass filtered to remove high frequency components. After the demodulation the spectrum of the signal is shifted an amount f_r downwards in frequency.

The earliest investigators used $f_r = f_0$ for demodulation. In this way the sign of the doppler frequency - and thereby the direction of flow - cannot be resolved, Figure 2.3a and 2.3b. For sign resolution two methods may be applied.

The one is to use a signal with frequency Δf smaller than f_0 for demodulation [63], [65], [66]. By this f_0 will be shifted to Δf. A positive dopplershift, f_d, will give a frequency $\Delta f + f_d$ while a negative, $-f_d$, will give a frequency $\Delta f - f_d$. Figure 2.3c and 2.3d shows the spectra before and after the demodulation in this case.

The other way to resolve the sign of the dopplershift is to use the quadrature components of the received signal as discussed in Chapter 5 [67].

In Figure 2.1 we have used the term *dopplersignal* for the demodulated signal. In the following we shall use this term only when $f_r = f_0$. The *complex dopplersignal*, $\hat{e}(t)$, is defined by the following equation

$$e(t) = \mathrm{Re}\{\hat{e}(t)e^{i\omega_0 t}\} \tag{2.3}$$

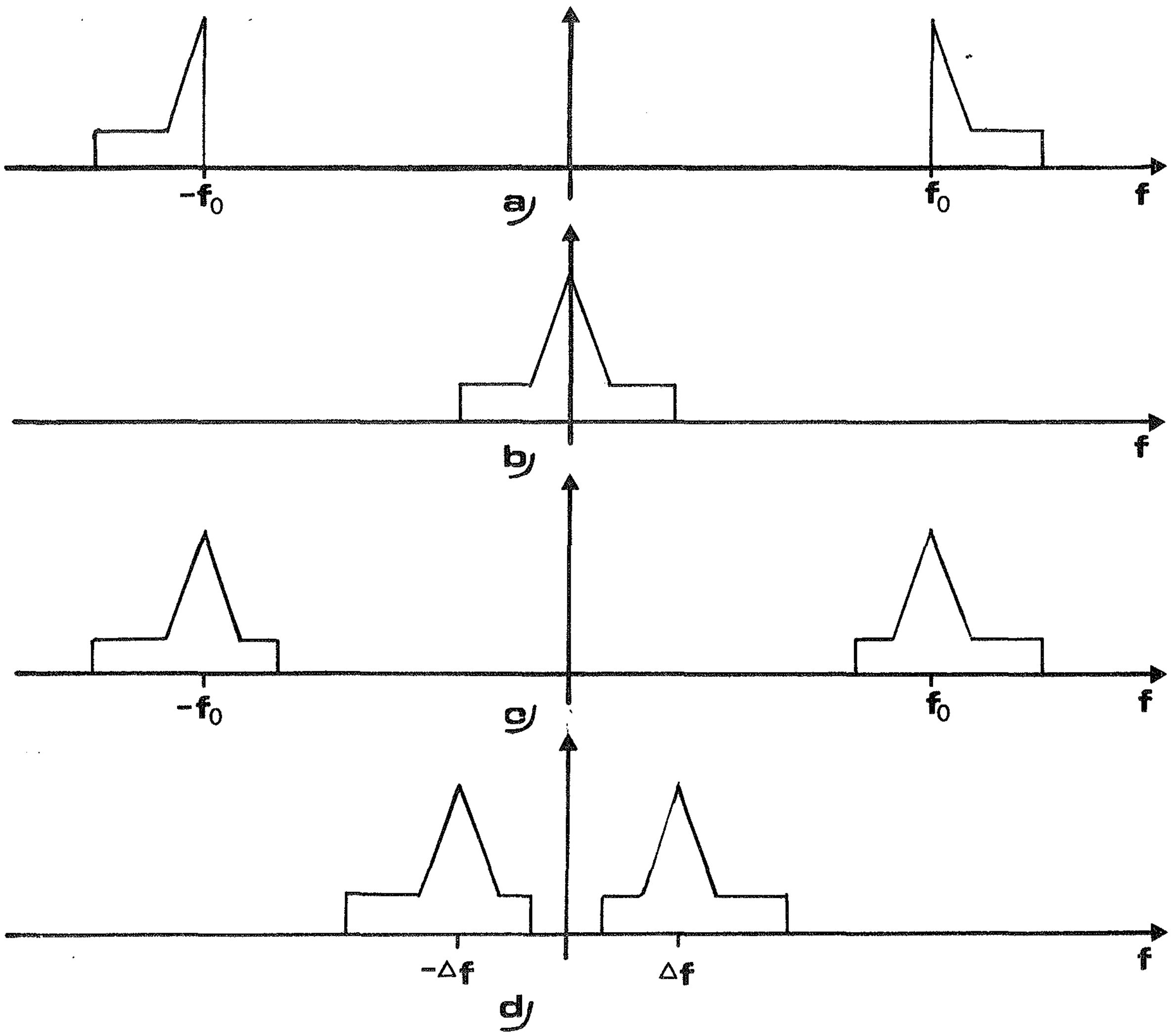

Figure 2.3. Synchronous demodulation.

a) Spectrum of received signal when all scatterers have velocities towards the transducers.

b) Demodulated spectrum by multiplication with signal of frequency f_0.

c) Spectrum of the received signal when both signs of dopplershift are present.

d) Resolution of the sign of the dopplershift by multiplication with a signal of frequency $f_0 - \Delta f$.

The high peak of the spectrum near f_0 *indicates the strong reflected signal from slowly moving targets such as vessel walls.*

where $e(t)$ is the narrowband received signal and ω_0 the angular frequency of the transmitted signal.

2.2. Pulsed wave meter (PW). [15],[18].

Both a single transducer and double transducers may be used for the PW doppler meter. A diagram of the meter with a single transducer is shown in Figure 2.4.

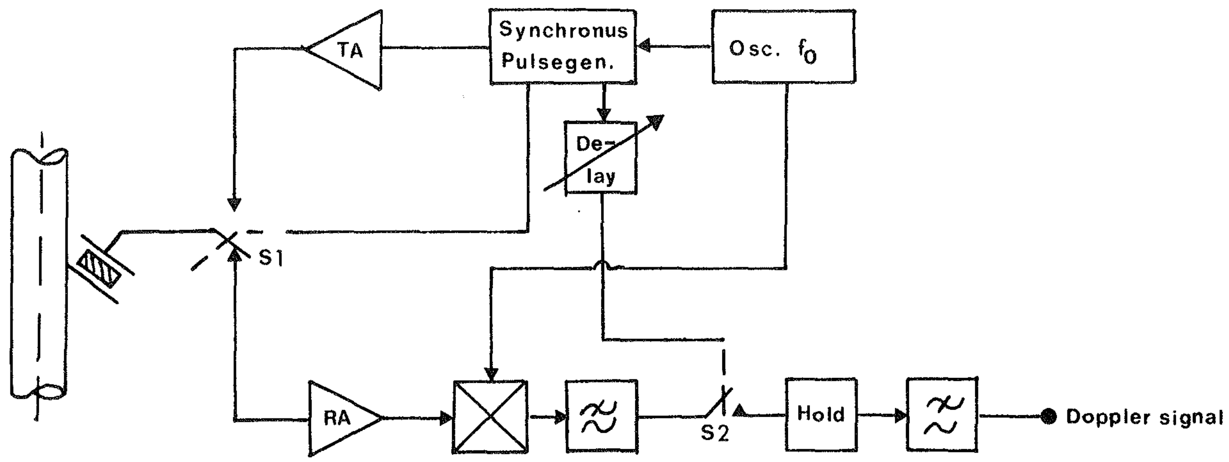

Figure 2.4. Pulsed wave doppler meter.

Coherent pulses of rf frequency, f_0, oscillations are generated by the pulse generator which is driven by a rf oscillator at frequency f_0 to maintain coherence. The pulses are transmitted by the transducer which is driven by the transmission amplifier, TA. During the transmission period the transducer is connected to TA by the switch S1. After the pulse transmission the transducer is connected to the receiving amplifier RA. The first lowpassfilter is used to remove the high frequency components generated in the multiplication. The filter must have so large bandwidth that the pulses may pass without distortion.

The signal is thus demodulated. A switch, S2, closes for a very short interval of time ($\approx 1\ \mu s$) a varyable delay after the pulse transmission. By this the signal reflected from the depth corresponding to the time delay is singled out. The conversion between delay, τ, and target depth, ℓ, is given by the following equation

$$\ell = \frac{c \cdot T}{2} \tag{2.4}$$

where c is the velocity of sound ($\approx$ 1530 m/s).

To maintain signal level a holding circuit is used. A lowpassfilter removes the high frequency components introduced in the sampling.

The signals for the PW-meter are shown in Figure 2.5. The numerical values are typical for a meter with f_0 = 2 MHz.

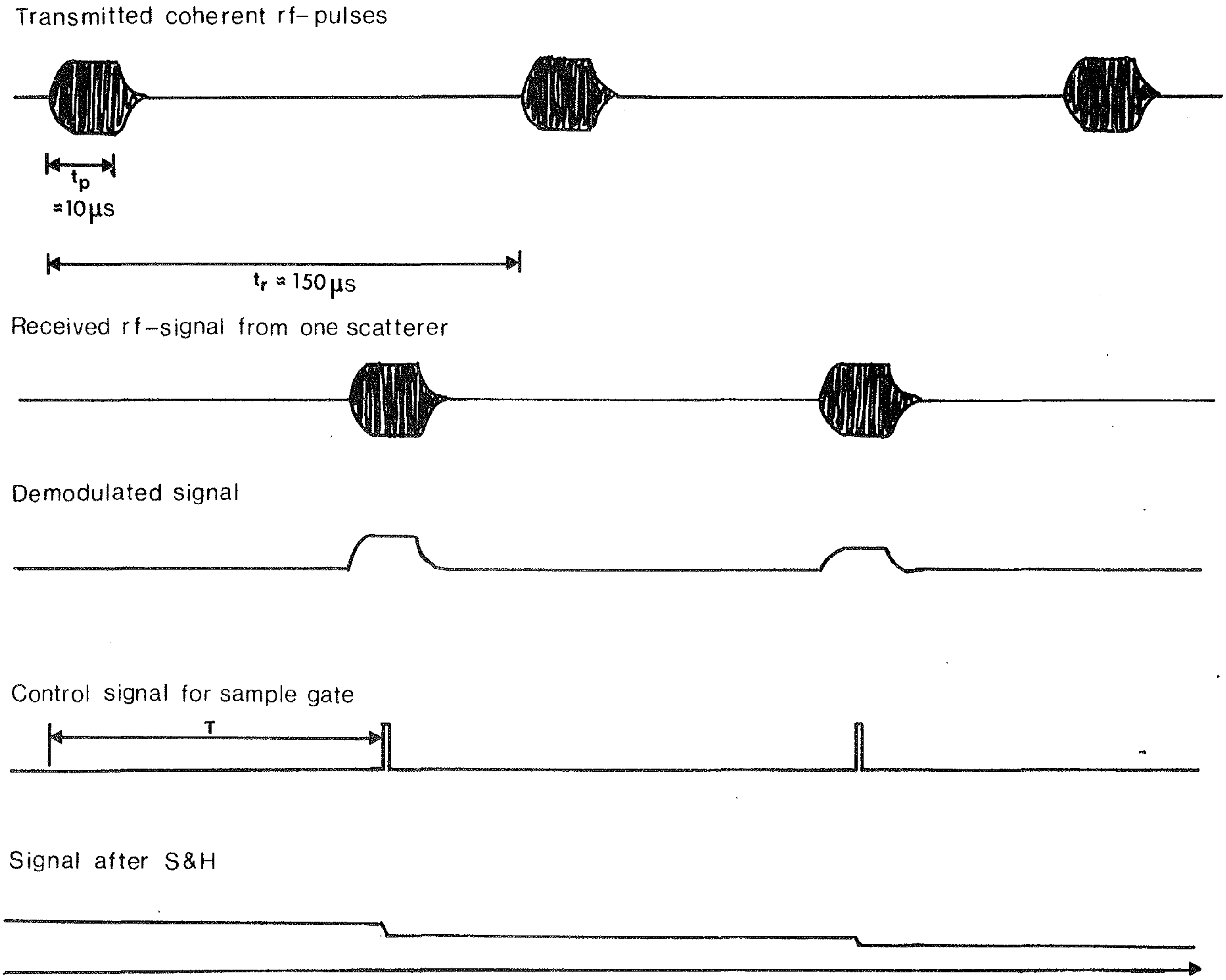

Figure 2.5. Signals in the pulsed flowmeter. The bandwidth of the system determines the risetime of the pulses.

The dopplersignal is sampled at the pulse repetition frequency. According to the Shannon sampling theorem the pulse repetition frequency has to be twice the maximum occuring doppler frequency. Or in other words, to avoid ambiguity in the received phase, the scatterer cannot move more than $\lambda/4$ in the direction of $\vec{n}_T + \vec{n}_R$ without being hit by a signal. If the offset frequency method is used to resolve the sign of the dopplersignal, the repetition frequency has to be twice that of the demodulated signal. The quadrature method (Chapter 5) to resolve the sign of the shift, is therefore the most optimum method concerning sampling rate.

If the sampling is performed before the next pulse is transmitted, range ambiguity is avoided because of the absorption of the wave in the tissue. For a given repetition frequency there is a limit on the measureable range, R.

$$R < \frac{c}{2f_r} \tag{2.5}$$

From above there is a limit of the maximum measurable velocity component along $(\vec{n}_T + \vec{n}_R)$

$$v < f_r \cdot \frac{c}{4f_0} \tag{2.6}$$

Combining these two expressions we get the limit of the range velocity product

$$v \cdot R < \frac{c^2}{8f_0} \tag{2.7}$$

The closing time of the gate is very short compared to the length of the transmitted pulse. The region of scatteres which are observed is therefore determined by the length of the pulse. The location of the observation region will be between $c\tau/2$ and $c(\tau - t_p)/2$ in front of the transducer, for a single transducer (Figure 2.6a). For double transducers the location will be as shown in Figure 2.6b.

Real observation regions will not have sharp boundaries as indicated in the figure. First of all the intensity of the transmitted beam and the sensitivity of the receiving transducer will have a smooth oscillatory decay at the boundaries. Second the system has finite bandwidth so that the pulses have rise and fall times different from zero. The signal from a scatterer will therefore increase smoothly as the scatterer enters the observation region, (see Section 3.5). A theoretical and experimental study of the form and weight function of the observation region is given in [25], [26] for two focused transducers.

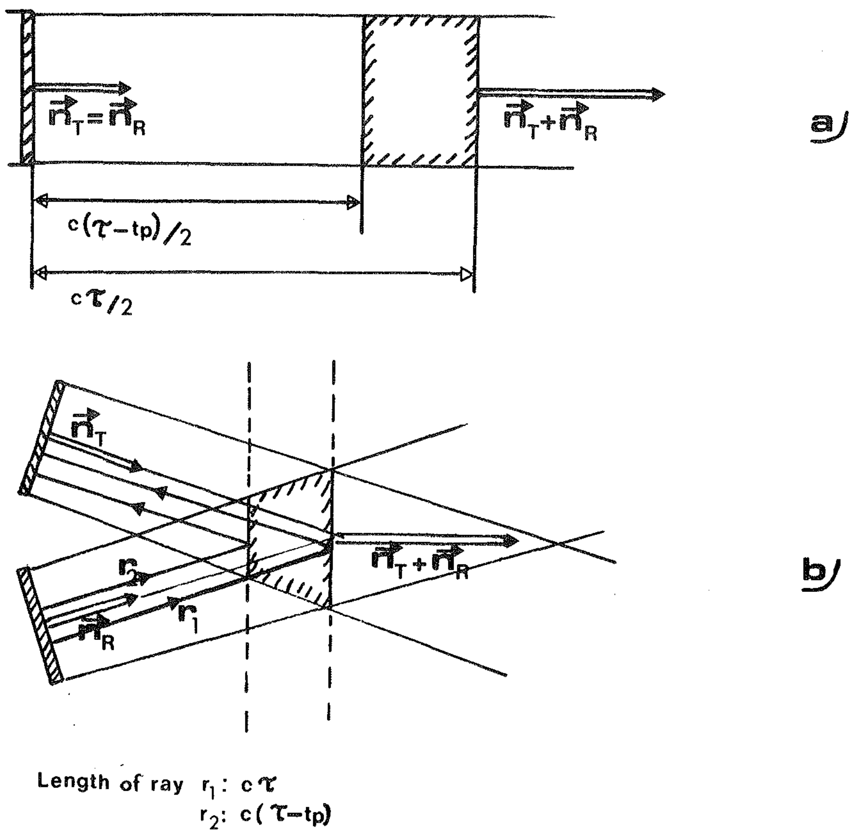

Figure 2.6. Idealized observation region for PW-meter.
a) single transducer, and
b) double transducers.

The length of the observation region along $(\vec{n}_T + \vec{n}_R)$ is determined by the pulse length. As discussed at the end of Chapter 1, the minimum pulse length is proportional to the inverse bandwidth Δf. Taking the constant of proportionality to be unity, the minimum longitudinal resolution length along $(\vec{n}_T + \vec{n}_R)$ is given by

$$\delta\ell_\ell = \frac{c}{2\Delta f} = \frac{1}{2\Delta f/f_0} \cdot \frac{c}{f_0} \tag{2.8}$$

The transversal resolution capability is determined by the beamwidth. The minimum focus diameter which may be obtained at a distance ℓ from a circular transducer of diameter d is [74]

$$d = 2.22\lambda \cdot \frac{\ell}{d} \tag{2.9}$$

where λ is the ultrasonic wavelength. This equation defines the diameter of the focus by the first zero of the intensity. Actually a diameter where the amplitude of the field has fallen to 10 dB of the axial value would be a better definition. At this point the sensitivity of the system to a scatterer will be 20 dB below that at the transducer axis. By this definition 2.22 should be exchanged by 1.72 in the above equation. The minimum resolution length transversal to the beam direction at a distance ℓ from the transducer will then be

$$\delta\ell_t = 1.72 \frac{c}{f_0} \cdot \frac{\ell}{d} \tag{2.10}$$

where we have inserted $\lambda = c/f_0$.

To get a small region of observation, a large, focused transducer with large bandwidth should be used. We also see that the minimum resolution length is inversely proportional to the frequency f_0. Practical values for aortic flow velocity measurement from the suprasternal notch are

$$d = 20\text{ mm},\quad \ell = 70\text{ mm},\quad f_0 = 2\text{ MHz},\quad \Delta f = 150\text{ kHz},\quad c = 1500\text{ m/s}$$

This gives

$$\delta\ell_\ell = 5\text{ mm} \qquad \delta\ell_t = 4.5\text{ mm} \tag{2.12}$$

2.3. The correlation doppler meter [5], [7].

For comparison we describe the correlation doppler meter. A diagram is shown in Figure 2.7. The source generates a continuous band limited random noise centered around the transducer resonance frequency. Pseudorandom coded signals may also be used. In this case the code has to be so long that range-ambiguity is avoided or coded pulses have to be used.

The received signal is after an amplification fed to a correlator which produces the crosscorrelation between the received signal and a delayed version of the transmitted signal.

The output of the correlator from a stationary target is given in Figure 2.8 for a Lorenzian shape of the noise spectrum. The signal delay time is τ_s, while the instrument delay time is τ_d. When the scatterer is moving, τ_s changes and the output of the correlator will oscillate with the doppler frequency. A moving target will therefore give a burst of oscillations at the doppler frequency when τ_s passes τ_d. τ_s is determined by the position of the scatterer along the direction of $\vec{n}_T + \vec{n}_R$.

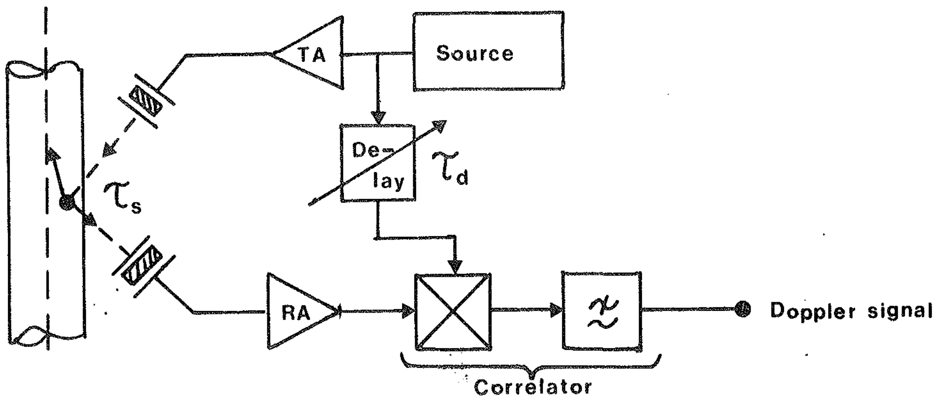

Figure 2.7. Correlation system for ultrasonic doppler measurements.

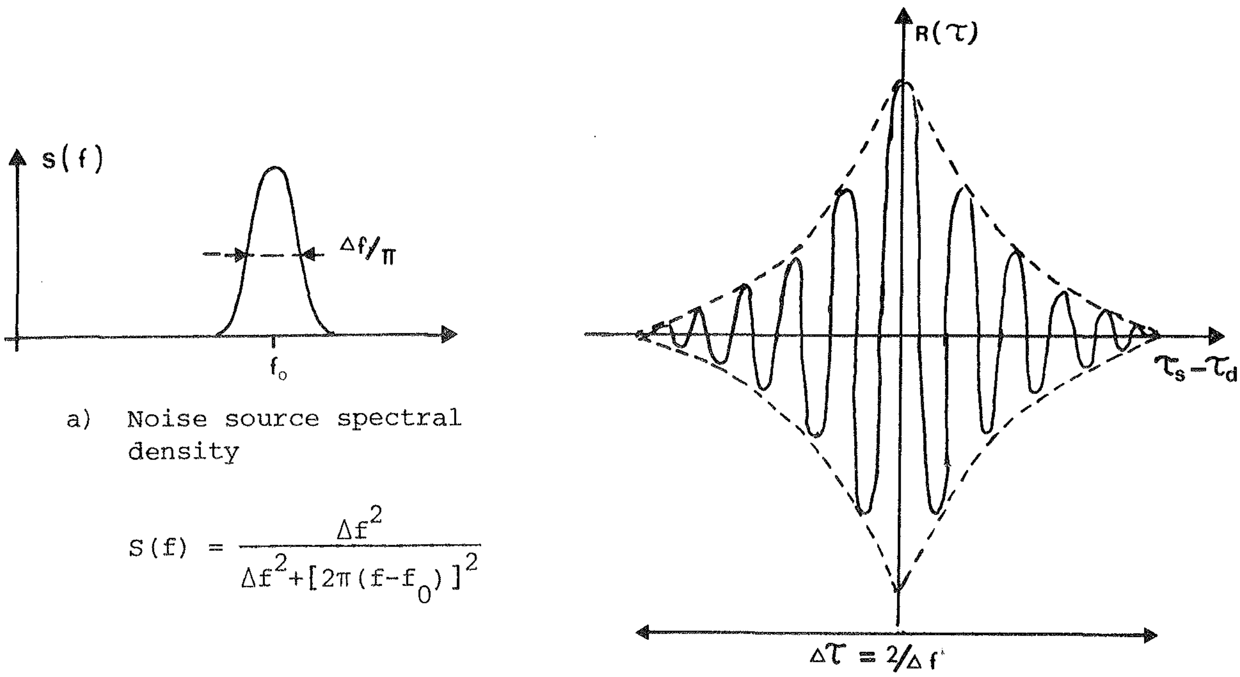

$$S(f) = \frac{\Delta f^2}{\Delta f^2 + [2\pi(f - f_0)]^2}$$

Figure 2.8. Transmitted noise spectrum a), and output of the correlator from a stationary target b) [7].

The longitudinal resolution of the instrument along $\vec{n}_T + \vec{n}_R$ is the same as for the pulsed doppler meter with minimum pulse length.

$$\delta \ell_{\ell} = c \cdot \Delta\tau = \frac{c}{2\Delta f} \tag{2.12}$$

If a single transducer operation is desired, the beam may be pulsed. The pulse repetition rate has to be so high that it meets the criterion of the Shannon sampling theorem at the maximum doppler frequency present. Range ambiguity is avoided by the correlation process.

2.4. Signal to noise ratio (S/N).

In doppler measurements there are three types of disturbances or noise:

a) Echos from targets outside the observation region caused by multiple path beams.

b) Echos from targets other than blood in the observation region.

c) Electronically generated noise.

Type a) and b) noise is proportional to the transmitted power as long as linear elasticity is prevailed. Fortunately the strongest signal of this type is reflected from slowly moving targets which gives small dopplershifts. They may therefore be removed by suitable *highpass filtering* of the doppler signal.

Since the doppler frequency is proportional to the utilized rf frequency, the cut off frequency of the highpass filter will also be proportional to the rf frequency used. Moreover the cut off frequency will depend upon the the state of activity of the person being examined, and in what part of the body the artery is located. In peripheral arteries the motion of artery walls and tissue around the artery is slower than near the heart, and a lower cut off frequency may therefore be used for peripheral arteries. In our case with aortic velocity measurement and f_0 = 2 MHz, filters in the range of 300 - 1200 Hz are used depending on the level of activity of the subject.

Since the lowest dopplershifts from the blood are also removed by this higpass filter, a *systematic error* is introduced in the measurement. This error will depend on the flow profile and the mean velocity. A further discussion of this error is given in Section 5.2E.

Electronically generated noise will mainly originate from the source receiving transducer and from the first stage in the receiving preamplifier. For the *CW meter* the noise bandwidth is given by the bandwidth of the last filter in the system.

In the *PW meter* the bandwidth of the preamplifier should be only slightly larger than that for the transducer for no degradation of the pulse risetimes with a minimum of noise addition. When the multiplication reference frequency equals f_0, the bandwidth of the first filter should be half that of the preamplifier.

Let the noise power density out of the preamplifier (with transducer at the input) be N_0 per unit frequency. If the amplifier bandwidth is Δf, the total noise power is $2N_0\Delta f$. This will also be the total noise power out of the video amplifier. Because of the *sampling*, the spectrum is shifted upwards and downwards in frequency by multiples of the sampling frequency f_s.

In Figure 2.9 the noise spectrum out of the video filter is indicated schematically. The bandwidth of the sampling filter is set to B. By the sampling, the total noise power out of the sampling filter will be the sum of the power contained in the shaded areas.

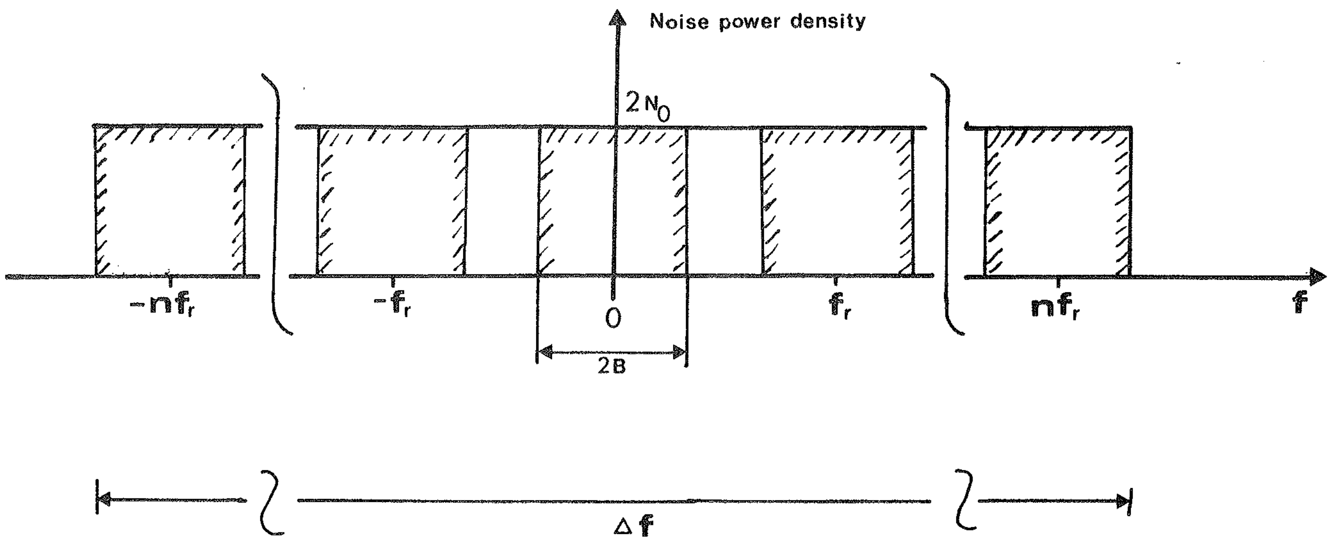

Figure 2.9. Schematic noise spectrum out of the demodulator filter. B is the bandwidth of the sample filter.

The noisepower in the dopplersignal will thus be (neglecting some small boundary errors that may arise because $\Delta f \neq 2(nf_r + B)$)

$$N_{CW} = 2N_0 \cdot 2B \qquad \text{CW meter}$$
$$N_{PW} = 2N_0 \cdot \frac{2B}{f_r} \Delta f \quad \text{PW-meter} \tag{2.13}$$

The received signal power, S, will in both cases be proportional to the peak transmitted power

$$S = \alpha \cdot P_{peak} \qquad \text{CW- and PW-meter} \tag{2.14}$$

For the CW-meter this is trivial. For the PW-meter this is given by the S&H circuit. If the minimum pulselength for the PW-meter is used, we have

$$t_p = \frac{1}{\Delta f} \tag{2.15}$$

In this case the average transmitted power will be

$$P_{avg} = P_{peak} \cdot \frac{f_r}{\Delta f} \qquad \text{PW-meter}$$
$$P_{avg} = P_{peak} \qquad \text{CW-meter} \tag{2.16}$$

The signal to noise power ratios will be in the two cases

$$\frac{S_{PW}}{N_{PW}} = \frac{\alpha \cdot \Delta f / f_r P_{avg}}{N_0 \cdot \frac{2B}{f_r} \Delta f} = \frac{\alpha}{N_0 2B} P_{avg} \qquad \text{PW-meter}$$
$$\frac{S_{CW}}{N_{CW}} = \frac{\alpha}{N_0 2B} P_{avg} \qquad \text{CW-meter} \tag{2.17}$$

When the minimum pulselength, Eq. (2.15), of the PW-meter is used it has the same S/N ratio as the CW-meter when the avereage transmitted power is the same.

If this minimum pulselength is not used, the PW-meter will have a poorer S/N-ratio than the CW-meter for the same average transmitted power. Thus, to get a good S/N-ratio for the PW-meter with a minimum average transmitted power, the minimum pulselength should be used. By this a high peak power may be transmitted and thereby a large received signal power. The maximum peak power must, however, be kept below the threshold value for damage of tissue. There is no sharp definition of this value but a peak power less than 1 Wcm^{-2} and a continuous power less than 0.1 Wcm^{-2} are usually considered safe for adult tissue [24]. If the peak power is limited by the damage level the S/N-ratio will decrease as the longitudinal resolution capability is increased.

For aortic flow-velocity measurement a logitudinal resolution of 5 mm and sometimes 10 mm is satifactory. From Eq. (2.8) this requires a bandwidth of 150 kHz and 75 kHz respectively of the transducers and the preamplifier.

No quantitative comparison between the S/N-ratio of the *correlation meter* and the CW- and PW-meters will be given in this work. The three types of noise described at the beginning of this paragraph will also occur for the correlation meter. The correlation meter has, however, the advantage over the PW-meter in that it is only the multipath echoes which have a signal delay in the tissue equal to τ_d that is observed. For the PW-meter all the multipath echoes that arrive at the sampling point disturb the measurement.

The only way to suppress the two first types of noise is to use a highpass filter as for the CW- and PW-meter. The electronic noise power is determined by the bandwidth of the correlator filter. This bandwidth is determined by the maximum doppler frequency present.

The types of noise described above will also occur for the correlation meter. Also the finite integration time of the correlator will introduce additional noise, because echos from targets outside the observation region are not fully averaged to zero. Since the echos from tissue are 40-70 dB stronger than those from blood, this type of noise is a drawback of the meter.

By *focusing* the beam, the intensity of the transmitted field and the sensitivity of the receiving transducer may be increased in the observation region. However, the region where the scattered signal is observed also becomes smaller. Hence the total received power is constant when focusing of the transduser is performed. Focusing will therefore not give an increase in the S/N ratio of the system as long as the original observation region is inside the artery.

When the observation region without focusing is not fully inside the artery, however, an increase in the S/N-ratio may be obtained by focusing (so that the observation region is kept fully within the artery).

2.5. Summary.

The basic priciples of the CW-, PW- and correlation meters have been described. The CW-meter gives no range resolution. Range resolution may be obtained by the PW-meter while a limit on the maximum measurable velocity occurs. With a correlation meter range resolution may be obtained with no limit of the maximum measurable velocity. The range resolution capability of the PW- and correlation meter is the same for equal transducer bandwidths.

The signal to noise power ratio for the CW- and PW-meters has been compared. For equal average transmitted power the CW- and PW-meter have the same minimum S/N ratio. Since the peak transmitted power is limited to avoid damage of tissue, there exists a minimum pulselength, and thereby a limited resolution capability of the PW-meter if the S/N-ratio is to be kept at the same level as for the CW-meter.

3. TRANSDUCER - THEORY AND EXPERIMENT

For transducers we use ceramic ferroelectric discs of a sintered lead-zirconate-titanate composition. They are operated in the thickness resonance mode. A survey of piezo and ferroelectric transducer materials is given in [27]. The most practical material for our purpose is the type PZT-5A and PZT-5H. (Trade mark from Brush & Clevite). They have suitable impedances so that matching may easily be performed. PZT-5A has the highest Curie point and thereby the best temperature stability.

For single transducers we use a circular disc, for double transducers a circular disc divided in two halves. Typical diameters are in the range of 15-24 mm. For resonance at 2 MHz the thickness is 1 mm.

The focusing capabilty of lenses and spherical transducer elements has been studied by Schlieren techniques.

To increase the bandwidth of the transducer, double layer acoustical impedance matching has been studied theoretically and experimentally. A large increase in bandwidth and a subsequently decrease in pulse rise time is obtained without introducing insertion losses in the transducer.

3.1. Radiation field. Focusing.

The field pattern from a radiator is usually divided into two parts, the nearfield and the farfield regions. There is no sharp definition of the boundary between these regions. They are characterized by that in the farfield region the extent of the radiator may be neglected when the field is calculated, while this cannot be done in the nearfield region. This implies that the emitted wave in the farfield region will be spherical with amplitude depending on the direction. The beam from the radiator will diverge by an angle, Θ, determined by its aperture

$$\sin\Theta = 1.11\,\frac{\lambda}{d} \qquad (3.1)$$

where Θ is defined in Figure 3.1. λ is the ultrasonic wavelength and d is the transducer diameter.

The calculation of the nearfield is very complex and may only be performed numerically. A numerical calculation based on exact equations is also difficult because of the finite extent of the transducer disc. At the boundary of the disc the element is surrounded by a material with lower modulus of elasti-

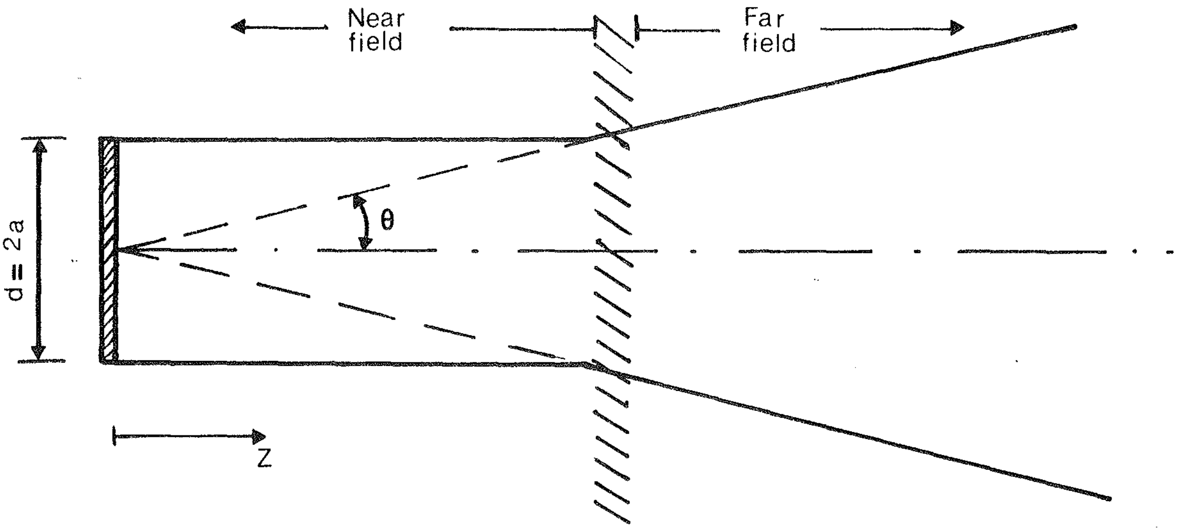

Figure 3.1. Indication of the near- and farfield regions of the transducer fieldpattern.

city. Thus the oscillations of the transducer surface will have larger amplitude at the boundary of the disc than in the middle. The motion will also deviate from being normal to the surface at the boundary.

A numerical calculation of the nearfield is given by Zemanek [29]. He has approximated the transducer by a piston vibrating with a uniform amplitude across the surface. A typical example of the result is given in Figure 3.2.

At 2 MHz λ equals 0.75 mm. The results given in Figure 3.2 therefore corresponds to a disc diameter of 7.5 mm. Our transducer has a diameter of more than twice this value. The pressure islands will therefore be smaller and more numerous. In Figure 3.3 a comparison between different transducer diameters is given.

These results show that a narrowing of the beam occours at a distance of 0.8 - 0.9 a^2/λ. This value seems to be almost independent of a. The radius of the beam where the intencity has fallen 6 dB is only 0.4 a. For a 2 MHz transducer of 20 mm diameter this corresponds to a distance of 11 cm. The diameter of the beam will be 8 mm.

Thus a selffocusing of the beam appears outside the nearfield region. After this point the beam diverges according to Eq. (3.1). The limit between the near- and farfield region may therefore be taken to

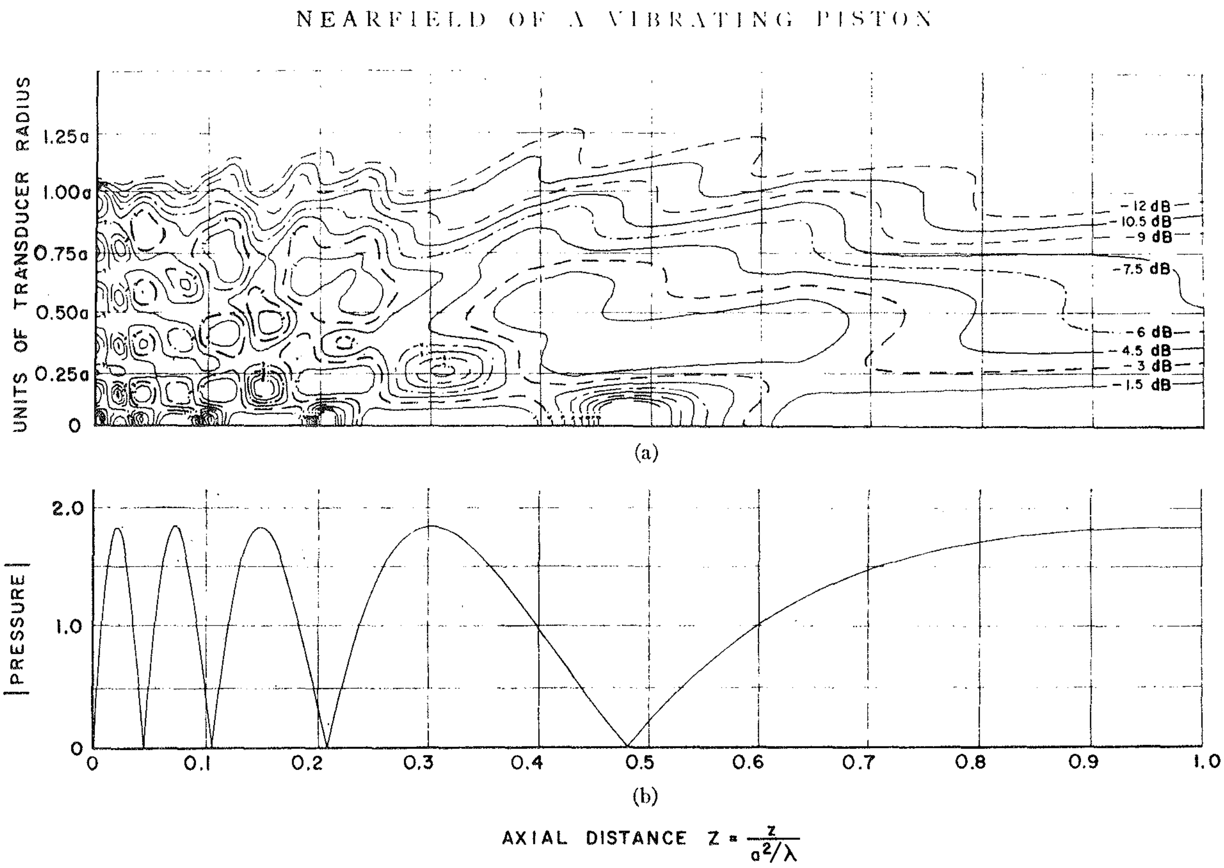

Figure 3.2. a) Detailed sound-pressure contours for circular uniform vibrating piston.
b) Magnitude of on-axis pressure variations. The results are given for $a/\lambda = 5.0$, where a is the disc radius and λ the wavelength [29].

$$z = 0.8\ a^2/\lambda \tag{3.2}$$

Schlieren studies of the transducer-field have not revealed this self-focusing. There may be two reasons for this. The one is that the resolvability of the Schlieren method is too crude to detect a decrease of 6 dB in wave amplitude. The other is that the self-focusing is not so large as indicated by the calculations. This would mean that the piston approximation of the transducer vibration is too crude.

In most applications the vessel will be in the nearfield of the transducers. The complicated field in this region will therefore affect the velocity measurement. As we shall see in Chapter 5, the measurement is affected in two ways. The one originates from the variations in the field amplitude which makes the

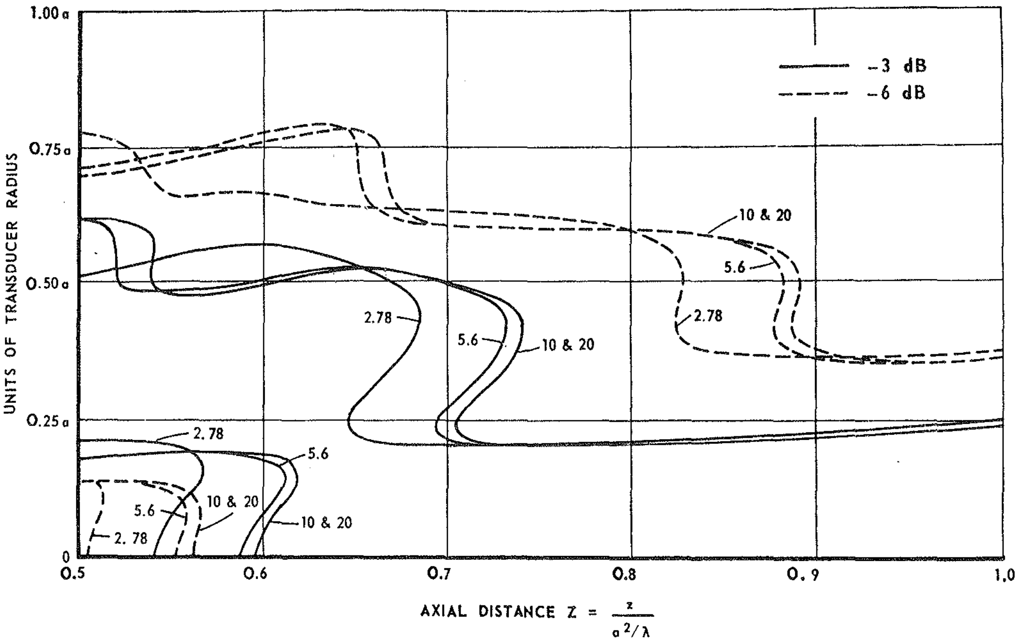

Figure 3.3. Comparison of computed -3 and -6 dB sound pressure contours for a/λ = 2.78, 5.62, 10 and 20. For 2 MHz transducers this corresponds to diameters of 4.2 mm, 8.4 mm, 15 mm, and 30 mm [29].

instrument sensitivity space dependent. The other originates from the complex variation of the phase of the field with position. By this different components of the velocity is measured at different points of space.

The most ideal field pattern should be a plane wave. This requires that the transducer is much larger than the wavelength and that the point of calculation is not too far from the transducer face and axis. For aortic blood velocity measurement from the suprasternal notch, the maximum practical transducer diameter is ≈20 mm, whereas the aortic depth is 70 mm. Therefore the planewave case cannot be obtained.

Focusing may be obtained by a transducer curved as a spherical shell, or by a lens in front of a plane transducer. The latter method introduces some reflection losses if antireflex treatment of the lens is not performed. In addition lossless lens meterial is difficult to obtain.

Figure 3.4 illustrates the two methods of focusing. For the first method the focal length is given by the radius of curvature of the transducer. In the second method the focal length, f, is given by geometrical optics to

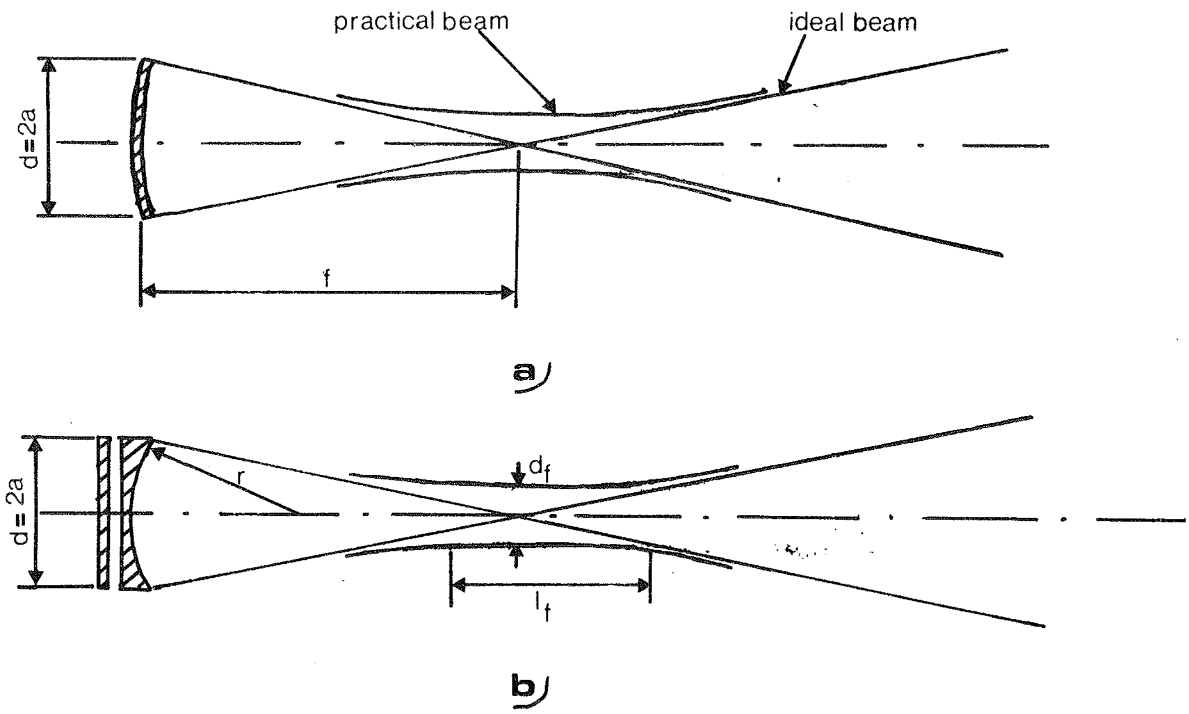

Figure 3.4. Focusing with a transducer formed as a spherical shell a) and using a planeconcave plastic lens b).

$$f = \frac{r}{1 - c_\ell/c_t} \tag{3.3}$$

where c_t is the wave velocity of the tissue, and c_ℓ is the wave velocity of the lens material. r is the radius of curvature for the lens surface. Since it is difficult to obtain $c_\ell < c_t$, r has to be negative, which means that the lens surface has to be concave.

The minimum focal diameter, d_f, is determined by the diffraction of the beam. From wave optics [74] the first zero of the intensity gives the value (Section 2.2).

$$d_f = 2.22\lambda \cdot \frac{f}{d} \tag{2.9}$$

Lens errors increase the practical focal diameter from this lower theoretical limit. If a biconcave lens is used, a larger radius of curvature of the lens surface is obtained. For narrow focal lengths this may decrease the lens error.

The longitudinal extent, ℓ_f, of the focus is given by

$$\ell_f = \left(\frac{f}{d}\right)^2 \cdot \lambda \tag{3.5}$$

Figure 3.5 shows a Schlieren foto of the field pattern from a curved transducer, f = 6 cm, and a plane transducer with a planeconcave lens, calculated f = 6 cm. In both cases a diameter of the main lobe at a distance of 6 cm from the transducer is

$$d_f = 5.3 \text{ mm} \tag{3.6}$$

The theoretical value is

$$d_f = 5 \text{ mm} \tag{3.7}$$

For the lens the diameter of the main lobe seems to be smaller at 5 cm distance from the lens than at the focus. In addition there are more sidelobes for the lens than for curved transducer. The intensity ratio between the first side lobe and the main lobe is -9 dB for the lens and -13 dB for the curved transducer. This is larger than the theoretical value which is -17.5 dB [74].

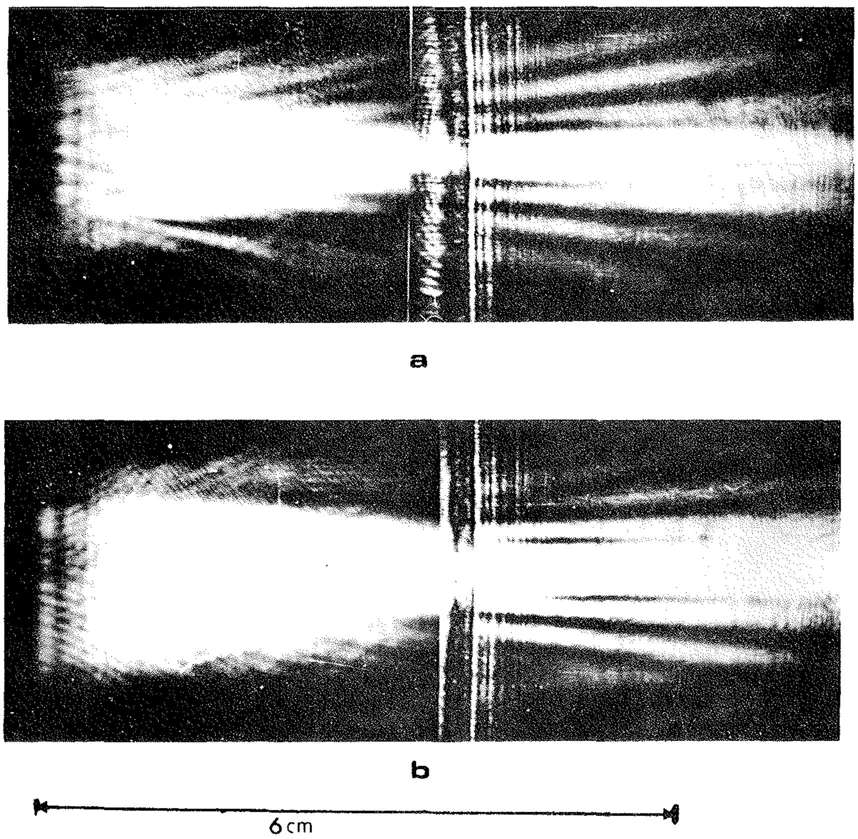

Figure 3.5. Schlieren study of fieldpattern of focused transducers.
a) Plane transducer with lens, calculated f = 6 cm.
b) Curved transducer with radius 6 cm.

3.2. Equivalent circuit of the transducer. Electrical matching.

The transducer may approximately be considered as a threeport device. One port is the electrical connections while the two others are the faces which interchanges acoustical power with the tissue and the backing. An equivalent circuit of a lossless transducerdisc is given in Figure 3.6 [28], [30]. The circuit is obtained under the approximation that the transducer faces vibrate with uniform amplitude.

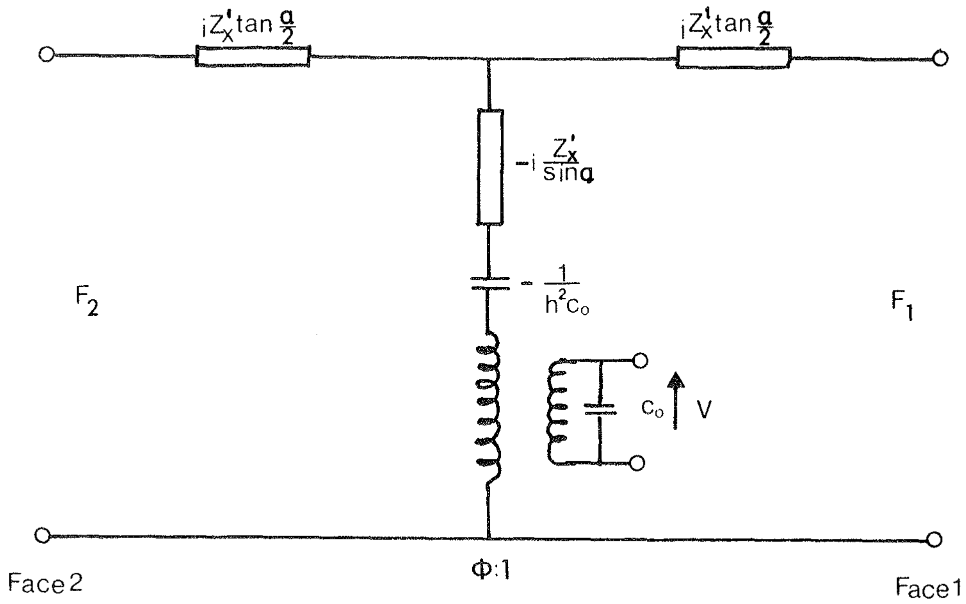

Figure 3.6. Lumped parameter complete equivalent circuit for a thickness mode transducer disc.

The voltage at the electrical port, V, is transformed to a force in the ideal transformer. The "voltages" and "currents" at the two acoustical ports are the forces and the velocity of vibration of the two transducerfaces. The parameteres in the figure are defined below.

t : Transducer thickness.

A : Transducer area.

h : Field developed/applied mechanical strain at constant charge of electrodes - in direction normal to the faces.

ε^S: Absolute dielectric constant at constant strain - in direction normal to the faces.

v_ℓ^D: Velocity of longitudinal wave at constant charge of the electrodes - in direction normal to the faces.

ρ : Density of the transducer material.

$C_0 = A\varepsilon^S/t$: Clamped capacitance of the transducer.

$\varphi = hC_0$: The ideal transformer voltage ratio.

$f_0 = v_\ell^D/2t$: The open circuit resonance frequency.

$\alpha/\pi = f/f_o$: Fractional frequency deviation.

$Z'_x = A\rho v_\ell^D$: Characteristic mechanical impedance of the transducer material

Typical values of these parameteres are given in Table 3.1.

PROPERTIES OF FERROELECTRIC COMPOSITIONS

	Material				
Physical constants	95 percent $BaTiO_3$ 5 percent $CaTiO_3$	PZT-4	PZT-5A	PZT-5H	PZT-7A
$\epsilon_{33}^T/\epsilon_0$ (free)	1200	1300	1700	3400	425
$\epsilon_{33}^S/\epsilon_0$ (clamped)	910	635	830	1470	235
h_{33} (10^8 v/m)	16.7	26.8	21.5	18.0	46.6
e_{33} (C/m²)	13.5	15.1	15.8	23.3	9.7
v_t^D (m/s)	5630	4600	4350	4560	4830
C_{33}^D (10^{10} N/m²)	17.7	15.9	14.7	15.7	17.6
ρ (10^3 kg/m³)	5.55	7.5	7.75	7.5	7.6
k_t	0.384	0.513	0.486	0.505	0.49
$Z = \rho v_t^D$ (10^6 kg/s m²)	31.2	34.5	33.7	34.2	35.7

Table 3.1 from [28].

Characteristic impedances and impedances pr. unit areas is denoted by unprimed letters in the following. The impedances used in the equivalent circuits are the unprimed values multiplied by the area of the transducer and are denoted with a prime.

Since we are only interested in the interaction between the front face and the electrical termination of the transducer, we reduce the circuit of Figure 3.6 to a two-port given in Figure 3.7 [28].

Two *resonance frequencies* of the transducers are often given as data. The one is the *short circuit* resonance frequency, f_0', and the other is the *open circuit* resonance frequency, f_0. These may suitably be discussed with reference to Figure 3.7b.

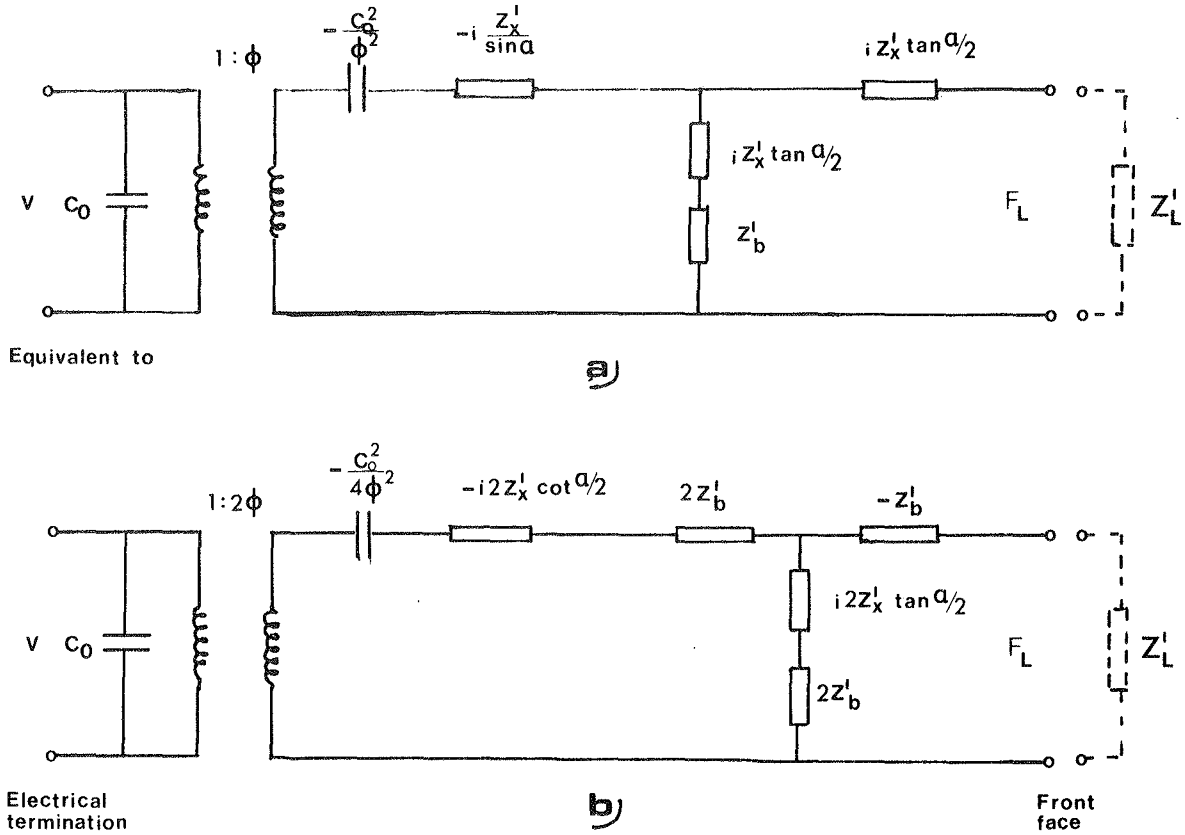

Figure 3.7. Equivalent twoport circuits for the transducer. V is the input/output voltage and F is the force on the transducer face. Z_b' is the impedance at the back face [28].

The equivalent circuit consists of a parallel tuned circuit $2Z_b' - i2Z_x' \tan \alpha/2$, which is at resonance at f_0, and a series tuned circuit $2Z_b' - i(2Z_x' \cot \alpha/2 - 2\varphi^2/\pi f C_0^2)$. If the load and backing impedances are approximately equal the branch $Z_L' - Z_b'$ will short circuit the parallel resonance circuit. When the electrical port is open, the clamped capacitance C_0 and the negative capacitance $-C_0^2/4\varphi^2$ will cancel and the transducer will resonance at a frequency which gives $\cot \alpha/2 = 0$, i.e. f_0 or its odd harmonics. The transducer thickness at this resonance is odd harmonics of the half wavelength, $\lambda/2 = v_\ell^D/2f_0$.

When the electrical port is short circuit, the resonance frequency is determined by that of the series resonance branch. The resonance frequency of this branch is therefore equal to the short circuit resonance frequency, f_0', when $Z_L' = Z_b'$.

When the transducer is driven by a low impedance source, maximum power output occurs at f_0'. For a receiving transducer this frequency also gives the minimum internal source resistance. f_0' may be expressed by f_0 [28]

$$f_0' = f_0\left(1 - \frac{4C_M}{C_E}\right)^{\frac{1}{2}}$$

$$C_M = \frac{1}{\pi^2 f_0 Z_x} \qquad C_E = \frac{C_0}{\varphi^2} \tag{3.8}$$

The higher resonance frequencies in the short circuit case will not be harmonics of f_0' because of the negative capacitance. This is easily seen by considering the resonance frequencies of the series branch.

For ceramics the value of the negative capacitance is so high that f_0 and f_0' differs by ca. 10 %. For quartz this difference is negligible.

When Z_b' and Z_L' differs and one of them becomes large, both the series and the parallel tuned circuit will affect the short circuit resonance. The resonance frequency is shifted towards lower values and becomes asymetric. When $Z_b' = \infty$, the open circuit resonance frequency will be $f_0/2$, i.e. the transducer thickness is $\lambda/4$.

When the back impedance is zero or infinite, the two-port will be lossless.

Approximately zero backing impedance may be obtained by mounting the transducer on a ring so that the main backing area is in contact with air only. Infinite impedance may be obtained by backing with a quarterwave layer which is terminated into air. This will, however, give a frequency dependent backing and in addition careful machining of the matching layer is necessary to obtain the right thickness.

The following impedance theorem for lossless twoports is illustrating.

Impedance matching theorem.

Suppose that a load impedance, Z_2, is connected to the second port of a lossless twoport circuit. The input impedance, Z_1, at port no. 1 is measured. If port one is terminated by Z_1^* the input impedance (Z_2 disconnected) at port two is Z_2^*.

The proof of the theorem is straight forward from the T- or π-equivalent of the twoport.

To apply this theorem to our case the transducer (Z_b = 0 or ∞) is loaded by the tissue and the input impedance Z_1 is measured. By electrical matching the receiver input impedance is made equal to Z_1^*. This makes the mechanical impedance of the transducer seen from the tissue, equal to the characteristic impedance of the tissue, which is real, and no acoustical reflection at the transducer face occurs.

This result is obtained with no regard to the material parameters of the transducer. If the electromechanical coupling is low, Z_1 will have a large phaseangle and a lossless matching network is difficult to achieve. Therefore the ceramic materials are the most suitable for our application.

When losses in the transducer, either internal or in the backing material occurs, this procedure will still give the right receiver impedance for maximum power transfer from acoustical to electrical energy. (Thevenins theorem). At this value of the receiver impedance, however, there will be acoustical reflection at the transducer face.

In our application it is the S/N-ratio which should be maximized and not the power transfer capabilities of the receiving transducer. For this reason a matching network is inserted between the transducer and the receiver so as to get the optimum source resistance for the preamplifier. The input impedance of the network seen from the transducer will then deviate from the values for maximum power transfer.

3.3. Transducer bandwidth. Acoustical impedance matching.

The relative half power bandwidth of a voltage driven transmitting transducer is given by [30].

$$\frac{\Delta f}{f_0} = \frac{2}{\pi} \frac{Z_b + Z_L}{Z_x} \tag{3.9}$$

as long as it is small. Z_b and Z_L are the back and load impedances of the transducer. For an airbacked 2 MHz transducer loaded with tissue on face 1 we have

$$Z_L = 1.5 \cdot 10^6 \text{ kg/sm}^2 \quad Z_b = 0 \quad Z_x = 33.7 \cdot 10^6 \text{ kg/sm}^2$$

$$\Delta f = 60 \text{ kHz} \tag{3.10}$$

Internal losses increase this bandwidth to 100 kHz. As discussed for the PW-meter this bandwidth is sufficient to obtain a longitudinal resolution between 5 and 10 mm.

To obtain a larger bandwidth a heavier loading of the transducer faces is necessary. There is two methods available for this.

The one is to use a high impedance absorbing backing material. This method introduces losses at the low signal level during reception which is a severe drawback in our application, where a low S/N-ratio is a problem.

The other method is to raise the load impedance at the front or back face by impedance matching layers. At the backface the matching layer is terminated into air to minimize power losses. If a matching on the front face only is used, the transducer is airbacked.

Kossoff [28] has considered the effect on the frequency responce of transducers by matching with quarterwave transformers to raise the face impedances. To obatin the desired characteristic impedance of the matching layer a mixture of metal powder, such as tungsten or aluminium, in araldite is used.

A large increase in bandwidth may be obtained by this method. However, it turns out that the risetime of pulses in wave phenomena is not uniquely determined by the bandwidth around the lowest resonance frequency. In a layered structure such as the transducer, there will exist an infinite number of resonance frequencies which tends towards infinity in magnitude. Therefore higher resonance bands should be taken into account, when calculating the pulse risetime from the frequency response. Because of the internal loss mechanisms in the transducer material the higher resonance frequencies are damped. It is therefore sufficient to consider a few of the lowest bands.

The significance of this phenomenon in the space-time domain is that several reflections from the faces in the structure has to occur before a steady state is obtained. Kossoff thus found that the risetime was first increased by increasing the bandwidth. The increase then fell off and for heavy matchings, the risetime was essentially independent of the bandwidth around the lowest resonance frequency.

The quarterwave matching has the disadvantage that it is difficult to foretell the impedance of the tungsten araldite mixture. Gradients in the powder-concentration may evolve during the solidification process. We therefore undertook a study of matching the transducer by two layers. By this method standard materials may be used for the layers and inaccuracy in the material parameters are therefor much smaller. A drawback with the double layer matching is that careful machining has to be performed on two layers instead of the one for the quarterwave matching.

3.4. Calculation of acoustical double layer impedance matching.

A. General.

Figure 3.8 schematically shows the structure of the transducer with two matching layers on the front face.

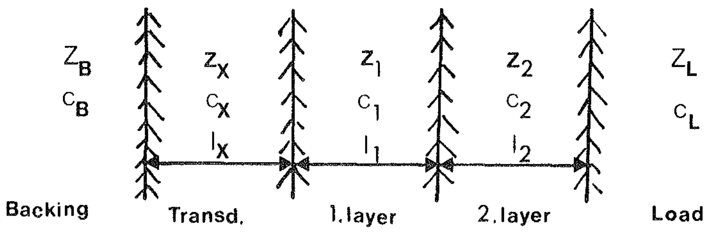

Figure 3.8. Layered structure for double layer matching of the transducer to the load. The transducer is backed with a material of characteristic impedance Z_B.

From the impedance transformation formula for a transmission line, we may calculate the impedance seen from any cut to the left or to the right in the structure [30]. The impedance seen to the left from the interface between layer one and two is

$$Z_{12} = Z_2 \frac{Z_L + iZ_2 \tan \alpha_2}{Z_2 + iZ_L \tan \alpha_2} \tag{3.11}$$

$$\alpha_2 = 2\pi \ell_2 / \lambda_2$$

The impedance seen from the left transducer face towards the load is

$$Z_{x1} = Z_1 \frac{Z_{12} + iZ_1 \tan \alpha_1}{Z_1 + iZ_{12} \tan \alpha_1} \tag{3.12}$$

$$\alpha_1 = 2\pi \ell_1 / \lambda_1$$

If a fixed real impedance Z_{x1} is wanted for a fixed frequency, the wave angle α_1 and α_2 must obey the following equalities

$$\tan^2\alpha_1 = \frac{Z_1^{\,2}(Z_L - Z_{x1})(Z_2^{\,2} - Z_{x1}Z_L)}{(Z_{x1}Z_2^{\,2} - Z_L Z_1^{\,2})(Z_1^{\,2} - Z_{x1}Z_L)} \tag{3.13}$$

$$\tan\alpha_2 = -\frac{Z_2}{Z_1}\,\frac{(Z_1^{\,2} - Z_{x1}Z_L)}{(Z_2^{\,2} - Z_{x1}Z_L)}\,\tan\alpha_1 \tag{3.14}$$

These requirements may be met only when the expression for $\tan^2\alpha_1$ is positive. A solution of the matching problem therefore exists only when the pair (Z_1, Z_2) belongs to a subset of the first quadrant of the plane, as indicated in Figure 3.9.

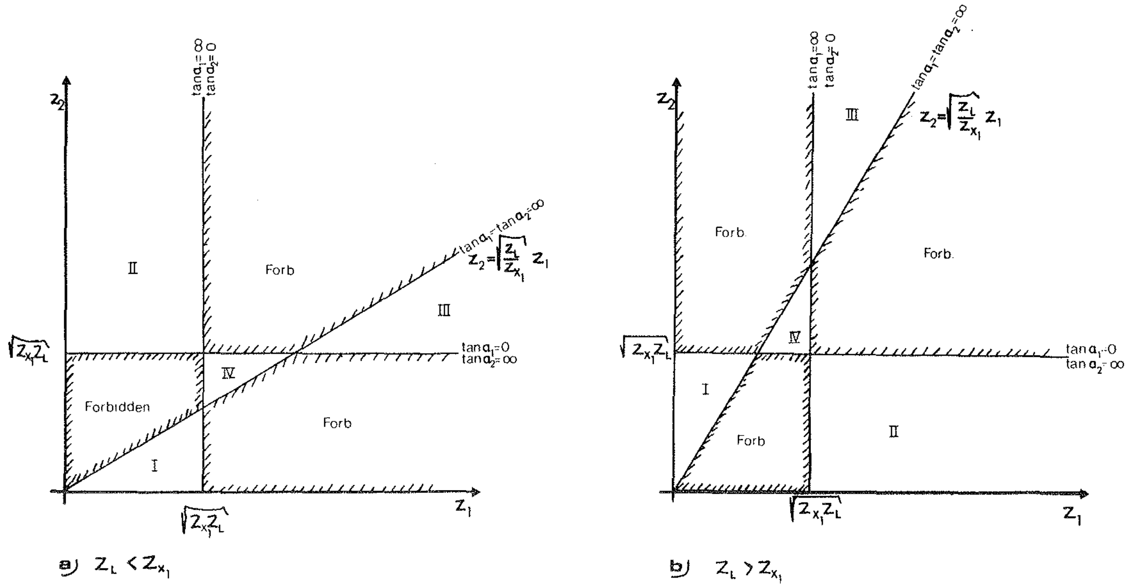

Figure 3.9. Regions in the Z_1-Z_2 plane where a double layer matching is obtainable a) $Z_L < Z_{x1}$ which is our case. b) $Z_L > Z_{x1}$.

Because of the periodicity of $\tan\alpha$ we may add an integer number of half wavelengths to the layer thickness. The sensitivity of the matching to frequency will, however, increase when half wavelengths are added in the layer thickness. In addition the layer thickness should be as small as possible for a good agreement between the transducer bandwidth and the pulse rise time.

Both the positive and negative root of $\tan^2\alpha_1$ gives a solution of the matching problem. For $\tan\alpha_i \geq 0$ we have $0 \leq \alpha_i < \pi/2$ which gives $0 \leq \ell_i < \lambda_i/4$. For $\tan\alpha_i \leq 0$ we have $\pi/2 < \alpha_i \leq \pi$ which gives $\lambda_i/4 < \ell_i \leq \lambda_i/2$. In regions I and II $\tan\alpha_1$ and $\tan\alpha_2$ will have opposite signs while in regions II and IV they have the same sign. The possibilities of the fundamental thicknesses of the matching layers are therefore

Region:	I	II	III	IV
$\tan\alpha_1 > 0$	$\ell_1 < \lambda_1/4$ $\lambda_2/4 < \ell_2 < \lambda_2/2$	$\ell_1 < \lambda_1/4$ $\ell_2 < \lambda_2/4$	$\ell_1 < \lambda_1/4$ $\lambda_2/4 < \ell_2 < \lambda_2/2$	$\ell_1 < \lambda_1/4$ $\ell_2 < \lambda_2/4$
$\tan\alpha_1 < 0$	$\lambda_1/4 < \ell_1 < \lambda_1/2$ $\ell_2 < \lambda_2/4$	$\lambda_1/4 < \ell_1 < \lambda_1/2$ $\lambda_2/4 < \ell_2 < \lambda_2/2$	$\lambda_1/4 < \ell_1 < \lambda_1/2$ $\ell_2 < \lambda_2/4$	$\lambda_1/4 < \ell_1 < \lambda_1/2$ $\lambda_2/4 < \ell_2 < \lambda_2/2$

Table 3.2. Thickness of the matching layers for positive and negative root of $\tan^2\alpha_1$.

To get thin layers, the positive root of $\tan\alpha_1$ should be chosen in regions II and IV. In regions I and III a more detailed calculation is necessary to make the best choice.

One might think that with two matching layers more internal reflections in the structure are necessary for a stationary field to arise, than with a single layer. In this way the connection between the pulse risetime and the bandwidth around the lowest resonance frequency should become less significant in the double layer case than in the single layer case. This is true for combinations of materials in regions I and III where the thickness of one of the layers always is above $\lambda_i/4$. In regions II and IV the thickness of both layers may be chosen less than $\lambda_i/4$ (positive root of $\tan^2\alpha_1$). The following expression for $\tan(\alpha_1+\alpha_2)$ may be calculated.

$$\tan(\alpha_1+\alpha_2) = \tan\alpha_1 \frac{(Z_1Z_2 + Z_xZ_L)(Z_2^2Z_{x1} - Z_1^2Z_L)}{Z_1(Z_2^2 - Z_{x1}Z_L)(Z_1Z_L + Z_2Z_{x1})} \tag{3.15}$$

The sign of $\tan(\alpha_1+\alpha_2)$ when $\tan\alpha_1 > 0$ is given in Table 3.3.

We thus see that in region II $\alpha_1+\alpha_2$ is less than $\pi/2$ which is the value of the waveangle for a quarter wave layer. Thus the total thickness observed by the wave of the layers for combination of materials in this region is less than that for a quarter wave layer. The significance between the bandwidth

Region:	I	II	III	IV
$\tan(\alpha_1+\alpha_2)$	> 0	> 0	< 0	< 0
Smallest value of $\alpha_1+\alpha_2$	$\pi < \alpha_1+\alpha_2 < \frac{3\pi}{2}$	$0 < \alpha_1+\alpha_2 < \frac{\pi}{2}$	$\frac{\pi}{2} < \alpha_1+\alpha_2 < \pi$	$\frac{\pi}{2} < \alpha_1+\alpha_2 < \pi$

Table 3.3. Sign of $\tan(\alpha_1+\alpha_2)$ when $\tan\alpha_1 > 0$.

around the lowest resonance frequency and the pulse risetime should therefore extend to higher values of the bandwidth for combinations in this region than for the quarter wave layer.

B. Method of numerical calculations.

a) The frequency of maximum power transmission for a voltage driven transducer with no backing and load matching is calculated. From the discussion above it follows that this frequency is equal to the resonance frequency, f_0', of the series tuned branch in Figure 3.7b.

b) Two materials whose impedances fit the requirements for a solution of the matching problem are chosen. The thickness of the layers is determined from Eq. (3.13) and (3.14) so that a real impedance Z_{x1} is obtained at the transducer face at the frequency of maximum power transmission determined above.

c) The voltage force transfer function $F/V_i(f)$ and the input admittance of the transmitting transducer is calculated. The frequency, f_1, for maximum power transmission with matching layers is found, i.e. the frequency that maximizes the real part $R^{-1}(f)$ of the input admittance of the transducer with matching layers.

d) The receiving transducer and matching layers are identical to the transmitting transducer. The electrical port is termiated by the resistance $R(f_1)$ parallelled with an inductance L so that the imaginary part of the input admittance is tuned out at f_1.

e) The force voltage transfer function $V_0/F(f)$ of the receiving transducer terminated as above is calculated. The total voltage insertion transfer function of a transmitter and receiver system as shown in Figure 3.10 is calculated. The divergence of the transmitted beam is neglected so that all the transmitted power is considered to hit the receiving transducer face. The effect of the wave reflected from the receiver on the transmitting transducer functioning is neglected. This is done because in the practical situation we are interested in the signal scattered from tissue.

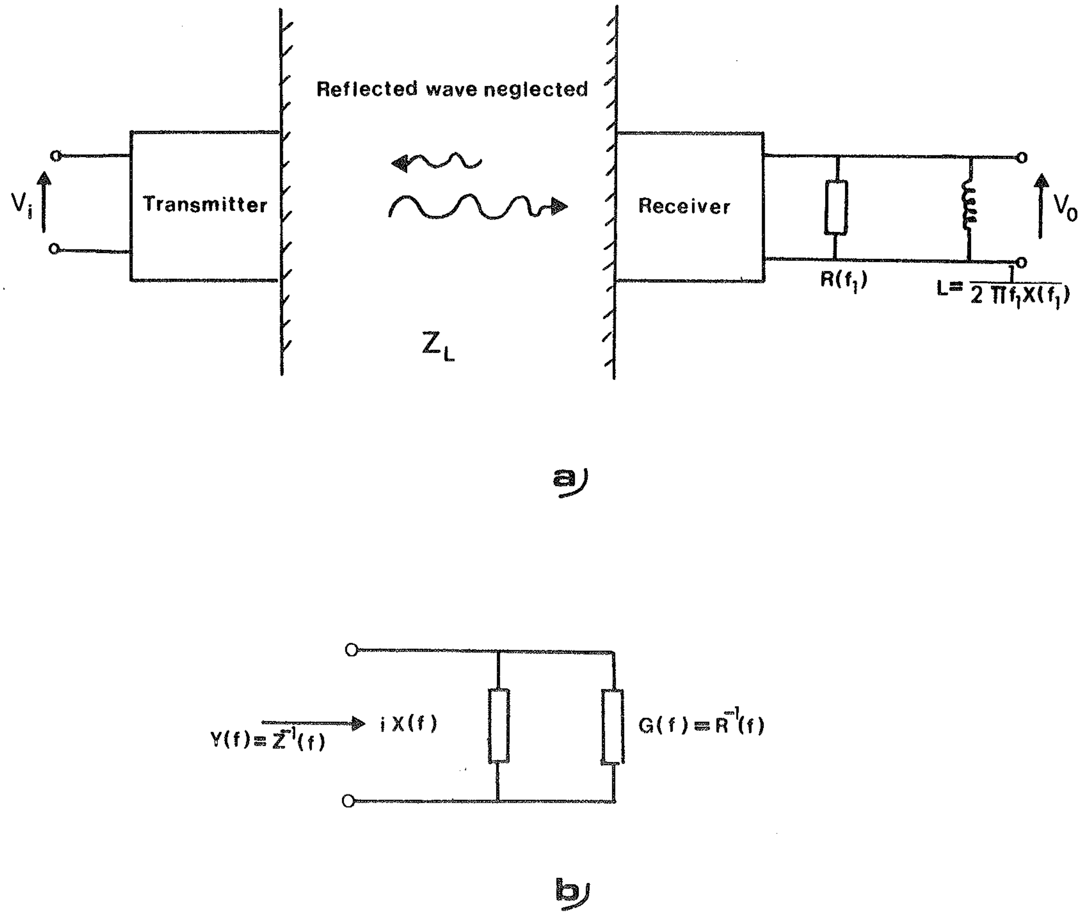

Figure 3.10. a) Schematic representation of transducers for calculation of transducer insertion transfer function.
b) Definition of input admittance Y(f), conductance G(f) and susceptance X(f) of the transducer.

C. Numerical results.

The input conductance, phase angle of the input impedance and voltage transfer function are given for three types of matching layers.

Araldite/Aluminium	Arald/Al
Aluminium/Mixture of 15 % W in Vinyl	Al/Vin 15 W
Nickel/Magnesium	Ni/Mg

The material listed first is that which is nearest the transducer face.

Results for the positive root of $\tan^2\alpha_1$ are given in Figure 3.12 a-f, while results for the negative root are given in Figure 3.12 i-k.

The calculations are performed mainly for the transducer material PZT-5A. The Arald/Al matching with the positive root at $\tan^2\alpha_1$ has been recalculated for a transducer made of PZT-5H for comparison (Figure 3.12 d).

Four values of the matching impedance have been studied. The values pr. unit area are

$$
\begin{aligned}
Z_{x1} = \; & 7.4\cdot 10^6 \ \mathrm{kg/sm^2} \\
& 12.0\cdot 10^6 \ \mathrm{kg/sm^2} \\
& 24.0\cdot 10^6 \ \mathrm{kg/sm^2} \\
& 33.7\cdot 10^6 \ \mathrm{kg/sm^2}
\end{aligned}
$$

Most of the results are given with air backing material whose characteristic impedance pr. unit area is

$$\text{Air:} \quad Z_b = 400 \ \mathrm{kg/sm^2}$$

To illustrate the effect of a larger backing impedance the Arald/Al matching with PZT-5A as transducer material and the positve root of $\tan^2\alpha_1$ has been studied (Figure 3.12 b) with a backing impedance pr. unit area of

$$Z_b = 7\cdot 10^6 \ \mathrm{kg/sm^2}$$

The sensitivity in matching performance to inaccurate machining of the layers is studied for the Arald/Al matching with positive root of $\tan^2\alpha_1$, Figure 3.12 c. The thickness of the layers is increased 10 % in turn, the other layer having the exact value.

Curves for quarter wave matchings are given in Figure 3.12 g. Results for an unmatched transducer with various types of backing impedances are shown in Figure 3.12 h.

The calculations are performed for a transducer disc of 20 mm diameter and 1 mm thickness. Data for the transducer is given in Table 3.4.

Material	$A[10^{-4}m^2]$	$t[10^{-3}m]$	f_0[MHz]	f'_0[MHz]	C_0[pF]	Φ[N/volt]	$Z'_x=AZ_x$ [10^3 ohm]
PZT-5A	3.14	1.0	2.175	1.96	2300	4.95	10.59
PZT-5H	3.14	1.0	2.28	2.01	4100	7.38	10.74

Table 3.4. Data for the transducer discs.

Data for the double matching layers are given in Table 3.5 for the positive root of $\tan^2\alpha_1$ and in table 3.6 for the negative root $\tan^2\alpha_1$. Data for the quarter wave matching layer is given in Table 3.7. We see that the sum of the wave angles for the Arald/Al composition for $\tan\alpha_1 > 0$ is less than 90^o as discussed in Section 3.4A.

The acoustical data of Al, Ni and Mg are taken from [31] and the data for the Vinyl/W compositions are taken from [32]. The Araldite used is 100 parts of Casting Resin D and 10 parts of Hardener 951, Ciba. The ultrasonic velocity is measured by the transit time of a pulse through a slab and the characteristic impedance is calculated as ρc, where ρ is the mass density of the slab.

The regions in the Z_1-Z_2 plane where solutions of the matching problem exist, are shown in Figure 3.11 for the four values of Z_{x1}, together with the positions of the three types of matching layers calculated. For all values of Z_{x1} the Arald/Al matching belongs to region II, while the Ni/Mg matching belongs to region III. The Al/vin 15 W matching belongs to region II for the two lowest values of Z_{x1}, while it belongs to region IV for the two largest values.

Combination of materials which belongs to region I has not been found. Calculations for other combinations of materials in region II, III and IV have been performed, and the results given seem to be typical for each region. The Arald/Mg composition indicated in Figure 3.11 gives the same results as the Arald/Al composition.

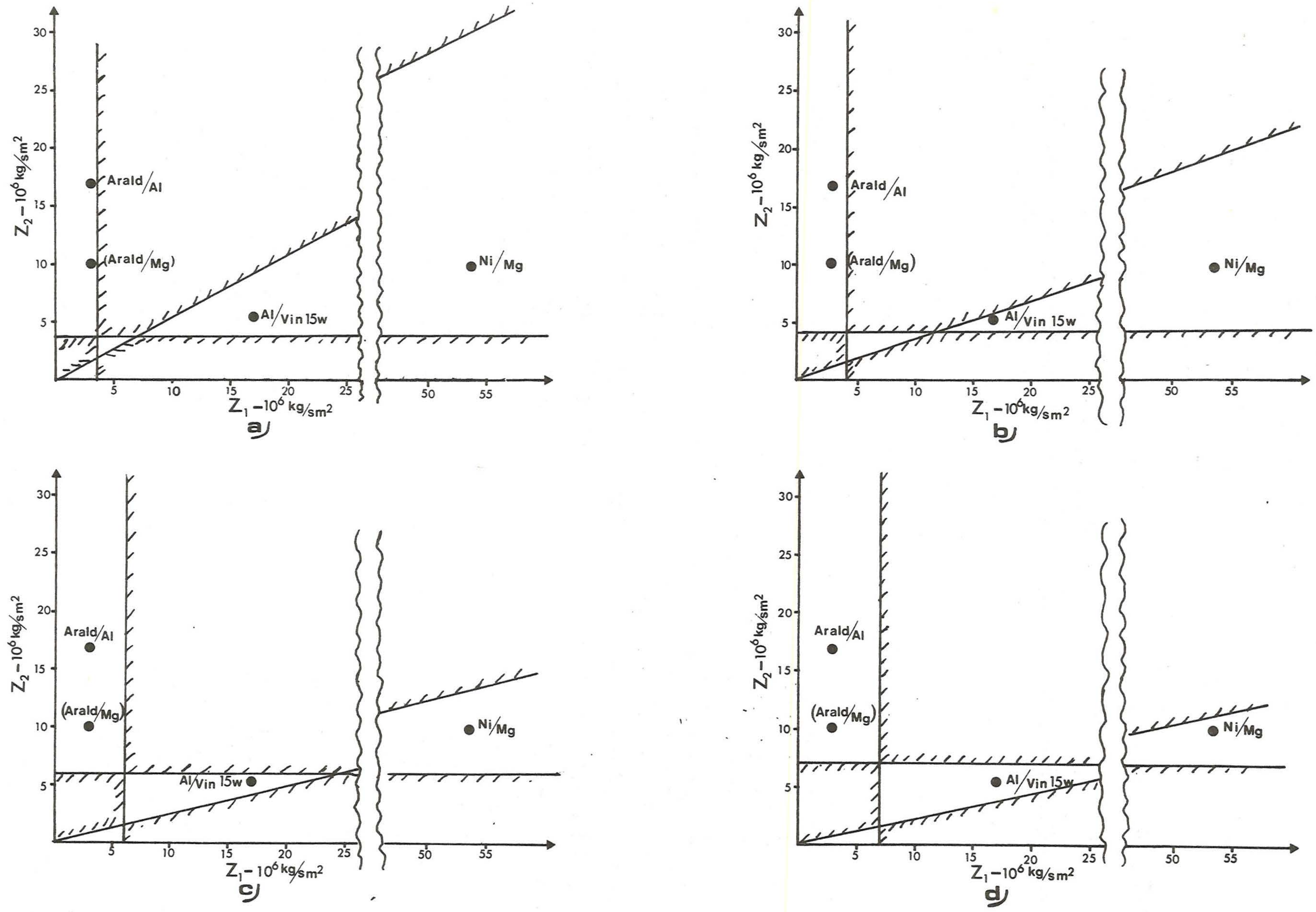

Figure 3.11. Regions in the Z_1-Z_2 plane where a solution of the double layer matching problem exists for the four values of Z_{x1} used.

Number of layer	Material	z_i [10^6 kg/sm^2]	c_i [m/s]	Wave-angle α_i [deg]	Thickness ℓ_i [mm]	z_{xl} [10^6 kg/sm^2]
1	Arald	3.0	2500	61.20 42.26 27.69 22.54	.2168 .1497 .0980 .0798	7.4 12.0 24.0 33.7
2	Al	17.3	6420	4.37 9.52 17.24 21.79	.0397 .0866 .1568 .1982	7.4 12.0 24.0 33.7
1	Al	17.3	6420	35.20 49.93 38.00 50.42	.3202 .4543 .3457 .4587	7.4 12.0 24.0 33.7
2	Vin 15 W	5.45	1400	106.20 96.34 84.44 77.60	.2107 .1912 .1675 .1539	7.4 12.0 24.0 33.7
1	Ni	53.5	6040	21.05 27.89 41.27 52.96	.1802 .2387 .3532 .4533	7.4 12.0 24.0 33.7
2	Mg	10.0	5770	113.43 106.48 97.86 94.06	.9276 .8688 .8003 .7692	7.4 12.0 24.0 33.7

Table 3.5. Data for double matching layers when the positive root of $\tan^2\alpha_1$ *is used.*

Number of layer	Material	Z_i [10^6 kg/sm^2]	c_i [m/s]	Wave-angle α_i [deg]	Thickness ℓ_i [mm]	Z_{x1} [10^6 kg/sm^2]
1	Arald	3.0	2500	118.80 137.74 152.31 157.46	.4209 .4880 .5397 .5579	7.4 12.0 24.0 33.7
2	Al	17.3	6420	175.63 170.48 162.76 158.21	1.5980 1.5511 1.4809 1.4315	7.4 12.0 24.0 33.7
1	Al	17.3	6420	144.80 130.07 142.00 129.58	1.3175 1.1834 1.2920 1.1790	7.4 12.0 24.0 33.7
2	Vin 15 W	5.45	1400	73.80 83.66 95.56 102.40	.1464 .1659 .1896 .2032	7.4 12.0 24.0 33.7
1	Ni	53.5	6040	158.95 152.11 138.73 127.04	1.3606 1.3021 1.1876 1.0875	7.4 12.0 24.0 33.7
2	Mg	10.0	5770	66.57 73.52 82.14 85.94	.5443 .6031 .6716 .7027	7.4 12.0 24.0 33.7

Table 3.6. Data for double matching layers when the negative root of $\tan^2\alpha_1$ is used.

Z_{x1} $[10^6\ kg/sm^2]$	Layer imp. Z_1 $[10^6\ kg/sm^2]$	Material % W in Vinyl	Wave vel. c [m/s]	Thickness [mm]
7.4	3.33	4	1800	.2391
12.0	4.24	8.7	1560	.2072
24.0	6.0	18	1340	.1780
33.7	7.1	40	820	.1089

Table 3.7. Data for quarter wave matching layer of Vinyl/ Wolfram composite.

D. Discussion.

For the two highest values of Z_{x1} for the Al/Vin 15 W matching, and for all calculated values of Z_{x1} for the Ni/Mg matching, the frequency of maximum conductance is shifted to a lower value than f_0'. This phenomenon is exaggerated when the negative root of $\tan^2\alpha_1$ is used.

The reason for this effect is that the high impedance matching layer (Al and Ni) which is in contact with the transducer face, limits the amplitude of vibration of this face, while the back face is free to move. The node of the vibration is therefore shifted from the middle of the transducer thickness, when both faces are free, towards the front face. The resonance therefore changes from half wavelength towards quarter wavelength. When $\tan\alpha_1 < 0$ is used, the thickness of these high impedance layers is increased and the effect is exaggerated.

For the Arald/Al layer the thickness of both layers is increased when $\tan\alpha_1 < 0$ is used and the performance becomes poorer.

The positive root of $\tan^2\alpha_1$ gives the best result for all material combinations and among these the Arald/Al composition gives by far the best result. The frequency response is very flat and symmetric for values of Z_{x1} up to above $12.0\cdot 10^6\ kg/sm^2$.

For this type of matching the 6 dB bandwidth of the total transfer function is increased from ca. 3% in the airbacked unmatched case to 30%. Increasing the backing impedance to $7.0\cdot 10^6\ kg/sm^2$ flattens the frequency response while losses are introduced. The bandwidth is not markedly increased except for $Z_{x1} = 7.4\cdot 10^6 kg/sm^2$,

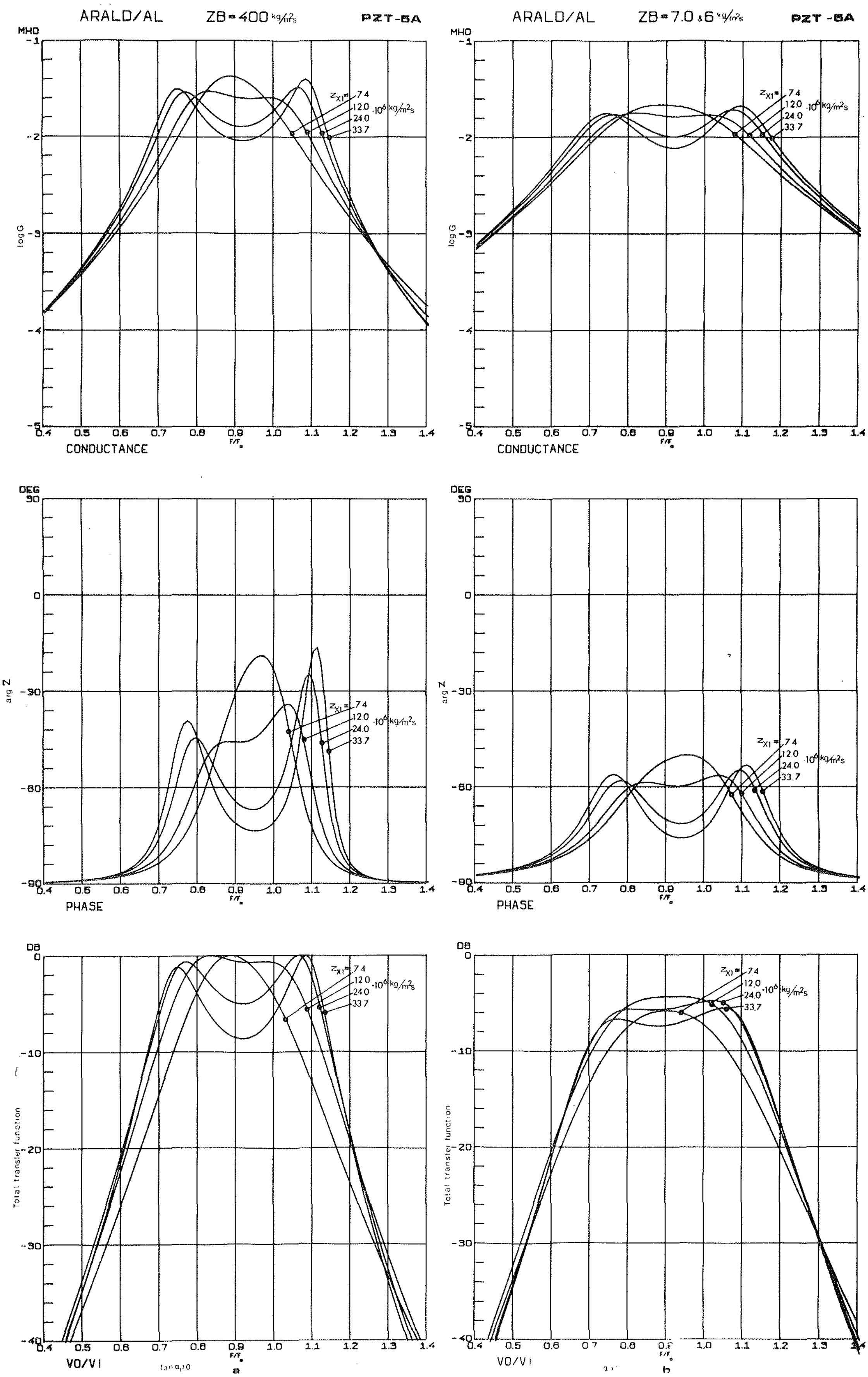

ARALD/AL
ZB=400 kg/m²s
PZT-5A
ARALD/AL
ZB=7.0·10⁶ kg/m²s
PZT-5A
MHO
log G
CONDUCTANCE
DEG
arg Z
PHASE
DB
Total transfer function
VO/VI
F/F0
Zx1= 7.4
12.0
24.0
33.7
·10⁶ kg/m²s
a
b

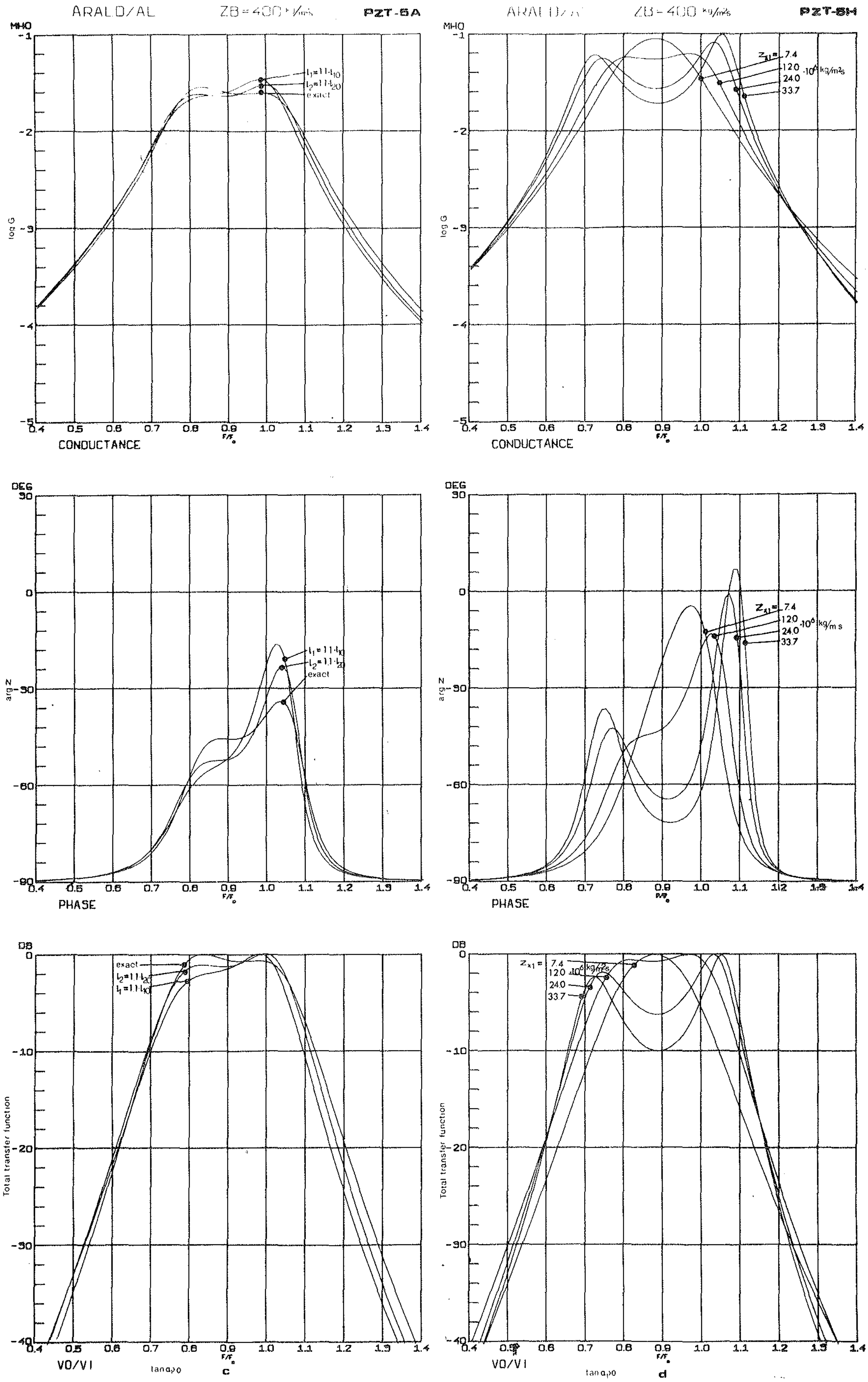
ARALDIT/AL
ZB=400
PZT-5A
PZT-5H
MHO
log G
CONDUCTANCE
F/F₀
DEG
arg Z
PHASE
DB
Total transfer function
VO/VI
exact
$l_1=1.1 \cdot l_{10}$
$l_2=1.1 \cdot l_{20}$
$Z_{x1}=$ 7.4, 120, 240, 337 $\cdot 10^6$ kg/m²s
c
d

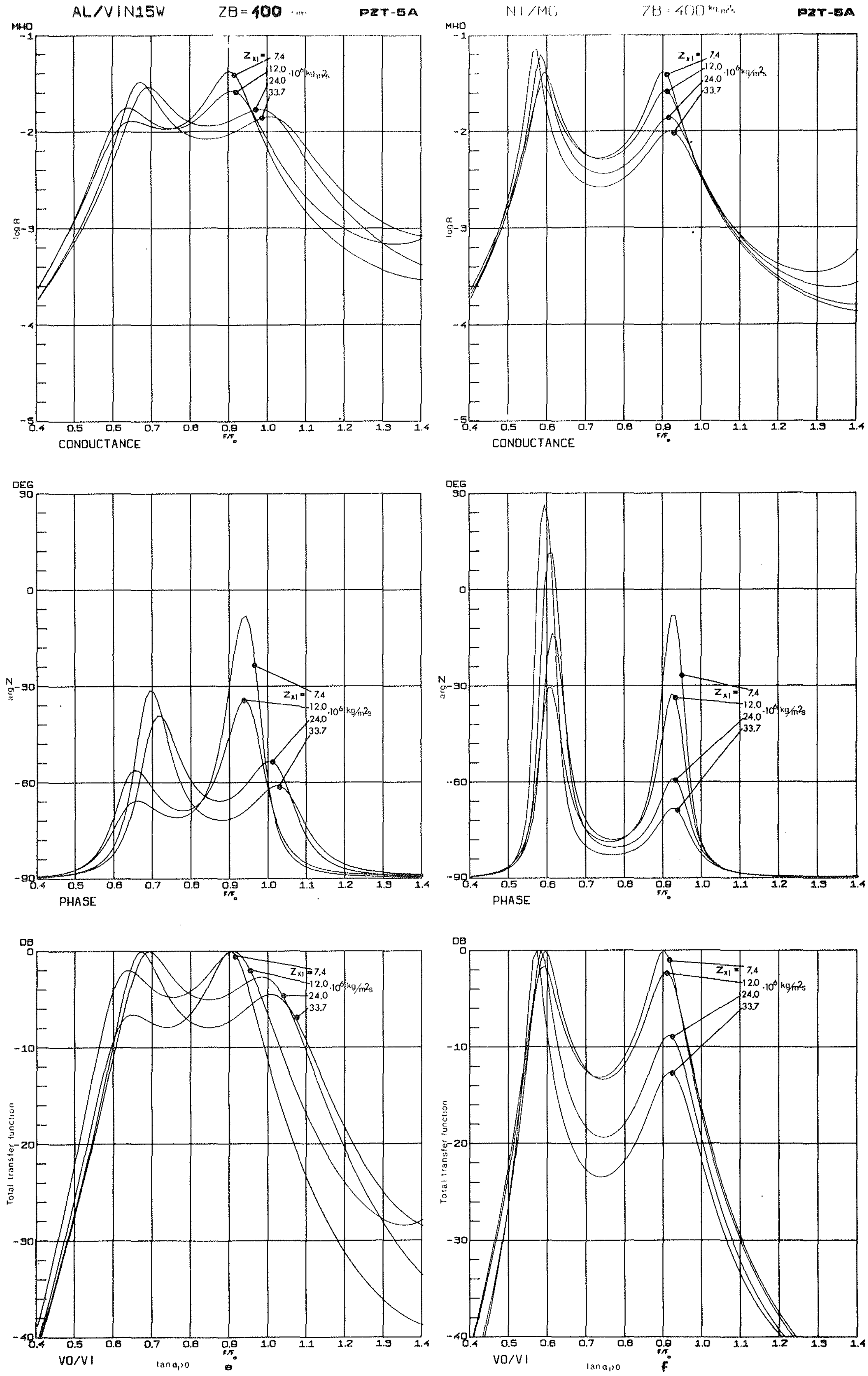

AL/VIN15W
ZB = 400
PZT-5A
NI/MG
ZB = 400
PZT-5A
MHO
logR
CONDUCTANCE
DEG
argZ
PHASE
DB
Total transfer function
VO/VI
F/F0
Z_{x1} = 7.4
12.0 $\cdot 10^6$ kg/m²s
24.0
33.7
e
f

QUARTERWAVE MATCHING ZB=400 kg/m²s PZT-5A

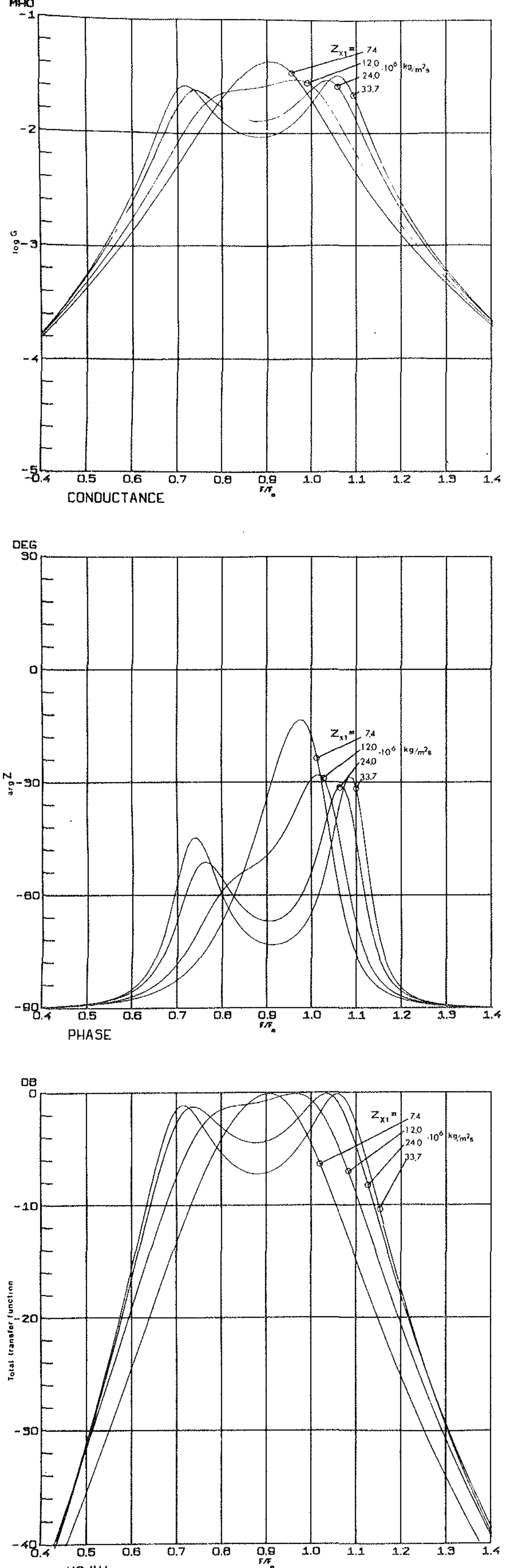

g

UNMATCHED BACKED ZX1 = 1.5 & 8 kg m/s PZT-5A

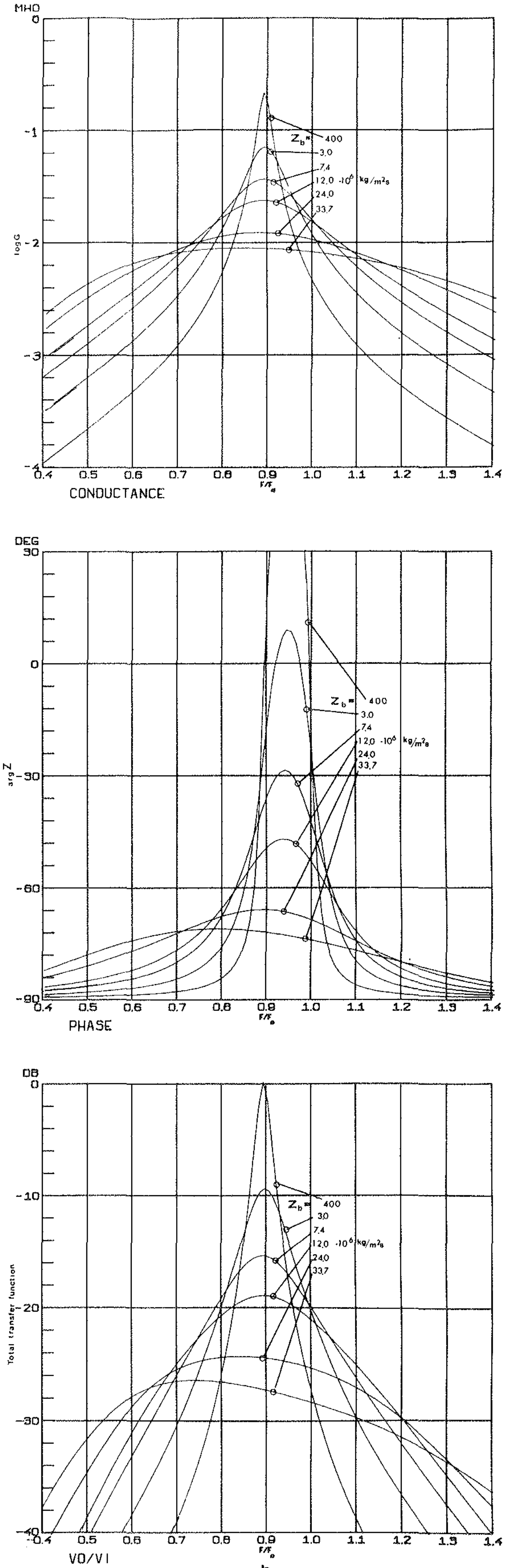

h

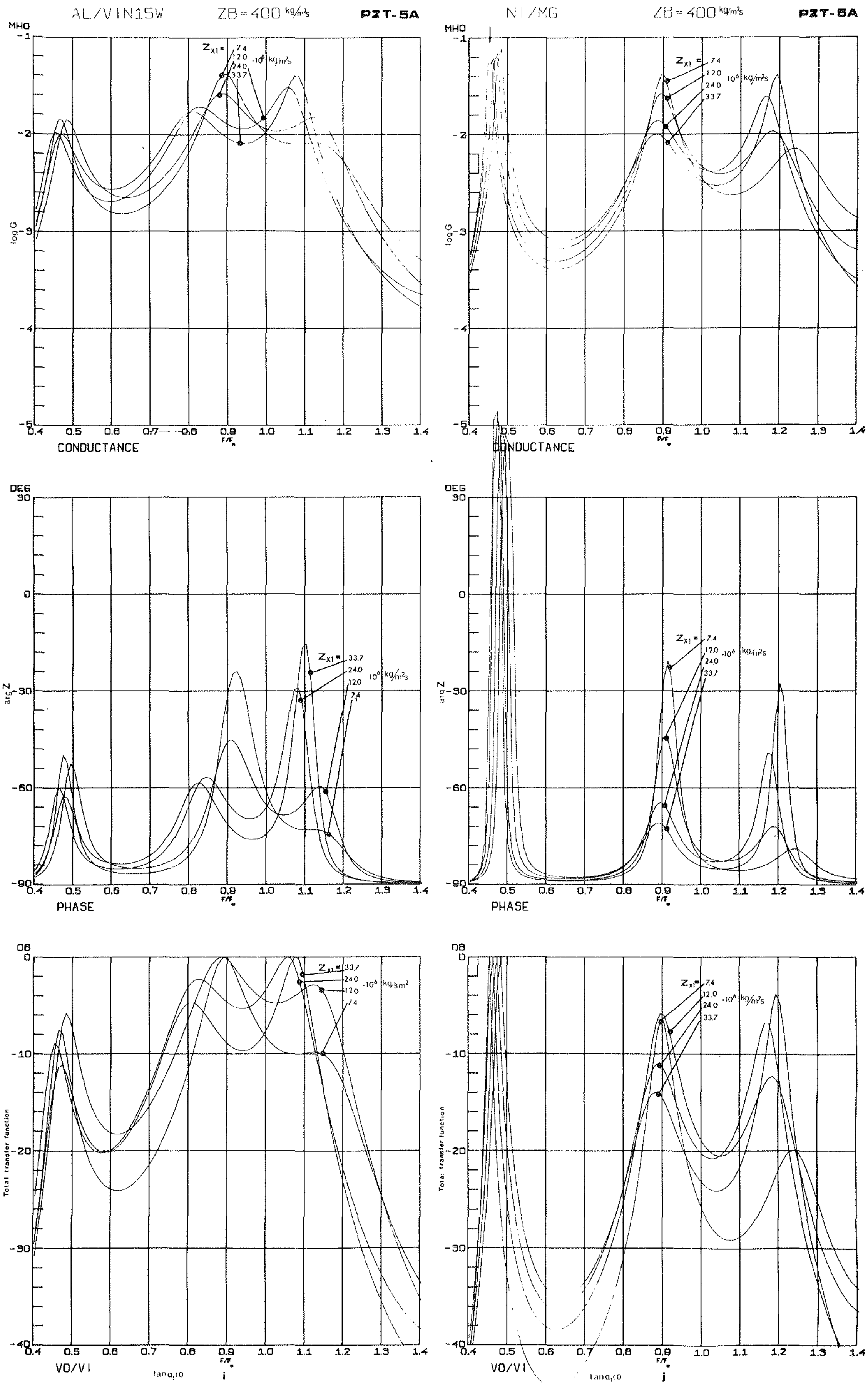
AL/VIN15W
ZB = 400 kg/m²s
PZT-5A
NI/MG
ZB = 400 kg/m²s
PZT-5A
MHO
log G
CONDUCTANCE
DEG
arg Z
PHASE
DB
Total transfer function
VO/VI
F/F₀
i
j

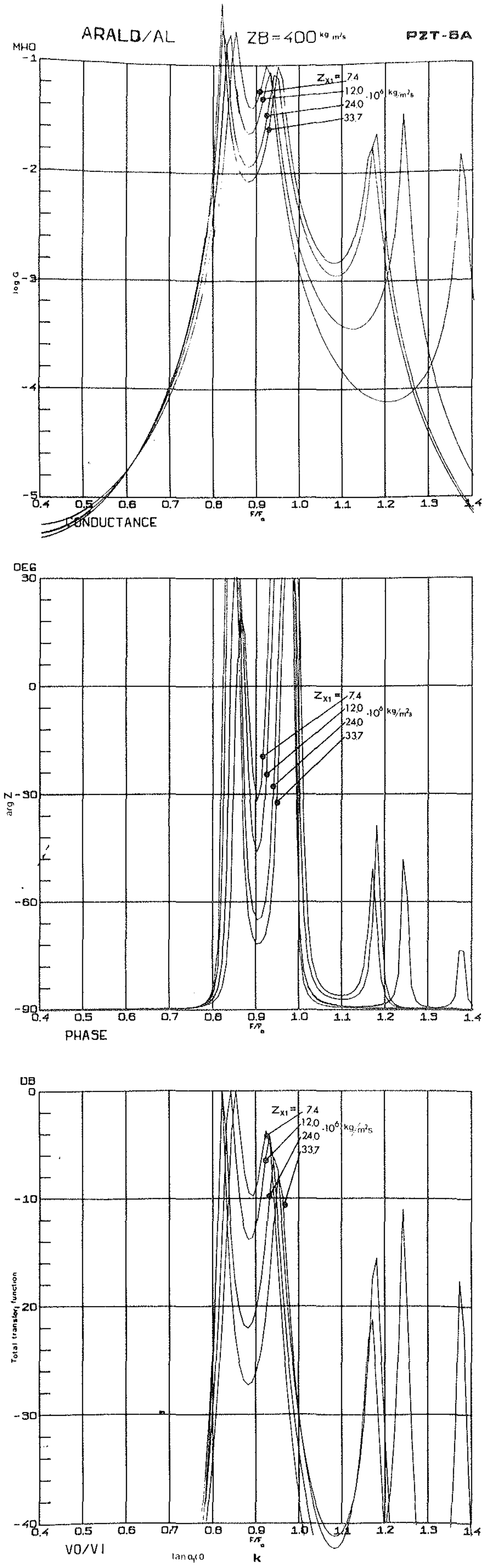

Figure 3.12. Numerical calculation of the frequency response for transducers with various type of matching layers. Each column shows the results for one type of matching, backing and transducer meterial, the type of which is written on the top. The abcissa on all figures is the frequency related to the open-circuit resonance frequency f_0. The upper figure shows a logaritmic plot of the input conductance which is given in mho's. The mid figure is the argument of the input impedance in deg, while the lower figure shows the total voltage transfer function for the transmitter receiver system shown in Figure 3.10.

where the backing increases the bandwidth with 50% above the value obtained with matching only. The increase in bandwidth for the highest values of Z_{x1} is small because the backing impedance is much lower than Z_{x1} at these values, Eq. (3.9).

The total transmitted power of a voltage driven transducer is given by

$$P = \tfrac{1}{2}|V|^2 \cdot G \tag{3.16}$$

The bandwidth of the conductance therefore gives the power transmission bandwidth. When the transducer is backed, power is also radiated into the backing which decreases the power radiated into the tissue.

It is interesting to note that the insertion losses for the matched and backed transducer are much smaller than for the unmatched and backed transducer, Figure 3.12 h. The high losses in the unmatched case originate from the large difference between the front and the back impedance of the transducer [30].

For the Arald/Al composition it is seen that the frequency of maximum V_0/V_i is shifted from the lower to the upper hump of the frequency response, as Z_{x1} is increased. Therefore there exists a value of Z_{x1} above $12 \cdot 10^6$ kg/sm^2 where an equal rippel of the frequency response is obtained. The internal losses in the transducer will decrease the ripple relative to that calculated. If this is not sufficient, a low impedance backing may be used to get low ripple.

The increase in bandwidth for the quarter wave matched transducer is approximately the same as for the Arald/Al matched transducer. For the quarter wave matched transducer the frequency of maximum V_0/V_i is at the upper hump of the frequency response for all values of Z_{x1} calculated. Thus an equal ripple transducer is not obtained in this way, although the departure from equal ripple is not large. Equal ripple might be obtained by choosing a thickness of the matching layer different from $\lambda/4$ at f_0'.

The single frequency matching method we have used is rather crude. Indeed, what we want is a good frequency response and a better method would be to choose the dimensions and impedances of the layers so as to get the best frequency response in some sense. In this case a double layer matching would have an advantage over the single layer matching in that more parameters are available for the shaping of the frequency response. The good results with the Arald/Al matching and the amount of work necessary for dimensioning the layers by a response shaping method, has made us postpone such a task.

3.5. Experimental study of transducer bandwidth and pulse risetime.

The bandwidth and pulse risetime of three transducers have been studied:

I PZT-5A Unmatched to load and airbacked.

II PZT-5H Matched with Arald/Al layers to load $Z_{x1} = 12 \cdot 10^6$ kg/sm^2 and air backed.

III PZT-5A Unmatched transducer backed with mixture of Araldite and W, 100 g W/40 cc Arald.

The Araldite for the double layer matching is 100 parts Casting Resin D and 10 parts of Hardener 951, Ciba. The backing is a mixture of Araldite (55 parts Casting Resin D and 45 parts of Polyamid Hardener 846, Ciba) and tungsten. 100 g W in 40 cm^3 Araldite gives an impedance of the matching layer of $\sim 7.0 \cdot 10^6$ kg/sm^2.

The measured input conductances of the transducers loaded with water and the phase angles of the input impedances are given in Figure 3.13.

The unmatched and airbacked transducer has a very low phase angle near resonance so that no parallel tuning inductance is used. A broad band transformer is used to raise the impedance from 8 Ω to 50 Ω which is the characteristic impedance of the coax transmission cable. The Arald/Al matched and the unmatched and backed transducer are shunted by inductances of 1.6 μH and 4.7 μH respectively. For the matched transducer a 1:4 broad band transformer raises the impedance to the coax level while for the backed transducer a 9:25 transformer is used.

The bandwidth of the unmatched and unbacked transducer is 100 kHz, which is the same as estimated in Section 3.3. The conductance and phase curve are almost the same as calculated in Figure 3.12 h, except for the resonance peak which is a little more damped because of the internal and the mounting losses.

The bandwidth of the matched transducer is 20 %, a little less than that calculated in Figure 3.12 d. The reduction is mostly at the upper end of the passband. Compared with Figure 3.12 c where the results for a 10 % increase in the layer thicknesses are given, we see that this reduction in bandwidth may arise when the layers are too thin.

The measured phase angle is also larger than that calculated in Figure 3.12 d. Besides the inaccuracy in the layer thickness, this may arise from deviation in the material parameters from the values used in the calculation.

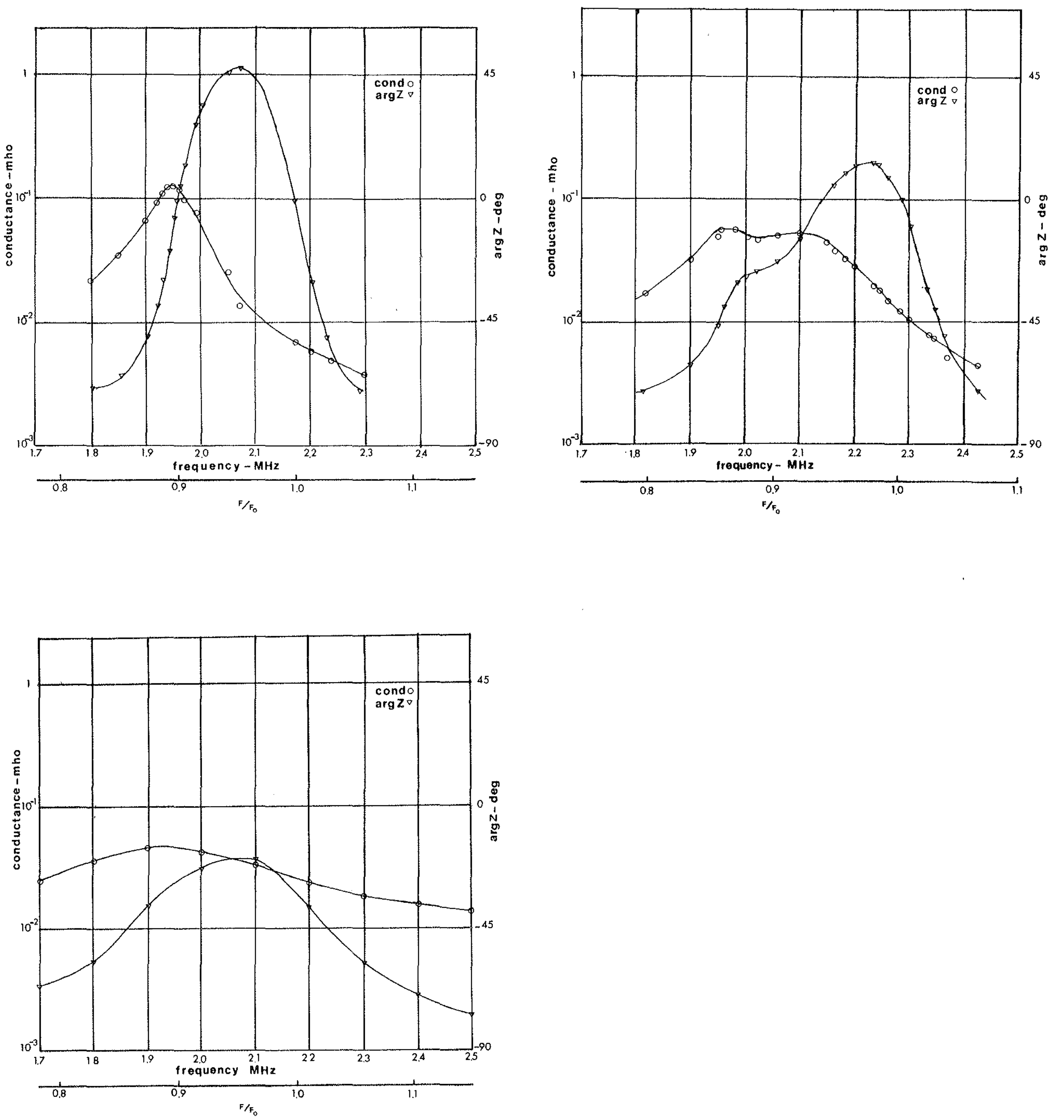

Figure 3.13. Experimental input conductance and argument of input impedance for

a) Transducer I

b) Transducer II

c) Transducer III

A decrease in the clamped dielectric constant, ε^S, of the transducer relative to the piezoelectric constant h will give a rise in the impedance phase angle. The measrued conductance is a little less than that calculated, as for the unmatched transducer. This may arise from internal and mounting losses.

For the unmatched and backed transducer the bandwidth is approximately 30 %. The measured conductance and phase angle is similar to that calculated for $Z_b = 7.4 \cdot 10^6$ kg/sm^2. Also here the measured phase angle is a little higher than that calculated which may arise from deviations in the material parameters from the values used in the calculations.

Figure 3.14 shows the pulse transmission capability for the three transducers. A rf pulse with rectangular envelope excites the transducer which radiates into water. The radiated pulse is reflected from a polished slab of brass and received.

The pulse risetime for the unmatched and unbacked transducer, Figure 3.14 a, is about 5 μs. The pulse shown will give a resolution of 10 mm. The risetime is decreased to 1.5 μs for the backed transducer, Figure 3.14 b, while a loss of -10 dB is introduced. Approximately the same risetime as this is obtained for the matched transducer with the much smaller loss of -3 dB compared to the unmatched and unbacked transducer. The losses probably occur in the matching.

Figure 3.14 d shows the smallest pulse obtainable for the matched transducer without seriously degrading the amplitude. The pulselength is 2 μs, which gives a resolution capability of 1.5 mm. The decay resonance consists of 2.5 cycles only so that a shorter pulse may be obtained. For imaging applications the transducer may be excited with a short and large pulse. By this a resolution capability of 1 mm is obtainable. This is about the same resolution capability as reported by Kossoff & al [33] for the quarter wave matched transducer.

The phase demodulated signal is shown in the lower trace of Figure 3.14. The amplitude and polarity of this signal is given by the phase difference between the received rf-pulse and the instrument local oscillator. This phase difference is adjusted for maximum positive amplitude.

The demodulator bandwidth is a little smaller than the transducer bandwidth in Figure 3.14 b,s,d. As discussed in Section 2.2 the amplitude of the demodulated pulse gives a weighting function to the observation region of the pulsed doppler meter.

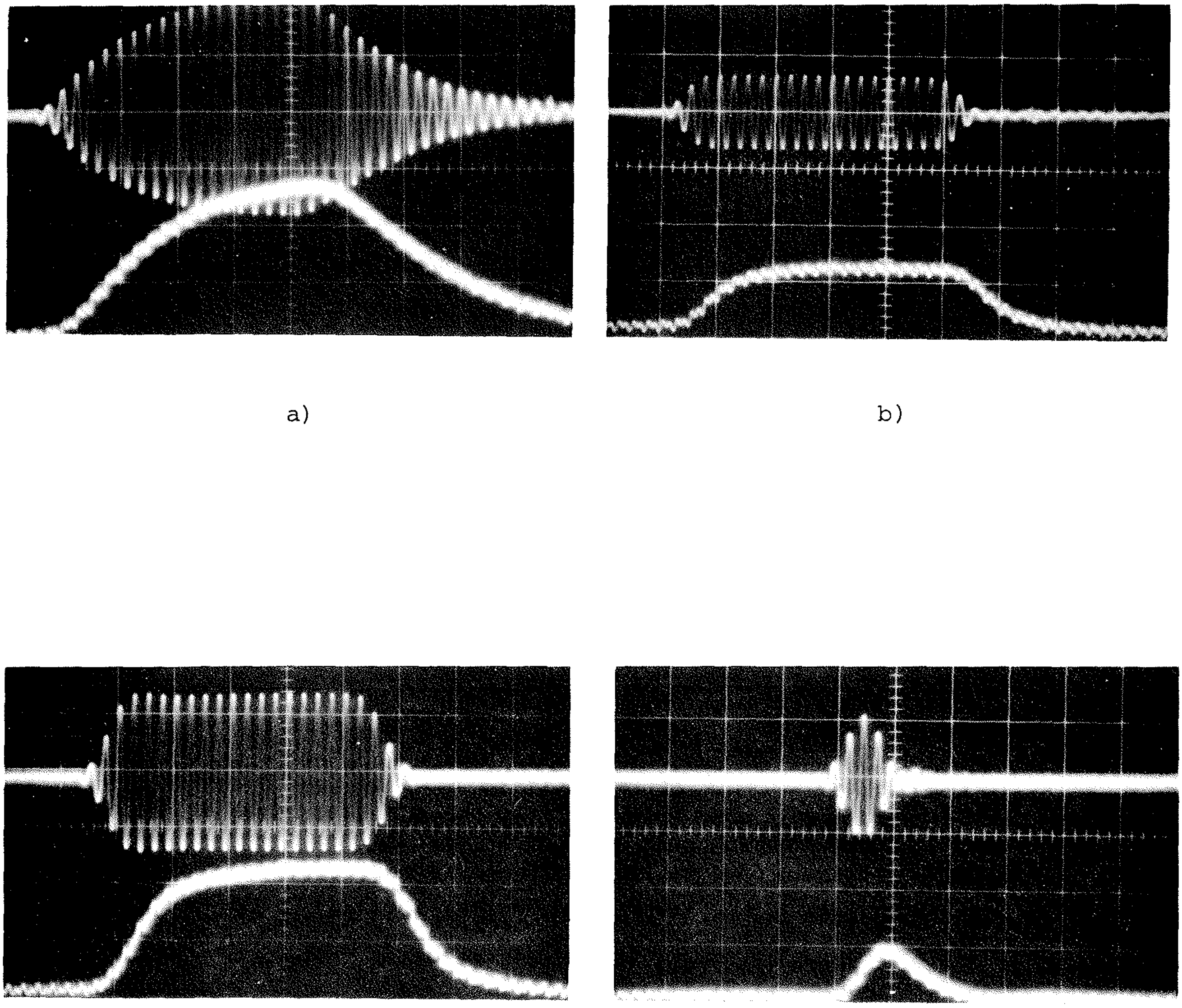

a) b)

c) d)

Figure 3.14. *Transducer pulse transmission. a) Unmatched airbacked transducer. b) Unmatched and backed with 100 g W/40 cm^3 Araldite. c) Arald/Al matched to load, airbacked. d) Shortest pulse for the Arald/Al matched transducer. The upper trace is the received rf signal and the lower trace is the phase demodulated signal*

Hor.: 2 μs/*div*
Ver.: Upper trace 0.5 V/div
Lower trace 0.2 V/div

3.6. Summary.

The transducer functioning and field pattern has been discussed. For diagnostic uses the nearfield region of the transducer is used. The results of Zemanek [29] shows that the field in this region is very complicated. His calculation is, however, based on the assumption of uniform amplitude of vibration for the transducer, which clearly is an approximation. A calculation which takes the variation in the vibration amplitude across the transducer face into account is therefore desirable.

Electrical and acoustical impedance matching has been discussed. The increase in bandwidth of the transducer by double layer acoustical impedance matching of the transducer to the load has been calculated for various types of matching layers.

A single frequency matching is performed and the need for dimensioning the matching layers by a response shaping method is discussed.

The Arald/Al matching has been tested out experimentally for a 2 MHz transducer. It is compared to an unmatched and unbacked transducer and a transducer unmatched to the load and backed with a mixture of 100 g W in 40 cm^3 Araldite, which gives an impedance of $7 \cdot 10^6$ kg/sm^2. A large decrease in pulse rise time to 15-20 % of the value for the unmatched and unbacked transducer is observed with a negligible introduction of losses. The resolution capability of the transducer is between 1 and 2 mm.

4. THE SCATTERING OF ULTRASOUND FROM BLOOD

In this chapter we study the scattering of ultrasound from blood. We first discuss the physical properties of blood and argue that the scattering can be considered to originate from stochastic fluctuations in the acoustic parameters of a continuum model of blood. These parameters may in turn be expressed by the concentration of cells and the scattered field may, therefore, be expressed by the fluctuations in this concentration.

A stochastic model for the concentration fluctuations of cells is presented and the stochastic properties of the cells are deduced from this model. Mathematical expressions for the scattered field and the signal out of the receiving transducer are given.

The wave velocity as a function of the mean cell concentration has been measured. The results are discussed with reference to the interaction between the cells and a numerical value is found for the cell concentration, above which the cells cannot be considered stochastically independent of each other.

With reference to this measurement the polar diagram for the differential scattering crossection of blood is given. The dependency of this polar diagram to the cell concentration is discussed.

4.1. Physical properties of blood.

Blood is a mixture of corpuscles in a surrounding liquid, the plasma. The physical properties of this mixture is very complex. We shall here mainly consider those properties which we feel are concerned with the flow of blood and the scattering of ultrasound from blood.

A. Composition of blood.

In normal man blood contains ca. 54 % (volume) liquid and ca. 46 % formed elements. Normal variations about these values are 5-10 % in both directions.

The *plasma* is about 90 % water by weight, most of the solid content being plasma protein, the remainder inorganic (1 %) and organic (1 %) components. The plasma proteins fall into four classifications - albumins, globulins, fibrinogen and lipoproteins.

Fibriniogen has the property of polymerizing to long fibrous threads, fibrin, under favourable circumstances. It is thus intimately concerned with the clotting of blood.

Plasma with the fibrinogen removed is called *serum*.

The formed elements consist of cells and of the blood platelets, which are actually minute fragments of cytoplasm of a specialized type. The cells are divided into two main groups, the *red cells (erythrocytes)* and the *white cells (leukocytes)*. The erythrocytes are not cells in the normal sense because they have no nuclei.

We give a brief summary of the size and amount of formed elements in blood.

Erythrocytes: The red cell count is 5 million per mm^3, a little more for men than for women. The cell is circular and flat like a biconcave disc of shape, with a diameter of about 7.5 µm and a thickness of about 1.5 µm. The volume is 80-90 μm^3.

From the data above we can get an idea of the mean distance between the cells. We can put a cell in each lattice point of a rectangular lattice and let the ratio between the long and short lattice sides be that of the ratio between the diameter and the thickness of the cell, Figure 4.1. The long axis of the lattice will then be about 10 µm, while the small axis will be about 2 µm.

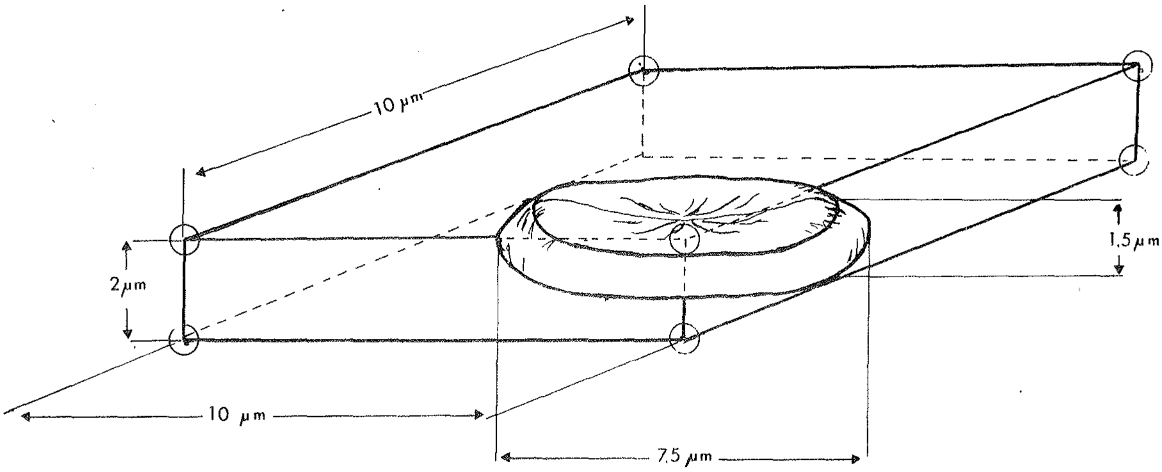

Figure 4.1. Mean distance calculations for red cells.

The red cell is composed of a membrane containing mostly hemoglobin inside. The shape of the cell has been studied by many workers. A review of this work is given by Y.C. Fung [34]. The shape seems to be determined by the osmotic pressure of the plasma across the cell membrane, and the elasticity of the thinwalled membrane.

Under normal conditions the cell is thinnest at the middle as shown in Figure 4.1.

The *largest possible packing* without deforming the cell corresponds to a volume percentage of 58 [35].

However, the cell has the property of undergoing large deformations. (Without this property the flow in capillaries would not be possible). It is thus possible to pack the cells closer than 58 % [36].

If there is a change in the osmotic pressure of the plasma relative to the cell membrane, the cell may swell from the biconcave to a more spherical form. The swelling may be so large that the membrane bursts. This phenomenon is called *hemolysis*.

Leukocytes: The normal white cell count is considered to be from 5000 to 8000 pr. mm^3. This is only 1/800th of the population density of erythrocytes. The cells are from 10 - 20 µm in diameter. If we put a white cell in each lattice point in a cubic lattice, the mean distance will be about 60 µm in all directions. Their volume occupation is 1/600th of the red cell volume.

Platelets: The normal count of platelets is 250.000 - 500.000 pr. mm^3, a concentration about 1/20th of that of the red cells. Their diameter is only 2.5 µm. Put in a cubic lattice their mean distance would be 12-15 µm. This is about 5-6 times the diameter so their volume occupation is even less than that of the leukocytes - 1/800th of the red cell volume.

The volume percent of red cells is called the *Hematocrit (HCT)*. This is, however, difficult to measure so that an operational definition of HCT has become more predominant. Blood is centrifuged under standardized conditions to separate plasma and corpuscles. HCT is then defined as volume percent of the centrifuged corpuscles to the volume of the blood. If the corpuscles were packed so close that no room for plasma was left, this definition would coincide with the previous definition. The volume percent of other cells than the red can be neglected.

B. Flow of blood.

The *specific gravity* of red cells is 1.10, that of plasma is 1.03. *Plasma* alone behaves like a Newtonian fluid with a coefficient of *viscosity about 1.2 cP*. When whole blood is tested in a viscometer, a non-Newtonian character is revealed. The viscosity varies with shear-rate, HCT, temperature and disease state, if any. A review of the blood flow properties is given by Y.C. Fung [37] and Charm and Kurland [38].

There is a question what happens to blood viscosity when the strain rate rate is reduced to zero. Cokelet & al [39] deduced the existence of a finite *yield stress*. They say that at vanishing shear rate the blood behaves like an elastic solid.

The yield stress or shear strength is determined by the cell-to-cell contact and the cell aggregate structure. When left without shear rate the red cells have a tendency to cluster together on their flat side, forming *rouleaux*. The rouleaux in their turn may lump to *aggregates*. The amount of rouleaux and aggregates will clearly affect the yield stress.

As the shear rate increases, the aggregates breaks down, and in large arteries like aorta the blood cells should be considered as individuals. The relation between the shear rate and the shear stress follows a square root law

$$\tau^{\frac{1}{2}} = K\gamma^{\frac{1}{2}} + C^{\frac{1}{2}} \tag{4.1}$$

where τ is the shear stress, γ the shear rate, C the yield stress and K the so called Casson viscosity [38].

R.H. Phibbs ([35] pp 53) has quick-frozen the flow in the femoral artery of a rabbit in less than 0.1 sec. as it rushed through the artery. The frozen blood is then prepared and photographed. The result is shown in Figure 4.2.

The photograph of Figure 4.2 shows a thin layer of plasma near the wall. This is called the *marginal layer*.

The most common opinion is that the cells have a tendency of moving towards the axis of the artery as the shear rate increases. There is, however, some uncertainties about this. Some investigators (Merill & al [43]) have failed to observe the effect by direct microscopic observation. We also see from Figure 4.2 that the marginal layer is not very distinct. However, at sufficiently low flow rates it is reasonable that a marginal layer should not develop, while it should do so at higher flow rates. This might explain why the effect has not been observed in some cases.

The steady flow of a Newtonian fluid through a straight circular pipe is governed by the *Poiseuille Hagenbach* equation

$$\dot{Q} = \frac{\pi p r^4}{8\nu L} \tag{4.2}$$

where $\dot{Q}$ is the volume of flow rate, r the radius of the tube, ν the viscosity and p/L the pressure gradient along the tube.

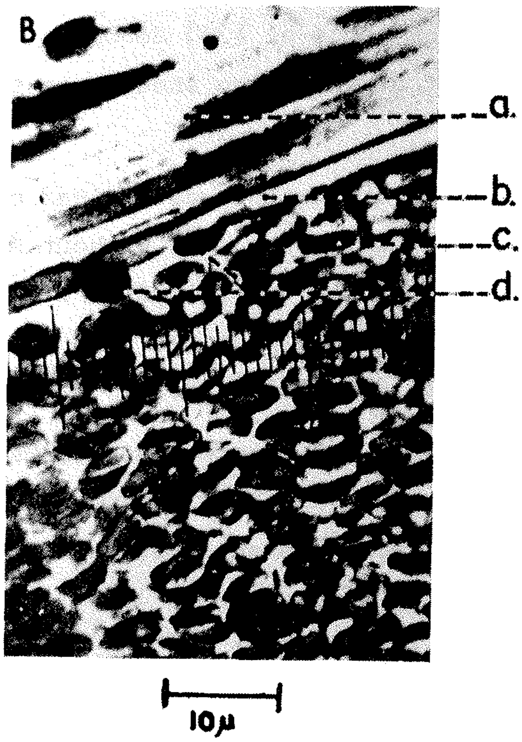

Figure 4.2. A cross section, 5μ thick, of the femoral artery of a rabbit, quickfrozen in less than 0.1 sec. as it rushed through the artery and subsequently prepared by freeze substitution. Note: (1) Most of the cells are "on edge", oriented by the shear, (2) They tend to be oriented with major diameter parallel to the wall, (3) Many of the cells are deformed by the crowding, the HCT is 34 %. The cell-free layer at the wall is irregular and thin;
a) smooth muscle of arterial wall.
b) internal elastic membrane.
c) erythrocyte
d) nucleus of endothelial cell (from work of R.H. Phibbs, Dept. of Biophys., Univ. of West Ontario. Published in [35]).

When a marginal layer develops, the resistance to flow decreases because of the lower viscosity in the marginal layer. The layer will have a lubricating effect.

When a *capillary viscometer* is used and the viscosity is calculated from Eq. (4.2), the apparent viscosity decreases with tube diameter when the diameter becomes less than 1 mm. This behaviour was reported by Fåhreaus and Lindquist [40] who studied blood suspensions, and by Dix and Scott-Blair [41] who studied clay suspensions and referred to it as the *sigma effect*.

The effect is controversial because certain investigators who have studied it, conclude that Fåhreaus and Lindquist merely did not recognize that the apparent viscosity of blood varies with shear rate. They were measuring this change in viscosity rather than a change due to tube diameter per se. [55].

Cokelet [53] analyzing the data of Fåhreaus and Lindquist concluded that an entrance effect which reduced the main concentration of cells in the tube, could account for a change in viscosity with tube diameter.

We emphasize at last that the Fåhreaus-Lindquist effect is due to calculating the viscosity from Poiseuilles equation and forcing into it pressure flow rate information obtained in the presence of, perhaps, a marginal layer and unknown cell distribution.

C. Scattering of ultrasound.

Little work has been done to study the *scattering of ultrasound* from blood. The scattering has generally been thought to stem from independent particles (the blood cells), each giving a reflected signal with a frequency according to the doppler equation (2.1).

The only experimental investigation to date has been done by Reid & al [44]. They conclude that in the HCT range from 7 to 40 % the scattering intensity is proportional to the HCT. The scattering was also proportional to the frequency in the fourth power.

Scattering from independent particles much smaller than the wavelength will give this result. The conclusion since then has been that the blood corpuscles behave as independent point scatterers and the scattering is mainly due to the red corpuscles.

S.W. Flax & al [48] were the first to give a theoretical investigation of the received signal from the blood. They used a very simple model of independent scatterers and studied mainly the effect of the received signal on the zero-counting detector.

W.R. Brody [45] has made a more thorough calculation of the received signal. His model is also based on the assumption of independent scatterers. He found that the power spectrum of the received signal was a map of the velocity profile in the region being studied. The power spectrum method is strictly applicable only for stationary flow. It can, however, be used as a good approximation when the doppler shift frequencies are much larger than the frequencies associated with the change of velocity with time.

From the previous data given of the density of the scatterers, it seems unlikely that the scatterers can be considered independent. In Figure 4.2 an example is given of the microstucture in blood during flow. The hematocrit is as low as 34 %, and still at this density there is a considerable deformation of the red cells because of the crowding.

The complex form of the far field from a point-scatterer will contain the space-time factor

$$\sim \varkappa(\vec{r})\ \frac{e^{i(kr-\omega_0 t)}}{r} \tag{4.3}$$

$$k = \frac{2\pi}{\lambda}$$

$\varkappa(\vec{r})$ is the angular dependency of the scattered field, k is the wave number, λ the wave length, r is the distance from the scatterer, ω_0 the angular frequency and t the time.

Let two scatterers have the position $\vec{\xi}_1$ and $\vec{\xi}_2$ as indicated in Figure 4.3. The scattered field from an incident plane wave

$$e^{-i(\vec{k}_0\vec{r} - \omega_0 t)} \tag{4.4}$$

will be

$$\alpha\sum_i \varkappa(\vec{r} - \vec{\xi}_i)\ \frac{e^{i(k|\vec{r}-\vec{\xi}_i| - \omega_0 t)}}{|\vec{r} - \vec{\xi}_i|} \tag{4.5}$$

When $\xi_i/r << 1$ we may use the farfield approximation

$$\left.\begin{aligned} |\vec{r} - \vec{\xi}_i| &= r - \vec{e}_r\cdot\vec{\xi}_i \\ \frac{1}{|\vec{r} - \vec{\xi}_i|} &= \frac{1}{r} \end{aligned}\right\} \quad i = 1,2 \tag{4.6}$$

Under this approximation we may also write

$$\varkappa(\vec{r} - \vec{\xi}_i) \approx \varkappa(\vec{r}) \tag{4.7}$$

since $\varkappa(\vec{r})$ depends slowly on space.

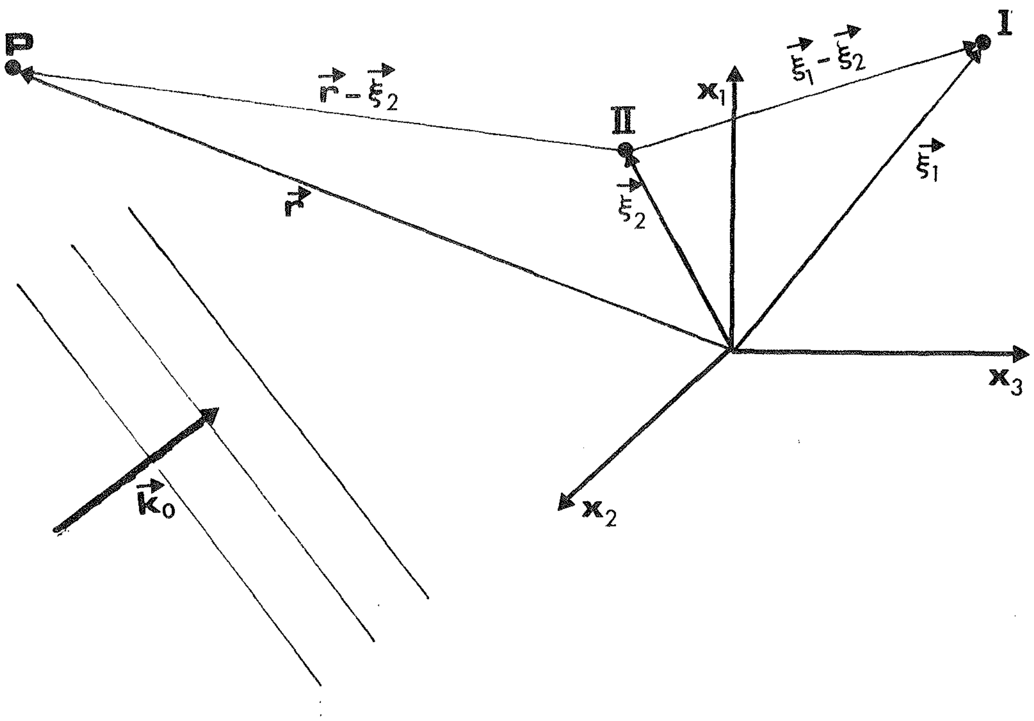

Figure 4.3. The scattering of a plane wave by two point particles.

Under this approximation the sum of the field from the two scatterers will be

$$\alpha\varkappa(\vec{r})\, e^{i\Delta\vec{k}\,\vec{\xi}_1}\left(1 + e^{i\Delta\vec{k}(\vec{\xi}_2-\vec{\xi}_1)}\right) \frac{e^{i(kr - \omega_0 t)}}{r} \tag{4.8}$$

$$\Delta\vec{k} = \vec{k}_i - k\vec{e}_r$$

If $\Delta\vec{k}(\vec{\xi}_2 - \vec{\xi}_1)$ equals π, the scattered field will be zero in this direction

It will more generally be possible to position two scatterers so that the output of the receiving transducer from these two scatterers practically cancel. (Section 4.3C). If we move one scatterer a small distance so that the phase of the field varies less than 10 % in both directions at the transducer, the output from the two scatterers will still practically cancel.

For a phase variation of less than 10 % we must have

$$|\Delta\vec{k}\cdot\Delta\vec{\xi}_i| < \frac{2\pi}{10} \tag{4.9}$$

where $\Delta\vec{\xi}_i$ is the variation in the position of the scatterer. When $\Delta\vec{\xi}_i$ is normal to the direction of $\vec{\Delta k}$, $|\Delta\vec{\xi}_i|$ can be very large. It is, however, previously emphasized that ξ_i/r is much smaller than unity when obtaining Eq. (4.6).

In the direction of $\vec{\Delta k}$ we must have $|\Delta\vec{\xi}_i| < 2\pi/10\Delta k$. The maximum value of Δk occurs in the reverse direction where $\Delta k = 2k_0 = 4\pi/\lambda$. In this direction we must have $|\Delta\xi_i| < \lambda/20$ which means that the variation in ξ_i must be less than $\lambda/10$.

If we form a rectangular volume element with two sides equal to $\lambda/4$ and the third equal to $\lambda/10$, this element will contain 12000 red cells at 2 MHz and 100 red cells at 10 MHz, on the average.

From the discussion above, it should follow that if the concentration of blood corcpuscles of all the elements of this size was the same, there should be no scattering of ultrasound from blood. This because the probability would be one, of finding a scatterer in such a position as to cancel the output of the transducer from another scatterer.

To get a scattered wave, a variation in the cell concentration between the elements is necessary. The deviation in the cell concentration from the mean value will be called the fluctuation of the concentration. The scattering may thus be considered to stem from the fluctuations in the cell concentration rather than from the cells as such. Because of the relative concentration of white blood cells and platelets to that of the red cells, it should also be sufficient to consider the red cells only as responsible for the scattering.

Consider wave motion in a gas of small particles or a suspension of small particles in a liquid. A characteristic dimension is the mean *collision frequency*, i.e. the mean number of collisions between particles pr. unit time. If the concentration of particles is dilute, the main type of collisions will be binary, i.e. only two particles are interacting during the collision. As the concentration increases, tripple and quadruple collisions become more probable.

In blood at normal concentration of cells (ca. 50 %), the cells are in contact almost all the time. The probablility that one cell at a given instant of time is not contacting at least one other cell is negligible. In this case the collision frequency has lost its meaning or should be made infinite.

When the collision frequency is high compared to the wave frequency, the medium will behave as a continuum to the wave motion. If the elasticity and density is constant in space and time, the medium will be completely transparent. There will only be some reflection and refraction of the wave at the boundaries. However, if the elastic parameters fluctuate throughout space and/or time, as in blood, there will be scattering. This is analogous to the scattering from discrete particles.

When the collision frequency is smaller than the wave frequency, the situation is different for the gas compared to the suspension of particles in the liquid. In the first case there will be no wave motion or the wave will be heavily damped. In the second case wave motion will be upheld by the liquid.

To a first approximation we may consider the liquid a continuum with the wave velocity somewhat changed by the existence of the particles. However, when we study scattering, the discreteness of the medium will enter in, and we can no longer consider the scattering to stem from the fluctuations in a continuum. To obtain the scattered field we must add all the contributions from the individual scatterers. During this summation the scatterers may be considered stochastically independent of eachother. This phenomenon is considered in more detail in the next two paragraphs.

Scattering of light from density fluctuations in pure liquids has been studied for a long time. Smoluchowski [46] was the first to suggest that the observed scattering of light from homogenous liquids, could stem from the thermodynamic fluctuations of the density from its mean equilibrium value.

Einstein [47] undertook a quantitative calculation of the scattering. He found the interesting result that there will be an interaction only between the incident wave and the Fourier component of the fluctuation, which satisfies the Bragg condition of reflection. This result applies to our work as well.

Other contributors in this field are Ornstein and Zernike [59], Komarov and Fischer [60].

4.2. Concentration fluctuations of blood cells.

In this section we shall make a stochastic treatment of fluctuations in the cell concentration. To do this we study an ensemble of infinite number of blood flow systems. The systems are indentical in all macroscopic physical quantities except for the cell concentration. The cell concentration will have a stochastic variation over the ensemble.

The macroscopic physical quantities are the hydrodynamic velocity field, the temperature field, the mean concentration of cells in blood, the density and compressibility of the blood cells, the shape of the cells, the viscosity, density and compressibility of the plasma.

To avoid confusion we shall at once define three types of average or expectation operations we shall use.

Def. I. Ensemble average.

Having defined the ensemble we may give a probability measure of a stochastic variable of the ensemble. By the ensemble average of the variable we define the expectation of the variable with respect to this probability measure. Symbolically we denote this operation by a bracket, $\langle(\cdot)\rangle$, or $E\{(\cdot)\}$. The last notation is more suitable for denoting conditional expectation $E\{x|y\}$.

Def. II. Time average

The time average of a stochastic variable x is defined by

$$\tilde{x} = \lim_{T\to\infty} \frac{1}{2T} \int_{-T}^{T} x(t)\,dt \tag{4.10}$$

For an ergodic system the time and ensemble average of a variable will be equal. A necessary condition for a system to be ergodic is that the ensemble averages of the system are stationary in time.

Def. III. Space average

The space average of a variable x is defined by

$$\bar{x} = \frac{1}{V} \int_V x(\vec{r})\,d^3r \tag{4.11}$$

V is the volume where the averaging is performed.
This definition especially applies to the velocity field as the mean velocity in the observation region. For stochastic processes depending on the space this definition also applies. A process is space ergodic if

$$\bar{x} = \langle x(\vec{r},t)\rangle \tag{4.12}$$

For the cell concentration this is the case when axial migration may be neglected.

A. Physical basis for the fluctuations.

Microscopic fluctuations in the macroscopic state (density, pressure, energy, electric field etc.) of a physical system is a well known phenomenon. Under thermodynamic equilibrium conditions, the probability of a deviation of a state variable from its mean value is proportional to

$$e^{-(W/kT)} \tag{4.13}$$

where W is the minimum work required to reversibly produce the deviation, k is the Bolzmann's constant and T is the temperature [57].

A loose, but intuitively attractive, interpretation of Eq. (4.13) is that there is an energy kT available which tends to move the system away from equilibrium in a random way. In the probability of a fluctuation it is the ratio of the energy required to produce the fluctuation to the energy available, that enters in by the negative exponential.

In a weak non-equilibrium situation, such as laminar flow with modest shear rate, Eq. (4.13) may be considered to have local validity. Under such conditions it is, however, not only the termal agitation which produces the fluctuations. The flow itself should give an additional fluctuating force. In large deviations from equilibrium, as in turbulent flow and whirls, the fluctuations produced by the flow might be dominating over the thermal fluctuations.

In our case we have a suspension of particles in a fluid where the energy is a complex function, not only of the local concentration, but also of the relative orientations and positions of the cells. In addition to translational and potential energy, the cells may have rotational energy. Both translational and rotational motion will experience an attenuating force from the viscous friction of the fluid.

At equilibrium the complex potential energy interaction between cells is demonstrated by the formation of roleaux and aggregates as discussed in Section 4.1. In the presence of shear gradients in velocity the roleaux and aggregates breaks down and the cells behave mostly as individuals with a large degree of interaction.

Following the situation in equilibrium, we put forth the hypothesis that the probability of a deviation of the number of cells in a small volume ΔV from the mean is proportional to

$$e^{-\frac{W}{\alpha(\vec{v})}} \tag{4.14}$$

As before W is the amount of energy required to produce the fluctuation. $\alpha(\vec{v})$ is a functional of the velocity field in the neighbourhood of our element which influences the situation in ΔV. It may be thought of as the random fluctuating energy available in the element. At equilibrium or uniform velocity we should have $\alpha = kT$.

The minimum of W determines the mean number of cells, n_0, occupying ΔV, i.e.

$$\frac{dW}{dn_0} = 0 \tag{4.15}$$

Expanding W in a power series in $n = n_T - n_0$, where n_T is the total cell concentration, we get

$$W(n) = \frac{1}{2!}\frac{d^2W}{dn_0^2}n^2 + \frac{1}{3!}\frac{d^3W}{dn_0^3}n^3 + \ldots.. \tag{4.16}$$

It seems reasonable that W may be approximated by the first term giving a quadratic dependency on n. This will give a Gaussian probability distribution for the number of cells in ΔV.

When the cells are stochastically independent of eachother, the probability of finding a cell in a volume ΔV is independent of how many cells there already are in ΔV. This is strictly true for point particles only which can be packed infinitely dense. For a diluted concentration of cells we may use this as an approximation since the probability is small that cells are so dense that the packing will be a problem.

The theory of Brownian motion is a stochastic process model for such a suspension of particles [51],[52]. The probability that the volume ΔV will occupy N particles is given by the Poisson distribution

$$P(N) = \frac{\nu^N}{N!}e^{-\nu} \tag{4.17}$$

$$\nu = n_0 \Delta V$$

From this we obatin

$$\langle N \rangle = n_0 \Delta V, \qquad \mathrm{Var}(N) = n_0 \Delta V \tag{4.18}$$

If ν is large, the Poisson distribution may be approximated by a Gaussian distribution

$$P(N) = \frac{1}{\sqrt{2\pi\nu}}e^{-\frac{(N-\nu)^2}{2\nu}} \tag{4.19}$$

As n_0 increases, the interaction between the particles becomes more frequent. This will increase the amount of energy necessary to produce the same fractional deviation of the population of ΔV from the mean, as compared to non-interacting point particles. As a result the variance of N will decrease from the linear dependency of n_0 given in Eq. (4.18), when interaction begins. When interaction between the cells occur, we have

$$Var(N) < n_0 \Delta V \tag{4.20}$$

The concentration of cells in the volume ΔV is defined by

$$n_T = N/\Delta V \tag{4.21}$$

Inserting this in Eq. (4.18) we get

$$\langle n_T \rangle = n_0 \; , \qquad Var(n_T) = n_0/\Delta V \tag{4.22}$$

If we divide the region of blood in small, equal elements ΔV_i, the concentrations in two different elements will be independent, since the particles are independent. We, therefore, have the covariance between the concentration in element k, n_{Tk}, and that in element ℓ, $n_{T\ell}$.

$$Cov(n_{Tk}, n_{T\ell}) = n_0 \frac{\delta_{k\ell}}{\Delta V} \tag{4.23}$$

Here $\delta_{k\ell}$ is the Kronecker delta. Passing to the limit when ΔV tends to zero, we have

$$Cov\{n_T(\vec{r}_1,t)\, n_T(\vec{r}_2,t)\} = n_0 \delta(\vec{r}_1 - \vec{r}_2) \qquad \text{variance} = \infty \tag{4.24}$$

where $\delta(\vec{r})$ is the Dirac δ-function. Physically volume elements ΔV smaller than the particle size have no meaning. Use of the δ-function means that the length of correlation for n_T is much smaller than a typical length scale under which we are studying the system. In our system such a typical scale is the wavelength. As discussed in Section 4.1, a volume element $\Delta V = \lambda^3/160$ can be considered a point, because all the scatterers inside this element will scatter waves with practically the same phase.

B. Mathematical model and correlation functions for the fluctuations.

The force giving rise to the fluctuations is connected to the microscopic motion of the cells. We have already defined our ensemble as a group consisting of an infinite number of systems where the hydrodynamic velocity field, the temperature field, the mean concentration of cells and the physical properties of cells and plasma are equal. The microscopic motion can now be descibed by a stochastic concentration current following stochastic laws over the ensemble. This current may cause the cells to move together at one position, giving a rise in concentration, while a dilution is taking place at another position. The change in concentration is given by the divergence of the current, div $\vec{j}$.

The stochastic properties of this current should clearly depend on the macroscopic motion of the blood which defines the ensemble. One should expect a turbulent flow to give a larger microscopic motion than laminar flow. A spiral tendency in the microscopic motion of the cells could be found in laminar flow with large shear gradients in velocity. Spiral motion has, however, no divergence and will not affect the concentration of cells, so that an additional term must account for axial migration, Section 4.1B.

Let $\vec{v}(\vec{r},t)$ be the hydrodynamic velocity field of blood. The total concentration current of cells may be written

$$\vec{j}_T(\vec{r},t) = n_T(\vec{r},t)\vec{v}(\vec{r},t) - D\nabla n_T(\vec{r},t) + \vec{j}(\vec{r},t) \qquad (4.25)$$

$\vec{j}_T$ is the total concentration current, n_T is the total concentration, and D is the diffusion constant. The first term is the convection term, the second represents the diffusion of cells when a concentration gradient is present, and the third term represents the microscopic stochastic motion of the cells. The continuity equation for the cells may be written in terms of the concentration $n_T(\vec{r},t)$

$$\frac{\partial n_T}{\partial t} + \text{div } \vec{j}_T = 0 \qquad (4.26)$$

Combining Eq. (4.25) and (4.26) and taking into account that blood is incompressible (i.e. $\nabla\vec{v} = 0$) the result is

$$\frac{\partial n}{\partial t} + \vec{v}\cdot\nabla n = D\nabla^2 n + \nabla\vec{j} \qquad (4.27)$$

We have used the fact that the gradients in time and space of the total concentration n_T is given by those of the fluctuation $n = n_T - n_0$. If the ensemble average, $n_0(\vec{r},t) = \langle n_T(\vec{r},t)\rangle$ is not constant in space, as in axial migration, the gradient of n_T will still be dominated by that of n.

Equation (4.27) is a stochastic differential equation for the fluctuation n. From this the stochastic properties of n may be deduced when those of $\vec{j}$ is established. Theoretically the stochastic properties of $\vec{j}$ may be deduced from a more detailed theory of the cell motion. This task, however, will be too ambigious for our purpose, and we shall merely state the properties by assumption.

We recall from Section 4.1 that at 2 MHz the "point" element of blood contains 12 000 cells while at 10 MHz the content is 100. It is therefore reasonable to assume a δ-correlation for the stochastic current.

$$\langle j_k(\vec{r},t)\, j_\ell(\vec{r} + \vec{\xi}, t + \tau)\rangle = \frac{\langle j^2(\vec{r},t)\rangle}{3}\, \delta_{k\ell}\, \delta(\vec{\xi})\, \delta(\tau) \tag{4.28}$$

j_k is a component of $\vec{j}$. $\delta_{k\ell}$ is the Kronecker delta which states that two components of $\vec{j}$ are uncorrelated. $\langle j^2\rangle$ is the variance of the magnitude of $\vec{j}$. The factor 1/3 follows from isotropy and zero correlation between the components of $\vec{j}$. We have $\langle j^2\rangle = \langle j_1{}^2\rangle + \langle j_2{}^2\rangle + \langle j_3{}^2\rangle = 3\langle j_i{}^2\rangle$, $i = 1,2,3$.

The stochastic properties of the concentration fluctuations are now contained in $\langle j^2\rangle$. For a time steady velocity field, $\langle j^2\rangle$, will be independent of time. As discussed above, it could yet depend on space because of the space dependency of $\vec{v}$.

By the Helmholz decomposition theorem for a vector field we may express $\vec{j}$ by a scalar potential $A(\vec{r},t)$ and a vector potential $\vec{B}(\vec{r},t)$.

$$\vec{j}(\vec{r},t) = -\nabla A(\vec{r},t) + \nabla \times \vec{B}(\vec{r},t) \tag{4.29}$$

Since divcurl is a zero operator it is only the scalar potential that affects the concentration fluctuation. There will, therefore, be no correlation between n and $\vec{B}$.

An analytic solution of Eq. (4.27) in shear flow is difficult. We shall, therefore, only give the solution when the velocity field is zero. The solution for a uniform velocity field will be the same if we use a coordinate system which follows the flow. The study of this special case will be a guide to an approximate solution in the case of shear flow.

When the velocity field is zero, Eq. (4.27) reduces to a simple diffusion equation with a source term. The solution may be obtained by the Greens function method [58].

$$n(\vec{r},t) = \int_{-\infty}^{\infty} dt_1 \int d^3r_1 \; G(\vec{r}_1,t_1)\nabla_{\vec{r}}\vec{j}(\vec{r} - \vec{r}_1, t - t_1)$$

$$= \int_{-\infty}^{\infty} dt_1 \int d^3r_1 \; \nabla G(\vec{r}_1,t_1)\vec{j}(\vec{r} - \vec{r}_1, t - t_1)$$

$$G(\vec{r},t) = H(t)\,\frac{e^{-r^2/4Dt}}{(4\pi Dt)^{3/2}} \tag{4.30}$$

$$H(t) = \begin{cases} 1 & t > 0 \\ 0 & t < 0 \end{cases}$$

From this expression we may obtain the autocorrelation function for n in space and time

$$\langle n(\vec{r},t)n(\vec{r} + \vec{\xi}, t + \tau)\rangle$$

$$= \int dt_1 \int dt_2 \int d^3r_1 \int d^3r_2 \sum_{k\ell} \frac{\partial G(\vec{r}_1,t_1)}{\partial x_{1k}} \frac{\partial G(\vec{r}_2,t_2)}{\partial x_{2\ell}} \langle j_k(\vec{r}-\vec{r}_1, t-t_1)\, j_\ell(\vec{r}+\vec{\xi}-\vec{r}_2, t+\tau-t_2)\rangle$$

$$= \int dt_1 \int dt_2 \int d^3r_1 \int d^3r_2 \sum_{k\ell} \frac{\partial G(\vec{r}_1,t_1)}{\partial x_{1k}} \frac{\partial G(\vec{r}_2,t_2)}{\partial x_{2\ell}} \frac{\langle j^2\rangle}{3} \delta_{k\ell}\delta(\vec{\xi}+(\vec{r}_1-\vec{r}_2))\delta(\tau+(t_1-t_2))$$

$$= \frac{\langle j^2\rangle}{3} \int dt_1 \int d^3r_1 \; \nabla G(\vec{r}_1,t_1) \; \nabla G(\vec{r}_1 + \vec{\xi}, t_1 + \tau)$$

Since the blood is at rest $\langle j^2\rangle$ is constant in both space and time and may be held outside the integration.
Integrating by parts over d^3r_1 we get

$$\langle n(\vec{r},t)n(\vec{r} + \vec{\xi}, t + \tau)\rangle$$

$$= -\frac{\langle j^2\rangle}{3} \int dt_1 \int d^3r_1 \; G(\vec{r}_1,t_1)\nabla^2 G(\vec{r}_1 + \vec{\xi}, t_1 + \tau)$$

$$= -\frac{\langle j^2\rangle}{3} \int dt_1 \int d^3r_1 \nabla^2 G(\vec{r}_1,t_1) \; G(\vec{r}_1 + \vec{\xi}, t_1 + \tau)$$

$$= -\frac{\langle j^2\rangle}{6} \int dt_1 \int d^3r_1 \{G(\vec{r}_1,t_1)\nabla^2 G(\vec{r}_1+\vec{\xi}, t_1+\tau) + \nabla^2 G(\vec{r}_1,t_1)G(\vec{r}_1+\vec{\xi}, t_1+\tau)\}$$

The Green's function satisfies the following differential equation

$$\frac{\partial G}{\partial t} - D\nabla^2 G = \delta(\vec{r})\delta(t)$$

$\nabla^2 G$ may be expressed by $\partial G/\partial t$ and the δ-functions from this equation. When this expression is inserted in the above integral, we get

$$\frac{\langle j^2\rangle}{6D} \int d^3r_1 \int dt_1 \{\delta(\vec{r}_1)\delta(t_1)G(\vec{r}_1 + \vec{\xi}, t_1 + \tau) + G(\vec{r}_1, t_1)\delta(\vec{r}_1 + \vec{\xi})\delta(t_1 + \tau)\} -$$

$$\frac{\langle j^2\rangle}{6D} \int d^3r_1 \int dt_1 \frac{\partial}{\partial t_1} \{G(\vec{r}_1, t_1)G(\vec{r}_1 + \vec{\xi}, t_1 + \tau)\}$$

The integration over t_1 in the last integral may be performed directly and the result is zero. In the first integral we have to differentiate between $\tau > 0$ and $\tau < 0$. We get

$$\frac{\langle j^2\rangle}{6D} G(\vec{\xi}, \tau) \qquad \tau > 0$$

$$\frac{\langle j^2\rangle}{6D} G(-\vec{\xi}, -\tau) \qquad \tau < 0$$

Since G is an even function in $\vec{\xi}$ we may write

$$\boxed{\langle n(\vec{r}, t)n(\vec{r} + \vec{\xi}, t + \tau)\rangle = \frac{\langle j^2\rangle}{6D} G(\vec{\xi}, |\tau|)} \tag{4.31}$$

In the limit $\tau \to 0$ we have

$$\boxed{\begin{aligned} &\langle n(\vec{r}, t)n(\vec{r} + \vec{\xi}, t)\rangle = \langle n^2\rangle\delta(\vec{\xi}) && \text{a)} \\ &\langle n^2\rangle = \frac{\langle j^2\rangle}{6D} && \text{b)} \end{aligned}} \tag{4.32}$$

This shows that on the scale that we are studying the problem, the fluctuations at a fixed time will be δ-correlated in space. Eq. (4.32) also relates the fluctuation of the stochastic current to the fluctuation in the concentration, via the dissipative process described by the diffusion constant.

The variance of n given by Eq. (4.32) is infinite as for all δ-correlated processes. As discussed in connection with Eq. (4.24), the physical quantity is the number of cells (or volume of cells) in a small volume ΔV. The variance of this quantity will be

Er ikke $\langle n^2\rangle$ variansen til n ?

$$\langle(n\Delta V)^2\rangle = \langle n^2\rangle\Delta V \tag{4.33}$$

$$\langle n^2 \rangle \leq n_0 \tag{4.34}$$

where the sign of equality appears when the interaction between the cells is weak, i.e. n_0 is low.

A bound on the diffusion constant may be estimated from the theory of Brownian motion of independent particles. The mobility ,μ, of a particle exposed to a force, $\vec{F}$, is defined by

$$\vec{v} = \mu \vec{F} \tag{4.35}$$

where $\vec{v}$ is the stationary velocity of the particle. The diffusion constant is related to the mobility through the Einstein relation

$$D = kT \cdot \mu \tag{4.36}$$

where k is the Boltzmann constant and T is the temperature. When the concentration of cells is raised until the interaction between the cells enters, the mobility will decrease. We may, therefore, write

$$D \leq kT \cdot \mu_{ind} \tag{4.37}$$

where μ_{ind} is the mobility for independent cells.

For a sphere of radius a in a liquid with viscosity ν, the mobility is given by the Stoke's law

$$\mu_{ind} = (6\pi \nu a)^{-1} \tag{4.38}$$

We could use this formula for an approximate estimation of the mobility (ν = 1.2 cP, Section 4.1). Taking the radius of the sphere to be 5μm, we get

dit was vage!

$$\mu_{ind} = 10^7 \text{ m/sNt}$$

The mobility may also be estimated from the red cell sedimentation rate. During the first hour cells sediment 2-5 mm in a 200 mm column of blood. Taking the volume of the cell to be 90 μ^3, the density of the cell to be 1.1 g/cm^3 and the mean density of the surrounding blood to be 1.06 g/cm^3 a sedimentation rate of 3 mm/hour gives the mobility

$$\mu = 2.4 \cdot 10^7 \text{ m/sNt}$$

These two values are very close, and from the Einstein relation an approximate value of D can be given ($\mu = 10^7$ m/sNt).

$$D \approx 5 \cdot 10^{-14} \ m^2/\mathrm{sec} \qquad (4.39)$$

From Eq. (4.30) and Eq. (4.31) it is seen that a correlation length for n could be defined by

$$\ell = 10\sqrt{D|\tau|} \qquad (4.40)$$

If $|\tau|$ is 1 sec, we have from the two equations above

$$\ell \approx 2 \cdot 10^{-4} \ \mathrm{cm} \qquad (4.41)$$

At 2 MHz $\ell/\lambda \approx 3 \cdot 10^{-4}$ while at 10 MHz $\ell/\lambda \approx 10^{-3}$. As discussed above this dimension could clearly be considered a point.

From Eq. (4.30) and (4.31) we have

$$\langle n(\vec{r},t)\, n(\vec{r} + \vec{\xi}, t + \tau)\rangle \underset{D \to 0}{\to} \langle n^2\rangle \delta(\vec{\xi}) \qquad (4.42)$$

The above discussion thus indicates that for all practical purposes the concentration fluctuations could be considered δ-correlated in space and constant in time.

The results of the above discussion may be summarized in two points: For zero velocity field we have

i. The fluctuation n will be δ-correlated in space when $\tau = 0$ regardless of the magnitude of the diffusion constant D.

ii. The fluctuation n will be approximately δ-correlated in space when $\tau \neq 0$ provided $\sqrt{D|\tau|}/\lambda \ll 1$. In our case the diffusion constant is so small that this condition will hold for all practical values of τ. This means that the change of the correlation function with τ is very slow.

We shall now make an extrapolation of the result for the zero velocity case to the case of a nonzero velocity field. A physical interpretation of Eq. (4.31) is that a fluctuation n at at position $\vec{r}$ at the time t diffuses out to the surroundings. At a time $t + \tau$ the information of this fluctuation has passed to all space because of instantaneous effect of the diffusion process.

The value of the correlation function will, however, be substantially different from zero only in a finite region of space defined by

$\xi < \ell$

where ℓ is given by Eq. (4.40).

If $\max_i |\nabla v_i| \cdot \ell \cdot \tau$ is much smaller than the path length $v\tau$ of a fluid element in the time τ, the flow will appear locally homogeneous to the diffusion. This requirement may be written

$$\ell << \frac{v}{\max_i |\nabla v_i|} \tag{4.43}$$

When this condition holds, the fluctuations may be considered locally δ-correlated.

By a transformation of the coordinates, the correlation function defined in the original coordinates becomes

$$<n(\vec{r},t)n(\vec{r} + \vec{\xi},t + \tau)> = <n^2>\delta\{\vec{\xi} - \int_t^{t+\tau} \vec{v}[\vec{r}(p),p]dp\} \tag{4.44}$$

Here $\vec{r}(\tau)$ is the path of the fluid element which at time t has the position $\vec{r}$.

The assumption of δ-correlation in space for all τ is equivalent to putting the diffusion constant to zero. From Eq. (4.32b) we see that it is consistent in the same approximation to set $<j^2>$ equal to zero since $<n^2>$ has to be finite. This implies that $\vec{j}$ has to be zero in probability and Eq. (4.27) takes on the simple form

$$\frac{\partial n}{\partial t} + \vec{v}\nabla n = 0 \tag{4.45}$$

with the solution

$$n(\vec{r},t) = f\{\vec{r} - \int_0^t dp\ \vec{v}[\vec{r}(p),p]\} \tag{4.46}$$

where $\vec{r}(\tau)$ once again is the path of the fluid element which at time t has the position $\vec{r}$. $f(\vec{r})$ is an arbitrary function which gives a sample function of the fluctuation at $t = 0$. Eq. (4.44) then shows that f has to be δ-correlated in space.

Eq. (4.46) demonstrates that the time dependency of the sample functions of the fluctuations is given by the convection only when diffusion is neglected. There will be no change with time of the sample function along a path of flow. We shall return to the effect of this approximation when we study the spectrum of the scattered ultrasound in Section 5.1 C.

As discussed above $\langle j^2\rangle$ should depend on both space and time under unsteady and shear flow. As a result $\langle n^2\rangle$ should also depend on space and time. In neglecting diffusion, $\vec{j} = \vec{0}$, $\langle n^2\rangle$ will be constant along the flow path of a fluid element. We must, however, bear in mind that $\vec{j} = \vec{0}$ is only an approximation, and violent motion of the blood in a local place for a short time may change $\langle n^2\rangle$ rather abruptly. Therefore, $\langle n^2\rangle$ should depend on time when we follow a fluid element under violent motion.

Under steady laminar flow $\langle n^2\rangle$ will be constant for all fluid elements. It may yet depend on space because the shear rate depends on space.

We, therefore, rewrite Eq. (4.44) in the form we shall use later

$$\boxed{\langle n(\vec{r},t)n(\vec{r}+\vec{\xi},t+\tau)\rangle = \langle n^2(\vec{r},t)\rangle\delta\{\vec{\xi} - \int_t^{t+\tau} \vec{v}[\vec{r}(p),p]dp\}} \tag{4.47}$$

C. Crosscorrelation between n and $\vec{j},A,\vec{B}$.

For zero or homogenous velocity field we get from Eq. (4.30)

$$\langle\vec{j}(\vec{r},t)n(\vec{r}+\vec{\xi},t+\tau)\rangle$$

$$= \sum_k \vec{e}_k \sum_\ell \int d^3r_1 \int_{-\infty}^{\infty} dt_1 \frac{\partial G(\vec{r}_1,t_1)}{\partial x_\ell} \langle j_k(\vec{r},t)j_\ell(\vec{r}+\vec{\xi}-r_1,t+\tau-t_1)\rangle$$

$$= \frac{\langle j^2\rangle}{3}\int d^3r_1 \int_{-\infty}^{\infty} dt_1 \nabla G(\vec{r}_1,t_1)\delta(\vec{\xi}-\vec{r}_1)\delta(\tau-t_1) \tag{4.48}$$

When we approximate the correlation function of $\vec{j}$ by a δ-function, we must bear in mind that the autocorrelation function is an even function in both $\vec{\xi}$ and τ. We therefore have

$$\int_{-\infty}^{\infty} dt_1 H(t_1)\delta(t_1+\tau) = \begin{cases} 1 & \tau > 0 \\ \frac{1}{2} & \tau = 0 \\ 0 & \tau < 0 \end{cases}$$

The crosscorrelation between $\vec{j}$ and n then will be

$$\langle\vec{j}(\vec{r},t)n(\vec{r}+\vec{\xi},t+\tau)\rangle = \begin{cases} \frac{\langle j^2\rangle}{3}\nabla G(\vec{\xi},\tau) & \tau > 0 \\ \frac{\langle j^2\rangle}{6}\nabla\delta(\vec{\xi}) & \tau = 0 \\ 0 & \tau < 0 \end{cases} \tag{4.49}$$

The rules for differention of correlation functions give the correlation function between n and the scalar potential for $\vec{j}$.

$$\langle A(\vec{r},t)n(\vec{r}+\vec{\xi},t+\tau)\rangle = \begin{cases} \frac{\langle j^2\rangle}{3} G(\vec{\xi},\tau) & \tau > 0 \\ \frac{\langle j^2\rangle}{6}\delta(\vec{\xi}) & \tau = 0 \\ 0 & \tau < 0 \end{cases}$$

where A is defined in Eq. (4.29)

As discussed when considering the autocorrelation function for n, we may approximate this crosscorrelation function by $\delta(\vec{\xi})$ for all practical values of τ. In the general case with nonzero velocity field we may write, taking Eq. (4.32b) and the variation of $\langle n^2\rangle$ with space and time into account

$$\boxed{\langle A(\vec{r},t)n(\vec{r}+\vec{\xi},t+\tau)\rangle = \begin{cases} 2D\langle n^2(\vec{r},t)\rangle\delta(\vec{\xi}-\int_t^{t+\tau}\vec{v}[\vec{r}(p),p]dp) & \tau > 0 \\ D\langle n^2(\vec{r},t)\rangle\delta(\vec{\xi}) & \tau = 0 \\ 0 & \tau < 0 \end{cases}} \tag{4.50}$$

$\vec{r}(p)$ is the path of the fluid element which at time t has the position $\vec{r}$. As discussed in connection with Eq. (4.29) we have

$$\boxed{\langle\vec{B}(\vec{r},t)n(\vec{r}+\vec{\xi},t+\tau)\rangle = \vec{0}} \tag{4.51}$$

D. Further discussion on the assumption of δ-correlation for the stochastic current.

The solution of Eq. (4.27) with $\vec{v}=\vec{0}$ may be rewritten in the following form [58]

$$n(\vec{r},t) = \int d^3r_1 G(\vec{r} - \vec{r}_1,t)n(\vec{r}_1,0) + \int d^3r_1 \int_0^t dt_1 \nabla_r G(\vec{r} - \vec{r}_1,t - t_1)\vec{j}(\vec{r}_1,t_1) \tag{4.52}$$

The first integral represents the decay of the initial distribution, $n(\vec{r},0)$, and the second integral represents the change of n caused by the stochastic current. Assuming the process to be stationary in space and time we have

$$\langle n(\vec{r},t)n(\vec{r} + \vec{\xi},t + \tau)\rangle = \langle n(\vec{0},0)n(\vec{\xi},\tau)\rangle = E\{E\{n(\vec{\xi},\tau)\,|\,n(\vec{0},0)\}\} \tag{4.53}$$

The conditional expectation of $n(\vec{\xi},\tau)$ given $n(\vec{r},0)$ may be obtained from Eq. (4.52), $\tau > 0$

$$E\{n(\vec{\xi},\tau)\,|\,n(\vec{r},0)\} = \int d^3r_1 G(\vec{\xi} - \vec{r}_1,\tau)E\{n(\vec{r}_1,0)\,|\,n(\vec{r},0)\}$$
$$+ \int d^3r_1 \int_0^\tau dt_1 \nabla_r G(\vec{\xi} - \vec{r}_1,\tau - t_1)E\{\vec{j}(\vec{r}_1,t_1)\,|\,n(\vec{r},0)\} \tag{4.54}$$

n is obtained from $\vec{j}$ by a time causal operator. When $\vec{j}$ is δ-correlated in time the conditional expectation

$$E\{\vec{j}(\vec{r}_1,t_1)\,|\,n(\vec{r},0)\}$$

will take on values different from zero only when $t_1 \leq 0$. This implies that the last integral in Eq. (4.54) vanishes. From the same equation we then see that $E\{n(\vec{\xi},\tau)\,|\,n(\vec{r},0)\}$ evolves by a homogenous diffusion equation

$$\frac{\partial E\{n(\vec{\xi},\tau)\,|\,n(\vec{r},0)\}}{\partial t} - D\nabla^2 E\{n(\vec{\xi},\tau)\,|\,n(\vec{r},0)\} = 0 \tag{4.55}$$

If $\vec{j}$ is not δ-correlated in time, $E\{\vec{j}(\vec{r}_1,t_1)|n(\vec{r},0)\}$ will take on values different from zero for $t_1 > 0$ and an inhomogenous term in Eq. (4.55) will occur.

It seems reasonable that on the scale we are studying the problem Eq. (4.55) should hold. This directly implies δ-correlation in time for $\vec{j}$. The δ-correlation in space must still be obtained by direct assumption comparing the cell scale in blood to the ultrasonic wave length.

To obtain the full correlation function for n we must calculate $E\{n(\vec{\xi},\tau)\,|\,n(\vec{0},0)\}$. Assuming Eq. (4.55) to be valid this function is given once $E\{n(\vec{r},0)\,|\,n(\vec{0},0)\}$ is given. This is given by the history of n before $t = 0$.

If $\vec{j}$ is the only force affecting n from $t = -\infty$ and δ-correlation in space of $\vec{j}$ is assumed, we have from Eq. (4.32)

$$E\{n(\vec{r},0)\,|n(\vec{0},0)\} = n^2(\vec{0},0)\,\delta(\vec{r}) \tag{4.56}$$

By Eq. (4.54) this gives, $\tau > 0$

$$E\{n(\vec{\xi},\tau)\,|n(\vec{0},0)\} = n^2(\vec{0},0)\,G(\vec{\xi},\tau) \tag{4.57}$$

Averaging over $n(\vec{0},0)$ and encountering stationary conditions in space and time, putting $\langle n^2(\vec{0},0)\rangle = \langle n^2(\vec{r},t)\rangle = \text{const}$, we get

$$\langle n(\vec{r},t)\,n(\vec{r} + \vec{\xi},t + \tau)\rangle = \langle n^2\rangle G(\vec{\xi},\tau) \qquad \tau > 0 \tag{4.58}$$

Being stationary the correlation function must be symmetric in τ. This implies that the absolute value of τ should be used when τ is negative.

In Section 4.2 B we have found a decrease in the diffusion constant with increasing concentration of cells. Eq. (4.40) indicates a decrease in the correlation length with increasing concentration. This may seem a little contradictory because we have often encountered that the cells will be stochastically independent of eachother only at very low concentrations, and that the degree of interaction between the cells increases with concentration.

The reason for this is that the scale on which we are studying the fluctuations is larger than that for the neighbouring interactions between the cells. Information of a fluctuation is only communicated by diffusion and since translational momentum and energy will be lost in the collision between cells, the diffusion constant decreases with concentration.

On this scale the fluctuations at one specified time will be δ-correlated in space for all practical concentrations n. The difference between the low concentration case and the high concentration case is contained in $\langle n^2\rangle$. For low concentration between the cells we will have $\langle n^2\rangle = n_0$, while in the high concentration case with interaction between the cells, $\langle n^2\rangle$ will decrease from this value as indicated in Eq. (4.34).

4.3. The scattering of ultrasound from concentration fluctuations of cells.

In the usual method of blood velocity measurements by ultrasound, the incident wave is transferred from a transducer at the skin or at the vessel-surface. Because of the inhomogeneity of the biological tissue, the wave will undergo refraction and scattering on its way to the blood. In the following these effects are neglected.

When entering the blood, the wave will pass into a medium with a velocity gradient. The wave motion in such a medium is generally very complex. The velocity of blood is, however, very small compared to that of the sound. A good approximation is therefore, to consider blood at rest with respect to wave-motion [50].

In a liquid we generally think of longitudinal acoustical waves. In a viscous liquid we may also have shear waves, but theese are heavily damped and are therefore neglected.

The cells are truly anisotropic scatterers. When blood is at rest, they are distributed randomly, some of them forming rouleaux and aggregates. In shear motion, however, the cells have a tendency of orienting themselves along the shear direction as discussed in the previous paragraph. This should give anisotropic properties concerning elastic wave motion, but there are arguments that the degree of anisotropy is not very high. First, the difference in elasticity and mass density between plasma and cells is not very high. Second, the packing of cells is dense. The membrane of the cells seems to behave like a football bladder around the hemoglobine molecules. The cells are, therefore, quite deformarble, providing almost the same properties of compressibility in all directions of the blood. In this text we treat the blood to have isotropic properties concerning wave motion.

A. Basic scattering theory.

In wave motion the fluid elements will oscillate around their elastic equilibrium position $\vec{r}$. Let $\vec{u}(\vec{r},t)$ be the velocity of displacement of such a fluid element at time t. We consider here only small displacements so that nonlinear terms can be neglected. The time change of the pressure, p, associated with adiabatic elastic compressions and rarefactions of the fluid can be written [49][54]

$$\frac{\partial p}{\partial t} = -\frac{1}{\varkappa}\nabla\vec{u} \qquad (4.59)$$

$\varkappa$ is the compressibility. Sometimes the bulk modulus or modulus of compression, $c = \varkappa^{-1}$, is used. The equation of motion for a small fluid element under elastic deformation will be

$$\frac{\partial(\rho\vec{u})}{\partial t} = -\nabla p \tag{4.60}$$

where ρ is the mass density of the fluid.

Both mass density and compressibility will change with time and position because of variations in cell concentration.

$$\begin{aligned} \rho(\vec{r},t) &= \rho_0 + \rho_1(\vec{r},t) \\ \varkappa(\vec{r},t) &= \varkappa_0 + \varkappa_1(\vec{r},t) \end{aligned} \tag{4.61}$$

Here the subscript 0 indicates mean values taken over a large volume. ρ_1 and $\varkappa_1$ are the local deviations from theese values. If the collision frequency is so high that we may consider the fluid as a continuum, ρ_1 and $\varkappa_1$ can be expressed directly by the fluctuation in cell concentration, n.

$$\rho_1(\vec{r},t) = \frac{d\rho}{dn_0}\, n(\vec{r},t) \qquad \varkappa_1(\vec{r},t) = \frac{d\varkappa}{dn_0}\, n(\vec{r},t) \tag{4.62}$$

When migration occurs n_0 will be space dependent. We then define $\rho_0(r,t) = \langle\rho(r,t)\rangle$ and $\varkappa_0(r,t) = \langle\varkappa(r,t)\rangle$. These variables vary so slowly in space that gradients will still mainly be given by those of ρ_1 and $\varkappa_1$.

If the condition on the collision frequency is not met, ρ_1 and $\varkappa_1$ cannot be expressed in this way by n. To treat the scattering in this case we have to consider individual particles suspended in a liquid. We leave the more detailed discussion of this case until the theory of the scattering is more developed.

In wave motion the time change in $\rho\vec{u}$ will be dominated by that of $\vec{u}$. We may, therefore, approximate Eq. (4.60) by

$$\frac{\partial\vec{u}}{\partial t} = -\frac{1}{\rho}\nabla p \tag{4.63}$$

Combining Eq. (4.63) and Eq. (4.59) and encountering slow time dependency of $\varkappa$ compared to p, we get

$$\nabla(\frac{1}{\rho}\nabla p) - \varkappa\frac{\partial^2 p}{\partial t^2} = 0 \tag{4.64}$$

This is the equation governing motion of pressure waves with small apmlitude in blood. Using Eq. (4.61) we may reorganize Eq. (4.64) to get

$$\boxed{\begin{aligned} &\nabla^2 p - \frac{1}{c^2}\frac{\partial^2 p}{\partial t^2} = \frac{1}{c^2}\frac{\varkappa_1}{\varkappa_0}\frac{\partial^2 p}{\partial t^2} + \nabla\left(\frac{\rho_1}{\rho}\nabla p\right) \\ &c^2 = \frac{1}{\rho_0 \varkappa_0} \end{aligned}} \tag{4.65}$$

Possible variations in c caused by migration are small and may be neglected. We may here remark that it is $\varkappa_1/\varkappa_0$ while it is ρ_1/ρ which enters into the right side of Eq. (4.65). $\varkappa_0$ is the mean value while ρ is the total local value. For blood the difference between the mean and local value for ρ and $\varkappa$ will be so small that inserting ρ_0 instead of ρ will be a very good approximation.

Eq. (4.65) has the appropriate form to be transformed into an inhomogeneous integral equation. We may consider it as an inhomogeneous wave equation with a source term determined by the solution p itself. We then have [49] [54]

$$\begin{aligned} p(\vec{r},t) = p_0(\vec{r},t) - \frac{1}{4\pi}\int_R d^3\xi \frac{1}{|\vec{r}-\vec{\xi}|}\Bigg\{&\frac{1}{c^2}\,\frac{\varkappa_1\left(\vec{\xi},t-\frac{|\vec{r}-\vec{\xi}|}{c}\right)}{\varkappa_0}\,\frac{\partial^2 p\left(\vec{\xi},t-\frac{|\vec{r}-\vec{\xi}|}{c}\right)}{\partial t^2} \\ &+ \nabla\left(\frac{\rho_1\left(\vec{\xi},t-\frac{|\vec{r}-\vec{\xi}|}{c}\right)}{\rho\left(\vec{\xi},t-\frac{|\vec{r}-\vec{\xi}|}{c}\right)}\,\nabla p\left(\vec{\xi},t-\frac{|\vec{r}-\vec{\xi}|}{c}\right)\right)\Bigg\} \end{aligned} \tag{4.66}$$

Here the operator ∇ should operate on the original space variable $\vec{\xi}$, not on $|\vec{r}-\vec{\xi}|/c$. R is the region containing scatterers.

We now let the incident wave be time harmonic with angular frequency ω_0.

$$p_0(\vec{r},t) = \mathrm{Re}\{\hat{p}_0(\vec{r})e^{i\omega_0 t}\} \tag{4.67}$$

ρ_1 and $\varkappa_1$ will be slowly varying with time compared to the wave. We, therefore, make the approximation

$$\begin{aligned} \varkappa_1\left(\vec{\xi},t - \frac{|\vec{r}-\vec{\xi}|}{c}\right) &= \varkappa_1(\vec{\xi},t) \\ \rho_1\left(\vec{\xi},t - \frac{|r-\vec{\xi}|}{c}\right) &= \rho_1(\vec{\xi},t) \end{aligned} \tag{4.68}$$

Because of the time dependency of ρ_1 and $\varkappa_1$, the total field $p(\vec{r},t)$ will not contain a single frequency. There will be a broadening of the incident spectrum because of diffusion. If blood is in motion, there will also be a doppler shift, as we will se later. We define the complex function $\hat{p}(\vec{r},t)$ by

$$p(\vec{r},t) = \mathrm{Re}\{\hat{p}(\vec{r},t)e^{i\omega_0 t}\} \tag{4.69}$$

The time dependency of $\hat{p}(r,t)$ will be slow like that for ρ_1 and $\varkappa_1$. We, therefore, also approximate

$$\hat{p}(\vec{\xi},t - \frac{|\vec{r} - \vec{\xi}|}{c}) \approx \hat{p}(\vec{\xi},t) \tag{4.70}$$

Eq. (4.66) now takes the form

$$\hat{p}(\vec{r},t) = \hat{p}_0(\vec{r}) - \int_R d^3\xi \frac{e^{-ik_0|\vec{r}-\vec{\xi}|}}{4\pi|\vec{r}-\vec{\xi}|}\{-k_0^2 \frac{\varkappa_1(\vec{\xi},t)}{\varkappa_0}\hat{p}(\vec{\xi},t) + \nabla(\frac{\rho_1(\vec{\xi},t)}{\rho(\vec{\xi},t)}\nabla\hat{p}(\vec{\xi},t))\} \tag{4.71}$$

$$k_0 = \frac{\omega_0}{c}$$

The last term in Eq. (4.71) may be integrated by parts and we get

$$\hat{p}(\vec{r},t) = \hat{p}_0(\vec{r}) + \int_R d^3\xi\{k_0^2 \frac{\varkappa_1(\vec{\xi},t)}{\varkappa_0}\hat{p}(\vec{\xi},t)G(\vec{r}-\vec{\xi}) + \frac{\rho_1(\vec{\xi},t)}{\rho(\vec{\xi},t)}\nabla_\xi\hat{p}(\vec{\xi},t)\nabla_\xi G(\vec{r}-\vec{\xi})\} \tag{4.72}$$

$$G(\vec{r}) = \frac{e^{-ik_0|\vec{r}|}}{4\pi|\vec{r}|}$$

The first term under the integral is a monopole source term, which stems from the fluctuations in the compressibility. The fluctuations in the density give the second term, which is a dipole term.

Eq. (4.72) can be solved by iteration. We then write $\varkappa_1 = \mu\tilde{\varkappa}_1$ and $\rho_1 = \mu\tilde{\rho}_1$ where $<[\int_V d^3r\tilde{\varkappa}_1(\vec{r},t)]^2> = V\cdot\varkappa_0$ and $<[\int_V d^3r\tilde{\rho}_1(\vec{r},t)]^2> = V\cdot\rho_0$, V is an arbitrary volume greater than zero. By this normalization μ will be much smaller than unity. To abbreviate the notation we write the integral operator in Eq. (4.72) μK. The equation then takes on the form

$$\hat{p} = \hat{p}_0 + \mu K\hat{p} \tag{4.73}$$

To a zero order approximation we write

$$\hat{p} = \hat{p}_0$$

Inserting this into the right side of Eq. (4.73) we get the first order approximation

$$\hat{p}_1 = \hat{p}_0 + \mu K\hat{p}_0$$

By iterating this procedure the higher order approximations are

$$\hat{p}_2 = \hat{p}_0 + \mu K\hat{p}_1 = \hat{p}_0 + \mu K\hat{p}_0 + \mu^2 K^2 \hat{p}_0 \tag{4.74}$$

- - - -

$$\hat{p}_n = \hat{p}_0 + \mu K\hat{p}_0 + \; . \; . \; . \; . \; . \; + \mu^n K^n \hat{p}_0$$

- - - -

The series in Eq. (4.74) can be given a direct physical interpretation. The zero order field is the incident field. This is scattered and gives $\mu K\hat{p}_0$, which we call the first order scattered field. This in turn is scattered and gives the second order scattered field $\mu^2 K^2 \hat{p}_0$, and so on.

If μ is small as in blood, the scattered field will decrease rapidly with increasing order. It is, therefore, sufficient to consider the first order scattered field, known as the Born approximation. To the first order the scattered field is then

$$\hat{p}_s(\vec{r},t) = \int_R d^3\xi \{ k_0^2 \frac{\varkappa_1(\vec{\xi},t)}{\varkappa_0} \hat{p}_0(\vec{\xi}) G(\vec{r}-\vec{\xi}) + \frac{\rho_1(\vec{\xi},t)}{\rho(\vec{\xi},t)} \nabla_\xi \hat{p}_0(\vec{\xi}) \nabla_\xi G(\vec{r}-\vec{\xi}) \} \tag{4.75}$$

The validity of the Born approximation when ρ_1 and $\varkappa_1$ cannot be considered small quantities is discussed in [54] for spheres. The result shows that in our case the Born approximation is very good.

When the cell concentration is so high that Eq. (4.62) holds we get, using the approximation $\rho \approx \rho_0$

$$\hat{p}_s(\vec{r},t) = \int_R d^3\xi \{ k_0^2 \frac{1}{\varkappa_0} \frac{d\varkappa}{dn_0} \hat{p}_0(\vec{\xi}) G(\vec{r}-\vec{\xi}) + \frac{1}{\rho_0} \frac{d\rho}{dn_0} \nabla_\xi \hat{p}_0(\vec{\xi}) \nabla_\xi G(\vec{r}-\vec{\xi}) \} n(\vec{\xi},t) \tag{4.76}$$

We are now in position to discuss the situation when the collision frequency condition is not met. As we have discussed above we may treat the scatteres as stochastic independent of eachother. We also consider scatterers which are much smaller than the wavelength and the field outside the scattering region. We may then neglect the variation in p_0 and G over the scatterer, which gives for one scatterer

$$\hat{p}_{si}(\vec{r},t) = k_0^2 \hat{p}_0(\vec{r}_i(t)) G(\vec{r} - \vec{r}_i(t)) \int_{V_i} d^3\xi \frac{\varkappa_1(\vec{\xi},t)}{\varkappa_0}$$
$$+ \nabla_{r_i} \hat{p}_0(\vec{r}_i(t)) \nabla_{r_i} G(\vec{r} - \vec{r}_i(t)) \int_{V_i} d^3\xi \frac{\rho_1(\vec{\xi},t)}{\rho(\vec{\xi},t)} \tag{4.77}$$

V_i is the region occupied by scatterer i and $\vec{r}_i(t)$ is the path of the scatterer. $\varkappa_1$ and ρ_1 are the differences in compressibility and density between the scatterer and the average values over a large volume of the blood. The integrals we write as $\gamma_\varkappa$ and γ_ρ

$$\gamma_{\varkappa i} = \int_{V_i} d^3\xi \frac{\varkappa_1(\vec{\xi},t)}{\varkappa_0} \qquad \gamma_{\rho i} = \int_{V_i} d^3\xi \frac{\rho_1(\vec{\xi},t)}{\rho(\vec{\xi},t)} \tag{4.78}$$

When the scatterers are homogeneous, i.e. ρ_1 and $\varkappa_1$ are constants, we have

$$\gamma_{\varkappa i} = \frac{\varkappa_1}{\varkappa_0} V_i \qquad \gamma_{\rho i} = \frac{\rho_1}{\rho} V_i$$

V is the volume of the scatterer.

We thus see that a cloud of isotropic and independent scatterers may be represented by

$$\begin{aligned} \frac{\rho_1(\vec{r},t)}{\rho(\vec{r},t)} &= \gamma_\rho \sum_i \delta(\vec{r} - \vec{r}_i(t)) \\ \frac{\varkappa_1(\vec{r},t)}{\varkappa_0} &= \gamma_\varkappa \sum_i \delta(\vec{r} - \vec{r}_i(t)) \end{aligned} \tag{4.79}$$

where $r_i(t)$ is the path of scatterer i. Inserting this into Eq. (4.75), the scattered field from such a cloud is obtained

$$\hat{p}_s(\vec{r},t) = \sum_i \{k_0^2\gamma_\varkappa\hat{p}_0(\vec{r}_i(t))G(\vec{r} - \vec{r}_i(t)) + \gamma_\rho\nabla_{r_i}\hat{p}_0(\vec{r}_i(t))\nabla_{r_i}G(\vec{r} - \vec{r}_i(t))\} \tag{4.80}$$

When the mean distance between the scatterers is much smaller than the wavelength, i.e., the "point" volume element considered in Section 4.1C contains many scatterers, the summation in Eq. (4.80) may be approximated by an integral

$$\hat{p}_s(\vec{r},t) = \int_R d^3\xi\, n_T(\vec{\xi},t)\{k_0^2\gamma_\varkappa\hat{p}_0(\vec{\xi})G(\vec{r} - \vec{\xi}) + \gamma_\rho\nabla_\xi\hat{p}_0(\vec{\xi})\nabla_\xi G(\vec{r} - \vec{\xi})\} \tag{4.81}$$

Here we write $n_T(\vec{\xi},t) = n_0 + n(\vec{\xi},t)$. The rest of the integrand is a very rapidly varying function of $\vec{\xi}$. The integral containing n_0 will, therefore, disappear, and again we see that the scattering may be considered to result from the concentration fluctuations of cells

$$\boxed{\hat{p}_s(\vec{r},t) = \int_R d^3\xi n(\vec{\xi},t)\{k_0{}^2\gamma_\varkappa \hat{p}_0(\vec{\xi})G(\vec{r} - \vec{\xi}) + \gamma_\rho \nabla_\xi \hat{p}_0(\vec{\xi})\nabla_\xi G(\vec{r} - \vec{\xi})\}} \tag{4.82}$$

This result is of the same form as that for large values of n_0 given in Eq. (4.76). It will, therefore, be used in the rest of this work. $\gamma_\varkappa$ and γ_ρ should then be defined by

$$\gamma_\varkappa = \int_V d^3\xi \frac{\varkappa_1(\vec{\xi},t)}{\varkappa_0} \qquad \gamma_\rho = \int_V d^3\xi \frac{\rho_1(\vec{\xi},t)}{\rho(\vec{\xi},t)} \quad \text{weak interaction} \tag{4.83a}$$

$$\gamma_\varkappa = \frac{1}{\varkappa_0}\frac{d\varkappa}{dn_0} \qquad \gamma_\rho = \frac{1}{\rho_0}\frac{d\rho}{dn_0} \quad \text{strong interaction} \tag{4.83b}$$

B. The scattering of a plane wave. Experimental investigation of the problem of stochastic dependence-independence of the scatterers.

We now calculate the scattered far-field ($\xi \in R \Rightarrow \xi/r << 1$) when the incident wave is a plane wave, i.e.

$$\hat{p}_0(\vec{r}) = Ae^{-i\vec{k}_0\vec{r}} \tag{4.84}$$

A is the amplitude and $\vec{k}_0$ is the incident wave vector $|\vec{k}_0| = 2\pi/\lambda$. To the first order in ξ/r we get

$$|\vec{r} - \vec{\xi}| = r - \vec{e}_r\cdot\vec{\xi}$$

$$\frac{1}{|\vec{r} - \vec{\xi}|} = \frac{1}{r}$$

$$G(\vec{r} - \vec{\xi}) = \frac{e^{-i(kr - \vec{k}_s\cdot\vec{\xi})}}{4\pi r} \tag{4.85}$$

$$\vec{e}_r = \frac{\vec{r}}{r} \qquad \vec{k}_s = k\cdot\vec{e}_r$$

Eq. (4.82) now takes the form

$$\hat{p}_s(\vec{r},t) = \frac{A}{4\pi}\frac{\omega^2}{c^2}\frac{e^{ikr}}{r}\left\{\gamma_\varkappa + \gamma_\rho\frac{\vec{k}_s\cdot\vec{k}_0}{k^2}\right\}\int_R d^3\xi n(\vec{\xi},t)e^{i(\vec{k}_s-\vec{k}_0)\vec{\xi}} \tag{4.86}$$

The coordinates and directions are given in Figure 4.4.

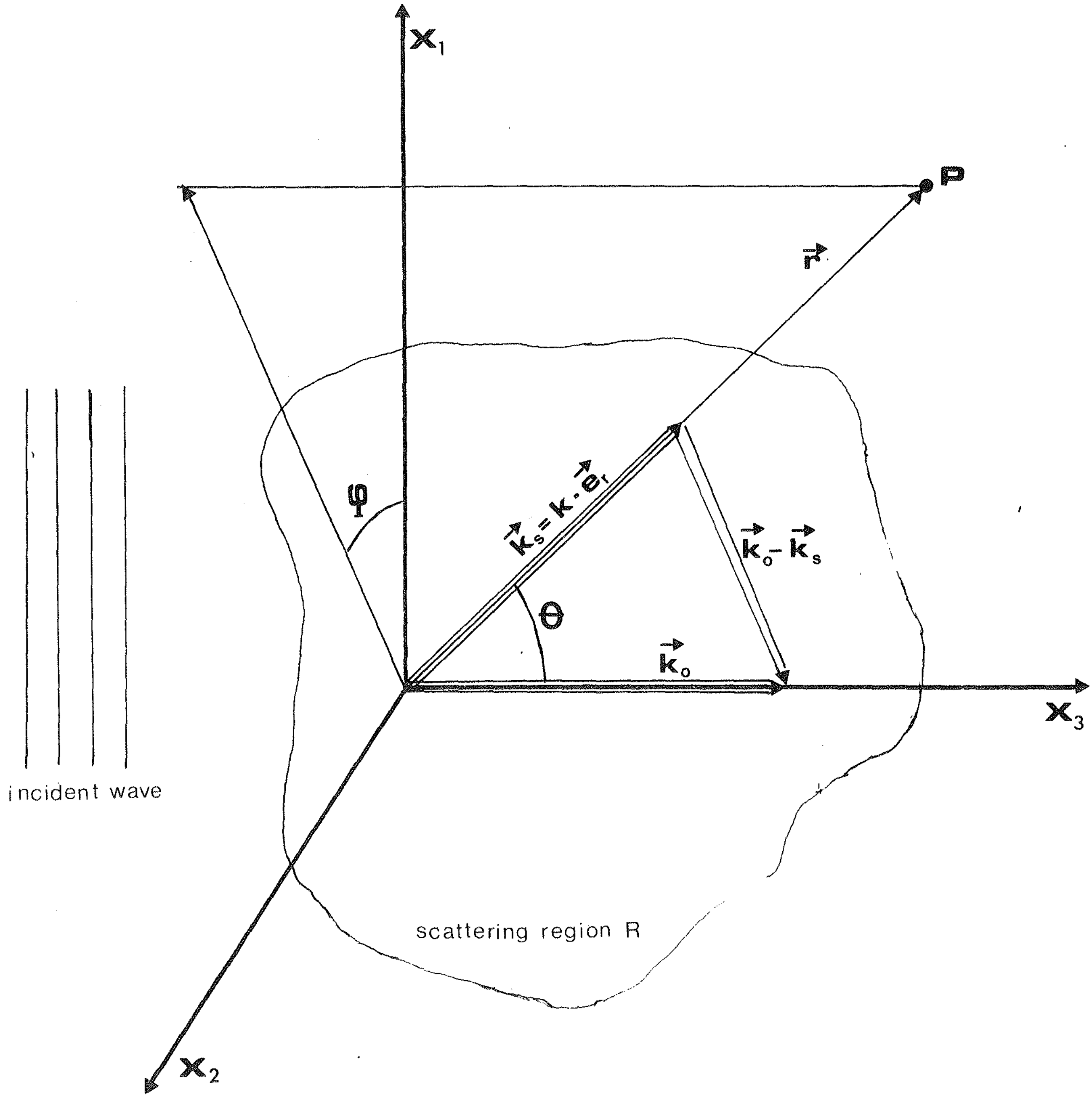

Figure 4.4. Illustrations to the scattering of a plane wave.

The volume integral is the Fourier space transform, $\hat{n}(\vec{q},t)$, of $n(\vec{r},t)$ over the region R. By the inverse theorem we may consider $n(\vec{r},t)$ to be composed of plane partial waves $\hat{n}(\vec{q},t)e^{-i\vec{q}\vec{r}}$. Eq. (4.86) then shows that we will get constructive interaction between the incident wave and the partial wave, $\hat{n}$, which satisfies the Bragg-condition of interference

$$\vec{q} = \vec{k}_s - \vec{k}_0 \tag{4.87}$$

The differential scattering crossection $I(\theta,\varphi)$ is defined by the equation

$$dP(\theta,\varphi) = I(\theta,\varphi)\,d\Omega \tag{4.88}$$

where dP is the mean power scattered in direction (θ,φ) through the differential solid angle $d\Omega$. This gives

$$I(\theta,\varphi) \sim r^2 \langle |p_s(r,\theta,\varphi,t)|^2 \rangle$$

$$\sim \frac{\omega^4}{c^4}\{\gamma_\varkappa + \gamma_\rho \cos\theta\}^2 \int d^3\xi_1 \int d^3\xi_2\, e^{i(\vec{k}_0-\vec{k}_s)(\vec{\xi}_1-\vec{\xi}_2)} \langle n(\vec{\xi}_1,t)\,n(\vec{\xi}_2,t)\rangle$$

From Eq. (4.47) we have

$$I(\theta,\varphi) \sim \frac{\omega^4}{c^4}\{\gamma_\varkappa + \gamma_\rho \cos\theta\}^2 \int_R d^3\xi \langle n^2(\vec{\xi},t)\rangle \tag{4.89}$$

When $\langle n^2\rangle$ is independent of space the scattered intensity will be proportional to the volume of R.

The space dependency of I is given by the factor

$$\{\gamma_\varkappa + \gamma_\rho \cos\theta\}^2 \tag{4.90}$$

The first term represents monopole scattering while the second represents dipole scattering. *The scattered intensity is anisotropic in contrast to the conclusion of Reid & al* [44]. *The scattered intensity is proportional to the frequency in the fourth power as found by Reid & al. Since* $\langle n^2\rangle$ *increases less than* n_0 *when interaction between the cells occurs, it will decrease from being proportional to* n_0, *Eq. (4.34), also in contrast to the results found by Reid & al.*

Treating the scattering as resulting from fluctuations in the parameters of a continuum, resolves the problem of calculating the correlation between the neighbouring cells. Because the wave length of the sound is long, we may approximate the correlation function of the parameter fluctuations by δ-functions, and the interaction between the cells is contained in $\langle n^2 \rangle$ like discussed in Section 4.2 D.

If the sign of $\gamma_\varkappa$ and γ_ρ are equal, the maximum scattered intensity will occur in the forwards direction. If the signs are opposite, the maximum scattered intensity will occur in the backwards direction. There will be directions with zero scattered intensity if

$$|\gamma_\varkappa/\gamma_\rho| \leq 1 \tag{4.91}$$

For plasma the density, ρ_p, is 1.03, while that for cells, ρ_c, is 1.10. A suspension of large particles in a liquid, like that of cells in the plasma, will give a linear dependency of the solution mass density on the mean fraction of cells. We thus have

$$\rho_0(n_0) = \rho_p + n_0(\rho_c - \rho_p) \tag{4.92}$$

Since $\rho_c > \rho_p$, γ_ρ will be positive.

The compressibility of the cells is smaller than that of the plasma and a decrease in solution compressibility with increasing concentration of cells should be expected. This gives a negative value of $\gamma_\varkappa$.

To get quantitative values of $\gamma_\varkappa$, the wave velocity

$$c_0 = (\rho_0 \varkappa_0)^{-\frac{1}{2}} \tag{4.93}$$

as a function of the HCT is measured. The results are given in Figure 4.5.

A physical explanation of the results can be given. At small cell concentrations the interaction between the cells will be weak. The compressibility will be determined by the plasma-plasma and the plasma-cell interaction, and will, therefore, be almost independent of the mean cell concentration, n_0. Since the density increases linearily with n_0, a decrease in c_0 is expected when n_0 increases from zero.

As n_0 increases and interaction between the cells becomes more dominant, the compressibility will decrease, and a subsequent increase in the wave velocity is observed.

The minimum of the wave velocity, therefore gives a limit of about 0.15 for the cell concentration above which the interaction between the cells cannot be neglected.

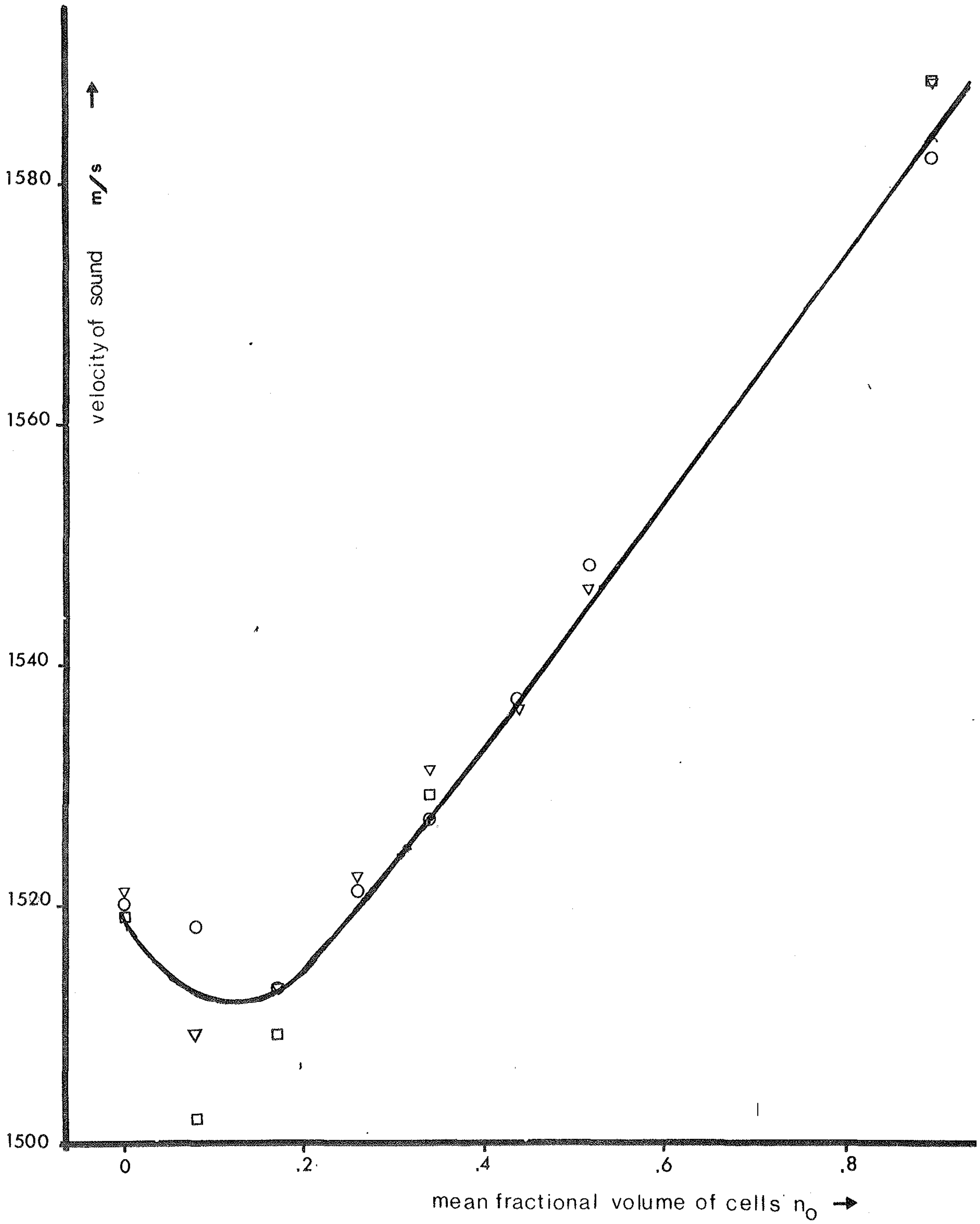

Figure 4.5. Measured velocity of sound for human blood at different values of HCT. The measurements are described in Appendix II.

From the measured results of c and Eqs. (4.92) and (4.93) the compressibility as a function of n_0 is calculated. The result is shown in Figure 4.6.

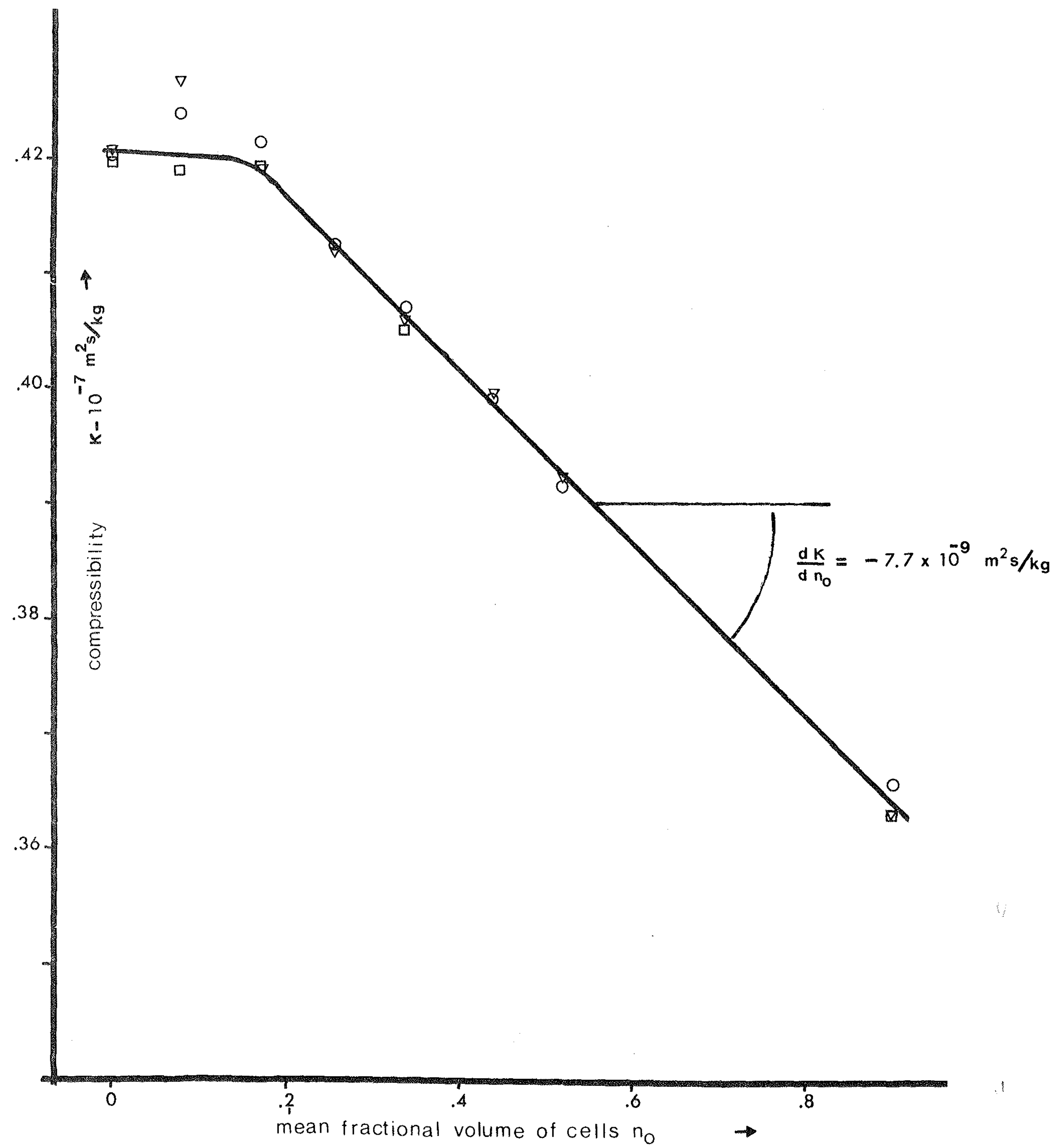

Figure 4.6. Variation of the compressibility $\varkappa$ *with HCT,* n_0*. The values are calculated from the measured values of* c *in Figure 4.5.*

Throughout the whole range of n_0 we have from Eq. (4.92)

$$\gamma_\rho = \frac{1}{\rho_0}\frac{d\rho}{dn_0} = \frac{\rho_c - \rho_p}{\rho_0} \approx 0.065 \tag{4.94}$$

From Figure 4.6 we have when n_0 is above 0.2

$$\gamma_\varkappa = \frac{1}{\varkappa_0}\frac{d\varkappa_0}{dn_0} \approx -0.2 \tag{4.95}$$

Because of the variation of $\varkappa_0$ with n_0 this expression will vary more than $\rho_0^{-1}d\rho/dn_0$ varies with n_0.

When n_0 is less than 0.2, $d\varkappa/dn_0$ will tend to zero. The expression for γ_ρ and $\gamma_\varkappa$ in Eq. (4.83a) should then be used. We approximate the cells by homogeneous scatterers whose density is ρ_c. The compressibility is taken to be the extrapolation of the curve in Figure 4.6 to $n_0 = 1.0$. When $n_0 < 0.2$ we obtain

$$\gamma_\rho = \frac{\rho_1}{\rho} V = .064\ V \qquad \gamma_\varkappa = \frac{\varkappa_1}{\varkappa_0} V = -0.155\ V \tag{4.96}$$

V is the volume of the cell. Thus, the monopole scattering will dominate when n_0 tends to zero also, although $d\varkappa/dn_0$ tends to zero.

A polar diagram for the scattered intensity is given in Figure 4.7. The values of γ_ρ and $\gamma_\varkappa$ from Eq. (4.94) and Eq. (4.95) is used.

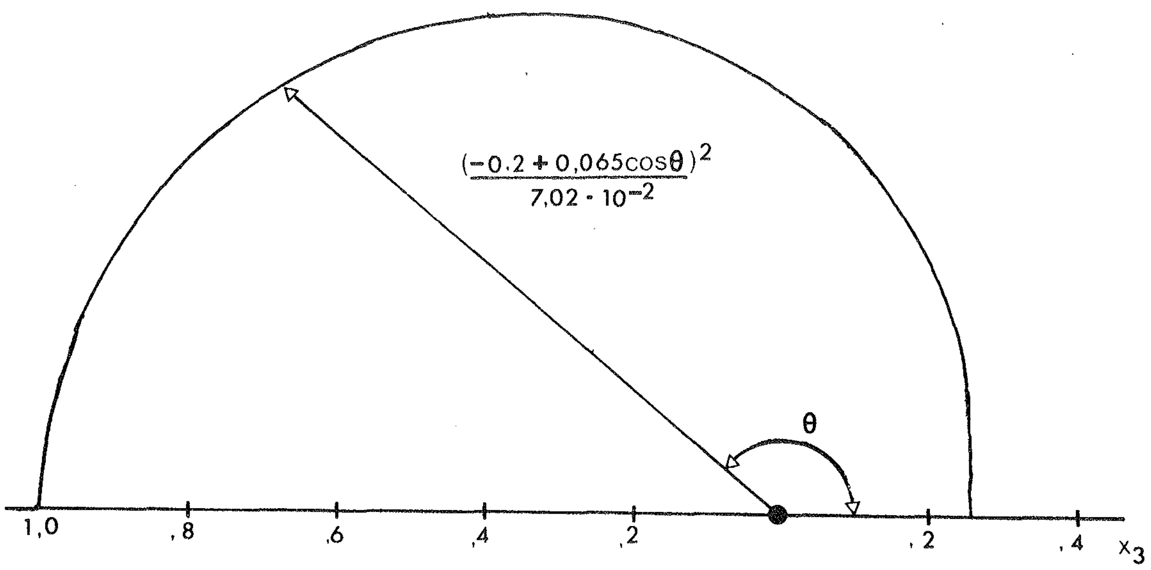

Figure 4.7. Polar diagram for the differential scattering crossection of a plane wave from blood. HCT ~ 40-50 %.

The variation with n_0 of the ratio between the monopole term and the dipole term is given in Figure 4.8. The ratio is almost constant.

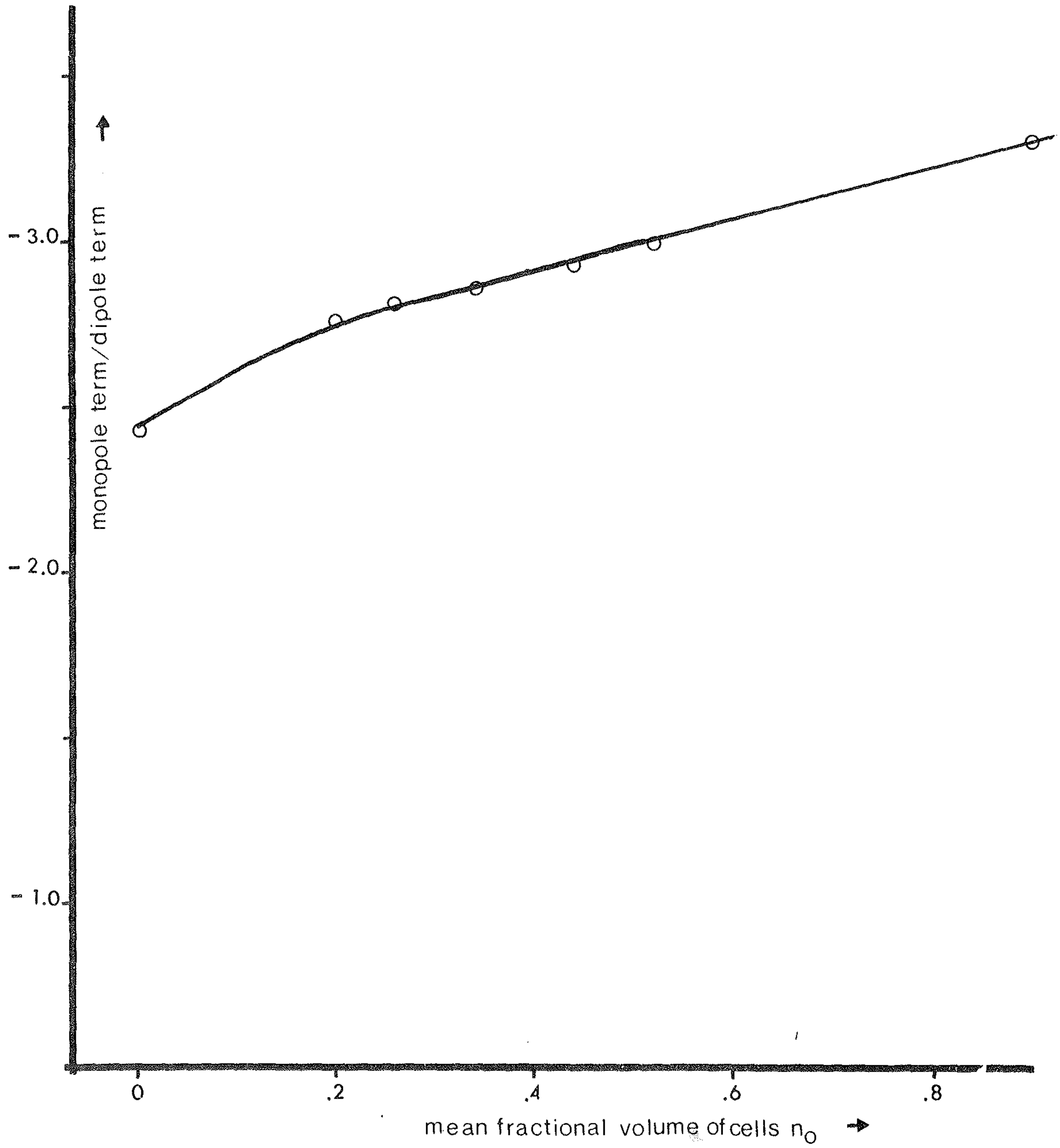

Figure 4.8. Variation of the ratio between the monopole and dipole terms in the scattered intensity.

C. The output of the receiving transducer from ultrasound scattered by blood.

The blood vessel will normally be in the near-field or near far-field region of the transmitting and receiving transducer. When we excite the transmitting transducer by a time harmonic voltage with angular frequency ω_0, the complex pressure amplitude of the transmitted wave may be written

$$\hat{p}_T(\omega_0,\vec{r}) = A_T(\omega_0,\vec{r})e^{-i\varphi_T(\omega_0,\vec{r})} \tag{4.97}$$

When the transducer is much larger than the wavelength, we may approximate φ_T in the near-field by

$$\begin{aligned} \varphi_T(\omega_0,\vec{r}) &= \vec{k}_T\cdot\vec{r} + c_T \\ \vec{k}_T &= \frac{\omega_0}{c}\vec{n}_T = \frac{2\pi}{\lambda}\vec{n}_T \end{aligned} \tag{4.98}$$

where $\vec{n}_T$ is the unit normal vector to the transducer face. In the far-field we always have

$$\begin{aligned} \varphi_T(\omega_0,\vec{r}) &= k_T\cdot r + \text{const} \\ k_T &= \frac{\omega_0}{c} = \frac{2\pi}{\lambda} \end{aligned} \tag{4.99}$$

The origin of the coordinate system is located in the centre of the transducer plane.

The scattered field may be represented by the following source density, see Eq. (4.82).

$$-k_0^2\gamma_\varkappa\hat{p}_T(\vec{r})n(\vec{r},t) + \gamma_\rho\nabla(n(\vec{r},t)\nabla\hat{p}_T(\vec{r})) \tag{4.100}$$

where we have omitted ω in p_T. As discussed above this density is composed of a monopole term and dipole term, the monopole term being the largest by a factor 3.

For the receiving transducer the following reciprocity theorem holds:

Let the transducer be excited with a voltage of angular frequency ω_0. *This gives rise to an emitted pressure wave with complex amplitude*

$$\hat{p}_R(\omega_0,\vec{r}) = A_R(\omega_0,\vec{r})e^{-i\varphi_R(\omega_0,\vec{r})} \tag{4.101}$$

where A_R *is the real amplitude and* φ_R *the phase. If a monopole source density with angular frequency* ω_0 *and magnitude* $m(\vec{r},t)$ *excites waves in a region* R, *the output from the receiving transducer is given by*

$$e_m(t) = -\alpha e^{i\omega_0 t} \int_R d^3\xi\, m(\vec{\xi},t)\,\hat{p}_R(\vec{\xi}) \tag{4.102}$$

where α *is a complex constant of proportionality. The time variation of* m *is supposed to be slow compared to the time delay of the wave motion between the source and the transducer.*

From this expression we may also calculate the output from a dipole source distribution. This can be done by representing the dipole distribution by two identical monopole distributions with opposite sign q and $-q$ and displaced a small distance $\vec{\ell}$ relative to eachother. The dipole density is then

$$\vec{d}(\vec{r},t) = \lim_{\vec{\ell}\to\vec{0},\, q\to\infty} \vec{\ell}\; q(\vec{r},t)$$

The transducer output from the dipole distribution is then

$$e_d(t) = \alpha e^{i\omega_0 t} \int_R d^3\xi\, \vec{d}(\vec{\xi},t)\,\nabla\hat{p}_R(\vec{\xi}) \tag{4.103}$$

Here again the time variation in $\vec{d}$ is slow. The proofs of these two statements for the uniform piston approximation of the transducer are found in Appendix III.

When Eqs. (4.102) and (4.103) are combined with Eq. (4.100) the output of the receiving transducer due to the ultrasound scattered by blood is given by

$$e(t) = \alpha e^{i\omega_0 t} \int_R d^3\xi \{k_0^{\,2}\gamma_\kappa \hat{p}_T(\vec{\xi})\,\hat{p}_R(\vec{\xi}) + \gamma_\rho \nabla\hat{p}_T(\vec{\xi})\,\nabla\hat{p}_R(\vec{\xi})\} n(\vec{\xi},t) \tag{4.104}$$

When a pulsed wave meter is used, a distribution of frequencies is transmitted. As shown in the previous section, the scattered intensity is proportional to the fourth power of the frequency. However, the relative width of the frequency band is so small (200 kHz/2 MHz) that the scattering may be considered to be frequency independent across this band. The effect of pulsing may, therefore, be incorporated by multiplying the transmitting transducer field pattern p_T by a window function $S(\vec{\xi})$. This is given by the intersection between the vessel and the range cell (see Section 2.2). By this the region of integration may be extended to the whole space. When a continuous wave meter is used, $S(\vec{\xi})$ should be the characteristic function of the vessel.

Using Eqs. (4.97) and (4.101) we may write this expression in a shorter form which we shall use later

$$\boxed{e(t) = e^{i\omega_0 t}|\alpha|\int_R d^3\xi R(\vec{\xi})e^{i\psi(\vec{\xi})}n(\vec{\xi},t)} \tag{4.105}$$

where we have defined

$$\begin{aligned}
R(\vec{\xi}) &= |A(\vec{\xi})| \\
\psi(\vec{\xi}) &= -\varphi_T(\vec{\xi}) - \varphi_R(\vec{\xi}) + \angle A(\vec{\xi}) + \angle|\alpha| \qquad (4.106) \\
A(\vec{\xi}) &= \{k_0^2\gamma_\varkappa A_T(\vec{\xi})A_R(\vec{\xi}) + \gamma_\rho[\nabla A_T(\vec{\xi})\nabla A_R(\vec{\xi}) - A_T(\vec{\xi})A_R(\vec{\xi})\nabla\varphi_T(\vec{\xi})\nabla\varphi_R(\vec{\xi}) \\
&\quad - iA_T(\vec{\xi})\nabla\varphi_T(\vec{\xi})\nabla A_R(\vec{\xi}) - i\nabla A_T(\vec{\xi})A_R(\vec{\xi})\nabla\varphi_R(\vec{\xi})]\}
\end{aligned}$$

$A_T(\vec{\xi})$ is now multiplied by $S(\vec{\xi})$.

$R(\vec{\xi})$ may be normalized in an appropriate way by taking a constant into α. When the transducers are large compared to the wave length, the plane wave approximation in the near-field may be acceptable, Eq. (4.98). In this case A_T and A_R will be slowly varying functions inside the observation region and their gradients can be neglected compared to those of the phases φ_T and φ_R. Inside the observation region we, therefore, have (Note: $\vec{k}_T = -\vec{k}_s$, Eq. (4.86))

$$R(\vec{\xi}) = A_T(\vec{\xi})A_R(\vec{\xi})k_0^2\{\gamma_\varkappa - \gamma_\rho\frac{\vec{k}_T\vec{k}_R}{k_0^2}\} \tag{4.107}$$

In this case we normalize R so that it is approximately unity inside the observation region. At the boundaries of the observation region the contribution from ∇A_T and ∇A_R cannot be neglected. The contribution to the integral from this part may, however, be neglected compared to the rest. This gives for large transducers:

$$e(t) = e^{i\omega_0 t}\alpha e^{-i[c_T+c_R]}\int d^3\xi R(\vec{\xi})n(\vec{\xi},t)e^{-i(\vec{k}_T+\vec{k}_R)\vec{\xi}} \tag{4.108}$$

where $R(\vec{\xi})$ is given by Eq. (4.107).

4.4. Summary.

The scattering of ultrasound from blood has been studied. The scattered wave is considered to result from fluctuations of the parameters about mean values in a continuum model of the blood. In this model the interaction between the blood cells is taken into account. Its effect is contained in the variance of the concentration fluctuations of cells $\langle n^2 \rangle$. A stochastic model of the concentration fluctuations of the blood cells has been given. This model enables us to calculate the mean scattered intensity.

The experimental findings of Reid & al [44] have been discussed in relation to our theory and measurements of the wave velocity in blood as a function of the mean cell concentration. We argue against three of their conclusions.

i) The cells can be considered independent up to a concentration of 10 % in contrast to their value of 40 %.

ii) The scattered intensity will be proportional to the cell concentration only at concentrations less than 10 %. When the cell concentration is above this value, the intensity will decrease from the proportional dependency of the concentration.

iii) The scattered intensity is anisotropic in contrast to their result. The degree of anisotropy is, however, not very high, Figure 4.7, so that inaccuracies in the measurements may lead to a conclusion of isotropy.

The scattered intensity is calculated to be proportional to the frequency in the fourth power which is in agreement with the experimental findings of Reid & al.

The output signal from the receiving transducer in blood flow measurements are calculated. In contrast to the results of Brody [45] the scattering anisotropy of blood and the interaction between the cells is taken into account. We are also able to handle nonstationary velocity fields.

5. ESTIMATION OF VELOCITY OF BLOOD FROM THE RECEIVED DOPPLER-SIGNAL

The analytic form of the received signal is given in Eq. (4.105). In this chapter we discuss methods of estimating the velocity of blood from this signal. We first show the relation between the received signal and the velocity field in the observation region, using the scattering theory developed in the previous chapter. Then the performance of mean velocity estimators is discussed, together with practical realizations of the estimators.

The use of power spectrum estimation is briefly discussed while practical methods for estimating power spectra are only given by references.

5.1. The relation between velocity field and received signal.

A. Synchronous demodulation. Quadrature components of the received signal.

Let

$$e(t) = \mathrm{Re}\{\hat{e}(t)e^{i\omega_0 t}\} \tag{5.1}$$

be the received signal. ω_0 is the angular frequency of the transmitted signal. $\hat{e}(t)$ is a complex lowpass signal. In our case $\omega_0 = 2\pi\cdot 2\cdot 10^6 s^{-1}$ and the maximum angular frequency component of $\hat{e}$ will be of the order of $2\pi\cdot 10^4 s^{-1}$. The quadrature components of $e(t)$ are defined by

$$\begin{aligned} e_1(t) &= \mathrm{Re}\ \hat{e}(t) \\ e_2(t) &= \mathrm{Im}\ \hat{e}(t) \end{aligned} \tag{5.2}$$

These signals may be obtained from $e(t)$ by multiplying with $\sin\omega_0 t$ and $\cos\omega_0 t$. The multiplication is followed by a lowpass filter which removes the high frequency components introduced in the multiplication. This is illustrated in Figure 5.1.

Assume that $\hat{e}(t)$ is Fourier transformable with the transform $\hat{E}(\omega)$ i.e.

$$\hat{e}(t) = e_1(t) + ie_2(t) \leftrightarrow \hat{E}(\omega) \tag{5.3}$$

For the complex conjugate of $\hat{e}$ we may easily verify that

$$\hat{e}^*(t) = e_1(t) - ie_2(t) \leftrightarrow \hat{E}^*(-\omega)$$

Hence

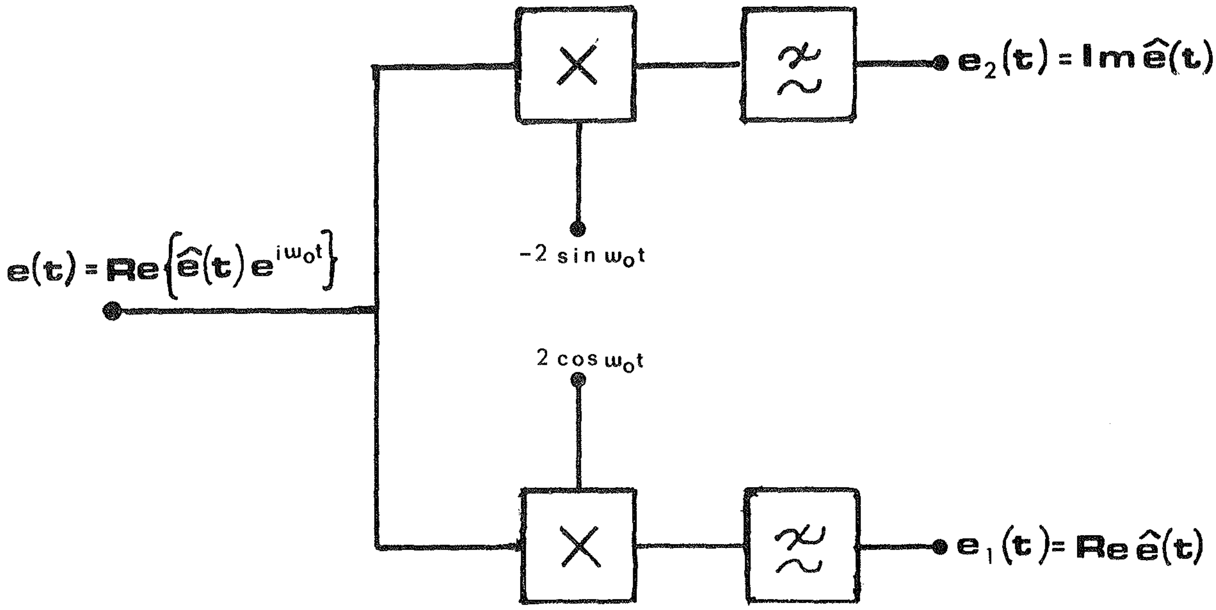

Figure 5.1. Quadrature demodulation.

$$e_1(t) \leftrightarrow \frac{1}{2}\{\hat{E}(\omega) + \hat{E}^*(-\omega)\}$$
$$e_2(t) \leftrightarrow \frac{1}{2i}\{\hat{E}(\omega) - \hat{E}^*(-\omega)\} \tag{5.4}$$

From Eq. (4.105) we have

$$\hat{e}(t) = |\alpha| \int d^3\xi R(\vec{\xi}) n(\vec{\xi},t) e^{i\psi(\vec{\xi})}$$
$$e_1(t) = |\alpha| \int d^3\xi R(\vec{\xi}) n(\vec{\xi},t) \cos \psi(\vec{\xi}) \tag{5.5}$$
$$e_2(t) = |\alpha| \int d^3\xi R(\vec{\xi}) n(\vec{\xi},t) \sin \psi(\vec{\xi})$$

B. Fourier-transform and power spectrum of the received signal.

$\hat{e}(t)$ may in general not have a Fourier-transform. We therefore study

$$\hat{e}_T(t) = \hat{e}(t) \cdot \chi_T(t) \tag{5.6}$$

$$\chi_T(t) = \begin{cases} 1 & t \in [-T,T] \\ 0 & t \notin [-T,T] \end{cases}$$

χ_T is the characteristic function of the set $[-T,T]$. In all practical cases $\hat{e}_T$ will have a Fourier-transform since $\hat{e}$ will have finite energy over a finite interval of time. $\hat{e}_T$ therefore belongs to $L_2[-T,T]$. The Fourier-transform of $\hat{e}_T(t)$, $\hat{E}_T(\omega)$ will be

$$\hat{E}_T(\omega) = |\alpha| \int d^3\xi R(\vec{\xi}) N_T(\vec{\xi},\omega) e^{i\psi(\vec{\xi})} \tag{5.7}$$

$N_T(\vec{\xi},\omega)$ is the time Fourier-transform of $n_T(\vec{\xi},t) = n(\vec{\xi},t)\chi_T$. $N_T(\vec{\xi},\omega)$ may be obtained from Eq. (4.27) with a special sample function $\vec{j}(\vec{r},t)$. When the transducers are not large compared to the wave length ψ will have a complicated variation of $\vec{\xi}$. The mathematical relation between the velocity field and the received signal will therefore be complicated.

We shall in this section study the case of large transcucers only so that the approximation of Eq. (4.98) holds, which gives

$$\hat{E}_T(\omega) = \alpha e^{-i(c_T+c_R)} \int d^3\xi R(\vec{\xi}) N_T(\vec{\xi},\omega) e^{-i(\vec{k}_T+\vec{k}_R)\vec{\xi}} \tag{5.8}$$

In this case R will be slowly varying inside the observation region. Taking the normation into α, R may be approximated by the characteristic function of the observation region.

Eq. (5.8) shows that in this approximation the received signal is the space Fourier transform of $R(\vec{\xi})n_T(\vec{\xi},t)$ with wave vector $-(\vec{k}_T + \vec{k}_R)$. This is the Bragg-condition of reflection discussed in Section 4.3B. The Fourier transform of the product of two functions in $\vec{r}$-space is equal to the convolution of the Fourier transforms of the individual factors in Fourier space. Thus we may express $\hat{E}_T(\omega)$ by

$$\hat{E}_T(\omega) = \alpha e^{-i(c_T+c_R)} \hat{R}(\vec{q}) * N_T(-(\vec{k}_T+\vec{k}_R) - \vec{q},\omega) \tag{5.9}$$

where $\hat{R}(\vec{q})$ is the Fourier transform of $R(\vec{\xi})$ and the convolution product in Fourier space is defined by

$$X(\vec{q}) * Y(\vec{k} - \vec{q}) = \frac{1}{(2\pi)^n} \int d^n q X(\vec{q}) Y(\vec{k} - \vec{q}) \tag{5.10}$$

n is the dimension of the space .

When a stochastic process, $x(t)$, is wide sense stationary, i.e. the mean and covariance are independent of time, we can define the power spectrum $G_{xx}(\omega)$ by [61]

$$G_{xx}(\omega) = \lim_{T\to\infty} \frac{1}{2T} <|X_T(\omega)|^2> \tag{5.11a}$$

or equivalently

$$G_{xx}(\omega) \leftrightarrow R_{xx}(\tau) \tag{5.11b}$$

where $R_{xx}(\tau)$ is the autocorrelation function of x.

$\hat{e}(t)$ is obtained from $n(\vec{\xi},t)$ by a linear operator Eq. (5.5). A necessary and sufficient condition for n to be wide sense stationary is that the velocity field is independent of time. Through the relation, Eq. (5.5), this will also be a necessary and sufficient condition for $\hat{e}(t)$ and thereby $e_1(t)$ and $e_2(t)$ to be wide sense stationary.

The problem of stationarity for $e(t)$, Eq. (5.1), is more complicated. It can be shown that the following relations are a necessary and sufficient condition for $e(t)$ to be wide sense stationary [61].

$$R_{e_1e_1}(\tau) = R_{e_2e_2}(\tau) \quad \text{a)} \qquad R_{e_1e_2}(\tau) = -R_{e_2e_1}(\tau) \quad \text{b)} \tag{5.12}$$

As we shall see in Section 5.1D, this holds approximately for steady velocity fields when the observation region is large along $\nabla\psi$ compared to the wave length. For practical band limited transducers this will be true. In this approximation, $e(t)$, will be wide sense stationary when the velocity field is time-steady.

For time-steady velocity fields we then have from Eq. (5.9)

$$G_{\hat{e}\hat{e}}(\omega) = |\alpha|^2 \lim_{T\to\infty} \frac{1}{2T} <|\hat{R}(\vec{q}) * N_T[-(\vec{k}_T+\vec{k}_R) - \vec{q},\omega]|^2> \tag{5.13}$$

When the observation region is small, $R(\vec{q})$ will broaden the received spectrum.

General properties of the correlation functions and power spectra for two real stochastic processes e_1 and e_2 are

$$R_{e_ie_i}(\tau) = R_{e_ie_i}(-\tau) \leftrightarrow G_{e_ie_i}(\omega) = G_{e_ie_i}(-\omega) \Rightarrow G_{e_ie_i} \text{ real valued} \quad i=1,2$$

$$R_{e_1e_2}(\tau) = R_{e_2e_1}(-\tau) \leftrightarrow G^*_{e_1e_2}(\omega) = G_{e_2e_1}(\omega) = G_{e_1e_2}(-\omega) \tag{5.14}$$

$$G_{\hat{e}\hat{e}}(\omega) = G_{e_1e_1}(\omega) + G_{e_2e_2}(\omega) + i\{G_{e_1e_2}(\omega) - G_{e_2e_1}(\omega)\}$$

If in addition e_1 and e_2 are the quadrature components of a wide sense stationary band limited process, Eq. (5.12) holds which implies that [61]

$$
\begin{aligned}
&G_{e_1e_1}(\omega) = G_{e_2e_2}(\omega) \\
&G_{e_1e_2}(\omega) = -G_{e_2e_1}(\omega) \\
&G^*_{e_1e_2}(\omega) = -G_{e_1e_2}(\omega), \Rightarrow G_{e_1e_2} \text{ and } G_{e_2e_1} \text{ are imaginary valued} \\
&G_{\hat{e}\hat{e}}(\omega) = 2\{G_{e_1e_1}(\omega) + iG_{e_1e_2}(\omega)\} \\
&G_{e_1e_1}(\omega) = G_{e_2e_2}(\omega) = \frac{1}{4}\{G_{\hat{e}\hat{e}}(\omega) + G_{\hat{e}\hat{e}}(-\omega)\} \\
&G_{e_1e_2}(\omega) = -G_{e_2e_1}(\omega) = \frac{1}{4i}\{G_{\hat{e}\hat{e}}(\omega) - G_{\hat{e}\hat{e}}(-\omega)\}
\end{aligned}
\tag{5.15}
$$

C. The received power spectrum from a homogeneous velocity field. Effect of diffusion and finite transit time.

In the case of a homogeneous velocity field we may directly calculate $N_T(\vec{q},\omega)$ from Eq. (4.27). We assume that the observation region is large, so that R is constant equal to unity inside the observation region. In this case we use

$$N_T(\vec{q},\omega) = \int_R d^3r \int_{-T}^{T} dt\ n(\vec{r},t)\, e^{i(\vec{q}\vec{r}-\omega t)} \tag{5.16}$$

which gives

$$N_T(\vec{q},\omega) = \frac{-i\vec{q}\ \vec{J}_T(\vec{q},\omega)}{q^2D + i(\omega - \vec{q}\vec{v})} + \text{boundary terms} \tag{5.17}$$

Since R is large, the boundary terms may be neglected. From Eq. (5.13) we calculate the power spectrum of $\hat{e}(t)$.

$$G_{\hat{e}\hat{e}}(\omega) = |\alpha|^2 \frac{6q^2D\langle n^2\rangle V}{(q^2D)^2 + (\omega - \vec{q}\vec{v})^2} \tag{5.18}$$

$$\vec{q} = -(\vec{k}_T + \vec{k}_R)$$

V is the volume of R. We have used the δ-correlation property of $\vec{j}$ and the relation between $<j^2>$ and $<n^2>$ from Eq. (4.32b) to calculate $<|\vec{J}(\vec{q},\omega)|^2>$.

The power spectrum of $\hat{e}$ is a Lorentzian line centered around the doppler-shift frequency

$$\omega_d = -(\vec{k}_T + \vec{k}_R)\vec{v} = -\frac{\omega_0}{c}(\vec{n}_T + \vec{n}_R)\vec{v} \tag{5.19}$$

$\vec{n}_T$ and $\vec{n}_R$ are the unit normal vectors of the transmitting and receiving transducer surfaces. The linewidth is determined by the diffusion constant. Physically this is intimately connected to the lifetime of the Fourier component of the fluctuation which interacts with the wave (see previous section). Following the flow we have from Eq. (4.55)

$$\frac{\partial E\{N(\vec{q},t)\,|\,n(\vec{r},0)\}}{\partial t} + q^2 D E\{N(\vec{q},t)\,|\,n(\vec{r},0)\} = 0 \tag{5.20}$$

$$\vec{q} = -(\vec{k}_T + \vec{k}_R)$$

The solution of this equations is

$$E\{N(\vec{q},t)\,|\,n(\vec{r},0)\} = N_0(\vec{q})\,e^{-Dq^2 t} \tag{5.21}$$

From this equation we could define a lifetime of the Fourier component $N_0(\vec{q})$

$$\tau_q = \frac{1}{Dq^2} \tag{5.22}$$

Eq. (5.18) gives the half power linewidth of the spectrum

$$\Delta\omega = 2q^2 D \tag{5.23}$$

This is twice the inverse lifetime of the interacting Fourier component.

Let the transmitting and receiving transducers be the same, i.e. $\vec{k}_T = \vec{k}_R = \omega_0/c\cdot\vec{n}$. The relative linewidth will be

$$\frac{\Delta\omega}{|\omega_d|} = 4\,\frac{\omega_0}{c}\,\frac{D}{|v_n|} \tag{5.24}$$

where v_n is the component of the velocity along $\vec{n}$. For $f_0 = 2$ MHz and the value of D given by Eq. (4.39) we get

$$\frac{\Delta\omega}{\omega_d} \approx \frac{10^{-9}\,[m/s]}{|v_n|\,[m/s]} \tag{5.25}$$

Practical values of v_n will be above 10^{-1} m/s and therefore the relative linewidth will be very small. This is another argument that the effect of diffusion may be neglected in calculating the correlation functions in Section 4.2.

When the observation region is small, additional broadening will occur due to the convolution with R in Eq. (5.13). Let the length of the observation region in the direction of $\vec{v}$ be L. Let also the coordinate system be oriented with the x_1 axis along $\vec{v}$. $R(\vec{q})$ may be approximated by

$$\hat{R}(\vec{q}) = \frac{\sin q_1/2\ L}{q_1/2} f(q_2,q_3) \tag{5.26}$$

Thus the "inaccuracy" of $(\vec{k}_T + \vec{k}_R)$ along $\vec{v}$ due to the convolution between R and N_T will be

$$\Delta(\vec{k}_T + \vec{k}_R)_1 = \frac{2\pi}{L} \tag{5.27}$$

This gives a broadening of the received spectrum of

$$\Delta\omega = 2\pi \cdot \frac{v}{L} \tag{5.28}$$

The relative broadening of the received line will be

$$\frac{\Delta\omega}{\omega_d} = \frac{\lambda}{2L} \tag{5.29}$$

This may also be considered to stem from the finite transit time of the scatterers through the observation region. Each scatterer will give a burst of oscillations at the doppler frequency with duration L/v. Due to the finite duration of these oscillations, there will be relative broadening in frequency of the received signal from one scatterer given by

$$\frac{\Delta\omega}{\omega_d} = \frac{2\pi \cdot v/L}{2\omega_0 \cdot v/c} = \frac{\lambda}{2L}$$

We thus see that when L is much larger than half the wavelength, we may consider $\hat{R}(\vec{q})$ to be a δ-function in Eq. (5.9) and Eq. (5.13).

The length of the observation region is approximately 5 mm and the wavelength is 0.75 mm. From Eq. (5.19) we calculate the broadening of the line due to the finite transit time

$$\frac{\Delta\omega}{\omega_d} = 7.5 \cdot 10^{-2} \tag{5.30}$$

which is a fairly good sharpness of the line. We may also remark here that the broadening is symmetric, which gives (Estimator type III, Section 5.2)

$$\omega_d = \frac{\int_{-\infty}^{\infty} d\omega \cdot \omega G_{\hat{e}\hat{e}}(\omega)}{\int_{-\infty}^{\infty} d\omega \cdot G_{\hat{e}\hat{e}}(\omega)} \tag{5.31}$$

D. Correlation functions and power spectrum of the doppler-signal in the case of zero diffusion.

From the last section it follows that the diffusion gives a negligible broadening of the received spectrum. To simplify the mathematical expressions we therefore neglect the diffusion in the following calculations.

The autocorrelation function of the complex doppler signal may be obtained from Eq. (5.5)

$$\begin{aligned} R_{\hat{e}\hat{e}}(\tau_1,\tau_2) &= \langle \hat{e}^*(\tau_1)\hat{e}(\tau_2)\rangle \\ &= |\alpha|^2 \int d^3\xi_1 d^3\xi_2 R(\vec{\xi}_1) R(\vec{\xi}_2) e^{i[\psi(\vec{\xi}_2)-\psi(\vec{\xi}_1)]} \langle n(\vec{\xi}_1,\tau_1) n(\vec{\xi}_2,\tau_2)\rangle \end{aligned}$$

Using the δ-correlation property of n given by Eq. (4.47), we may perform the integration over ξ_2.

$$\boxed{R_{\hat{e}\hat{e}}(\tau_1,\tau_2) = |\alpha|^2 \int d^3\xi R(\vec{\xi}) R(\vec{\zeta}) \langle n^2(\vec{\xi},\tau_1)\rangle e^{i[\psi(\vec{\zeta})-\psi(\vec{\xi})]}} \tag{5.32}$$

where $\vec{\zeta}$ is given by

$$\vec{\zeta} = \vec{\xi} + \int_{\tau_1}^{\tau_2} dp\ \vec{v}[\vec{\xi}(p),p]dp \tag{5.33}$$

$\vec{\xi}(p)$ is the path of the fluid element which at time τ_1 has the position $\vec{\xi}$, i.e. $\vec{\zeta} = \vec{\xi}(\tau_2)$.

Similarly we obtain for the correlation functions of the quadrature components of the doppler signal

$$
\begin{aligned}
R_{e_1e_1}(\tau_1,\tau_2) &= |\alpha|^2\int d^3\xi R(\vec{\xi})R(\vec{\zeta})<n^2(\vec{\xi},\tau_1)>\cos\,\psi(\vec{\xi})\cos\,\psi(\vec{\zeta}) \\
R_{e_2e_2}(\tau_1,\tau_2) &= |\alpha|^2\int d^3\xi R(\vec{\xi})R(\vec{\zeta})<n^2(\vec{\xi},\tau_1)>\sin\,\psi(\vec{\xi})\sin\,\psi(\vec{\zeta}) \\
R_{e_1e_2}(\tau_1,\tau_2) &= |\alpha|^2\int d^3\xi R(\vec{\xi})R(\vec{\zeta})<n^2(\vec{\xi},\tau_1)>\cos\,\psi(\vec{\xi})\sin\,\psi(\vec{\zeta}) \\
R_{e_2e_1}(\tau_1,\tau_2) &= |\alpha|^2\int d^3\xi R(\vec{\xi})R(\vec{\zeta})<n^2(\vec{\xi},\tau_1)>\sin\,\psi(\vec{\xi})\cos\,\psi(\vec{\zeta})
\end{aligned}
\tag{5.34}
$$

The last expressions may be further simplified by the following relations

$$
\begin{aligned}
\cos x\cos y &= \tfrac{1}{2}[\cos(x-y) + \cos(x+y)] \\
\sin x\sin y &= \tfrac{1}{2}[\cos(x-y) - \cos(x+y)] \\
\sin x\cos y &= \tfrac{1}{2}[\sin(x-y) + \sin(x+y)]
\end{aligned}
$$

We then note that the sum terms give rapidly oscillating functions compared to the rest of the integrand. If the observation region is extending some wavelengths along $\nabla\psi$ (as it is with band limited transducers), these terms will give a negligible contribution to the integral. Neglecting these terms we get

$$
\boxed{
\begin{aligned}
R_{e_1e_1}(\tau_1,\tau_2) &= R_{e_2e_2}(\tau_1,\tau_2) = \frac{1}{2}\,\mathrm{Re}\{R_{\hat{e}\hat{e}}(\tau_1,\tau_2)\} \\
&= \frac{|\alpha|^2}{2}\int d^3\xi R(\vec{\xi})R(\vec{\zeta})<n^2(\vec{\xi},\tau_1)>\cos[\psi(\vec{\zeta}) - \psi(\vec{\xi})] \\
R_{e_1e_2}(\tau_1,\tau_2) &= -R_{e_2e_1}(\tau_1,\tau_2) = \frac{1}{2}\,\mathrm{Im}\{R_{\hat{e}\hat{e}}(\tau_1,\tau_2)\} \\
&= \frac{|\alpha|^2}{2}\int d^3\xi R(\vec{\xi})R(\vec{\zeta})<n^2(\vec{\xi},\tau_1)>\sin[\psi(\vec{\zeta}) - \psi(\vec{\xi})]
\end{aligned}
}
\tag{5.35}
$$

For timesteady velocity fields the expressions above will be functions of $\tau_2 - \tau_1$ only, Eq. (5.33). This implies that the quadrature components are stationary in the wide sense, as discussed in Section 5.1B. If in addition the above approximation is acceptable, Eq. (5.12) is satisfied, which implies that that the rf-signal is stationary in the wide sense, as discussed in the same section.

For large transducers where the plane wave approximation is acceptable, we have

$$\begin{aligned} \psi(\vec{\xi}) &= \vec{q}\,\vec{\xi} + \Theta \\ \vec{q} &= -(\vec{k}_T + \vec{k}_R) = -\frac{\omega_0}{c}(\vec{n}_T + \vec{n}_R) \end{aligned} \tag{5.36}$$

In the above expressions we may then insert

$$\begin{aligned} \nabla\psi &= \vec{q} \\ \psi(\vec{\zeta}) - \psi(\vec{\xi}) &= \vec{q}\int_{\tau_1}^{\tau_2} \vec{v}[\vec{\xi}(p),p]dp \end{aligned} \tag{5.37}$$

For a timesteady, rectilinear velocity field this expression is further reduced to

$$\psi(\vec{\zeta}) - \psi(\vec{\xi}) = \vec{q}\,\vec{v}(\vec{\xi})[\tau_2 - \tau_1] \tag{5.38}$$

In this case the correlation function takes the form

$$\boxed{R_{\hat{e}\hat{e}}(\tau) = |\alpha|^2\int d^3\xi R[\vec{\xi}]R[\vec{\xi} + \vec{v}(\vec{\xi})\tau]\langle n^2(\vec{\xi})\rangle e^{i\vec{q}\vec{v}(\vec{\xi})\tau}} \tag{5.39}$$

In the approximation of Eq. (5.35) $R_{e_1e_1}$ and $R_{e_2e_2}$ is obtained as one half of the real and imaginary part of the above expression, respectively.

For further analysis we restrict ourselves to consider timesteady, rectilinear flow only. The system of reference is oriented so that the ξ_3 axis is along $\vec{v}$. The position vector in the ξ_1-ξ_2 plane we call $\vec{\sigma}$. As discussed at the end of Section 4.2B, $\langle n^2\rangle$ should be constant along a stream line and will therefore not depend on ξ_3. The correlation function of $\hat{e}$ may then be written

$$\boxed{\begin{aligned} R_{\hat{e}\hat{e}}(\tau) &= |\alpha|^2\int d^2\sigma f[\vec{\sigma},v(\vec{\sigma})\tau]\langle n^2(\vec{\sigma})\rangle e^{i\vec{q}\vec{v}(\vec{\sigma})\tau} \\ f[\vec{\sigma},v(\vec{\sigma})\tau] &= \int d\xi_3 R[\vec{\xi}]R[\vec{\xi} + \vec{v}(\vec{\sigma})\tau] \end{aligned}} \tag{5.40}$$

The power spectrum of the process may now be obtained by taking the Fourier transform of the correlation function

$$\boxed{G_{\hat{e}\hat{e}}(\omega) = |\alpha|^2 \int d^2\sigma \langle n^2(\vec{\sigma})\rangle \frac{F[\vec{\sigma}, \frac{\omega - \vec{q}\,\vec{v}(\vec{\sigma})}{v(\vec{\sigma})}]}{v(\vec{\sigma})}} \tag{5.41}$$

where we have defined

$$F(\vec{\sigma},\omega) = \int_{-\infty}^{\infty} d\tau\; f[\vec{\sigma},\tau] e^{-i\omega\tau} \tag{5.42}$$

The power spectra of e_1 and e_2 are obtained from Eq. (5.41) by the use of Eq. (5.15).

The physical interpretation of the above expressions is that a fluctuation travelling along a stream-line through $\vec{\sigma}$ gives a burst of oscillations in the doppler signal as it passes through the observation region. The power spectrum of the burst is a frequency line given by F and centered around $\omega = \vec{q}\,\vec{v}(\vec{\sigma})$. The average power is proportional to $\langle n^2(\vec{\sigma})\rangle$.

The width of the frequency line is determined by the inverse transit time. To be more explicit we shall further specialize to a weighting function that is constant, equal to unity inside the observation region (Figure 5.2)

$$R(\vec{\xi}) = H[\vec{q}\,\vec{\xi} - k] - H[\vec{q}\{\vec{\xi} - \vec{L}(\vec{\sigma})\} - k] \tag{5.43}$$

$H(x)$ is the Heavyside unit step function. We now obtain

$$f(\vec{\sigma},\tau) = \begin{cases} L(\vec{\sigma}) - |\tau| & |\tau| < L(\vec{\sigma}) \\ 0 & \text{else} \end{cases} \tag{5.44}$$

$$\frac{1}{v(\vec{\sigma})} F[\vec{\sigma}, \frac{\omega - \vec{q}\,\vec{v}(\vec{\sigma})}{v(\vec{\sigma})}] = 2L(\vec{\sigma}) \frac{T_t(\vec{\sigma})}{2} \left\{ \frac{\sin[(\omega - \vec{q}\,\vec{v}(\vec{\sigma}))\frac{T_t(\vec{\sigma})}{2}]}{(\omega - \vec{q}\,\vec{v}(\vec{\sigma}))\frac{T_t(\vec{\sigma})}{2}} \right\} \tag{5.44}$$

where

$$T_t(\vec{\sigma}) = \frac{L(\vec{\sigma})}{v(\vec{\sigma})}$$

is the transit time through the observation region of the fluid element which passes through $\vec{\sigma}$. When T_t is sufficiently large, we may use the following approximation

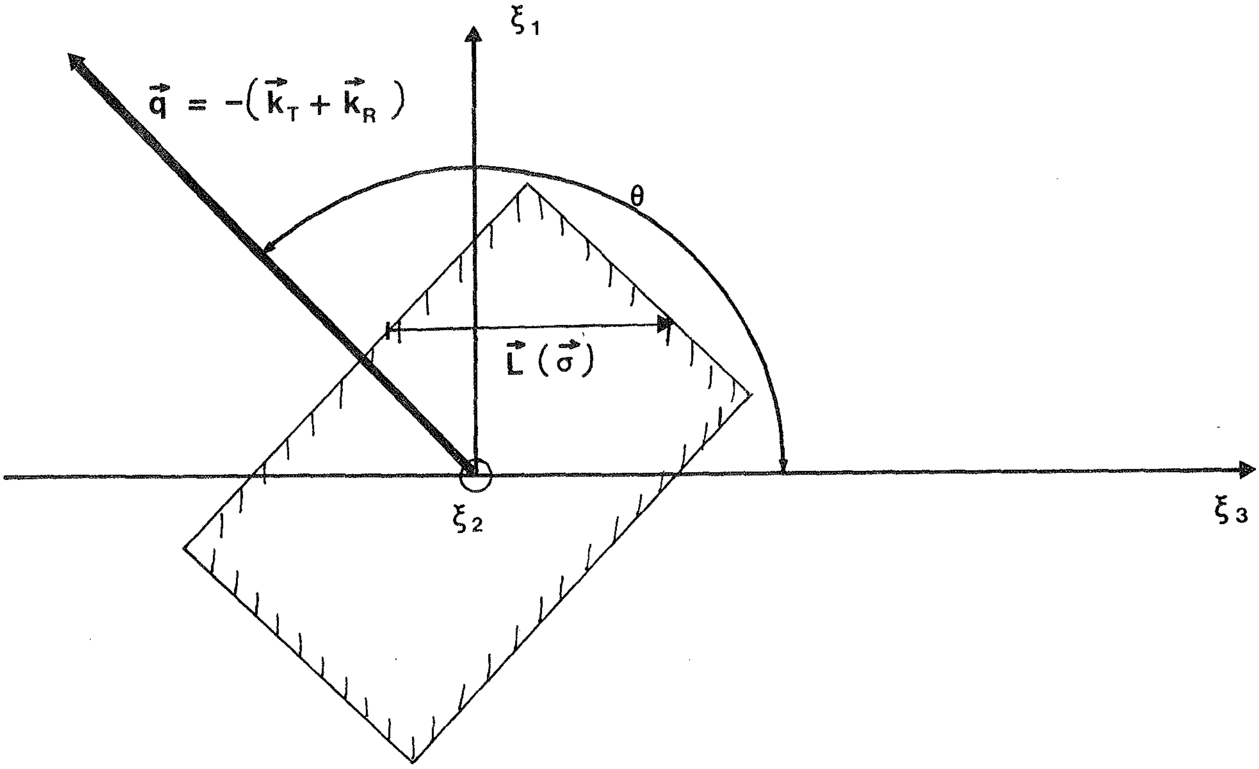

Figure 5.2. Illustration of the observation region weighting function given in Eq. (5.43).

$$\frac{1}{v(\vec{\sigma})} F[\vec{\sigma}, \frac{\omega - \vec{q}\vec{v}(\vec{\sigma})}{v(\vec{\sigma})}] \approx 2\pi L(\vec{\sigma})\delta[\omega - \vec{q}\vec{v}(\vec{\sigma})] \tag{5.45}$$

This approximation is useful for other forms of $R(\vec{\xi})$ which appears in practice, provided the transit time is sufficiently large. For the general form of R we define the equivalent sensitivity length by

$$L(\vec{\sigma}) = \int d\xi_3 R^2(\vec{\xi}) \tag{5.46}$$

Equivalent to the above approximation is also to put

$$R[\vec{\xi}]\, R[\vec{\xi} + \vec{v}(\vec{\xi})\tau] \approx R^2(\vec{\xi})$$

For large transit times the following approximation of the power spectrum may therefore be used

$$\boxed{G_{\hat{e}\hat{e}}(\omega) = 2\pi|\alpha|^2 \int d^2\sigma \langle n^2(\vec{\sigma})\rangle L(\vec{\sigma})\delta[\omega - \vec{q}\vec{v}(\vec{\sigma})]} \tag{5.47}$$

In Appendix IV it is shown that this expression may be further simplified to

$$\boxed{G_{\hat{e}\hat{e}}(\omega) = 2\pi|\alpha|^2 \int_{\Gamma(\omega)} dp \frac{L(\vec{\sigma})\langle n^2(\vec{\sigma})\rangle}{|\nabla \vec{q}\vec{v}(\vec{\sigma})|}} \tag{5.48}$$

$\Gamma(\omega)$ is the family curves in the $\vec{\sigma}$-plane satisfying the relation

$$\omega = \vec{q}\vec{v}(\vec{\sigma}) \tag{5.49}$$

p is the arc length parameter along Γ.

The above equation may be given the following physical interpretation: The scattering density in the σ-plane giving a specified angular frequency ω is given by $L(\vec{\sigma})\langle n^2(\vec{\sigma})\rangle$ where $\vec{\sigma}$ satifies Eq. (5.49). The density in the frequency domain is given by

$$\frac{L(\vec{\sigma})\langle n^2(\vec{\sigma})\rangle}{|\nabla \vec{q}\vec{v}(\vec{\sigma})|} \tag{5.50}$$

because the frequency domain and the σ-plane are related through Eq. (5.49). The scattered intensity at a given angular frequency ω is therefore given by integration over the curves $\Gamma(\omega)$.

Example I. Time steady plug flow in a straight vessel.

In plug flow the velocity is constant across the vessel. The doppler signal is given by Eq. (5.5) with the solution in Eq. (4.46) for n.

$$\hat{e}(t) = |\alpha|\int d^3\xi R(\vec{\xi}) f(\vec{\xi} - \vec{v}t) e^{i(\vec{q}\vec{\xi} + \theta)}$$

$$\hat{e}(t) = \hat{a}(t) e^{i\vec{q}\vec{v}t}$$

where we have defined

$$\hat{a}(t) = |\alpha|\int d^3\xi R(\vec{\xi} + \vec{v}t) f(\vec{\xi}) e^{i(\vec{q}\vec{\xi} + \theta)} \tag{5.51}$$

The signal is thus a stochastically amplitude modulated oscillation at the doppler frequency. The correlation function of the complex envelope is given by

$$R_{\hat{a}\hat{a}}(\tau) = \langle \hat{a}^*(t)\hat{a}(t+\tau)\rangle$$

$$= |\alpha|^2 \int d^3\xi R(\vec{\xi}) R(\vec{\xi} + \vec{v}\tau)\langle n^2(\vec{\xi})\rangle \tag{5.52}$$

By using a system of reference oriented with the ξ_3-axis along $\vec{v}$ as above, we obtain

$$R_{\hat{a}\hat{a}}(\tau) = |\alpha|^2 \int d^2\sigma \langle n^2(\vec{\sigma})\rangle f(\vec{\sigma}, v(\vec{\sigma})\tau) \tag{5.53}$$

where f is given in Eq. (5.40). Assuming the weighting function R given in Eq. (5.43) and the transit length L constant across the vessel, we get

$$R_{\hat{a}\hat{a}}(\tau) = \begin{cases} |\alpha|^2 V\overline{\langle n^2\rangle}\left[1 - \dfrac{|\tau|}{T_t}\right] & |\tau| < T_t \\ 0 & \text{else} \end{cases} \tag{5.54}$$

$$T_t = L/|v|$$

$\overline{\langle n^2\rangle}$ is the mean fluctuation across the vessel defined by

$$\overline{\langle n^2\rangle}\cdot A = \int d^2\sigma \langle n^2(\vec{\sigma})\rangle$$

where A is the area of the vessel cross section. $V = A\cdot L$ is the volume of the observation region and T_t is the transit time. The power spectrum of the envelope is given by

$$G_{\hat{a}\hat{a}}(\omega) = |\alpha|^2 V\overline{\langle n^2\rangle}\, \frac{\sin^2 \frac{\omega T_t}{2}}{\frac{\omega^2 T_t}{2}} \tag{5.55}$$

The envelope is thus lowpass with bandwidth inversely proportional to the transit time. We shall return to this phenomenon in Chapter 6, where we study the variance of mean velocity estimators.

The correlation function of the complex doppler signal will be

$$R_{\hat{e}\hat{e}}(\tau) = R_{\hat{a}\hat{a}}(\tau)e^{i\vec{q}\vec{v}\tau} \tag{5.56}$$

The quadrature components of the doppler signal is given by

$$\begin{aligned} e_1(t) &= a_1(t)\cos(\vec{q}\vec{v}t) - a_2(t)\sin(\vec{q}\vec{v}t) \\ e_2(t) &= a_1(t)\sin(\vec{q}\vec{v}t) + a_2(t)\cos(\vec{q}\vec{v}t) \end{aligned} \tag{5.57}$$

where we have defined

$$a_1(t) = \mathrm{Re}\{a(t)\} = |\alpha| \int d^3\xi R(\vec{\xi} + \vec{v}t) f(\vec{\xi}) \cos(\vec{q}\,\vec{\xi} + \theta)$$
$$a_2(t) = \mathrm{Im}\{a(t)\} = |\alpha| \int d^3\xi R(\vec{\xi} + \vec{v}t) f(\vec{\xi}) \sin(\vec{q}\,\vec{\xi} + \theta) \tag{5.58}$$

The correlation functions for a_1 and a_2 are

$$R_{a_1a_1}(\tau) = \frac{|\alpha|^2}{2} \int d^3\xi R(\vec{\xi}) R(\vec{\xi} + \vec{v}\tau) \langle n^2(\vec{\xi})\rangle [1 + \cos 2(\vec{q}\vec{\xi} + \theta)]$$
$$R_{a_2a_2}(\tau) = \frac{|\alpha|^2}{2} \int d^3\xi R(\vec{\xi}) R(\vec{\xi} + \vec{v}\tau) \langle n^2(\vec{\xi})\rangle [1 - \cos 2(\vec{q}\vec{\xi} + \theta)] \tag{5.59}$$
$$R_{a_1a_2}(\tau) = R_{a_2a_1}(\tau) = \frac{|\alpha|^2}{2} \int d^3\xi R(\vec{\xi}) R(\vec{\xi} + v\tau) \langle n^2(\vec{\xi})\rangle \sin 2(\vec{q}\vec{\xi} + \theta)$$

Cos $2(\vec{q}\,\vec{\xi} + \theta)$ and $\sin 2(\vec{q}\,\vec{\xi} + \theta)$ will be rapidly oscillating functions compared to the rest of the integrand. When the observation region extends several wavelengths along $\vec{q}$, we may then use the following approximation in analogy to that in Eq. (5.35).

$$R_{a_1a_1}(\tau) = R_{a_2a_2}(\tau) = \frac{1}{2} R_{\hat{a}\hat{a}}(\tau)$$
$$R_{a_1a_2}(\tau) = R_{a_2a_1}(\tau) = 0 \tag{5.60}$$

The correlation functions of the quadrature components are

$$R_{e_1e_1}(\tau) = \frac{|\alpha|^2}{2} \int d^3\xi R(\vec{\xi}) R(\vec{\xi} + \vec{v}\tau) \langle n^2(\vec{\xi})\rangle \{\cos \vec{q}\,\vec{v}\tau + \cos(2\vec{q}\,\vec{\xi} + 2\theta + \vec{q}\,\vec{v}\tau)\}$$
$$R_{e_2e_2}(\tau) = \frac{|\alpha|^2}{2} \int d^3\xi R(\vec{\xi}) R(\vec{\xi} + \vec{v}\tau) \langle n^2(\vec{\xi})\rangle \{\cos \vec{q}\,\vec{v}\tau - \cos(2\vec{q}\,\vec{\xi} + 2\theta + \vec{q}\,\vec{v}\tau)\}$$
$$R_{e_1e_2}(\tau) = \frac{|\alpha|^2}{2} \int d^3\xi R(\vec{\xi}) R(\vec{\xi} + \vec{v}\tau) \langle n^2(\vec{\xi})\rangle \{\sin \vec{q}\,\vec{v}\tau + \sin(2\vec{q}\,\vec{\xi} + 2\theta + \vec{q}\,\vec{v}\tau)\}$$
$$R_{e_2e_1}(\tau) = -\frac{|\alpha|^2}{2} \int d^3\xi R(\vec{\xi}) R(\vec{\xi} + \vec{v}\tau) \langle n^2(\vec{\xi})\rangle \{\sin \vec{q}\,\vec{v}\tau - \sin(2\vec{q}\,\vec{\xi} + 2\theta + \vec{q}\,\vec{v}\tau)\} \tag{5.61}$$

Assuming $\vec{q}$ to be along $\vec{v}$ and using the same system of reference as above, we get for R given by Eq. (5.43)

$$R_{e_1e_1}(\tau) = \frac{1}{2}|\alpha|^2 V\overline{<n^2>}\left\{f(\tau/T_t)\cos q v \tau + g(\tau/T_t)\ \frac{\sin q(L - v\tau)\cos(2\theta)}{qL}\right\}$$

$$R_{e_2e_2}(\tau) = \frac{1}{2}|\alpha|^2 V\overline{<n^2>}\left\{f(\tau/T_t)\cos q v \tau - g(\tau/T_t)\ \frac{\sin q(L - v\tau)\cos(2\theta)}{qL}\right\}$$

$$R_{e_1e_2}(\tau) = \frac{1}{2}|\alpha|^2 V\overline{<n^2>}\left\{f(\tau/T_t)\sin q v \tau + g(\tau/T_t)\ \frac{\sin q(L - v\tau)\sin(2\theta)}{qL}\right\}$$

$$R_{e_2e_1}(\tau) = -\frac{1}{2}|\alpha|^2 V\overline{<n^2>}\left\{f(\tau/T_t)\sin q v \tau - g(\tau/T_t)\ \frac{\sin q(L - v\tau)\sin(2\theta)}{qL}\right\} \tag{5.62}$$

where

$$f(\tau) = \begin{cases} 1 - |\tau| & |\tau| < 1 \\ 0 & \text{else} \end{cases}$$

$$g(\tau) = \begin{cases} 1 & |\tau| < 1 \\ 0 & \text{else} \end{cases}$$

$$T_t = \frac{L}{|v|}$$

The last term in the expressions will depend on θ. For the worst case value of θ its maximum value will be $1/qL = \lambda/2\pi L|\vec{n}_T + \vec{n}_R|$ times that of the maximum value of the first. For $L = 0.8\lambda$ and single transducer, we get $1/qL = 1/10$. Normal values using band limited transducers is $L = 5\text{-}20\ \lambda$. The relative contribution of this term is therefore negligible, except when $|\tau|$ is in the neigbourhood of T_t. This region in τ is, however, so small compared to the region where the first term is much larger than the last, that this term may be neglected for all τ. This discussion gives a quantitative justification of the approximation performed in Eq. (5.35) and (5.60), which will be used in the rest of this work.

Example II. Blunt velocity profile in a straight circular vessel.

The time steady blunt profile in a circular tube is defined by [48]

$$v(\sigma) = v_0\left[1 - \frac{\sigma^p}{a^p}\right] \qquad \sigma < a \tag{5.63}$$

$$\bar{v} = v_0\,\frac{p}{p + 2}$$

a is the radius of the tube and σ is the radial distance from the tube axis to the point where the velocity is calculated. $\bar{v}$ is the mean velocity across the vessel.

For $p = 2$ a parabolic profile is obtained and in the limit $p \to \infty$ plug flow results. Profiles for different values of p are shown in Figure 5.3. The mean velocity is the same for all the profiles.

We assume that the sensitivity length, L, defined in Eq. (5.46) and $\langle n^2 \rangle$ is constant across the vessel. Orienting the ξ_3-axis along the tube axis we get from Eq. (5.40)

$$R_{\hat{e}\hat{e}}(\tau) = |\alpha|^2 \langle n^2 \rangle V \cdot 2\int_0^1 dx x f[v_0(1 - x^p)\tau] e^{i\vec{q}\,\vec{v}_0(1-x^p)\tau} \tag{5.64}$$

where $V = \pi a^2 L$ and

$$f(v\tau) = \frac{1}{L}\int d\xi_3 R(\vec{\xi}) R(\vec{\xi} + \vec{v}\tau)$$

If we further specialize to the form of R given in Eq. (5.43) we obtain

$$f(x) = \begin{cases} 1 - \dfrac{|x|}{L} & |x| < L \\ 0 & \text{else} \end{cases} \tag{5.65}$$

Since $G_{\hat{e}\hat{e}}(\omega)$ is real, it follows that $R_{\hat{e}\hat{e}}(-\tau) = R^*_{\hat{e}\hat{e}}(\tau)$. It is therefore sufficient to calculate $R_{\hat{e}\hat{e}}$ for $\tau > 0$. The normalized autocorrelation function takes the form

$$\rho_{\hat{e}\hat{e}}(\tau) = \frac{R_{\hat{e}\hat{e}}(\tau)}{R_{\hat{e}\hat{e}}(0)} = \begin{cases} e^{i\vec{q}\,\vec{v}_0\tau}\, 2\displaystyle\int_0^1 dx\cdot x\left[1 - \frac{v_0\tau}{L}(1-x^p)\right] e^{-i\vec{q}\,\vec{v}_0\tau x^p} & \tau < \dfrac{L}{v_0} \\[2ex] e^{i\vec{q}\,\vec{v}_0\tau}\, 2\displaystyle\int_{(1-\frac{L}{v_0\tau})^p}^1 dx\cdot x\left[1 - \frac{v_0\tau}{L}(1 - x^p)\right] e^{-i\vec{q}\,\vec{v}_0\tau x^p} & \tau > \dfrac{L}{v_0} \end{cases} \tag{5.66}$$

For $p = 1,2$ an analytic expression for the integrals may be obtained. For $p = 4$, $\rho_{\hat{e}\hat{e}}(\tau)$ may be expressed by Fresnel-integrals and for arbitrary p the integrals take the form of incomplete γ-functions with complex arguments.

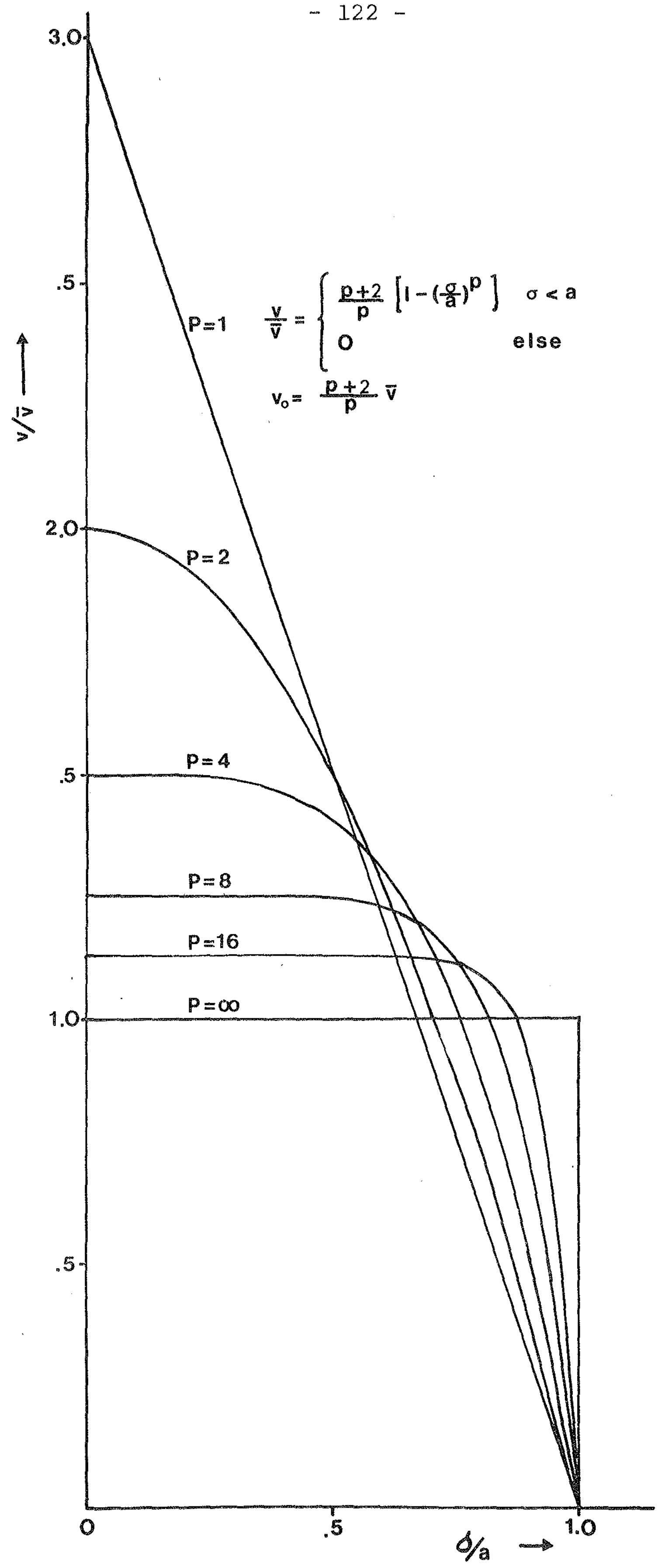

Figure 5.3. Blunt velocity profiles in a circular tube. $\bar{v}$ *is the mean velocity and* a *is the radius of the tube.*

The normalized correlation functions for the quadrature components of the doppler signal are given by

$$\rho_{e_ie_i}(\tau) = \frac{R_{e_ie_i}(\tau)}{R_{e_ie_i}(0)} = \mathrm{Re}\{\rho_{\hat{e}\hat{e}}(\tau)\} \qquad i = 1,2$$

$$\rho_{e_1e_2}(\tau) = -\rho_{e_2e_1}(\tau) = \frac{R_{e_1e_2}(\tau)}{R_{e_1e_1}(0)} = \mathrm{Im}\{\rho_{\hat{e}\hat{e}}(\tau)\}$$

For $0 \leq \tau \leq L/v_0$

$$\rho_{e_1e_1}(\tau) = \rho_{e_2e_2}(\tau) = 2\int_0^1 dx\cdot x[1 - \frac{v_0\tau}{L}(1 - x^p)]\cos[\vec{q}\,\vec{v}_0\tau(1 - x^p)]$$

$$\rho_{e_1e_2}(\tau) = \rho_{e_2e_1}(\tau) = 2\int_0^1 dx\cdot x[1 - \frac{v_0\tau}{L}(1 - x^p)]\sin[\vec{q}\,\vec{v}_0\tau(1 - x^p)] \tag{5.67}$$

For $\tau > L/v_0$ the lower integration bound is interchanged with $(1 - L/v_0\tau)^p$ as in Eq. (5.66). Values for negative τ are obtained from those of positive τ by the even symmetry of $\rho_{e_1e_1}$ and $\rho_{e_2e_2}$ and the odd symmetry of $\rho_{e_1e_2}$ and $\rho_{e_2e_1}$.

Numerical calculations of $\rho_{e_1e_1}(\tau)$ and $\rho_{e_1e_2}(\tau)$ are given in Figure 5.4 and Figure 5.5 for the profiles shown in Figure 5.3.

We observe that the lag enters as $v_0\tau$ which for each p is proportional to $\bar{v}\tau$ or τ/T_d, where $\bar{v}$ is the mean velocity and T_d is the periode of its corresponding doppler frequency.

The length of the observation region is $\vec{q}\,\vec{L}/2\pi = 10$ which from Eq. (5.36) and Figure 5.2 gives

$$L = 10\,\frac{\lambda}{\cos\theta|\vec{n}_T + \vec{n}_R|}$$

The transit time will then be 10 T_d, which implies that the received doppler signal will contain 10 oscillations. For a pulsed wave meter this corresponds to a length of 10 oscillations of the transmitted pulse. For single transducer $\vec{n}_T = \vec{n}_R \Rightarrow |\vec{n}_T + \vec{n}_R| = 2.$ $\theta = 0$ then gives

$$L = 5\lambda \quad (= 3.75 \text{ mm for } f_0 = 2 \text{ MHz})$$

$T_t = L/\bar{v}$ is the average transit time through the observation region.

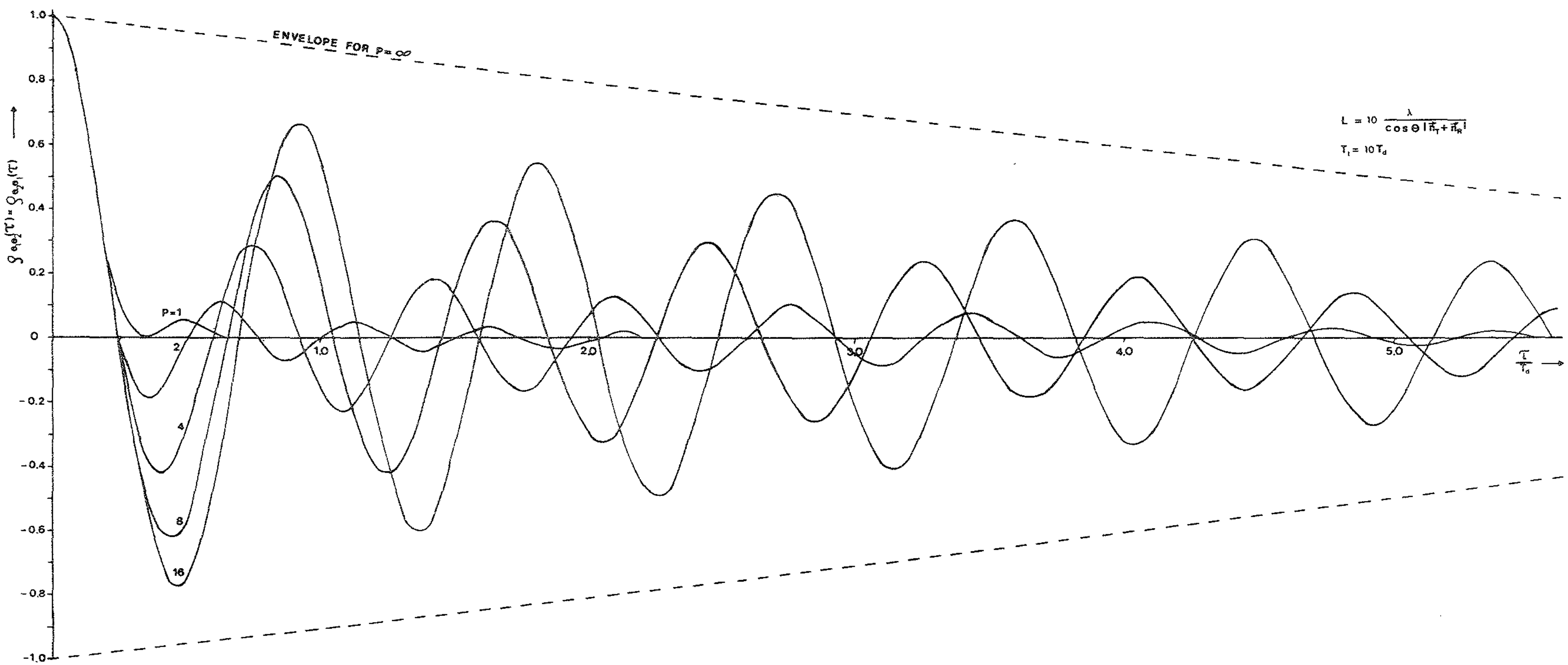

Figure 5.4. Autocorrelation functions of the quadrature components of the doppler signal for the blunt profiles.

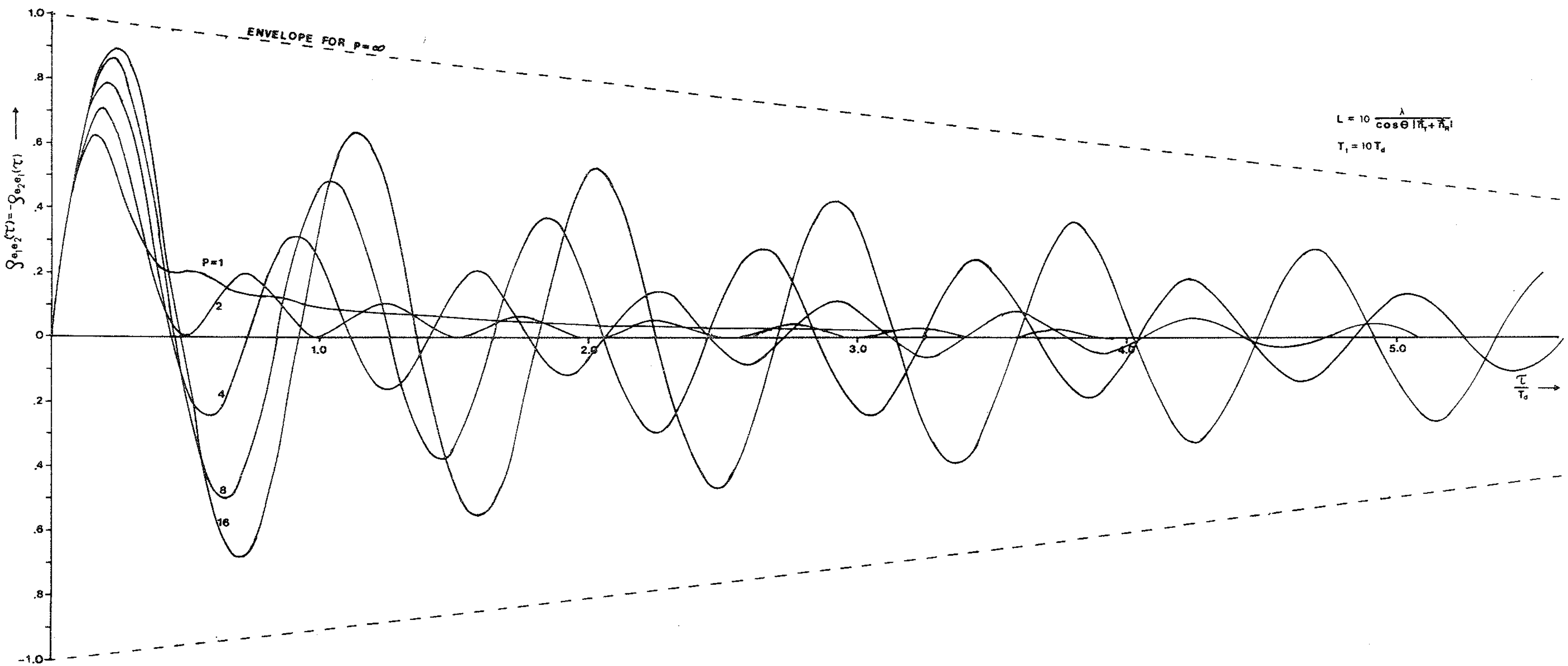

Figure 5.5. Crosscorrelation functions between the quadrature components of the doppler signal for the blunt profiles.

Since the mean velocity of the profiles is the same, the first zero of $\rho_{e_1e_1}(\tau)$ seems to be determined, within the accuracy of the figure, by this velocity for $p = 2,4,8,16$. Calculations for $p = 3, 6$ has also been performed and give the same result. The distance between the other zeros of $\rho_{e_1e_1}$ is within the accuracy of the figure, determined by the doppler frequency of the maximum velocity present.

A more detailed analysis shows that these results are only approximate. For $p = 2$ they are exact in the limit of infinite transit time while for $p = 4$ they are approximate even in this limit. For $p = \infty$ the mean and max. velocities are equal and the result is true for all values of the transit times where the last term of Eq. (5.62) may be neglected.

The approximate power spectrum when neglecting the broadening effect of the finite transit time, may be obtained from Eq. (5.48). Normalizing to unit total power we get

$$G_{\hat{e}\hat{e}}(\omega) = \begin{cases} \dfrac{4\pi}{p\omega_0\left(1-\dfrac{\omega}{\omega_0}\right)^{1-\frac{2}{p}}} & \omega \in [\min(0,\omega_0),\ \max(0,\omega_0)] \quad \omega_0 = \vec{q}\,\vec{v}_0 \\ 0 & \text{else} \end{cases} \tag{5.68}$$

This spectrum is shown in Figure 5.6. The spectrum will also be broadened due to the nonzero bandwidth of F in Eq. (5.41). This bandwidth is inversely proportional to the velocity and thereby to the doppler frequency. Thus the broadening will be greatest at the upper end of the spectrum and zero at $\omega = 0$. This broadening will also remove the singularity for $p > 2$.

As p increases, the bandwidth of $G_{\hat{e}\hat{e}}(\omega)$ decreases. This is directly reflected in an increased correlation time of the doppler signal as shown in Figure 5.4 and 5.5. An increase of the transit time will also decrease the bandwidth. However, for small values of p (= 1,2,3) the bandwidth of the approximate spectrum of Eq. (5.68) is so large that normal values of the transit length (L = 5-20 λ) will have little effect on the bandwidth. The correlation function of the doppler signal is therefore essentially independent of the transit length for low values of p.

For larger values of p transit time broadening will play a dominant role in the total bandwidth of the signal, and in this case the correlation function will be more sensitive to the length of the observation region. Increasing this length will increase the correlation time of $\hat{e}(t)$ and in the limit

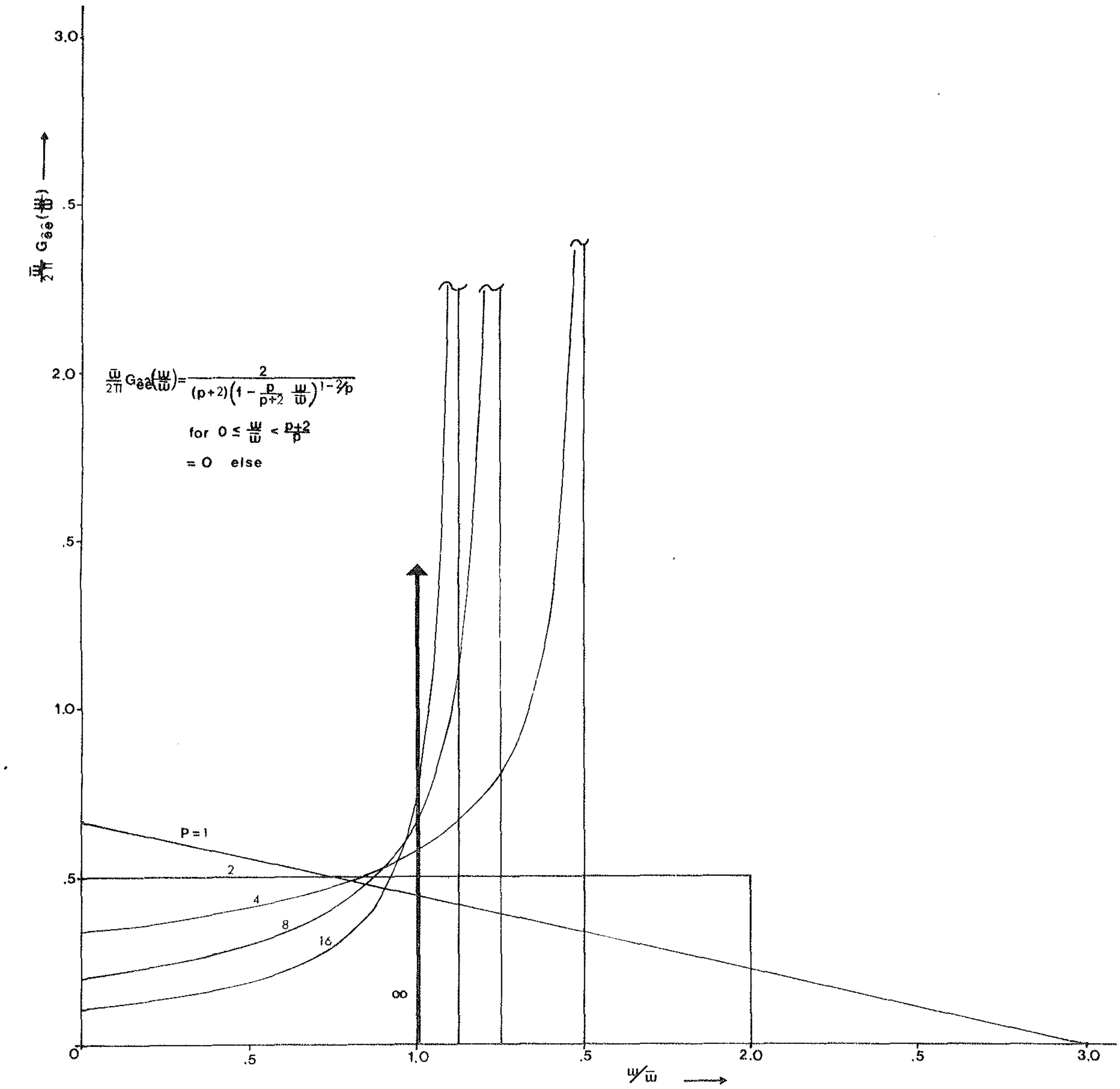

Figure 5.6. Power spectra of the doppler signal from the blunt velocity profiles. $\bar{\omega}$ is the mean angular frequency of the spectrum.

$p \to \infty$ the envelope of the correlation function will entirely depend on the length of the observation region as shown in Eq. (5.62).

We shall return to this dependency of the correlation functions on the length of the observation region in the next chapter where we study the variance of mean velocity estimators.

E. Denpendency of the received power spectrum on the illumination of the artery. Broadening of the spectrum with small transducers and focusing.

The received power spectrum will clearly depend on the illumination of the artery. An approximate calculation of the spectrum for special cases is given by Flax & al [48] and Brody [45]. We shall here only give a brief discussion of the effect.

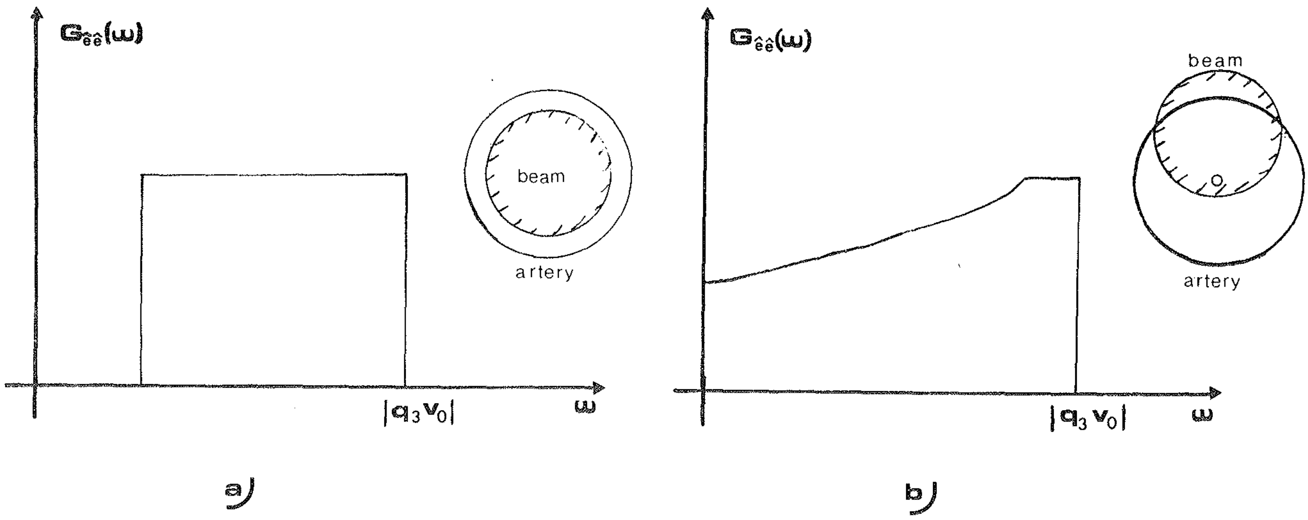

Figure 5.7. Received power spectrum from a parabolic profile when the width of the transducer beam is smaller than the artery cross section.
a) The axis of the transducer and artery coincide. The smallest velocities are not observed.
b) The axis of the transducer is parallel to the axis of the artery but does not coincide with it, so that all velocities are observed but not with full weight.

For a single transducer and pulsed flowmeter, the observation region will approximately be a disc with cross section equal to that of the beam and thickness determined by the transmitted pulse (Section 2.2). We have used this approximation in the proceeding section. If the beamwidth is smaller than the cross section, all velocities will not be observed with full weight.

The received power spectrum will therefore be changed as indicated in Figure 5.7 for a parabolic profile.

In most cases the transducer axis will form an angle θ with the axis of the artery. This reduces the doppler frequency. If the size of the observation region is so large compared to the artery that $L(\vec{\sigma})$ is independent of $\vec{\sigma}$ over the whole artery cross section, the width of the transducer beam will have no effect on the received power spectrum. This is indicated in Figure 5.8.

For $L(\vec{\sigma})$ to be independent of $\vec{\sigma}$ over the artery, the length of the observation region has to be less than L_1. If the transducer is rectangular,

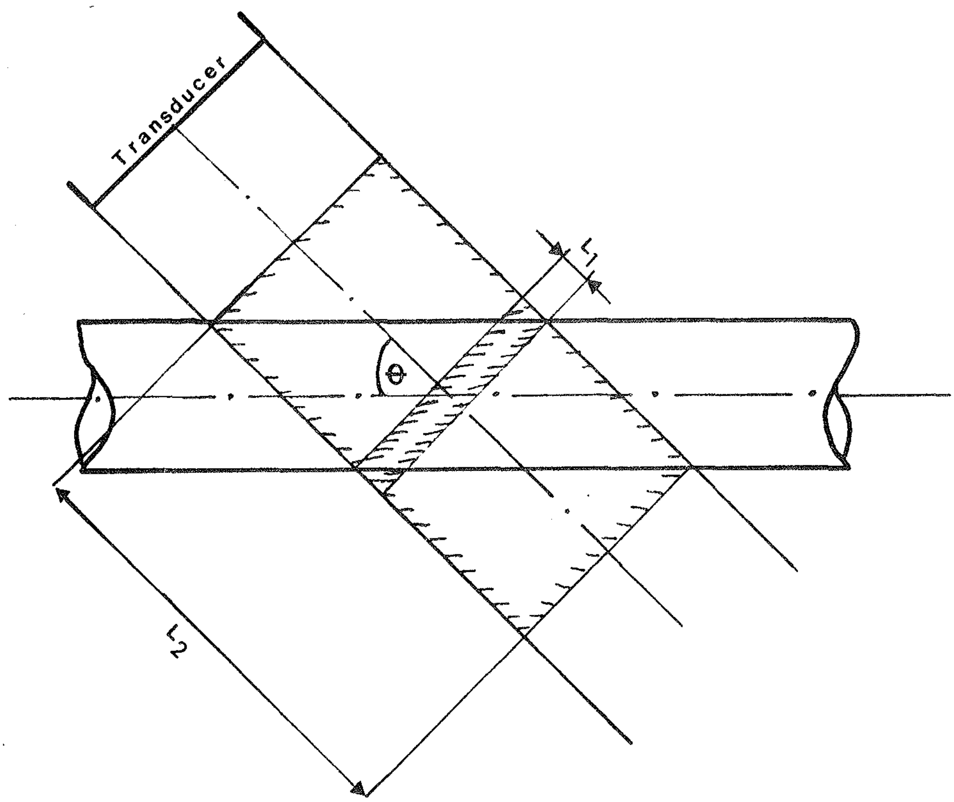

Figure 5.8. Maximum length L_1 of the observation region for no degradation of the power spectrum.

$L(\vec{\sigma})$ will also be independent of $\vec{\sigma}$ if the length of the observation region is larger than L_2. For a circular transducer whose diameter compared to that of the artery is so large that the curvature of the beam may be neglected across the artery, there will be practically no degradation of the spectrum too when $L_1 > L_2$.

In the discussion of the power spectra it is assumed that the transducers are so large that the plane-wave approximation may be performed. When this is not the case, there will be a change in the received power-spectrum which by its entrance in the formula may be divided into two groups.

i) In the nearfield $R(\vec{\xi})$ will vary across the observation region, giving different weight to different parts of the region. This will give an amplitude modulation of the received signal from a single scatterer and thus a broadening of the spectrum from this scatterer.

ii) In the nearfield the phases φ_T and φ_R will deviate from the plane-wave variation. This will give an additional broadening of the received spectrum from a moving scatterer as indicated in Figure 5.9.

The reason for these two effects is that the scatterer is illuminated with a distribution of plane monochromatic waves with different $\vec{k}$-vectors. Hence, a distribution of doppler shifts will be reflected. Since the receiver transducer is small, it will be sensitive to a distribution of reflected $\vec{k}$-vektors and thus a distribution of doppler-shifts will be received.

The situation is somewhat analogous to the broadening of the spectrum by the convolution with $\hat{R}$ in Eq. (5.13). In this case, however, a single $\vec{k}$-vector is transmitted, $\vec{k}_T$, and the receiver is sensitive to a single direction of $\vec{k}$-vectors only, given by $\vec{k}_R$. Thus additional broadening of the spectrum occurs when the transducers become small.

When focused transducers are used, there will be a broadening in the $\vec{k}$-spectrum of the transducer field patterns and thus a broadening of the received power spectrum too.

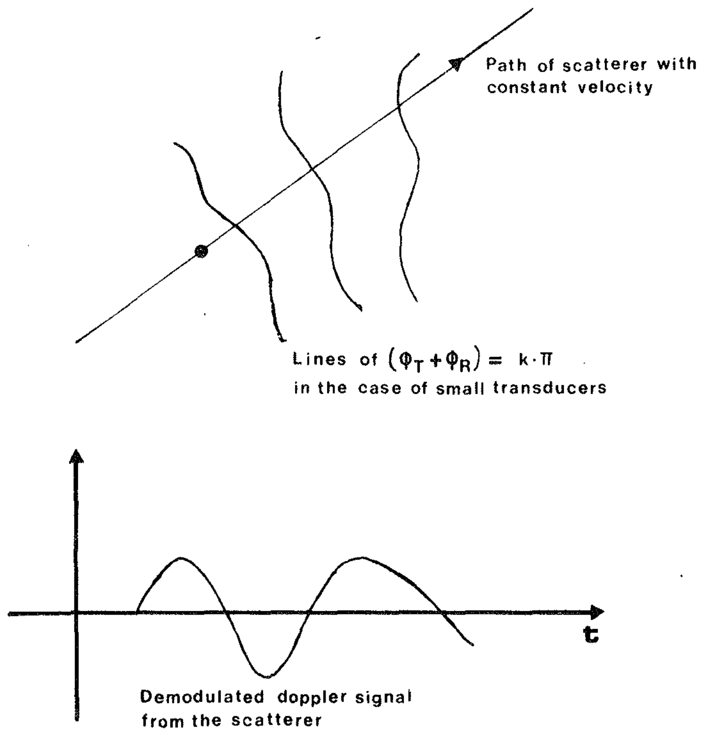

Figure 5.9. Illustration to the broadening of the received spectrum in the case of small transducers.

5.2. Velocity and velocity field estimators.

A. General.

By a velocity estimator we mean a device that performs an operation on the received signal to get an estimate of the mean velocity of blood in the observation region. Similarly, velocity field estimators give an estimate of the velocity field in the observation region.

Velocity field estimation may be obtained from the power spectrum. As we have seen in the previous paragraph, the power spectrum is a unique map of the velocity field once the transducer field patterns and the region of observation are known. The inverse map is, however, not unique. First of all only a component of the velocity in each point is measured. Secondly, the received signal is obtained by integration over the observation region. Changes of the velocity field inside the observation region is not uniquely resolved.

The pulsed and correlation velocity meter has an advantage over the continuous wave meter in that a small observation region may be obtained. In many practical cases the observation region is so small that the velocity field will be essentially constant within this region. The region may then be scanned across the vessel to obtain the profile [62, 64]. In the case of nonsteady flow, a multigating of the received signal is preferable to obtain a simultaneous observation of regions of different depths along the ulstrasonic beam [63].

By scanning the observation region, the measured profile will be a convolution of the real profile and the observation region. The real profile may then be obtained by a deconvolution operation [62].

The power spectrum is strictly defined only for a stationary process. This implies that the velocity field has to be time steady. When the field is nonsteady we can estimate the power spectrum over so short an interval of time that the velocity field may be considered stationary in this interval.

The finite estimation time introduces a fundamental unbiased stochastic error in the estimate. This error cannot be avoided unless additional information of the system is taken into account. Such information may be that the flow is periodic. This is a good approximation to the healthy cardiovascular system at constant conditions of moderate work. In this case estimation may be performed over equivalent intervals in the cardiac cycle for many cycles, to reduce the variance of the estimate.

Other information may be taken into account by modelling the cardiovascular system, as done by Aaslid [69], and using estimation techniques as developed in connection to control problems, i.e. the Kalman-Busy filter.

$G_{\hat{e}\hat{e}}$ has to be calculated from $G_{e_1e_1}$, $G_{e_2e_2}$, $G_{e_2e_1}$ and $G_{e_1e_2}$, Eq. (5.14). This requires four synchronous demodulators and two power spectrum estimates. If the observation region is so large that $e(t)$ can be considered wide sense stationary, Eq. (5.15) is valid, and only two powerspectrum estimates are necessary.

When only one sign of the doppler shifts is present in the signal, $e_2(t)$ will be the Hilbert transform of $e_1(t)$ multiplied by the sign of the doppler shift. This gives [61]

$$G_{\hat{e}\hat{e}}(\omega) = \begin{cases} 4G_{e_1e_1}(\omega) & \begin{array}{l}\omega > 0 \text{ pos. doppler shift} \\ \omega < 0 \text{ neg. doppler shift}\end{array} \\ 0 & \text{else} \end{cases} \tag{5.69}$$

In this case $G_{\hat{e}\hat{e}}(\omega)$ may be calculated from $G_{e_1e_1}(\omega)$ and only one spectrum estimate is necessary. If the sign of the doppler shift is known, only one demodulator is necessary.

There are two methods that avoid the difficulties above using only one spectrum estimate.

The first method is to use the offset frequency technique for demodulation described in Chapter 2. [63], [65], [66].

The other method is to use the difference in the phase between the Fourier transform of $e_1(t)$, $E_1(\omega)$, and of $e_2(t)$, $E_2(\omega)$. For positive doppler frequencies, i.e., velocity towards the transducer, the phase of E_1 will be $\pi/2$ greater than that of E_2 at this frequency. Negative doppler shifts will produce a phase of E_1 $\pi/2$ less than that of E_2.

The above phenomenon is used by MacKay [65]. The phase of $E_1(\omega)$ is advanced by $\pi/4$, while that of $E_2(\omega)$ is delayed by $\pi/4$. By this $e_1(t) \rightarrow A(t)$ and $e_2(t) \rightarrow B(t)$. $A - B$ then gives the signal from targets with positive doppler shifts, while $A + B$ gives the signal from targets with negative doppler shifts.

Spectrum analysis may be performed by a digital computer using a Fast Fourier transform algorithm, or by a bank of narrow bandpass filters with center frequencies spread over the interesting frequency band. The real time sweeping filter method used in some instruments is not applicable for blood velocity measurements because of the rapid change of velocity with time. However, a sweeping filter combined with time compression is useful.

To estimate the cross correlation spectrum $G_{e_i e_j}$ a digital computer is preferable. It is, therefore, desirable to avoid the need for this calculation, and, hence, the two methods above are especially useful.

In the offset frequency method only one demodulator and filter channel is necessary while complexity is increased by the offset frequency generator. The repetition frequency in the PW meter must be twice the maximum frequency occuring at the sample position. This technique, therefore, requires a higher repetition frequency than the quadrature method, which decreases the maximum measurable depth for a given velocity.

An offset spectrum may, however, be obtained from the quadrature components

$$e_1(t)\cos\omega_1 t - e_2(t)\sin\omega_1 t = \mathrm{Re}\{\hat{e}(t)e^{i\omega_1 t}\} \tag{5.70}$$

This method is especially useful for the PW meter since minimum repetition frequency for a given doppler shift may be used and only one spectrum estimation is necessary.

The *velocity estimators* will suffer from the same shortcoming as the velocity field estimators in that it is only an average of the component of the velocity along the $\vec{k}$-vectors in the transducer field pattern that may be measured.

The earliest used velocity estimator was the *zero crossing* detector. As indicated by the name, the detector essentially counts the number of zero crossings of the doppler signal in a defined interval of time. This was taken as an estimate of the velocity.

The estimator evidently works well when the doppler signal is composed of a single frequency. For pulsed and correlation velocity meters with focused transducers the observation region may be made so small that this is approximately true.

When the observation region cannot be made small, as for the continuous wave meter, the zero crossing detector has to be calibrated according to the actual velocity field [48]. This limits the use of this estimator.

In many cases, as with measurements in the aorta, it is desirable to illuminate the whole lumen of the artery even when using range resolution, this being the most practical way of getting a simultaneous observation of the whole cross section of flow. Here the zero crossing detector will be of no use as well.

A very attractive velocity estimator has been suggested by Brody [45]. It is based on the following formula whose validity we show follows from our model of the scattering of the ultrasound

$$\hat{\bar{v}}_I = \text{const}\{\langle \dot{e}_2(t)e_1(t)\rangle - \langle \dot{e}_1(t)e_2(t)\rangle\} \quad \text{Type I} \tag{5.71}$$

$\hat{\bar{v}}$ is the estimate of the mean velocity in the observation region. The hat indicates an estimate and the bar indicates the mean.

An estimator which uses only the first term of this equation has been presented by Arts and Roevros [70].

The estimator based on Eq. (5.71) has the advantage over the zero crossing detector that its validity holds regardless of the velocity profile. The multiplication may be performed by analog integrated circuits. Available multiplicators have, however, shown to have unacceptable long time stability for the instrument to be operated without access to skilled technical people.

From Bussgang's Theorem [76], it follows that an estimator based on the following equation could be used as well

$$\hat{\bar{v}}_{II} = \text{const}\langle \dot{e}_2(t)\,\text{sgn}\; e_1(t)\rangle \quad \text{Type II} \tag{5.72}$$

where the signum function is defined by

$$\text{sgn}\; e_1 = \begin{cases} +1 & e_1 > 0 \\ -1 & e_1 < 0 \end{cases} \tag{5.73}$$

This estimator is much simpler to realize electronically and a suggestion is given in Figure 5.15. It proves to have very good long time stability.

Eq. (5.71) may be expressed by $G_{\hat{e}\hat{e}}(\omega)$ to form the basis of a third estimator operating in the frequency domain.

$$\hat{\bar{v}}_{III} = \text{const} \int d\omega\; \omega G_{\hat{e}\hat{e}}(\omega) \quad \text{Type III} \tag{5.74}$$

The validity of these three estimators is proved in the following from our model of the scattering process.

When noise is present in the signal, a systematic error in the estimates occurs. This is also discussed and it turns out that this error will be the same for all three estimators. When the ensemble averages are estimated by integration for a finite time, additional errors in the estimates occur. For the practical realizations of estimator I and II with AGC given in Section 5.3 this estimator uncertainty is investigated experimentally in Section 7.2B. A theoretical discussion of this error is given in Chapter 6.

B. Estimator Type I, $<\dot{e}_2 e_1> - <\dot{e}_1 e_2>$.

We shall prove that the ensemble average of $<\dot{e}_2 e_1>$ and $<\dot{e}_1 e_2>$ is proportional to a vector weighted average of the instantaneous velocity field in the observation region. This will be done for the general model with diffusion of the concentration fluctuations.

Expectation value.

From Eq. (5.5) we have

$$\begin{aligned} e_1(t) &= |\alpha| \int d^3\xi R(\vec{\xi}) \cos \psi(\vec{\xi})\ n(\vec{\xi},t) \\ e_2(t) &= |\alpha| \int d^3\xi R(\vec{\xi}) \sin \psi(\vec{\xi})\ n(\vec{\xi},t) \end{aligned} \tag{5.75}$$

From Eq. (4.27) and Eq. (4.29) we may express $\dot{e}_2$ by

$$\dot{e}_2(t) = |\alpha| \int d^3\xi R \sin\psi \frac{\partial n}{\partial t}$$

$$\dot{e}_2 = -|\alpha| \int d^3\xi R \sin\psi\, \vec{v}\nabla n + D|\alpha| \int d^3\xi R \sin\psi\, \nabla^2 n - |\alpha| \int d^3\xi R \sin\psi\, \nabla^2 A$$

This expression may be integrated by parts. We then invoke that $\nabla\vec{v} = 0$. This is not strictly necessary since $\vec{v}\nabla n$ should be written $\nabla(\vec{v}n)$ in the case of a compressible fluid. The result is

$$\dot{e}_2(t) = |\alpha| \int d^3\xi \vec{v}\nabla(R\sin\psi)n + D|\alpha| \int d^3\xi \nabla^2(R\sin\psi)n - |\alpha| \int d^3\xi \nabla^2(R\sin\psi)A \tag{5.76}$$

By multiplying this expression by $e_1(t)$ from Eq. (5.75) and averaging, we get

$$<\dot{e}_2(t)e_1(t)> = |\alpha|^2\int d^3\xi_1\int d^3\xi_2\{\vec{v}(\xi_1,t)\nabla_{\vec{\xi}_1}[R(\vec{\xi}_1)\sin\psi(\vec{\xi}_1)]$$

$$\times R(\vec{\xi}_2)\cos\psi(\vec{\xi}_2)<n(\vec{\xi}_1,t)n(\vec{\xi}_2,t)>$$

$$+ D\nabla^2_{\vec{\xi}_1}[R(\vec{\xi}_1)\sin\psi(\vec{\xi}_1)]R(\vec{\xi}_2)\cos\psi(\vec{\xi}_2)<n(\vec{\xi}_1,t)n(\vec{\xi}_2,t)>$$

$$- \nabla^2_{\vec{\xi}_2}[R(\vec{\xi}_1)\sin\psi(\vec{\xi}_1)]R(\vec{\xi}_2)\cos\psi(\vec{\xi}_2)<A(\vec{\xi}_1,t)n(\vec{\xi}_2,t)>\}$$

From Eq. (4.47) and Eq. (4.50) we have

$$\begin{aligned}<n(\vec{\xi}_1,t)n(\vec{\xi}_2,t)> &= <n^2(\vec{\xi}_1,t)>\delta(\vec{\xi}_2-\vec{\xi}_1)\\ <A(\vec{\xi}_1,t)n(\vec{\xi}_2,t)> &= D<n^2(\vec{\xi}_1,t)>\delta(\vec{\xi}_2-\vec{\xi}_1)\end{aligned} \tag{5.77}$$

Inserting this into the expression above, the diffusion term and the stochastic current term cancel. Integration over $\vec{\xi}_2$ gives

$$<\dot{e}_2(t)e_1(t)> = |\alpha|\int d^3\xi\vec{v}(\vec{\xi},t)\nabla[R(\vec{\xi})\sin\psi(\vec{\xi})]R(\vec{\xi})\cos\psi(\vec{\xi})<n^2(\vec{\xi},t)>$$

Evaluating the gradient gives

$$<\dot{e}_2(t)e_1(t)> = |\alpha|^2\int d^3\xi<n^2>[R^2\cos^2\psi\nabla\psi + R\sin\psi\cos\psi\nabla R]\vec{v}$$

$R\nabla R$ may be written as $\frac{1}{2}\nabla R^2$. When this term is integrated by parts, we get

$$<\dot{e}_2e_1> = |\alpha|^2\int d^3\xi R^2\{<n^2>\cos^2\psi\nabla\psi - \frac{1}{4}\nabla[\sin 2\psi<n^2>]\}\vec{v}$$

By evaluating the gradient of the last term and using $\cos 2\psi = 2\cos^2\psi - 1$ we get

$$\boxed{\begin{aligned}&<\dot{e}_2(t)e_1(t)> = \int d^3\xi\vec{K}_1(\vec{\xi},t)\vec{v}(\vec{\xi},t)\\ &\vec{K}_1(\vec{\xi},t) = \frac{|\alpha|^2}{2}R^2(\vec{\xi})[<n^2(\vec{\xi},t)>\nabla\psi(\vec{\xi}) - \tfrac{1}{2}\sin 2\psi(\vec{\xi})\nabla<n^2(\vec{\xi},t)>]\end{aligned}} \tag{5.78}$$

Similarly we get

$$\boxed{\begin{aligned}&<\dot{e}_1(t)e_2(t)> = -\int d^3\xi\vec{K}_2(\vec{\xi},t)\vec{v}(\vec{\xi},t)\\ &\vec{K}_2(\vec{\xi},t) = \frac{|\alpha|^2}{2}R^2(\vec{\xi})[<n^2(\vec{\xi},t)>\nabla\psi(\vec{\xi}) + \tfrac{1}{2}\sin 2\psi(\vec{\xi})\nabla<n^2(\vec{\xi},t)>]\end{aligned}} \tag{5.79}$$

The difference between these two expressions gives

$$\boxed{\begin{aligned} &\langle \dot{e}_2(t)e_1(t)\rangle - \langle \dot{e}_1(t)e_2(t)\rangle = \int d^3\xi K(\vec{\xi},t)\nabla\psi(\vec{\xi})\vec{v}(\vec{\xi},t) \\ &K(\vec{\xi},t) = |\alpha|^2 R^2(\vec{\xi})\langle n^2(\vec{\xi},t)\rangle \end{aligned}} \tag{5.80}$$

To get an estimate of the magnitude of the weighting factor, we may calculate $\{\langle e_1{}^2\rangle + \langle e_2{}^2\rangle\}$. From Eq. (5.75) we get

$$\langle e_1{}^2(t)\rangle = |\alpha|^2 \int d^3\xi_1 d^3\xi_2 R(\vec{\xi}_1)R(\vec{\xi}_2)\cos\psi(\vec{\xi}_1)\cos\psi(\vec{\xi}_2)\langle n(\vec{\xi}_1,t)n(\vec{\xi}_2,t)\rangle$$

Inserting the correlation function for n from Eq. (5.77) and integrating over ξ_2, we get

$$\langle e_1{}^2(t)\rangle = |\alpha|^2 \int d^3\xi R^2(\vec{\xi})\cos^2\psi(\vec{\xi})\langle n^2(\vec{\xi},t)\rangle$$

$$\langle e_1{}^2(t)\rangle = \frac{|\alpha|^2}{2}\int d^3\xi R^2(\vec{\xi})[1 + \cos 2\psi(\vec{\xi})]\langle n^2(\vec{\xi},t)\rangle \tag{5.81}$$

Similarly we get

$$\langle e_2{}^2(t)\rangle = \frac{|\alpha|^2}{2}\int d^3\xi R^2(\vec{\xi})[1 - \cos 2\psi(\vec{\xi})]\langle n^2(\vec{\xi},t)\rangle \tag{5.82}$$

The sum of these two expressions give

$$\boxed{\langle e_1{}^2(t)\rangle + \langle e_2{}^2(t)\rangle = |\alpha|^2 \int d^3\xi R^2(\vec{\xi})\langle n^2(\vec{\xi},t)\rangle = \int d^3\xi K(\vec{\xi})} \tag{5.83}$$

For large transducers where the plane wave approximation is acceptable we have

$$\begin{aligned} &\nabla\psi = -(\vec{k}_T + \vec{k}_R) \\ &|\nabla\psi| = \omega_0/c\,|\vec{n}_T + \vec{n}_R| \end{aligned} \tag{5.84}$$

When the transducers become smaller, the magnitude of $\nabla\psi$ will not change appreciably. An estimate of the mean velocity along $\nabla\psi$ in the observation region is therefore

$$\boxed{\hat{v}_I(t) = \frac{c}{\omega_0|\vec{n}_T + \vec{n}_R|}\cdot\frac{\langle \dot{e}_2(t)e_1(t)\rangle - \langle \dot{e}_1(t)e_2(t)\rangle}{\langle e_1{}^2(t)\rangle + \langle e_2{}^2(t)\rangle}} \tag{5.85}$$

This estimator has been suggested by Brody [45].

In the expression for $\vec{K}_1$ and $\vec{K}_2$ we see that $\sin 2\psi$ will be a very rapidly oscillating function compared to the rest of the integrand, Eq. (5.78) and Eq. (5.79). This is also true for $\cos 2\psi$ in the expressions for $\langle e_1^2 \rangle$ and $\langle e_2^2 \rangle$, Eq. (5.81) and Eq. (5.82). In most cases $\langle n^2 \rangle$ will be slowly varying with space so that $\nabla \langle n^2 \rangle$ will be small. We may, therefore, neglect these terms. Under this approximation we have

$$\langle \dot{e}_2(t)e_1(t)\rangle = -\langle \dot{e}_1(t)e_2(t)\rangle = \frac{|\alpha|^2}{2}\int d^3\xi R^2(\vec{\xi})\langle n^2(\vec{\xi},t)\rangle \nabla\psi(\vec{\xi})\vec{v}(\vec{\xi},t)$$

$$\langle e_1^2(t)\rangle = \langle e_2^2(t)\rangle = \frac{|\alpha|^2}{2}\int d^3\xi R^2(\vec{\xi})\langle n^2(\vec{\xi},t)\rangle \tag{5.86}$$

The following simplified expression may then be used as a velocity estimate

$$\boxed{\hat{v}_I(t) = \frac{c}{\omega_0|\vec{n}_T + \vec{n}_R|}\cdot\frac{\langle \dot{e}_2(t)e_1(t)\rangle}{\langle e_1^2(t)\rangle} = -\frac{c}{\omega_0|\vec{n}_T + \vec{n}_R|}\cdot\frac{\langle \dot{e}_1(t)e_2(t)\rangle}{\langle e_2^2(t)\rangle}} \tag{5.87}$$

This estimator has been suggested by Arts and Roevros [70].

The estimator gives a vector weighted average of the velocity field inside the observation region. At each point it is only the component of $\vec{v}$ along $\nabla\psi$ that is observed. In addition different points are given different weight because of R.

C. Estimator Type II, $\langle \dot{e}_2 \,\mathrm{sgn}\, e_1 \rangle$.

The doppler signal is obtained from the concentration fluctuation by a linear operator, Eq. (5.5). Assuming Gaussian properties of n, Eq. (4.16), therefore implies Gaussian properties of the doppler signal.

Even with non Gaussian properties of the concentration fluctuation the independency of n at different points in space together with the Central-Limit theorem [75] implies Gaussian properties of the doppler signal. To see this we approximate the integral in Eq. (5.5) by a sum over small cubes ΔV. From the independence of n the terms of the sum will be independent random variables satisfying the requirements for the Central-Limit theorem to hold. As $\Delta V \to 0$, the number of terms tends towards infinity while the variance of each term is proportional to $\langle n^2 \rangle \Delta V$. In the limit the Central-Limit theorem then implies Gaussian properties of the integral.

For two Gaussian variables, y_1 and y_2, with zero mean and distribution given by Eq. (VII.7) we may directly calculate

$$\langle y_1 \operatorname{sgn} y_2\rangle = \int_{-\infty}^{\infty} dy_1 \int_0^{\infty} dy_2 y_1 p(y_1,y_2) - \int_{-\infty}^{\infty} dy_1 \int_{-\infty}^{0} dy_2 y_1 p(y_1,y_2)$$

$$= \sqrt{\frac{2}{\pi}}\ \frac{\langle y_1 y_2\rangle}{\sqrt{\langle y_2{}^2\rangle}} \tag{5.88}$$

Especially we obtain from this

$$\langle |y|\rangle = \langle y \operatorname{sgn} y\rangle = \sqrt{\frac{2}{\pi}\langle y^2\rangle} \tag{5.89}$$

From these expressions we see that the following relations hold

$$\frac{\langle \dot{e}_2 \operatorname{sgn} e_1\rangle}{\langle |e_1|\rangle} = \frac{\langle \dot{e}_2 e_1\rangle}{\langle e_1{}^2\rangle} \qquad \frac{\langle \dot{e}_1 \operatorname{sgn} e_2\rangle}{\langle |e_2|\rangle} = \frac{\langle \dot{e}_1 e_2\rangle}{\langle e_2{}^2\rangle}$$

From Eq. (5.87) we then see that the following expressions may be used as a velocity estimate

$$\boxed{\hat{v}_{II}(t) = \frac{c}{\omega_0|\vec{n}_T + \vec{n}_R|}\cdot\frac{\langle \dot{e}_2(t) \operatorname{sgn} e_1(t)\rangle}{\langle |e_1(t)|\rangle} = -\frac{c}{\omega_0|\vec{n}_T + \vec{n}_R|}\cdot\frac{\langle \dot{e}_1(t) \operatorname{sgn} e_2(t)\rangle}{\langle |e_2(t)|\rangle}} \tag{5.90}$$

The above result is a special case of a more general result first derived for Gaussian variables by Bussgang [76]. This reference states that for a rather general nonlinear function, $g(x)$, the following relation holds

$$\langle x_1 g(x_2)\rangle = k\langle x_1 x_2\rangle$$

where k is a constant of proportionality. This result was later established for a special class of non Gaussian variables by Barrett and Lampard [85] and their work was further develpoed by Brown [77]. In Appendix VIII we discuss conditions for the result to hold.

Remark. The following illustrates the nature of the previous two estimators. Neglecting diffusion and ∇R in Eq. (5.76) we have

$$<\dot{e}_2(t)*e_1(t)> \approx |\alpha| \int d^3\xi \vec{v}\, R \cos\, \psi \nabla\psi <n*e_1> \tag{5.91}$$

where the star indicates a generalized product, for instance ordinary or sign multiplication.

We divide the region of integration into small cubes, ΔV_i, that $\vec{v}\nabla\psi$ may be considered approximately constant in this region. This gives

$$<\dot{e}_2(t)*e_1(t)> \approx |\alpha| \sum_i \vec{v}_i \nabla\psi_i \int_{\Delta V_i} d^3\xi\, R \cos\, \psi <n*e_1> \tag{5.92}$$

In the same way we get

$$<e_1(t)*e_1(t)> \approx |\alpha| \sum_i \int_{\Delta V_i} d^3\xi\, R \cos\, \psi <n*e_1> \tag{5.93}$$

Let α_i be defined by

$$\alpha_i \Delta V_i = |\alpha| \int_{\Delta V_i} d^3\xi\, R \cos\, \psi <n*e_1> \tag{5.94}$$

If $\alpha_i > 0$ and does not vary too much with i, there is a strong indication that the following expression may form the basis of a mean velocity estimator

$$\frac{<\dot{e}_2(t) * e_1(t)>}{<e_1(t) * e_1(t)>} = \frac{\sum_i \vec{v}_i \nabla\psi_i \alpha_i \Delta V_i}{\sum_i \alpha_i \Delta V_i} \tag{5.95}$$

D. Estimator Type III $\int d\omega \quad \omega G_{\hat{e}\hat{e}}(\omega)$.

For a stationary velocity field we shall show that the following estimator

$$\boxed{\hat{v}_{III} = \frac{c}{\omega_0 |\vec{n}_T + \vec{n}_R|} \cdot \frac{\int d\omega \quad \omega G_{\hat{e}\hat{e}}(\omega)}{\int d\omega \quad G_{\hat{e}\hat{e}}(\omega)}} \tag{5.96}$$

gives a vector weighted average of the velocity field in the observation region. To do this we show the validity of the following relations

$$\frac{1}{2\pi}\int d\omega\ \omega\ G_{\hat{e}\hat{e}}(\omega) = \langle \dot{e}_2(t)e_1(t)\rangle - \langle \dot{e}_1(t)e_2(t)\rangle \tag{5.97}$$

$$\frac{1}{2\pi}\int d\omega\ G_{\hat{e}\hat{e}}(\omega) = \langle e_1^{\ 2}(t)\rangle + \langle e_2^{\ 2}(t)\rangle \tag{5.98}$$

In Eq. (5.14) $G_{\hat{e}\hat{e}}$ is expressed by $G_{e_1e_1}$, $G_{e_2e_2}$, $G_{e_2e_1}$ and $G_{e_1e_2}$. We observe that $G_{e_ie_i}$ are even functions of ω while $[G_{e_1e_2} - G_{e_2e_1}]$ is odd. We therefore get

$$\int d\omega\ \omega\ G_{\hat{e}\hat{e}}(\omega) = \int d\omega\ i\omega\{G_{e_1e_2}(\omega) - G_{e_2e_1}(\omega)\}$$

$$= \int d\omega\{G_{\dot{e}_2e_1}(\omega) - G_{\dot{e}_1e_2}(\omega)\} \tag{5.99}$$

$$\int d\omega\ G_{\hat{e}\hat{e}}(\omega) = \int d\omega\{G_{e_1e_1}(\omega) + G_{e_2e_2}(\omega)\} \tag{5.100}$$

The rules for the correlation functions and power spectra of the derivatives of a stochastic process in Appendix VI are used. The integral of the power spectrum is related to the correlation functions taken at zero lag as given in Eqs. (5.97) and (5.98).

When the observation region is so large (as in all practical cases) that e(t) may be considered stationary, Eq. (5.15) is valid and Eq. (5.96) takes the form

$$\boxed{\hat{v}_{III} = \frac{c}{\omega_0|\vec{n}_T + \vec{n}_R|}\cdot\frac{\int d\omega\ G_{\dot{e}_2e_1}(\omega)}{\int d\omega\ G_{e_1e_1}(\omega)}} \tag{5.101}$$

This is the frequency domain representation of the simplified estimator of Arts and Roevros.

E. Effect of noise on estimator performance.

The types of noise that disturb the measurement are described in Section 2.4. Signals from slowly moving targets other than blood will give high intensity of low frequency shifts which do not come from the blood flow. The output of the estimator will, therefore, give a too low estimate of the mean velocity.

Usually this low frequency disturbance is removed by highpass filtering. By this the signal from the slowly moving blood is also removed. If there exist low velocities in the observation region this will give a velocity estimate which is too high. The error depends on the relative magnitude of the low frequency to the high frequency components of the signal received from the blood in the observation region. In Figure 5.10 the effect of this highpass filtering is demonstrated for a parabolic and square profile when the whole artery lumen is observed as in Figure 5.8.

The *electronic noise* $w(t)$ from transducer and preamplifier may be described by its analytical signal $\hat{w}(t)e^{i\omega_0 t}$

$$w(t) = \mathrm{Re}\{\hat{w}(t)e^{i\omega_0 t}\}$$

where $\qquad\qquad\qquad\qquad\qquad\qquad\qquad\qquad\qquad\qquad\qquad\qquad\qquad\qquad\qquad\qquad$ (5.102)

$$\hat{w}(t) = w_1(t) + iw_2(t)$$

is lowpass. By quadrature demodulation the signals on the two channels will be

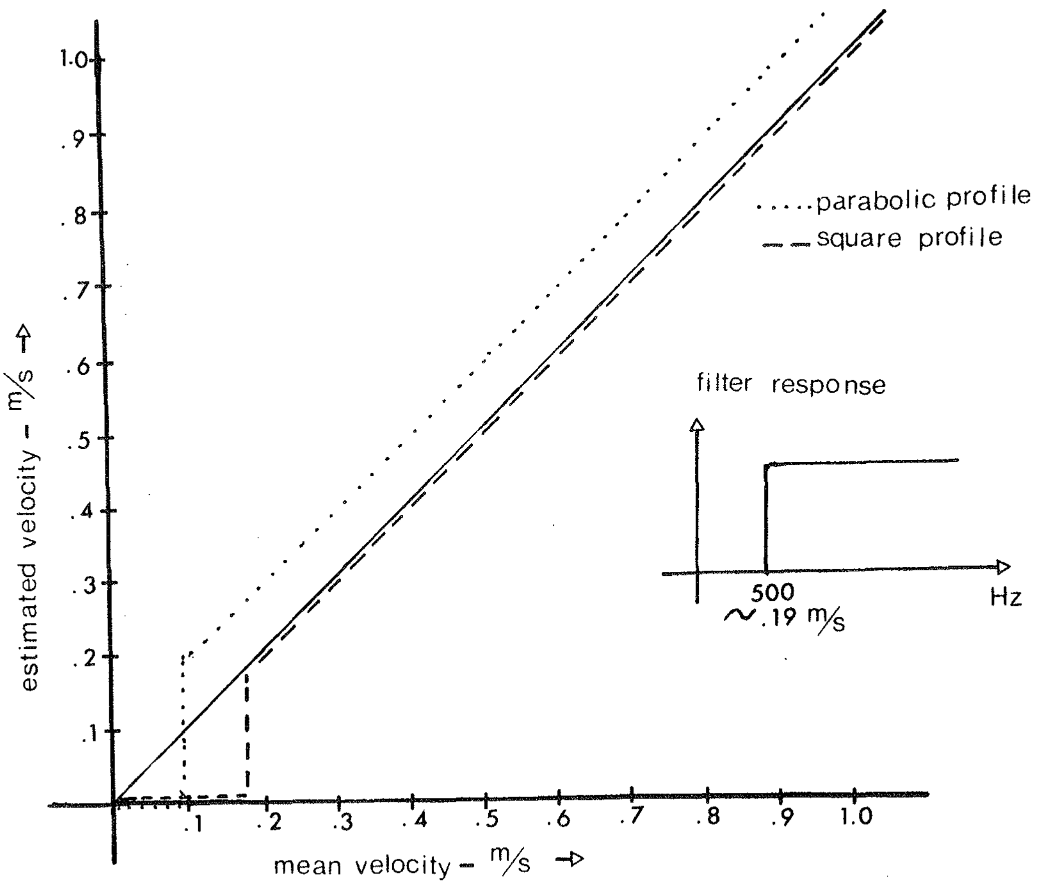

Figure 5.10. Effect of estimator performance when a highpass filter is used.

$$s_1(t) = e_1(t) + w_1(t)$$
$$s_2(t) = e_2(t) + w_2(t) \tag{5.103}$$

If the transfer function of the preamplifier is symmetric around ω_0, the auto-correlation function of $\hat{w}$ will be real. Since, [61],

$$R_{\hat{w}\hat{w}}(\tau) = 2[R_{w_1 w_1}(\tau) + iR_{w_1 w_2}(\tau)] \tag{5.104}$$

we see that the process w_1 and w_2 will be uncorrelated. By this

$$\langle\dot{w}_2(t)w_1(t)\rangle = \langle\dot{w}_1(t)w_2(t)\rangle = 0 \tag{5.105}$$

Since $\hat{e}(t)$ and $\hat{w}(t)$ obviously are independent, we immediately have

$$\langle\dot{s}_2(t)s_1(t)\rangle = \langle\dot{e}_2(t)e_1(t)\rangle$$
$$\langle\dot{s}_1(t)s_2(t)\rangle = \langle\dot{e}_1(t)e_2(t)\rangle \tag{5.106}$$

The numerator in the estimators are, however, affected by the electronic noise

$$\langle s_1^{\,2}(t)\rangle = \langle e_1^{\,2}(t)\rangle + \langle w_1^{\,2}(t)\rangle$$
$$\langle s_2^{\,2}(t)\rangle = \langle e_2^{\,2}(t)\rangle + \langle w_2^{\,2}(t)\rangle \tag{5.107}$$

The estimator type I and III will, therefore, give a too low value, $\hat{\bar{v}}'$, of $\hat{\bar{v}}$.

$$\frac{\langle\dot{s}_2 s_1\rangle - \langle\dot{s}_1 s_2\rangle}{\langle s_1^{\,2}\rangle + \langle s_2^{\,2}\rangle} = \frac{\langle\dot{e}_2 e_1\rangle - \langle\dot{e}_1 e_2\rangle}{\langle e_1^{\,2}\rangle + \langle e_2^{\,2}\rangle} \cdot \frac{1}{1 + \dfrac{\langle w_1^{\,2}\rangle + \langle w_2^{\,2}\rangle}{\langle e_1^{\,2}\rangle + \langle e_2^{\,2}\rangle}} \tag{5.108}$$

or

$$\boxed{\hat{\bar{v}}' = \hat{\bar{v}}\,\frac{1}{1 + N/S} \qquad \text{Estimator type I and III}} \tag{5.109}$$

where N/S is the noise to signal power ratio.

Similarly we get for estimator type I

$$\frac{\langle \dot{s}_2 \operatorname{sgn} s_1 \rangle}{\langle |s_1| \rangle} = \frac{\langle \dot{e}_2 e_1 \rangle + \langle \dot{w}_2 w_1 \rangle}{\langle e_1{}^2 \rangle + \langle w_1{}^2 \rangle} \tag{5.110}$$

In the same way as above we get the following output of estimator type II.

$$\boxed{\hat{\bar{v}}' = \hat{\bar{v}} \frac{1}{1 + N/S} \quad \text{Estimator type II}} \tag{5.111}$$

We thus see that the noise immunity of all three estimators are the same. The noise dependency of the estimator outputs are shown graphically in Figure 5.11. We see that for the reduction in estimator output to be less than 10 % the S/N-ration has to be greater than 9.54 dB.

If the transfer function of the preamplifier is nonsymmetric, the expectation values $\langle \dot{w}_1 w_2 \rangle$ and $\langle \dot{w}_2 w_1 \rangle$ will no longer be zero and a bias error in the estimates will occur.

For practical estimators the expectation values are estimated for a finite interval of time. The electronic noise will then increase the stochastic unsystematic error in the estimate in addition to the systematic error calculated above.

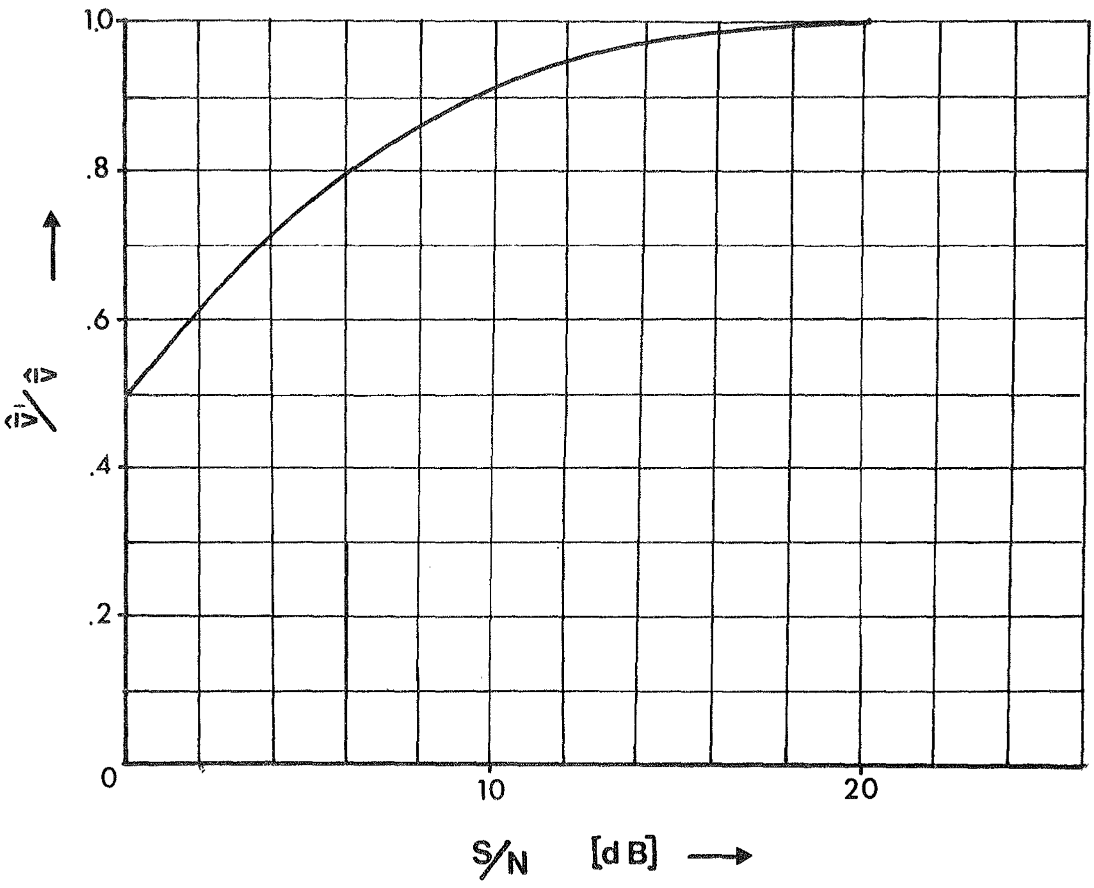

Figure 5.11. Reduction in estimator output when electronic noise is present in the signal.

5.3. Practical estimators.

A. Introduction.

In the previous paragraph the estimators are given by ensemble averages. To calculate ensemble averages from measured data is, in general, difficult because we are observing a single event in the sample space. If, however, the system is ergodic, the ensemble averages are equal to the time averages by definition. The flow system is ergodic when the velocity field is stationary.

When the velocity field is stationary, the ensemble averages may, therefore, be estimated by a lowpass filter with real poles only. For a nonconstant velocity field the ensemble averages will change with time. The lowpass filtering technique may still be used, but the integration time of the filter must be made so short that ensemble averages, and hence the velocity field, may be considered essentially constant in this interval of time.

The limited integration time introduces an unbiased stochastic error in the estimate which can not be avoided unless additional information of the system is taken into account, as discussed at the beginning of the previous paragraph.

If the integration time is too long, error is introduced because of the smoothing of the lowpassfilter. Hence, for a given velocity field as a function of space and time there exists an optimum filter which minimizes the estimation error.

Estimators based on the first two principles have been built and tested out experimentally. The realizations are discussed in the following. Estimators based on the third principle are in the field of standard power spectrum estimation techniques. We have performed no experimental work using this principle except using commercial instruments. Brody [45] has given a survey of methods applicable in connection to pulsatile flow. We may also refer to the general litterature [71], [72].

B. Realization of estimator type I and II.

Figure 5.12 shows a block diagram realization of the estimator given in Eq. (5.85).

To remove signals from slowly moving tissue a highpassfilter with cutoff frequency of about 100 Hz for peripheral arteries and from 300 - 1000 Hz for aorta, the last values depending on the activity of the heart. Thus, when the velocity becomes very small in the diastole, there will be a signal dropout at the input of the estimator. This is unwanted for the functioning of the divisor circuit, because the numerator becomes small. This effect may be avoided by the use of an AGC-circuit [70] which amplifies the noise in the diastole. This may be done like indicated in Figure 5.13.

The numerator is fed to a device which integrates the difference between the numerator and a reference voltage. The output of the integrator is fed to a voltage controlled amplifier.

For the system to be stable there is a lower limit of the time constant of the integrator. This limit depends on the type of lowpass filter used. To avoid this difficulty the input of the integrator may be taken from the input of the filter. In this way the AGC-loop may be made so fast that the numerator is kept essentially constant. The divisor circuit may then be avoided. This

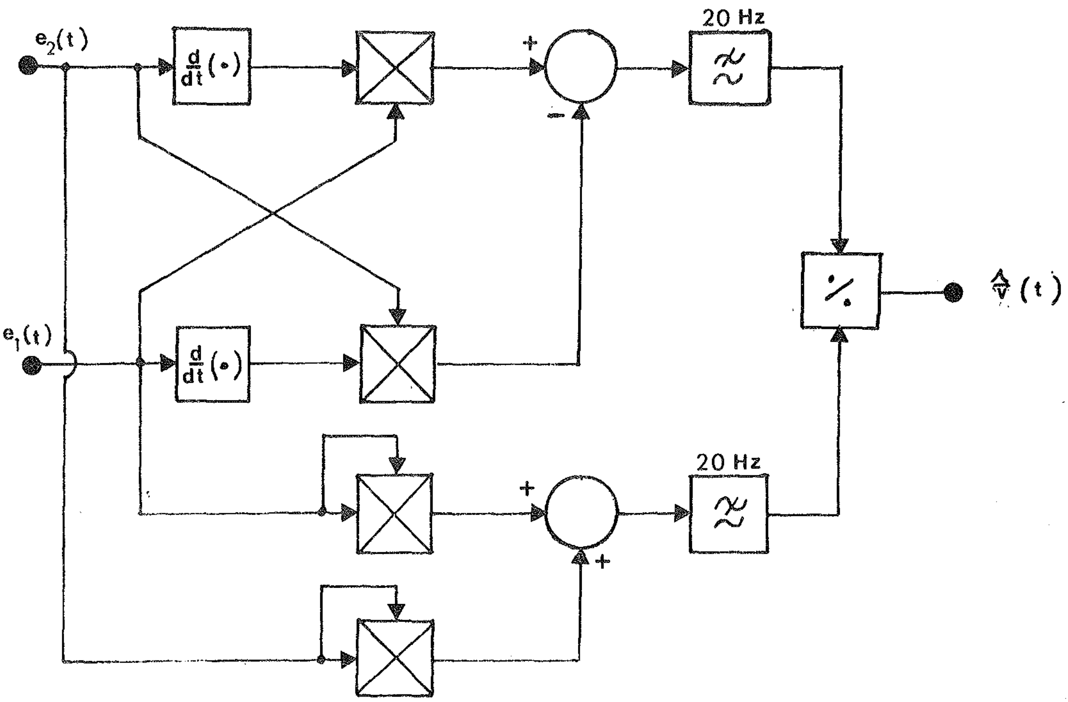

Figure 5.12. Estimator based on Eq. (5.85).

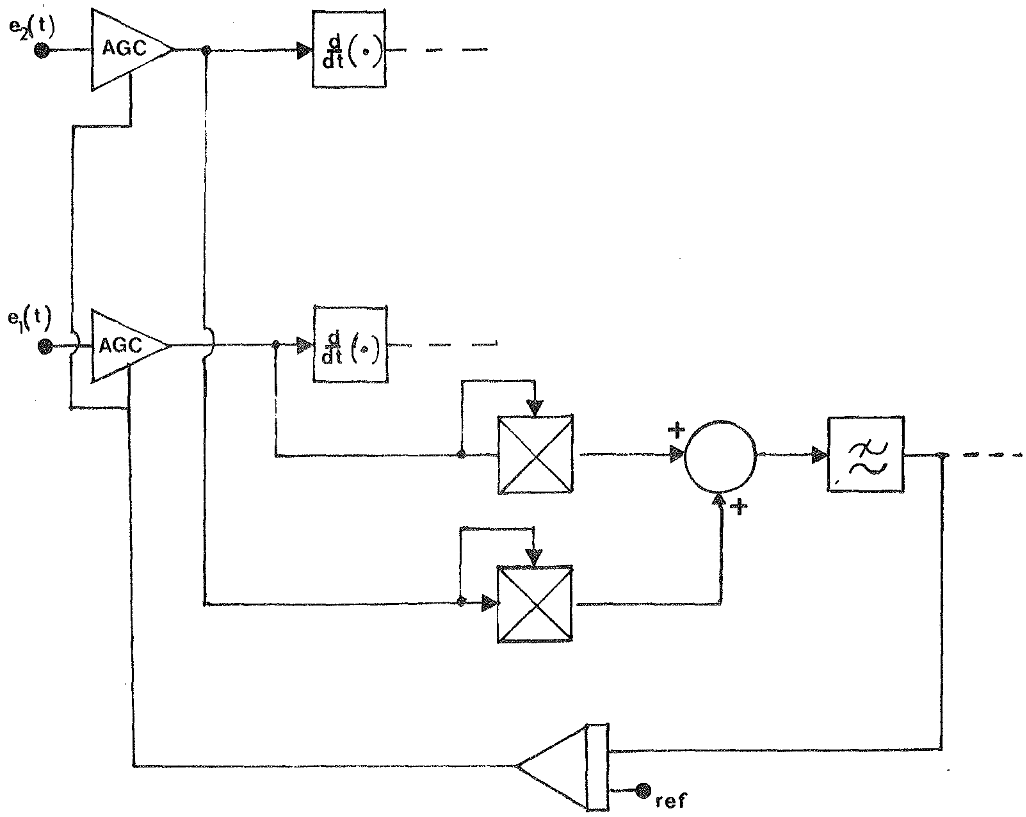

Figure 5.13. AGC-arrangement to keep the numerator sufficiently large in the estimator of Figure 5.12.

is a great practical advantage because a sufficiently stable divisor circuit is difficult to produce.

The voltage controlled amplifiers in Figure 5.13 must have identical characteristics for the system to work. This is difficult to achieve in practice and it is, therefore, preferable to decouple the AGC-loop for e_2 and e_1. The resulting practical estimator is given in Figure 5.14.

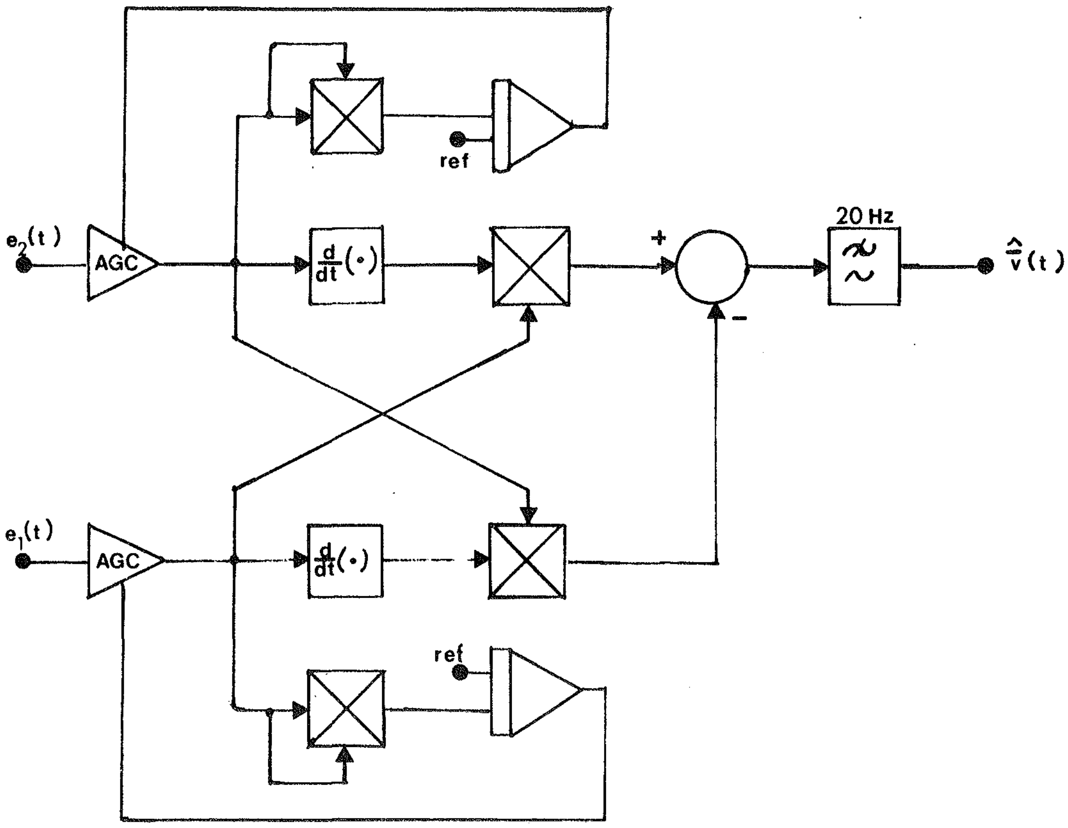

Figure 5.14. Practical estimator based on Eq. (5.85).

Similarly, a practical estimator based on Eq. (5.87) may be obtained by avoiding the branch giving $\dot{e}_1 \cdot e_2$ in Figure 5.14.

A practical estimator based on Eq. (5.90) is given in Figure 5.15. This estimator has the advantage over the previous ones in that it does not use ordinary multipliers. Hence, its long time stability is essentially given by that of passive components only, and exceeds that of the previous ones by a large amount.

$e_2(t)$ is fed from the differentiator circuit to a gate a and via an inverter to a second gate $\bar{a}$. These gates are complementary - one is open when

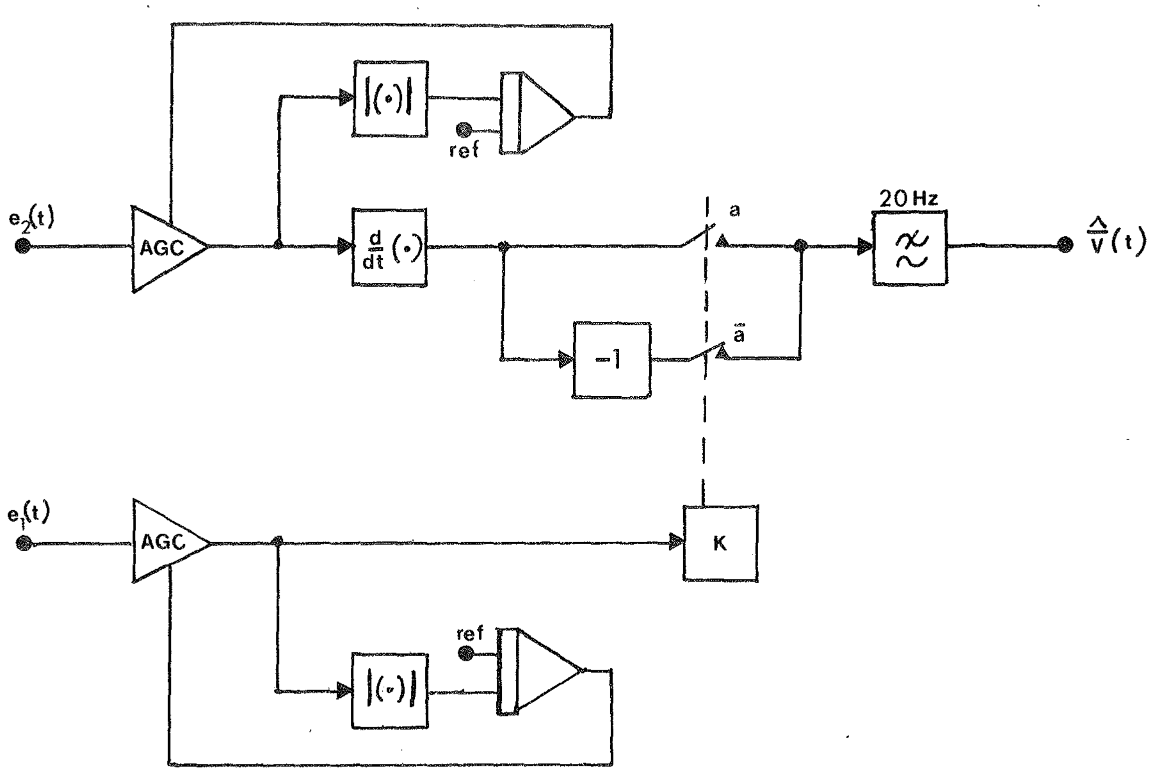

Figure 5.15. Practical estimator based on Eq. (5.90).

the other is closed. The gates are controlled by the sign of e_1 through a suitable circuit K. The gain control of e_1 is not necessary but improves the functioning of the system.

The variance of the estimates will depend on the AGC-time constant. This is discussed in more detail in Chapter 6, while an experimental study of this phenomenon is given in Chapter 7.

5.4. Summary.

The mathematical relation between the velocity field in the observation region and the power spectrum of the received signal is given for timesteady flow. The effect of diffusion is discussed and it is found that it can be neglected.

When the observation region becomes small, the spectrum is broadened because of the finite transit time of blood through the observation region. Additional broadening of the spectrum occurs when the transducers become small or focusing is used.

However, the mean frequency shift of the spectrum is not affected by this broadening.

The dependency of the power spectrum to the ultrasonic illumination of the artery is discussed. It is found that careful positioning of the transducer is necessary, so that the whole arterial lumen is observed, if the mean velocity of flow through the artery is to be measured.

The validity of three mean velocity estimators is proved from the scattering theory developed in the previous paragraph. The expectation values give a vector weighted average of the velocity field in the observation region.

When electronic noise is present in the signal, the output of the mean velocity estimators are reduced. For this reduction to be less than 10 % the signal to noise power ratio has to be greater than 9.55 dB, which is achieved in most cases.

Practical realizations of the estimators are discussed.

6. VARIANCES OF MEAN VELOCITY ESTIMATORS.

In this chapter we study the variances of the mean velocity estimators given in the previous chapter. The analysis is based on the theory of filtering and spectral estimation of stochastic processes. A brief review of the necessary results is given in Appendix V together with derivations of expressions for the zeroth and first moment of a power spectrum estimate.

Estimator I is essentially a correlator. We especially emphasize the influence on the estimator variance of the velocity profile and integration time of the averaging filter.

In calculating correlation functions limiting and quantization of the signals are commonly used to reduce complexity of signal processing [81], [82], [83], [84].

As we have already seen for estimator II, by the use of hard limiting for one of the signals, the multiplier may be avoided. The hard limited signal may also be delayed in a digital shift register if an estimate of the value of the correlation function for non-zero lag is wanted. Limiting of the signals before correlation also reduces the effect of noisy variations in signal amplitude as discussed by Yerbury [82].

As follows from Bussgang's relation, Section 5.2C, the form of the correlation function when one of the signals is distorted by a nonlinear device, will be the same as that without distortion. If both signals pass through a nonlinear device, the correlation function will be distorted too. However, for a vast class of nonlinearities, including amplitude limiters, a peak in the undistorted correlation function [75] also gives a peak in the distorted correlation function. For target detection in radar and sonar it is only the peak which is interesting, and the distortion, therefore, has a negligible effect.

When the input signal to noise ratio of one or both of the signals is small, the correlation coefficient, i.e. the correlation function divided by the square root of the signal variances, is small. In this case the form of the correlation function with limiters in both channels will be approximately the same as that without limiters [75]. This is a common situation when correlation is used.

The uncertainty of an estimate we define as the square root of the variance. The variance will decrease with increasing integration time, T, of the correlator and will asymptotically be $\sim T^{-1}$ when $T \to \infty$ (strong filtering, Section 6.2D). The uncertainty is then $\sim T^{-\frac{1}{2}}$.

The variance in the estimate of the correlation function is changed when nonlinear devices are inserted in one or both channels. Yerbury has concidered the case for low values of the input signal to noise ratio. He finds that the variance is increased by $\pi/4$ when a hard limiter is inserted in one of the channels. This means that to obtain the same variance as without limiter $4/\pi$ longer integration time is needed (strong filtering). Using a limiter in both channels, the variance is increased by $\pi^2/6$. Similar values are given for a discrete time correlator by Hagen [81] and Hagen and Farley [84].

In our case we are estimating the correlation function at zero lag with a signal to noise ratio at both channels well above 0 dB. The normalized correlation coefficient is therefore of the order of unity and the approximations of Yerbury and Hagen & al. are not satisfactory.

When the correlation coefficient between the signals is high, i.e. negligible noise, our calculations show that the correlator variance is reduced when hard clipping in one of the channels is introduced. This is the situation in our case. However, the velocity is obtained as the ratio between two variables which cannot be estimated without uncertainty. Our calculations then show that although the variance of denumerator and numerator themselves are reduced by hard clipping in one channel, the variance of their ratio is increased. It is found that for estimator II the avariance is increased by 1.14 for parabolic profile, compared to that of estimator I. The ratio of the uncertainties is $\sqrt{1.14} = 1.07$. For the blunt profile with $p = 16$ the factors are 1.27 and 1.13 respectively.

In all our calculations Gaussian properties of the doppler signal is assumed in accordance with the discussion in Section 5.2C.

6.1. Introduction.

Realizations of the mean velocity estimators in the previous chapter may be written as

$$\tilde{\bar{v}} = k\,\frac{p}{q} \qquad k = \frac{c}{\omega_0 |\vec{n}_T + \vec{n}_R|} \qquad \text{a)}$$

where p and q take different forms for the three estimators.

$$\left.\begin{aligned} p &= \int_{\mathbb{R}} d\tau h_p(t-\tau)\dot{e}_2(\tau)e_1(\tau) \\ q &= \int_{\mathbb{R}} d\tau h_q(t-\tau)e_1^2(\tau) \end{aligned}\right\} \quad \text{Estimator type I} \qquad \text{b)}$$

$$\left.\begin{aligned} p &= \int_{\mathbb{R}} d\tau h_p(t-\tau)\dot{e}_2(\tau)\operatorname{sgn} e_1(\tau) \\ q &= \int_{\mathbb{R}} d\tau h_q(t-\tau)\left|e_1(\tau)\right| \end{aligned}\right\} \quad \text{Estimator type II} \qquad \text{c)} \tag{6.1}$$

$$\left.\begin{aligned} p &= -\int_{\mathbb{R}} d\omega i\omega\tilde{G}_{e_2e_1}(\omega) \quad \text{or} \quad \int_{\mathbb{R}} d\omega\cdot\omega\tilde{G}_{\hat{e}\hat{e}}(\omega) \\ q &= \int_{\mathbb{R}} d\omega\tilde{G}_{e_1e_1}(\omega) \quad \text{or} \quad \int_{\mathbb{R}} d\omega\,\tilde{G}_{\hat{e}\hat{e}}(\omega) \end{aligned}\right\} \quad \text{Estimator type III} \qquad \text{d)}$$

$$\mathbb{R} = (-\infty, \infty)$$

$\tilde{}$ indicates the finite time estimate of both the velocity and the power spectrum. h_p and h_q are the impulse responses of the denumerator and numerator filters respectively.

In Section 5.3 we have shown how the division may be eliminated by an AGC-circuit in estimator type I and II. It is difficult to analyze the variance in this case because of the nonlinearity of the AGC-loop. We shall, therefore, only indicate by an example how the variance in this case is related to that when using a division.

We shall study the functioning of estimator I and II for plug flow in a straight vessel. The quadrature components of the doppler signal are given in Eq. (5.57) and may be rewritten as

$$\begin{aligned} e_1(t) &= a(t)\cos[\vec{q}\,\vec{v}\,t + \theta(t)] \\ e_2(t) &= a(t)\sin[\vec{q}\,\vec{v}\,t + \theta(t)] \end{aligned} \tag{6.2}$$

$a(t)$ and $\theta(t)$ are lowpass with bandwidth proportional to the inverse transit time. In taking derivatives we may, therefore, neglect the time variation of these functions compared to the doppler oscillation given by $\vec{q}\,\vec{v}\,t$. This gives

$$\dot{e}_2(t) = \vec{q}\,\vec{v}\,e_1(t) \tag{6.3}$$

and the estimator outputs are

$$\tilde{\tilde{v}}_I(t) = \frac{\vec{q}\vec{v}}{q} \frac{\int d\tau h_p(t-\tau)e_1^2(\tau)}{\int d\tau h_q(t-\tau)e_1^2(\tau)}$$

$$\tilde{\tilde{v}}_{II}(t) = \frac{\vec{q}\,\vec{v}}{q} \frac{\int d\tau h_p(t-\tau)|e_1(\tau)|}{\int d\tau h_q(t-\tau)|e_1(\tau)|} \tag{6.4}$$

If h_p and h_q are identical, the time dependent term will disappear and a sharp estimate of the velocity component of $\vec{v}$ along $\vec{q}$ with zero variance results. In fact the zero variance will also occur if no filters are used. This is rather strange, but as we shall see later, this is a special situation for plug flow. In this case the numerator and the denumerator, having nonzero variances themselves, are so correlated that their ratio has zero variance. This is not true for more realistic velocity profiles, e.g. like those shown in Figure 5.3. These profiles converge towards plug flow when $p \to \infty$, but numerical calculations show that the convergence of the estimator variance to zero with increasing p is very slow. For p increasing from 2 to 16 gives a decrease in estimator variance of less than 70 %.

When an AGC-circuit is used instead of the division, this adjusts $a(t)$ so that the variation around the mean value is decreased. If the AGC-loop is made too fast, distortion of the doppler oscillation is introduced. Thus it is not possible to obatin zero variance of $a(t)$ and a nonzero variance of the velocity estimate will result in the case of plug flow as well. However, experiments indicate that the difference in the variance between the estimator with AGC and division is very small for realistic velocity profiles. (Section 7.2B).

When the complete estimator in Eq. (5.85) is used, we get

$$\langle \dot{e}_2 e_1 \rangle - \langle \dot{e}_1 e_2 \rangle = \vec{q}\,\vec{v}\,a^2(t)$$

$$\langle e_1^2 \rangle + \langle e_2^2 \rangle = a^2(t) \tag{6.5}$$

In this estimator the rapid doppler oscillations are eliminated before filtering. When an averaging filter with bandwidth 20 Hz is used, the doppler oscillations will have frequencies 10-100 times this bandwidth. The variances at the output of the filters will, therefore, be the same for this estimator and the simplified estimator of Arts & Roevros.

We now return to the general situation. In Section 5.2 we have proved that $k\langle p\rangle/\langle q\rangle$ gives a vector weighted average of the velocity in the observation region. The important question is now: To what extent does the estimators given in Eq. (6.1) give an approximate value of this expression.

We shall answer this question by calculating the expectation value and variance of $\tilde{\bar{v}}$.

A good estimator should be unbiased, i.e. $\tilde{\bar{v}} = \hat{\bar{v}}$, and have a small variance. The requirement of being unbiased is not very strict since the bias has to be compared to the variance. Thus an estimator with bias may be preferred among unbiased estimators if it has smaller variance and the bias is small compared to the square root of the variance.

To simplify the calculations, we assume that the relative variance of the numerator in Eq. (6.1) is small. We may then approximate the division by a series expansion. To the second order we get

$$\tilde{\bar{v}} = k\,\frac{\langle p\rangle}{\langle q\rangle}\,[1 - ab + b^2] \qquad a = \frac{\delta p}{\langle p\rangle} \qquad b = \frac{\delta q}{\langle q\rangle} \tag{6.6}$$

where we have used the notation

$$\delta x = x - \langle x\rangle \tag{6.7}$$

From this expression we calculate the expectation value and variance of the mean velocity estimate

$$\langle\tilde{\bar{v}}\rangle = k\,\frac{\langle p\rangle}{\langle q\rangle}\,\{1 - \langle ab\rangle + \langle b^2\rangle\} \qquad \text{a)}$$

$$\langle\delta\tilde{\bar{v}}^2\rangle = k^2\,\frac{\langle p\rangle^2}{\langle q\rangle^2}\,\{\langle a^2\rangle - 2\langle ab\rangle + \langle b^2\rangle\} \qquad \text{b)} \tag{6.8}$$

$$\text{Relative bias:}\quad \frac{\langle\tilde{\bar{v}}\rangle - \hat{\bar{v}}}{\hat{\bar{v}}} = \langle b^2\rangle - \langle ab\rangle \qquad \text{c)}$$

$$\text{Relative variance:}\quad \frac{\langle\delta\tilde{\bar{v}}^2\rangle}{\hat{\bar{v}}^2} = \langle a^2\rangle - 2\langle ab\rangle + \langle b^2\rangle \qquad \text{d)}$$

Thus for the estimators to be unbiased we must have $\langle ab\rangle = \langle b^2\rangle$.

In the following we shall relate these expressions to the velocity field and the integration time of the filters.

6.2. Analytical expressions for estimator variances.

We shall make use of the results presented in Appendix V, VI and VII. We also study the variances for time steady velocity profiles only. This implies wide sense stationarity of the doppler signal as discussed in Section 5.1D. We also assume Gaussian properties of the signals and the effect of diffusion is neglected. The denumerator and numerator filters and integration times are assumed to be identical. Especially we use the dc-normalization of the filter responces as given in Eq. (V.6).

A. Estimator type I.

For p and q defined in Eq. (6.1b) we obtain by the use of Eq. (V.4)

$$\langle p(t)\rangle = \int_{\mathbb{R}} d\tau h(\tau)\langle \dot{e}_2 e_1\rangle = \langle \dot{e}_2 e_1\rangle = R_{\dot{e}_2 e_1}(0)$$
$$\langle q(t)\rangle = \int_{\mathbb{R}} d\tau h(\tau)\langle e_1{}^2\rangle = \langle e_1{}^2\rangle = R_{e_1 e_1}(0) \tag{6.9}$$

where the normalization of Eq. (V.6) for h is used. We thus see that the numerator and denumerator for themselves are unbiased, although their ratio may still not be. For $\langle a^2\rangle$, $\langle b^2\rangle$ and $\langle ab\rangle$ given in Eq. (6.6-8) we obtain by the use of Eq. (V.4)

$$\langle a^2\rangle = \int_{\mathbb{R}\times\mathbb{R}} d\tau_1 d\tau_2 h(\tau_1)h(\tau_1 - \tau_2)\zeta_{\dot{e}_2 e_1,\dot{e}_2 e_1}(\tau_2)$$

$$\langle b^2\rangle = \int_{\mathbb{R}\times\mathbb{R}} d\tau_1 d\tau_2 h(\tau_1)h(\tau_1 - \tau_2)\zeta_{e_1{}^2,e_1{}^2}(\tau_2) \tag{6.10}$$

$$\langle ab\rangle = \int_{\mathbb{R}\times\mathbb{R}} d\tau_1 d\tau_2 h(\tau_1)h(\tau_1 - \tau_2)\zeta_{\dot{e}_2 e_1,e_1{}^2}(\tau_2)$$

where we have defined the normalized covariance functions

$$\zeta_{\dot{e}_2e_1,\dot{e}_2e_1}(\tau) = \frac{C_{\dot{e}_2e_1,\dot{e}_2e_1}(\tau)}{R^2_{\dot{e}_2e_1}(0)}$$

$$\zeta_{\dot{e}_2e_1,e_1^2}(\tau) = \frac{C_{\dot{e}_2e_1,e_1^2}(\tau)}{R_{\dot{e}_2e_1}(0)R_{e_1e_1}(0)} \tag{6.11}$$

$$\zeta_{e_1^2,e_1^2}(\tau) = \frac{C_{e_1^2,e_1^2}(\tau)}{R^2_{e_1e_1}(0)}$$

Assuming Gaussian properties we can relate the covariance functions above to the correlation functions of the quadrature components.

$$C_{\dot{e}_2e_1,\dot{e}_2e_1}(\tau_1,\tau_2) = \langle\dot{e}_2(\tau_1)e_1(\tau_1)\dot{e}_2(\tau_2)e_1(\tau_2)\rangle$$

$$- \langle\dot{e}_2(\tau_1)e_1(\tau_1)\rangle\langle\dot{e}_2(\tau_2)e_1(\tau_2)\rangle \tag{6.12}$$

The fourth moment of four Gaussian variables may be expressed by second moments, [75]. The following result is then obtained

$$C_{\dot{e}_2e_1,\dot{e}_2e_1}(\tau_1,\tau_2) = R_{\dot{e}_2\dot{e}_2}(\tau_1,\tau_2)R_{e_1e_1}(\tau_1,\tau_2) + R_{\dot{e}_2e_1}(\tau_1,\tau_2)R_{e_1\dot{e}_2}(\tau_1,\tau_2) \tag{6.13}$$

Similarly we obtain for the other covariance functions

$$C_{\dot{e}_2e_1,e_1^2}(\tau_1,\tau_2) = 2R_{\dot{e}_2e_1}(\tau_1,\tau_2)R_{e_1e_1}(\tau_1,\tau_2)$$

$$C_{e_1^2,e_1^2}(\tau_1,\tau_2) = 2R^2_{e_1e_1}(\tau_1,\tau_2) \tag{6.14}$$

For wide sense stationary processes we obtain

$$C_{\dot{e}_2e_1,\dot{e}_2e_1}(\tau) = R_{e_1e_1}(\tau)R_{\dot{e}_2\dot{e}_2}(\tau) + R_{\dot{e}_2e_1}(\tau)R_{e_1\dot{e}_2}(\tau)$$

$$C_{\dot{e}_2e_1,e_1{}^2}(\tau) = 2R_{\dot{e}_2e_1}(\tau)R_{e_1e_1}(\tau) \qquad (6.15)$$

$$C_{e_1{}^2e_1{}^2}(\tau) = 2R^2_{e_1e_1}(\tau)$$

The correlations functions above are found in Eq. (5.35). To obtain the correlation functions for the derivatives we use the formulas of Appendix VI. We note that the derivative of $R(\vec{\zeta})$ will be small compared to that of $\cos\psi(\vec{\zeta})$. We also have $\dot{R}(\vec{\zeta}) = 0$ for $\tau = 0$.

We thus obtain

$$R_{\dot{e}_2e_1}(0) = R_{e_1\dot{e}_2}(0) = \frac{|\alpha|^2}{2}\int d^3\xi R^2(\vec{\xi})\langle n^2(\vec{\xi})\rangle\vec{v}(\vec{\xi})\nabla\psi(\vec{\xi})$$

$$(6.16)$$

$$R_{e_1e_1}(0) = R_{e_2e_2}(0) = \frac{|\alpha|^2}{2}\int d^3\xi R^2(\vec{\xi})\langle n^2(\vec{\xi})\rangle$$

From the mean velocity estimator formula of Eq. (5.87) we have

$$R_{\dot{e}_2e_1}(0) = \hat{v}\,\overline{|\nabla\psi|}\,R_{e_1e_1}(0)$$

where $\qquad\qquad\qquad\qquad\qquad\qquad\qquad\qquad\qquad\qquad\qquad\qquad\qquad (6.17)$

$$\overline{|\nabla\psi|} = \frac{\omega_0}{c}\,|\vec{n}_T + \vec{n}_R|$$

is the approximate length of $\nabla\psi$ and $\hat{v}$ is the average of the velocity component along $\nabla\psi$.

Let R be normalized so that its mean value over some wave lengths is unity. We define the sensitivity volume, S, of the observation region in analogy to the sensitivity length in Eq. (5.46)

$$S = \int d^3\xi R^2(\vec{\xi}) \qquad (6.18)$$

The mean fluctuation, $\overline{\langle n^2\rangle}$, in the observation region is defined by

$$S\overline{\langle n^2\rangle} = \int d^3\xi R^2(\vec{\xi})\langle n^2(\vec{\xi})\rangle \qquad (6.19)$$

The normalized covariance function of Eq. (6.11) may now be written as

$$\zeta_{\dot{e}_2e_1,\dot{e}_2e_1}(\tau) = \rho_{e_1e_1}(\tau)\rho_{\dot{e}_2\dot{e}_2}(\tau) + \rho_{\dot{e}_2e_1}(\tau)\rho_{e_1\dot{e}_2}(\tau)$$

$$\zeta_{\dot{e}_2e_1,e_1^2}(\tau) = 2\rho_{\dot{e}_2e_1}(\tau)\rho_{e_1e_1}(\tau) \tag{6.20}$$

$$\zeta_{e_1^2,e_1^2}(\tau) = 2\rho^2_{e_1e_1}(\tau)$$

where we have defined the following functions, whose expressions are obtained from Eq. (5.35) neglecting $\dot{R}(\zeta)$

$$\rho_{\dot{e}_2\dot{e}_2}(\tau) = \frac{R_{\dot{e}_2\dot{e}_2}(\tau)}{\hat{\bar{v}}^2|\nabla\psi|^2R_{e_1e_1}(0)} = \frac{R_{\dot{e}_2\dot{e}_2}(\tau)}{R^2_{\dot{e}_2e_1}(0)/R_{e_1e_1}(0)}$$

$$= \int d^3\xi\tilde{R}(\vec{\xi})\tilde{R}(\vec{\zeta})[\tilde{\vec{v}}(\vec{\xi})\nabla\tilde{\psi}(\vec{\xi})][\tilde{\vec{v}}(\vec{\zeta})\nabla\tilde{\psi}(\vec{\zeta})]<\tilde{n}^2(\vec{\xi})>\cos[\psi(\vec{\zeta}) - \psi(\vec{\xi})]$$

$$\rho_{\dot{e}_2e_1}(\tau) = \rho_{e_1\dot{e}_2}(\tau) = \frac{R_{\dot{e}_2e_1}(\tau)}{R_{\dot{e}_2e_1}(0)} \tag{6.21}$$

$$= \int d^3\xi\tilde{R}(\vec{\xi})\tilde{R}(\vec{\zeta})\tilde{\vec{v}}(\vec{\zeta})\nabla\tilde{\psi}(\vec{\zeta})<n^2(\vec{\xi})>\cos[\psi(\vec{\zeta}) - \psi(\vec{\xi})]$$

$$\rho_{e_1e_1}(\tau) = \frac{R_{e_1e_1}(\tau)}{R_{e_1e_1}(0)} = \int d^3\xi\tilde{R}(\vec{\xi})\tilde{R}(\vec{\zeta})<\tilde{n}^2(\vec{\xi})>\cos[\psi(\vec{\zeta}) - \psi(\vec{\xi})]$$

where we have defined the following normalized functions

$$\tilde{R}(\vec{\xi}) = \frac{R(\vec{\xi})}{\sqrt{S}} \qquad \tilde{\vec{v}}(\vec{\xi}) = \frac{\vec{v}(\vec{\xi})}{\hat{\bar{v}}}$$

$$<\tilde{n}^2(\vec{\xi})> = \frac{<n^2(\vec{\xi})>}{\overline{<n^2>}} \qquad \tilde{\psi}(\vec{\xi}) = \frac{\psi(\vec{\xi})}{|\nabla\psi|} \tag{6.22}$$

We may here remark that

$$\rho_{e_1e_1}(0) = \rho_{\dot{e}_2e_1}(0) = 1 \tag{6.23}$$

while

$$\rho_{\dot{e}_2\dot{e}_2}(0) = \frac{\widehat{\overline{v^2}}}{\hat{\bar{v}}^2} \tag{6.24}$$

where

$$\widehat{\overline{v^2}} = \int d^3\xi \tilde{R}^2(\vec{\xi}) \langle \tilde{n}^2(\vec{\xi})\rangle [\vec{v}(\vec{\xi}) \nabla\tilde{\psi}(\vec{\xi})]^2$$

$$\hat{\bar{v}} = \int d^3\xi \tilde{R}^2(\vec{\xi}) \langle \tilde{n}^2(\vec{\xi})\rangle \vec{v}(\vec{\xi}) \nabla\tilde{\psi}(\vec{\xi}) \tag{6.25}$$

The normalization for $\rho_{e_1e_1}$ and $\rho_{\dot{e}_2e_1}$ is, therefore, the usual one used to define the correlation coefficient between two stochastic processes. The normalization used for $\rho_{\dot{e}_2\dot{e}_2}$ is only "natural" in our context where the normalization is determined by that we are interested in relative variances and covariances of p and q.

B. Estimator type II.

For p and q defined in Eq. (6.1c) we obtain by the use of Eq. (V.4)

$$\langle p(t)\rangle = \int_{\mathbb{R}} d\tau h(\tau) \langle \dot{e}_2 \operatorname{sgn} e_1\rangle = \langle \dot{e}_2 \operatorname{sgn} e_1\rangle = R_{\dot{e}_2 \operatorname{sgn} e_1}(0)$$

$$\langle q(t)\rangle = \int_{\mathbb{R}} d\tau h(\tau) \langle |e_1|\rangle = \langle |e_1|\rangle = R_{e_1 \operatorname{sgn} e_1}(0) \tag{6.26}$$

Thus the numerator and denumerator are unbiased for themselves as for estimator type I.

For $\langle a^2\rangle$, $\langle b^2\rangle$ and $\langle ab\rangle$ defined in Eqs. (6.6-8) we obtain

$$\langle a^2\rangle = \int_{\mathbb{R}\times\mathbb{R}} d\tau_1 d\tau_2 h(\tau_1) h(\tau_1 - \tau_2) \zeta_{\dot{e}_2 \operatorname{sgn} e_1, \dot{e}_2 \operatorname{sgn} e_1}(\tau_2)$$

$$\langle b^2\rangle = \int_{\mathbb{R}\times\mathbb{R}} d\tau_1 d\tau_2 h(\tau_1) h(\tau_1 - \tau_2) \zeta_{|e_1|,|e_1|}(\tau_2) \tag{6.27}$$

$$\langle ab\rangle = \int_{\mathbb{R}\times\mathbb{R}} d\tau_1 d\tau_2 h(\tau_1) h(\tau_1 - \tau_2) \zeta_{\dot{e}_2 \operatorname{sgn} e_1, |e_1|}(\tau_2)$$

where the normalized covariance functions are defined by

$$\zeta_{\dot{e}_2 \text{sgn}\, e_1, \dot{e}_2 \text{sgn}\, e_1}(\tau) = \frac{C_{\dot{e}_2 \text{sgn}\, e_1, \dot{e}_2 \text{sgn}\, e_1}(\tau)}{R^2_{\dot{e}_2 \text{sgn}\, e_1}(0)}$$

$$\zeta_{\dot{e}_2 \text{sgn}\, e_1, |e_1|}(\tau) = \frac{C_{\dot{e}_2 \text{sgn}\, e_1, |e_1|}(\tau)}{R_{\dot{e}_2 \text{sgn}\, e_1}(0) R_{e_1 \text{sgn}\, e_1}(0)} \tag{6.28}$$

$$\zeta_{|e_1|, |e_1|}(\tau) = \frac{C_{|e_1|, |e_1|}(\tau)}{R^2_{e_1 \text{sgn}\, e_1}(0)}$$

From Eq. (5.88) we then obtain

$$R_{\dot{e}_2 \text{sgn}\, e_1}(0) = \frac{R_{\dot{e}_2 e_1}(0)}{\sqrt{\frac{\pi}{2} R_{e_1 e_1}(0)}}$$

$$R_{e_1 \text{sgn}\, e_1}(0) = \langle |e_1| \rangle = \sqrt{\frac{2}{\pi} R_{e_1 e_1}(0)} \tag{6.29}$$

For zero lag the covariance functions above may be caculated directy

$$C_{\dot{e}_2 \text{sgn}\, e_1, \dot{e}_2 \text{sgn}\, e_1}(0) = \langle \dot{e}_2(t) \,\text{sgn}\, e_1(t) \dot{e}_2(t) \,\text{sgn}\, e_1(t) \rangle$$

$$- \langle \dot{e}_2(t) \,\text{sgn}\, e_1(t) \rangle \langle \dot{e}_2(t) \,\text{sgn}\, e_1(t) \rangle \tag{6.30}$$

We here note that $(\text{sgn}\, e_1)^2 = 1$, and using Eq. (6.29) we obtain

$$C_{\dot{e}_2 \text{sgn}\, e_1, \dot{e}_2 \text{sgn}\, e_1}(0) = R_{\dot{e}_2 \dot{e}_2}(0) - \frac{2}{\pi} \frac{R^2_{\dot{e}_2 e_1}(0)}{R_{e_1 e_1}(0)} \tag{6.31}$$

The normalized covariance function for zero lag is, Eqs. (6.29), (6.28) and (6.21)

$$\zeta_{\dot{e}_2 \text{sgn}\, e_1, \dot{e}_2 \text{sgn}\, e_1}(0) = \frac{\pi}{2} \rho_{\dot{e}_2 \dot{e}_2}(0) - 1 \tag{6.32}$$

Similarly we obtain for the other covariance functions of Eq. (6.24) at zero lag

$$\zeta_{\dot{e}_2 \mathrm{sgn}\, e_1, |e_1|}(0) = \frac{\pi}{2} - 1$$
$$\zeta_{|e_1|,|e_1|}(0) = \frac{\pi}{2} - 1 \tag{6.33}$$

The covariance functions for non-zero lag are calculated in Appendix VII and we merely write down the results here

$$\zeta_{\dot{e}_2 \mathrm{sgn}\, e_1, \dot{e}_2 \mathrm{sgn}\, e_1}(\tau) = \rho_{\dot{e}_2\dot{e}_2}(\tau) \arcsin \rho_{e_1e_1}(\tau) + \frac{1 + \rho^2_{\dot{e}_2e_1}(\tau) - 2\rho_{\dot{e}_2e_1}(\tau)\rho_{e_1e_1}(\tau)}{\sqrt{1 - \rho^2_{e_1e_1}(\tau)}} - 1$$

$$\zeta_{\dot{e}_2 \mathrm{sgn}\, e_1, |e_1|}(\tau) = \rho_{\dot{e}_2e_1}(\tau) \arcsin \rho_{e_1e_1}(\tau) + \sqrt{1 - \rho^2_{e_1e_1}(\tau)} - 1 \tag{6.34}$$

$$\zeta_{|e_1|,|e_1|}(\tau) = \rho_{e_1e_1}(\tau) \arcsin \rho_{e_1e_1}(\tau) + \sqrt{1 - \rho^2_{e_1e_1}(\tau)} - 1$$

C. Estimator type III.

We assume that Eq. (5.15) holds. In accordance with Appendix V an estimate of $\hat{G}_{\hat{e}\hat{e}}(\omega)$ may be

$$\hat{G}_{\hat{e}\hat{e}}(\omega) = \frac{2}{T} \{E_1^* E_1(\omega) + iE_1^*(\omega)E_2(\omega)\} \tag{6.35}$$

where $E_i(\omega)$, $i = 1,2$, is the finite time Fouriertransform of $e_i(t)$ in the interval $[t - T, t]$. From (V.23-26) we obtain

$$\begin{aligned} p_a(t) &= \int_{\mathbb{R}} d\omega\, \omega \hat{G}_{\hat{e}\hat{e}}(\omega) \\ &= \frac{4\pi}{T} \int_{t-T}^{t} d\tau [-i\dot{e}_1(\tau)e_1(\tau) + \dot{e}_2(\tau)e_1(\tau)] \\ &\quad - \frac{2\pi}{T} [e_2(t)e_1(t) - e_2(t - T)e_1(t - T) - ie_1{}^2(t) + ie_1{}^2(t - T)] \end{aligned}$$

By integration of the first term we obtain

$$p_a(t) = \frac{4\pi}{T}\int_{t-T}^{t} d\tau\ \dot{e}_2(\tau)e_1(\tau) - \frac{2\pi}{T}\,[e_2(t)e_1(t) - e_2(t - T)e_1(t - T) + ie_1^{\,2}(t) - ie_1^{\,2}(t - T)] \qquad a)$$

$$(6.36)$$

$$q_a(t) = \int_{\mathbb{R}} d\omega\ \hat{G}_{\hat{e}\hat{e}}(\omega) = \frac{4\pi}{T}\int_{t-T}^{t} d\tau[e_1^{\,2}(\tau) + ie_1(\tau)e_2(\tau)] \qquad b)$$

We could also start with the simplified expression of Eq. (5.101) and use the following estimates

$$\hat{G}_{e_1e_2}(\omega) = \frac{1}{T}\,E_1^*(\omega)E_2(\omega)$$

$$\hat{G}_{e_1e_1}(\omega) = \frac{1}{T}\,|E_1(\omega)|^2 \qquad (6.37)$$

The numerator and denumerator estimates would then be

$$p_b(t) = \int_{\mathbb{R}} d\omega\ i\omega\ \hat{G}_{e_1e_2}(\omega) = \frac{2\pi}{T}\int_{t-T}^{t} d\tau\ \dot{e}_2(\tau)e_1(\tau) - \frac{\pi}{T}\,[e_2(t)e_1(t) - e_2(t - T)e_1(t - T)] \qquad a)$$

$$(6.38)$$

$$q_b(t) = \int_{\mathbb{R}} d\omega\ G_{e_1e_1}(\omega) = \frac{2\pi}{T}\int_{t-T}^{t} d\tau\ e_1^{\,2}(\tau) \qquad b)$$

The denumerator and numerator of the above two variants of estimator III are unbiased

$$\langle p_a(t)\rangle = 2\langle p_b(t)\rangle = 4\pi R_{\dot{e}_2e_1}(0)$$

$$\langle q_a(t)\rangle = 2\langle q_b(t)\rangle = 4\pi R_{e_1e_1}(0) \qquad (6.39)$$

We have used stationarity which implies $\langle e_1^{\,2}(t)\rangle = \text{const}$ and Eq. (5.12) which implies $\langle e_2(t)e_1(t)\rangle = 0$.

The finite time estimates of these two estimators will have different stochastic variations around the mean values and for the a) variant complex values of p_a and q_a will occur. It would therefore be reasonable to use only the real part of Eq. (6.35) as an estimate of $\hat{G}_{\hat{e}\hat{e}}(\omega)$. The ratio between the magnitude of the boundary terms and the integral in Eqs. (6.36a) and (6.38a) will, however, be $\sim T^{-1}$. When the velocity is substantially different from zero (i.e. $R_{\dot{e}_2 e_1}(0) \neq 0$), the integral term will dominate.

$e_1(\tau)e_2(\tau)$ may also be neglected in Eq. (6.36b) since $R_{e_1 e_2}(0) = 0$ while $R_{e_1 e_1}(0) \neq 0$. Under these approximations the two variants of the estimators are identical.

We shall calculate the variance of the approximated expressions. We then note that we can write

$$\begin{aligned} p(t) &= 2\pi \int_{\mathbb{R}} d\tau \; h(t - \tau)\dot{e}_2(\tau)e_1(\tau) \\ q(t) &= 2\pi \int_{\mathbb{R}} d\tau \; h(t - \tau)e_1^{\,2}(\tau) \end{aligned} \tag{6.40}$$

where

$$h(t) = \begin{cases} \frac{1}{T} & 0 < t < T \\ 0 & \text{else} \end{cases}$$

These expressions are the same as that of Estimator I and we can use Eq. (6.10). The integrals are of the form

$$\int_{\mathbb{R}\times\mathbb{R}} d\tau_1 d\tau_2 h(\tau_1)h(\tau_1 - \tau_2)F(\tau_2) = \frac{1}{T^2}\int_0^T d\tau_1 \int_{\tau_1 - T}^{\tau_1} d\tau_2 F(\tau_2)$$

The last integral may be treated as a function of τ_1 and by partial integration the following expression for the integral is obtained.

$$\frac{1}{T}\int_{-T}^{T} d\tau [1 - \frac{|\tau|}{T}] \; F(\tau)$$

$\langle a^2\rangle$, $\langle b^2\rangle$ and $\langle ab\rangle$ for estimator III may now be written

$$\langle a^2\rangle = \frac{1}{T}\int_{-T}^{T} d\tau [1 - \frac{|\tau|}{T}]\ \zeta_{\dot{e}_2e_1,\dot{e}_2e_1}(\tau)$$

$$\langle b^2\rangle = \frac{1}{T}\int_{-T}^{T} d\tau [1 - \frac{|\tau|}{T}]\ \zeta_{e_1{}^2,e_1{}^2}(\tau) \qquad (6.41)$$

$$\langle ab\rangle = \frac{1}{T}\int_{-T}^{T} d\tau [1 - \frac{|\tau|}{T}]\ \zeta_{\dot{e}_2e_1,e_1{}^2}(\tau)$$

where the covariance functions are given in Eq. (6.20).

D. Strong filtering.

We denote the filtering strong when the integration time of the filters are much longer than the correlation time of the input signals. In the frequency domain this means that the filter bandwidth is much smaller than the bandwidth of the input signal.

In our case the filter bandwidth is 20 Hz, while the bandwidth of $\dot{e}_2e_1$ or $\dot{e}_2\mathrm{sgn}\ e_1$ will be twice that of the doppler signals which for parabolic profiles ranges from 1000-5000 Hz. The filtering is thus cleareIy strong.

When a pulsed meter with small observation region is used, or the flow profile is very flat, the bandwidth of the doppler signal is determined by the transit time (Example II, Section 5.1D). For the filtering to be strong in this case the integration time has to be large compared to the transit time.

As shown in Eq. (V.10) the variance of the filter output will be $\sim T^{-1}$. For estimator I and III we may express the integral of the covariance functions by integrals of the power spectra

$$\langle a^2\rangle = \frac{1}{T}\int_{\mathbb{R}} d\tau\ h^2(\tau)\int_{\mathbb{R}} d\tau\{\rho_{e_1e_1}(\tau)\rho_{\dot{e}_1\dot{e}_1}(\tau) + \rho^2_{\dot{e}_2e_1}(\tau)\}$$

$$= \frac{1}{(2\pi)^2T}\int_{\mathbb{R}} d\omega|H(\omega)|^2\int_{\mathbb{R}} d\omega\ \omega^2\{G^2_{e_1e_1}(\omega) + |G_{e_1e_2}(\omega)|^2\}$$

$$= \frac{1}{4(2\pi)^2T}\int_{\mathbb{R}} d\omega|H(\omega)|^2\int_{\mathbb{R}} d\omega\ \omega^2|G_{\hat{e}\hat{e}}(\omega)|^2$$

$$\langle b^2\rangle = \frac{2}{T}\int_{\mathbb{R}} d\tau\ h^2(\tau)\int_{\mathbb{R}} d\tau\ \rho^2_{e_1e_1}(\tau) = \frac{2}{(2\pi)^2T}\int_{\mathbb{R}} d\omega|H(\omega)|^2\int_{\mathbb{R}} d\omega\ G^2_{e_1e_1}(\omega)$$

$$\langle ab\rangle = \frac{2}{T}\int_R d\tau\, h^2(\tau)\int_R d\tau\, \rho_{\dot{e}_2 e_1}(\tau)\rho_{e_1 e_1}(\tau) \tag{6.42}$$

$$= \frac{2}{(2\pi)^2 T}\int_R d\omega |H(\omega)|^2 \int_R d\omega\, i\omega G_{e_2 e_1}(\omega) G_{e_1 e_1}(\omega)$$

where we have used Eq. (5.15) and the following relation for Fourier transforms

$$\int_{\mathbb{R}} dt\, f(t)g(t) = \frac{1}{2\pi}\int_{\mathbb{R}} d\omega\, F^*(\omega)G(\omega)$$

Due to the nonlinearities no such simple relations exists for estimator II.

Examination shows that when the profile becomes flat (p > 3) for the blunt profile), the transit time will have a dominating effect in the above formulas so that the approximate form of $G_{\hat{e}\hat{e}}$ in Eq. (5.47) is not useful.

6.3. Discussions and numerical examples.

We shall compare the variances of the three types of estimators. It is found that estimator I and III are equal provided pure integration is used for averaging in estimator I. Estimator I and II are compared by approximate analytical discussions and by numerical calculations for the blunt profiles in Figure 5.3.

A. Comparison between estimator type I and III.

When the integration time is so large that the approximations of Eq. (6.40) are valid, estimator I will be identical to estimator III when the averaging filter of Eq. (6.40) is used. We also note that the variance of the mean frequency estimate of the spectrum is independent of the spectral window used in the spectrum estimate (Appendix V).

B. Comparison between estimator type I and II.

We first discuss the case when the integration time is so short that the impulse responses of the filters may be approximated by δ-functions. In this case we get

Estimator type I:

$$\langle a^2\rangle = \zeta_{\dot{e}_2 e_1, \dot{e}_2 e_1}(0) = \frac{\overline{\hat{v}^2}}{\hat{\bar{v}}^2} + 1$$

$$\langle b^2\rangle = \zeta_{e_1^2, e_1^2}(0) = 2 \tag{6.43}$$

$$\langle ab\rangle = \zeta_{\dot{e}_2 e_1, e_1^2}(0) = 2$$

These results are given directly by Eqs. (6.10), (6.20) and (6.23-24). From Eqs. (6.27), (6.32-33) and (6.23-24) we obtain

Estimator type II

$$\langle a^2\rangle = \zeta_{\dot{e}_2 \mathrm{sgn}\, e_1, \dot{e}_2 \mathrm{sgn}\, e_1}(0) = \frac{\pi}{2}\frac{\overline{\hat{v}^2}}{\hat{\bar{v}}^2} - 1$$

$$\langle b^2\rangle = \zeta_{|e_1|, |e_1|}(0) = \frac{\pi}{2} - 1 \approx .57 \tag{6.44}$$

$$\langle ab\rangle = \zeta_{\dot{e}_2 \mathrm{sgn}\, e_1, |e_1|}(0) = \frac{\pi}{2} - 1 \approx .57$$

We see that the variances of the denumerator and numerator by themselves are much greater for estimator type I than for estimator type II. This is due to the ordinary multiplication used in estimator I. By this it is the square of the amplitude of the doppler signal, that enters into the filters while for estimator II it is only the absolute value of the amplitude which enters, Eq. (6.4). In this way variations in the magnitude of this amplitude has much greater effect in the first estimator compared to the second. (See Section 7.2B).

For the approximation of Eq. (6.6) to hold $\langle b^2\rangle$ has to be small. The signals, therefore, has to be filtered so that the magnitude of $\langle b^2\rangle$ has decreased from the values of Eqs. (6.43-44). However, to proceed with an analytical discussion which gives insight, although the numerical results are not fully correct, we insert Eqs. (6.43-44) into Eq. (6.8)

Estimator type I

Relative bias: 0

Relative variance: $\dfrac{\overline{\hat{v}^2}}{\hat{\bar{v}}^2} - 1$ (6.45)

Estimator type II.

Relative bias: $\quad 0$

$$\text{Relative variance:} \quad \frac{\pi}{2}\left[\frac{\widehat{\overline{v^2}}}{\hat{\bar{v}}^2} - 1\right] \tag{6.46}$$

The bias of both estimators are zero in this approximation. The variance of estimator type II is, however, $\pi/2$ greater than that of estimator type I. This is interesting since it occurs although the variances of p and q are smallest for the last estimator. It is thus the covariance between p and q which is responsible for this result (Eq. (6.8)).

The uncertainty in the velocity estimate is the square root of the variance. The ratio of the uncertainty of estimator I to estimator II is then $\sqrt{\pi/2} \approx 1.25$ in this approximation.

When the averaging time of the filters is so long that the approximation of Eq. (6.6) is acceptable, numerical calculations show that the ratios of the estimator uncertainties are reduced to 1.07 for parabolic profile and 1.13 for the blunt profile with $p = 16$ (Example II).

For plug flow $\widehat{\overline{v^2}} = \hat{\bar{v}}^2$ and the relative variances will be zero as already stated in Section 6.1.

For the blunt profiles in Example II, Section 5.1D, we obtain with $\langle n^2 \rangle$ constant and $R(\vec{\xi})$ given in Eq. (5.43).

$$\begin{array}{lll} \text{Estimator I} & \text{Relative variance:} & \dfrac{1}{p+1} \\[2ex] \text{Estimator II} & \text{Relative variance:} & \dfrac{\pi}{2}\,\dfrac{1}{p+1} \end{array} \tag{6.47}$$

When the integration time is not negligible we shall only discuss the case of plug flow analytically. For the blunt profile analytical solutions may be given for $p = 1,2$. These are, however, complicated and we, therefore, prefer to give the numerical results only. We shall in the following also specialize to the filter in Eq. (6.40). The variances are then given by Eq. (6.41) for estimator type I and by substituting the appropriate expressions for the covariance functions, Eq. (6.34), the expressions for estimator type II is obtained.

Example I. Plug flow in a straight vessel.

The correlation functions of the doppler signal for plug flow in a straight vessel are given in Eq. (5.62). The normalized correlation functions will be, neglecting the last term

$$
\begin{aligned}
&\rho_{e_1e_1}(\tau) = \rho_{e_2e_2}(\tau) = f(\frac{\tau}{T_t})\cos \vec{q}\,\vec{v}\,\tau \\
&\rho_{e_1e_2}(\tau) = -\rho_{e_2e_1}(\tau) = f(\frac{\tau}{T_t})\sin \vec{q}\,\vec{v}\,\tau \\
&\rho_{\dot{e}_2\dot{e}_2}(\tau) = f(\frac{\tau}{T_t})\cos \vec{q}\,\vec{v}\,\tau \\
&\rho_{\dot{e}_2e_1}(\tau) = \rho_{e_1\dot{e}_2}(\tau) = f(\frac{\tau}{T_t})\cos \vec{q}\,\vec{v}\,\tau
\end{aligned}
\tag{6.48}
$$

The covariance functions of estimator type I will then be

$$
\begin{aligned}
&\zeta_{\dot{e}_2e_1,\dot{e}_2e_1}(\tau) = 2f^2(\frac{\tau}{T_t})\cos^2 \vec{q}\,\vec{v}\,\tau \\
&\zeta_{\dot{e}_2e_1,e_1{}^2}(\tau) = 2f^2(\frac{\tau}{T_t})\cos^2 \vec{q}\,\vec{v}\,\tau \\
&\zeta_{e_1{}^2,e_1{}^2}(\tau) = 2f^2(\frac{\tau}{T_t})\cos^2 \vec{q}\,\vec{v}\,\tau
\end{aligned}
\tag{6.49}
$$

From this we have, Eq. (6.41)

$$
\langle a^2\rangle = \langle b^2\rangle = \langle ab\rangle = \frac{2}{T}\int_{-T}^{T} d\tau\left[1 - \frac{|\tau|}{T}\right] f^2(\frac{\tau}{T_t})\cos^2 \vec{q}\,\vec{v}\,\tau \tag{6.50}
$$

When T and T_t are some periods of the doppler signal long, we may approximate $\cos^2 \vec{q}\,\vec{v}\tau = (1 + \cos 2\vec{q}\,\vec{v}\tau)/2$ by 1/2

$$
\langle a^2\rangle = \langle b^2\rangle = \langle ab\rangle = \frac{1}{T}\int_{-T}^{T} d\tau\left[1 - \frac{|\tau|}{T}\right] f^2(\frac{\tau}{T_t}) = A(\frac{T}{T_t})
$$

$$
A(\frac{T}{T_t}) = \begin{cases} 1 - \dfrac{2}{3}\dfrac{T}{T_t} + \dfrac{1}{6}\dfrac{T^2}{T_t{}^2} & \dfrac{T}{T_t} < 1 \\[2ex] \dfrac{T_t}{T}\left[\dfrac{2}{3} - \dfrac{1}{6}\dfrac{T_t}{T}\right] & \dfrac{T}{T_t} > 1 \end{cases} \tag{6.51}
$$

Since $\langle a^2\rangle$, $\langle b^2\rangle$ and $\langle ab\rangle$ are equal, both estimator bias and variance will be zero as already stated in Section 6.1.

As discussed in Example I, Section 5.1D, the doppler signal is an amplitude modulated oscillation at the doppler frequency. This is also given by Eq. (6.2). The bandwidth of the envelope is proportional to the inverse transit time T_t^{-1}, Eq. (5.55), and it is therefore the ratio of T_t to the filter integration time, T, that determines $\langle a^2\rangle$, $\langle b^2\rangle$ and $\langle ab\rangle$.

Since all the functions of Eq. (6.48) are identical, the covariance functions of estimator type II, Eq. (6.34), takes the following form

$$\zeta_{\dot{e}_2 \mathrm{sgn}\, e_1, \dot{e}_2 \mathrm{sgn}\, e_1}(\tau) = \zeta_{\dot{e}_2 \mathrm{sgn}\, e_1, |e_1|}(\tau) = \zeta_{|e_1|,|e_1|}(\tau) = \zeta_{II}(\tau)$$
$$\zeta_{II}(\tau) = \rho_{e_1e_1}(\tau)\arcsin\rho_{e_1e_1}(\tau) + \sqrt{1-\rho^2_{e_1e_1}(\tau)} - 1 \tag{6.52}$$

From Eq. (6.41) with the covariance functions of estimator I replaced by those of estimator II we obtain

$$\langle a^2\rangle = \langle b^2\rangle = \langle ab\rangle = \frac{1}{T}\int_{-T}^{T} d\tau \left[1 - \frac{|\tau|}{T}\right]\zeta_{II}(\tau) \tag{6.53}$$

Thus for estimator II also the bias and variance are zero for plug flow as already stated in Section 6.1.

The integral in Eq. (6.53) can only be evaluated numerically. This is done and the result is shown as the upper limit of the variances of estimator II ($p = \infty$) for the blunt profiles in Figure 6.4 - 6. Eq. (6.51) is also shown in these figures as the upper limit of the variances of estimator I. The uncertainty in the velocity estimate (zero) is also indicated in Figure 6.7 as the lower limit of the blunt profiles when $p \to \infty$.

Example II. Blunt velocity profile in a straight circular vessel.

We shall study the estimator variances for the profiles of Example II of Section 5.1D. As there, we assume $\langle n^2\rangle$ to be constant across the vessel. From Eq. (6.25) we obtain

$$\hat{v} = \frac{p}{p+2} v'_0 \qquad \widehat{v^2} = \frac{p^2}{(p+2)(p+1)} {v'_0}^2 \tag{6.54}$$

$v'_0 = v_0 \cos\theta$ where θ is given in Figure 5.2. From Eqs. (6.43-44) we then obtain

$$\zeta_{\dot{e}_2e_1,\dot{e}_2e_1}(0) = \frac{2p + 3}{p + 1} \qquad \zeta_{e_1{}^2,e_1{}^2}(0) = \zeta_{\dot{e}_2e_1,e_1{}^2}(0) = 2$$

$$\zeta_{\dot{e}_2\mathrm{sgn}\ e_1,\dot{e}_2\mathrm{sgn}\ e_1}(0) = \frac{\pi}{2}\frac{p + 2}{p + 1} - 1 \tag{6.55}$$

$$\zeta_{|e_1|,|e_1|}(0) = \zeta_{\dot{e}_2\mathrm{sgn}\ e_1,|e_1|}(0) = \frac{\pi}{2} - 1$$

Numerical calculations for nonzero lag may be performed by the use of Eqs. (6.20-21-34) and Eq. (5.67). This gives for $0 \leq \tau \leq L/v_0$

$$\rho_{\dot{e}_2e_1}(\tau) = \frac{-\dot{\rho}_{e_2e_1}(\tau)}{-\dot{\rho}_{e_2e_1}(0)} = 2\,\frac{p+2}{p}\int_0^1 dx\cdot x(1-x^p)[1 - \frac{v_0\tau}{L}(1-x^p)]\cos[\vec{q}\,\vec{v}_0\tau\,(1-x^p)]$$

$$\rho_{\dot{e}_2\dot{e}_2}(\tau) = \frac{-\ddot{\rho}_{e_2e_2}(\tau)}{(-\dot{\rho}_{e_2e_1}(0))^2/\rho_{e_1e_1}(0)} = 2\left(\frac{p+2}{p}\right)^2\int_0^1 dx\cdot x(1-x^p)^2[1 - \frac{v_0\tau}{L}(1-x^p)]\cos\vec{q}\,\vec{v}_0\tau[1-x^p] \tag{6.56}$$

For $\tau > L/v_0$ the lower integration limit has to be interchanged with $(1 - L/v_0\tau)^p$ as in Eq. (5.66). The values for $\tau < 0$ are obtained from those at $\tau > 0$ since all the functions except ρ_{e1e2} and ρ_{e2e1} are even. These last two functions are odd.

In calculating the derivatives we have neglected the derivative of $1 - \frac{v_0\tau}{L}(1 - x^p)$ since it represents only a slowly varying amplitude modulation of the rapid doppler oscillation cos or sin $\vec{q}\,\vec{v}_0\tau(1 - x^p)$, Figure 5.4 and 5.5.

Numerical calculations of the estimator covariance functions are shown in Figures (6.1-3) for $p = 2, 8, \infty$. We see that the lag τ enters into the formulas as $v_0\tau$ which again is proportional to $\bar{v}\tau$ or τ/T_d where $\bar{v}$ is the mean velocity of flow and T_d is the periode of its corresponding doppler frequency.

The transit length of the observation region is the same as in Figures 5.4-5. As discussed in connection to these figures, the covariance functions for small values of p will be little affected by variations in the transit length since the bandwidth of the doppler signal is dominated by the velocity profile itself. For larger values of p, transit time broadening gives significant contribution to the total bandwidth of the doppler signal, and thus the correlation time increases when the transit length increases.

$\langle a^2\rangle$, $\langle b^2\rangle$ and $\langle ab\rangle$ are found by multiplying the curves of Figures 6.1 6.2 and 6.3 respectively with $\frac{1}{T}[1 - |\tau|/T]$ and then integrating from $-T$ to T (Eq. (6.41)). We then immediately see

I. $\langle a^2\rangle$, $\langle b^2\rangle$ and $\langle ab\rangle$ will be greater for estimator type I than for estimator type II. This is in accordance with the previous discussion. Their envelope also increases monotonously with increasing p. When p increases, the envelope of the estimator correlation functions are limited by the envelope for plug flow, $p = \infty$. Thus $\langle a^2\rangle$, $\langle b^2\rangle$ and $\langle ab\rangle$ tends to an upper limit when $p \to \infty$.

II. For small values of p, variations in the transit length has little effect on $\langle a^2\rangle$, $\langle b^2\rangle$ and $\langle ab\rangle$ since it has little effect on the estimator covariance functions. The sensitivity of these functions to the transit length increases with increasing p. An increase in the transit length gives an increase in the value of $\langle a^2\rangle$, $\langle b^2\rangle$ and $\langle ab\rangle$. This stems from the increase in the correlation time of the doppler signal which increases the envelope of the estimator covariance function for nonzero lag.

III. When $T \ll T_t = L/\bar{v}$, variations in the transit length will have little effect on the value of $\langle a^2\rangle$, $\langle b^2\rangle$ and $\langle ab\rangle$. This is because the variation of the estimator covariance functions within $[-T,T]$ is little affected by changes in the correlation length of the doppler signal. It is the values at the tails of the correlation functions which are mostly affected by changes in the correlation time.
Thus the sensitivity to variations in the transit length increases monotonously as T increases up to a limit for $T \to \infty$.

IV. When $T \gg T_t$ the integration over τ in Eq. (6.41) will simply give the area under the estimator covariance functions. This is the case of strong filtering discussed in Section 6.2D, and $\langle a^2\rangle$, $\langle b^2\rangle$ and $\langle ab\rangle$ will be proportional to T^{-1}.

$\sqrt{\langle a^2\rangle}$, $\sqrt{\langle b^2\rangle}$ and $\sqrt{\langle ab\rangle}$ are shown in Figures 6.4-6 for $p = 2,8,16,\infty$. The square root of the relative variance, the relative uncertainty, of the velocity estimate is shown in Figure 6.7. The relative bias is practically zero.

The discussion in point I above is immediately seen to hold. As in the previous discussion we also see that although the numerator and denumerator variances of estimator type I are greater than those of estimator type II, the variance of the velocity estimate is smaller. When $\langle a^2 \rangle$, $\langle b^2 \rangle$ and $\langle ab \rangle$ tends to an upper limit when $p \to \infty$, the value for plug flow, the velocity variance tends to the lower limit zero. The ratio of the uncertainty of the velocity estimate of estimator II to estimator I is seen to have decreased to approximately 1.1 from the approximate value of $\sqrt{\pi/2}$ estimated at the beginning of this section.

In the practical estimator tested in the experiments of the next chapter we use an averaging filter with 3 real poles at 20 Hz. This gives an attenuation of 9 dB at this frequency. The frequency response of the filter in Eq. (6.40) is

$$e^{-\frac{i\omega T}{2}} \frac{\sin \frac{\omega T}{2}}{\frac{\omega T}{2}} \tag{6.57}$$

The 9 dB bandwidth of this filter is

$$\Delta f_{9dB} \approx \frac{0.7}{T} \tag{6.58}$$

$\Delta f_{9dB} = 20$ Hz gives $T = 35$ ms. A mean velocity of 30 cm/s gives a mean doppler frequency for $f_0 = 2$ MHz of 750 Hz, which gives $T_d = 1.33$ ms. Thus $T/T_d \approx 30$ and the following uncertainties in the estimates of the velocity, denumerator and numerator results for parabolic profile

$$\begin{aligned}
&\frac{\sqrt{\langle \delta\tilde{\bar{v}}^2 \rangle}}{\hat{\bar{v}}} \approx .08 && \text{Estimator I and II} \\
&\sqrt{\langle a^2 \rangle} \approx \begin{cases} .15 & \text{Estimator I} \\ .10 & \text{Estimator II} \end{cases} \\
&\sqrt{\langle b^2 \rangle} \approx \begin{cases} .13 & \text{Estimator I} \\ .07 & \text{Estimator II} \end{cases} \\
&\sqrt{\langle ab \rangle} \approx \begin{cases} .13 & \text{Estimator I} \\ .07 & \text{Estimator II} \end{cases}
\end{aligned} \tag{6.59}$$

We shall return to these values in the next chapter where we experimentally study the estimators.

When the transit length is increased by a factor of two, i.e. $T_t = 20\ T_d$, the variances increase by 3 % for $p = 2$, and 15-20 % for $p = 16$. This illustrates the discussion of point II. It is also interesting to note that although spectral spreading due to finite transit time decreases the accuracy with which we can determine the velocity of one scatterer, the situation is opposite when many scatterers are present such as in blood. We give a physical explanation of this phenomenon in the next section.

C. Relation between variances and the magnitude of the velocity.

Theorem. For a constant geometrical form of a timesteady velocity profile we obtain the following relations in the case of strong filtering, $(T >> T_t)$.

$$\left.\begin{array}{l}\langle a^2\rangle \\ \langle b^2\rangle \\ \langle ab\rangle\end{array}\right\} \sim \frac{1}{\hat{\bar{v}}}$$

$$\frac{\sqrt{\langle\delta\tilde{\bar{v}}^2\rangle}}{\hat{\bar{v}}} \sim \frac{1}{\sqrt{\hat{\bar{v}}}} \qquad (6.60)$$

Proof.

From Eq. (5.39) we see that the lag τ enters into the formulas of the correlation functions as $v\,\tau$. For a constant form of the velocity profile we therefore, by a suitable scaling, may express the estimator covariance functions as functions of $\hat{\bar{v}}\tau$. (By further scaling these may be written as functions of τ/T_d where T_d is the periode of the doppler frequency corresponding to $\hat{\bar{v}}$, as we have already used in Figures 5.4-5 and 6.2-4. By using a filter of the form Eq. (V.9) we see from Eqs. (V.10), (6.10) and (6.27) that we have to evaluate integrals of the form

$$\frac{1}{T}\int_{\mathbb{R}} d\tau_1 h^2(\tau_1) \int_{\mathbb{R}} d\tau_2 f(\hat{\bar{v}}\tau_2)$$

Changing variable of integration

$$\hat{\bar{v}}\tau_2 = x$$

The integrals take the form

$$\frac{1}{\hat{\bar{v}}T}\int_{\mathbb{R}} d\tau_1 h^2(\tau_1) \int_{\mathbb{R}} dx f(x) \qquad (6.61)$$

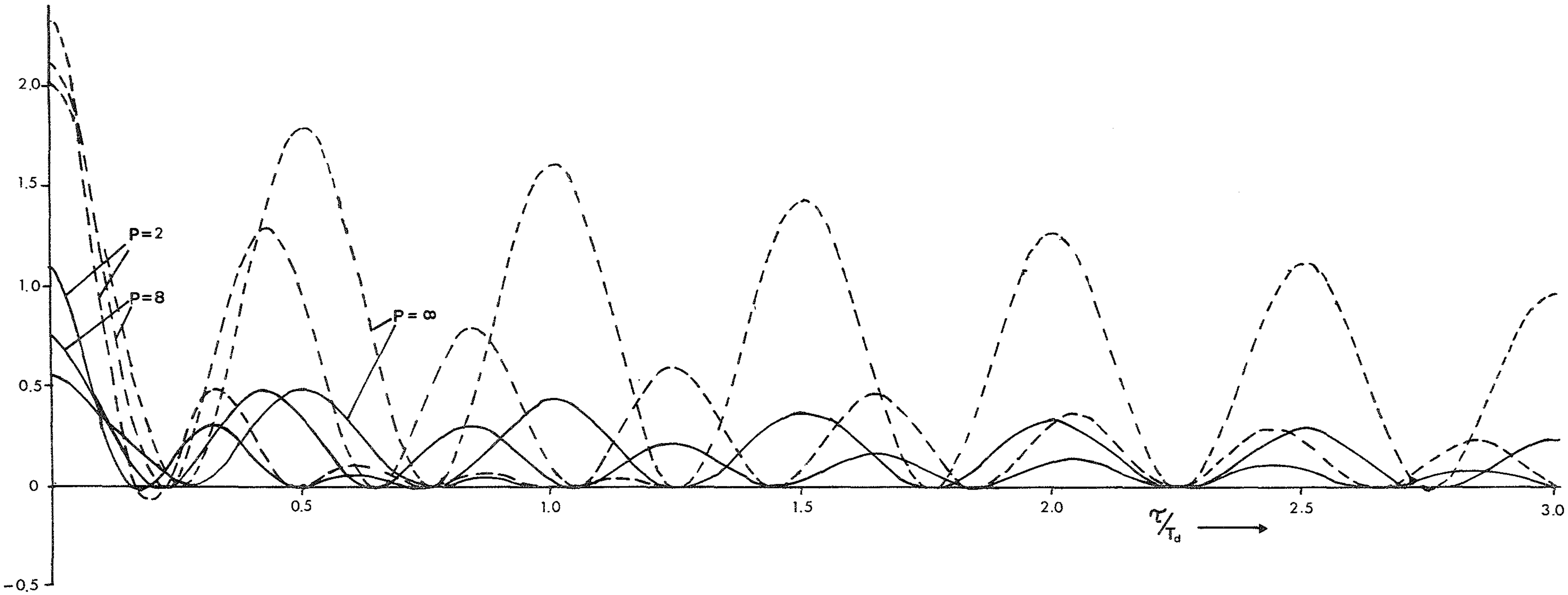

– – – $\int \dot{e}_2 e_1, \dot{e}_2 e_1$ Estimator type I

——— $\int \dot{e}_2 \mathrm{sgn}\, e_1, \dot{e}_2 \mathrm{sgn}\, e_1$ Estimator type II

$L = 10 \dfrac{\lambda}{\cos\theta\, |\vec{n}_T + \vec{n}_R|}$ $T_t = 10\, T_d$

Figure 6.1. Auto covariance function for the estimator denumerator before filtering.

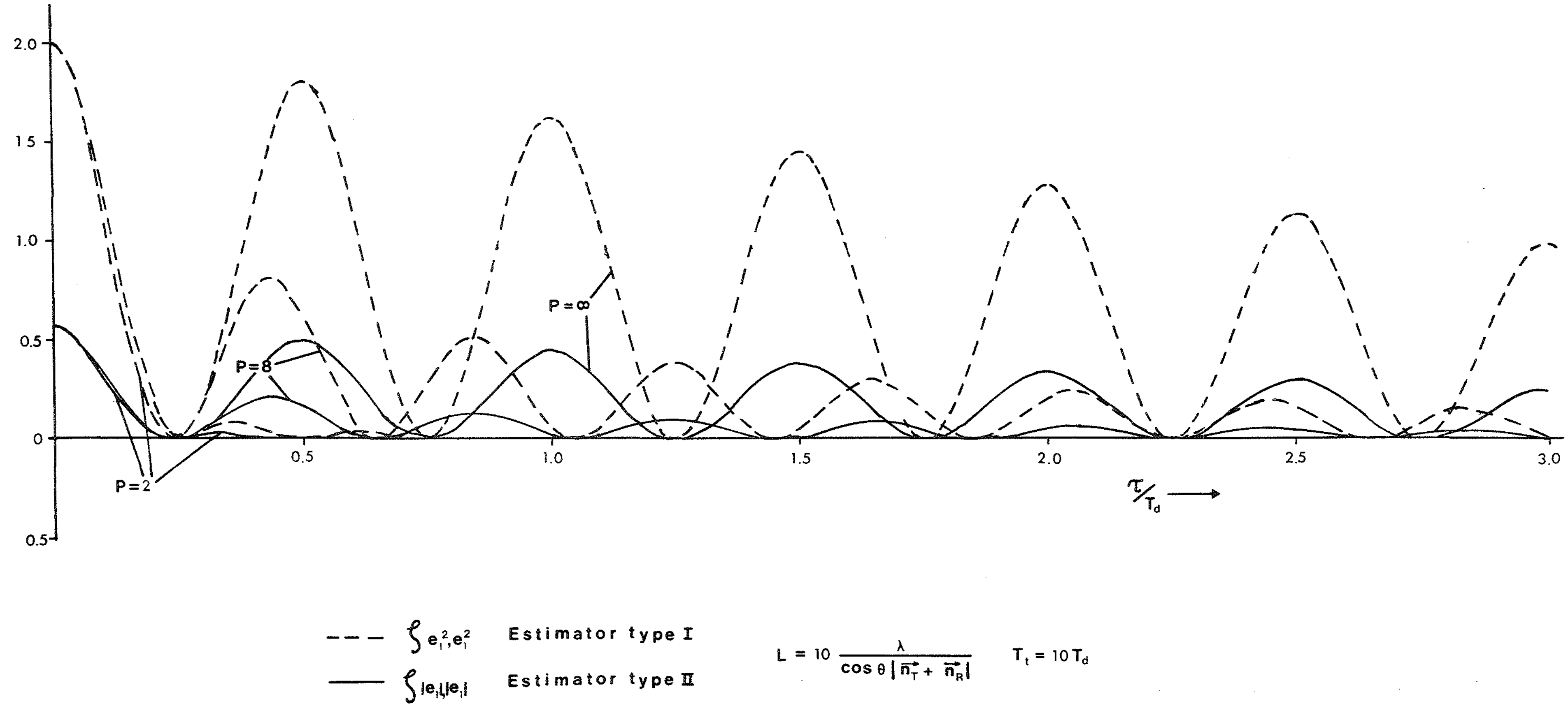

Figure 6.2. Auto covariance function for estimator numerator before filtering.

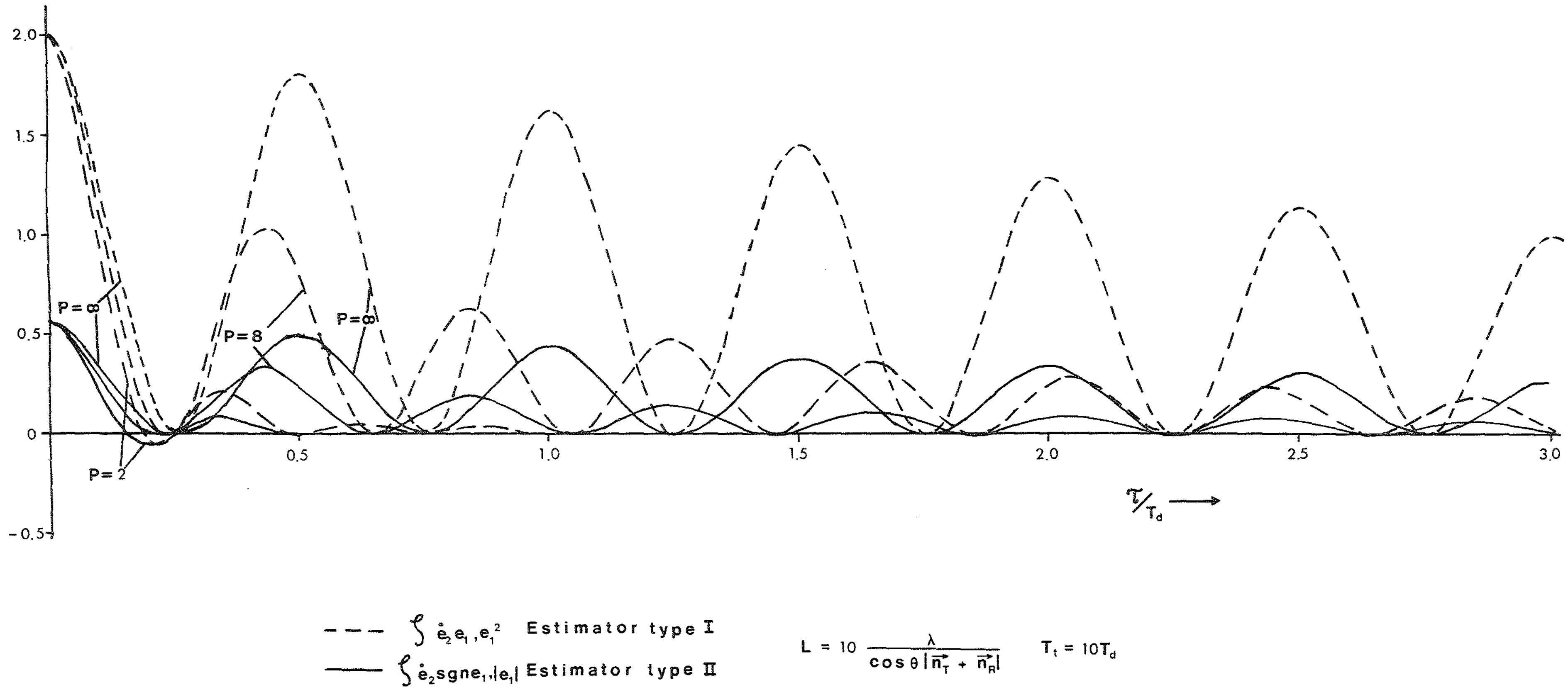

Figure 6.3. Cross covariance function between the estimator numerator and denumerator before filtering.

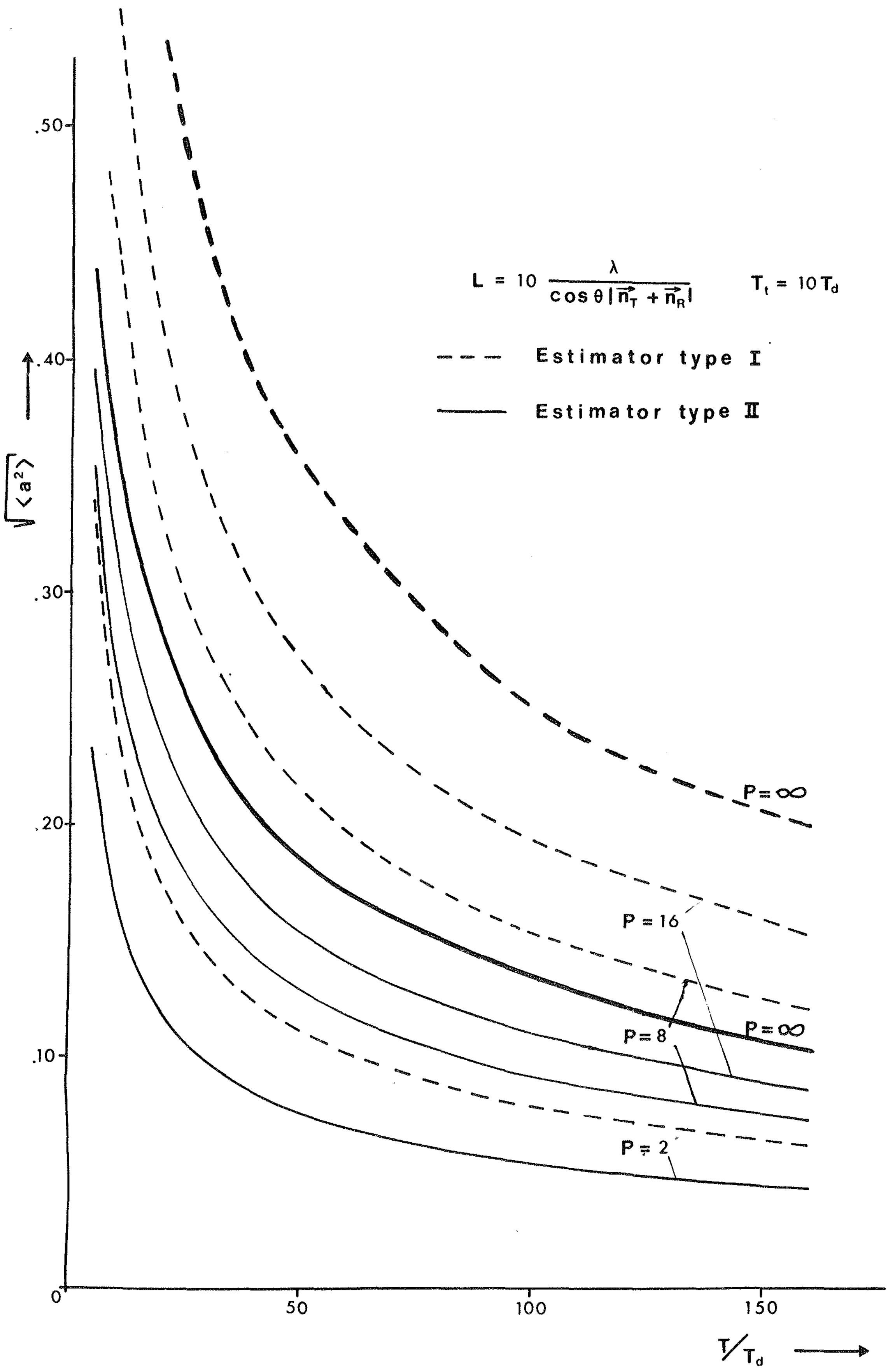

Figure 6.4. Relative variance of estimator denumerator.

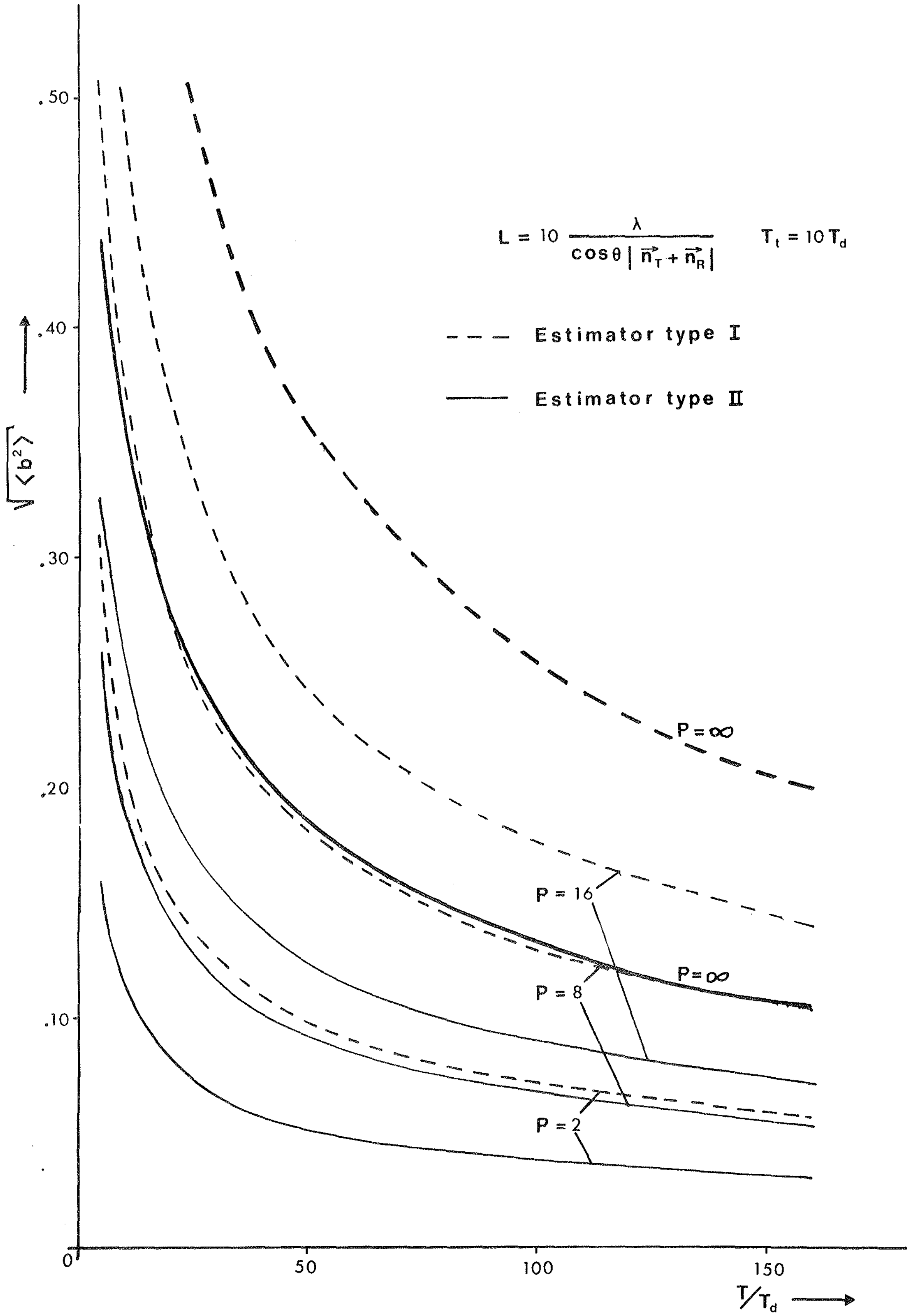

Figure 6.5. Relative variance of estimator numerator.

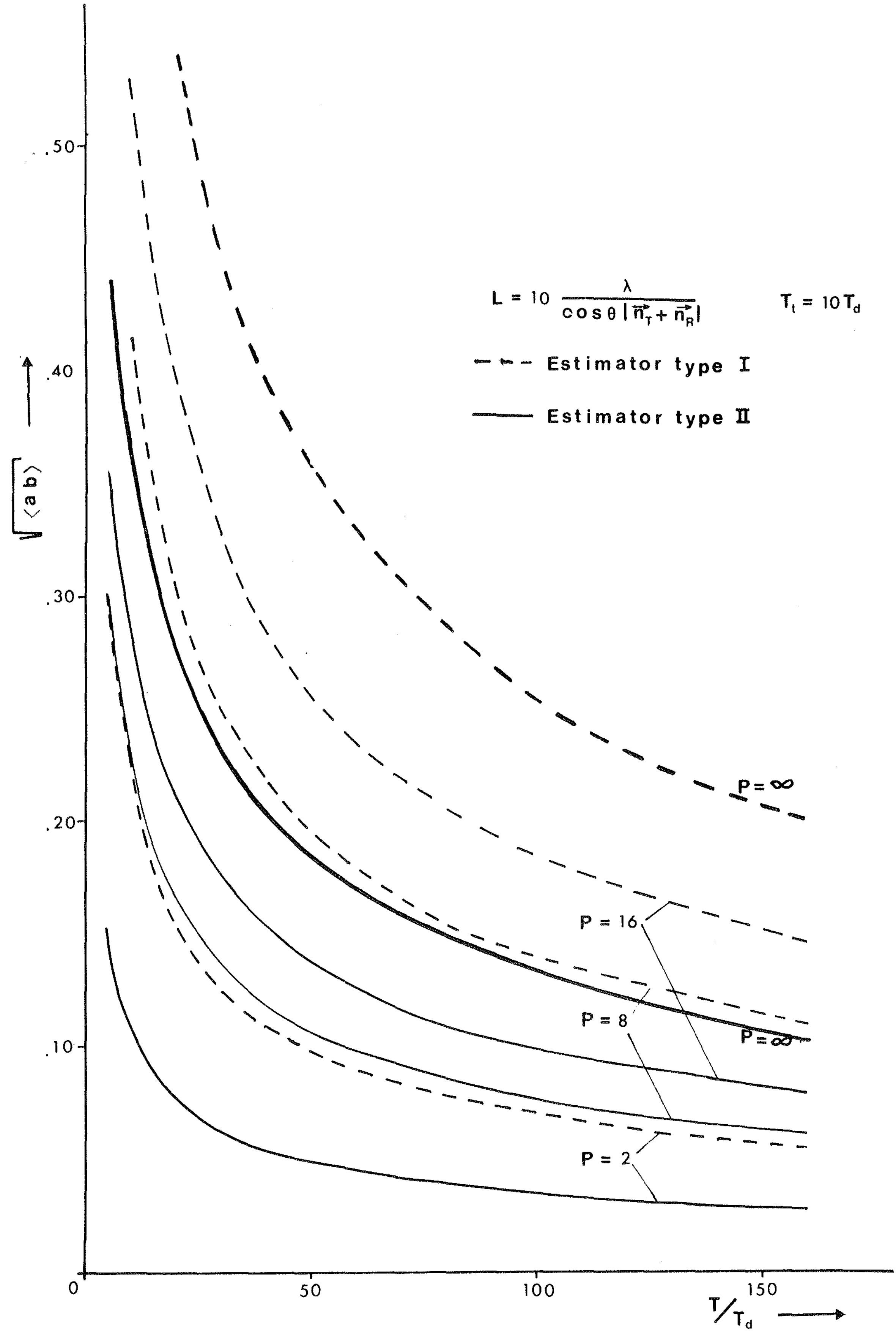

Figure 6.6. Relative covariance between estimator, denumerator and numerator.

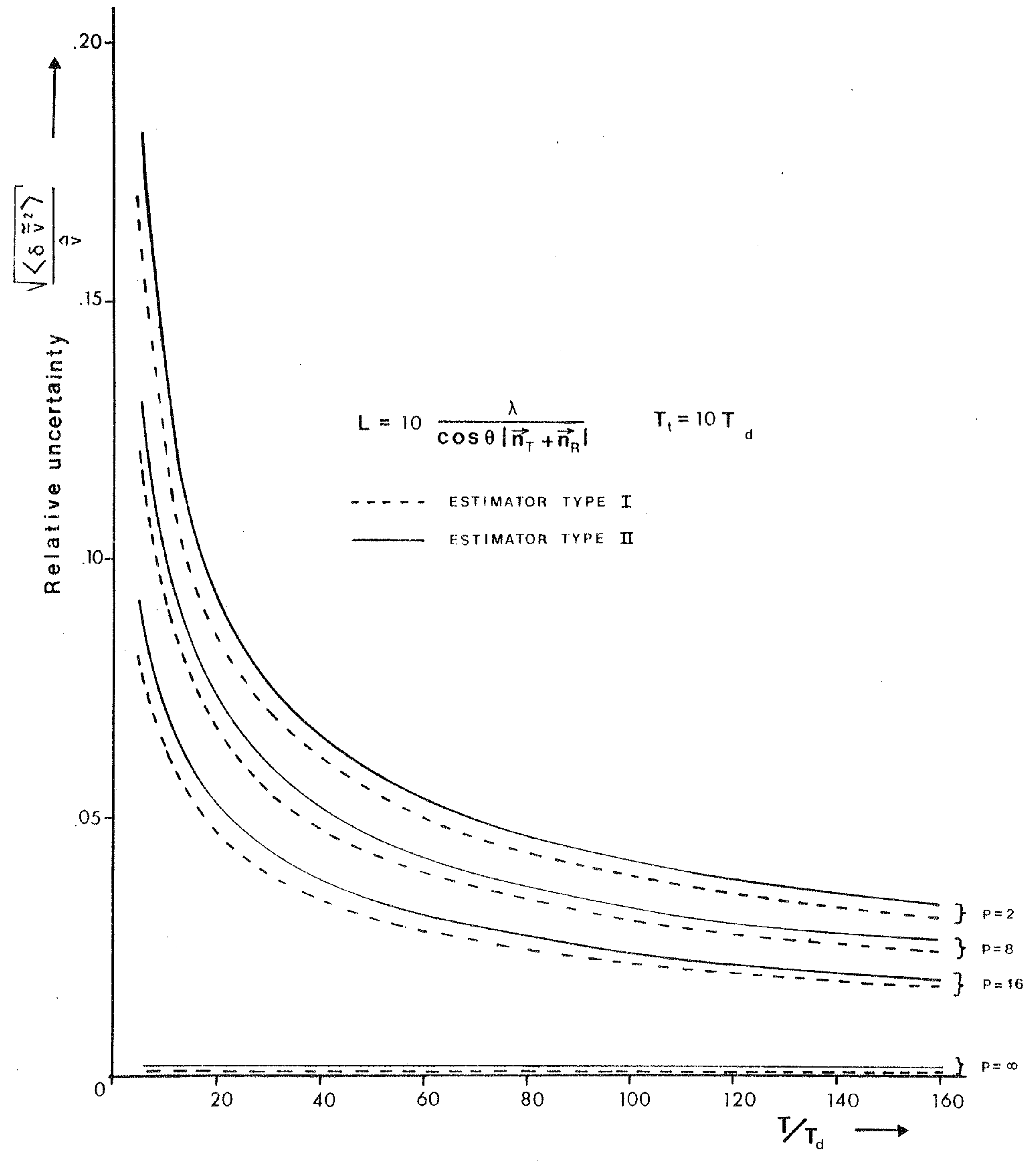

Figure 6.7. Relative uncertainty of velocity estimate.

Thus $\langle a^2\rangle$, $\langle b^2\rangle$ and $\langle ab\rangle$ will be proportional to $\hat{\bar{v}}^{-1}$. From Eq. (6.8) we then see that the relative variance is also proportional to $\hat{\bar{v}}^{-1}$. Thus the relative uncertainty which is the square root of the relative variance will be proportional to $\hat{\bar{v}}^{-\frac{1}{2}}$.

Remark.

If the integration time is not so long that the approximation of Eq. (V.7) may be performed, we see from Eqs. (V.4) and (V.9) that we have to evaluate integrals of the following form

$$\frac{1}{T^2}\int_{\mathbb{R}\times\mathbb{R}} d\tau_1 d\tau_2 h_0\left(\frac{\tau_1}{T}\right)h_0\left(\frac{\tau_1-\tau_2}{T}\right)f(\hat{\bar{v}}\tau_2)$$

and by a change in the variables of integration $r = \hat{\bar{v}}\tau_1$, $s = \hat{\bar{v}}\tau_2$ we obtain

$$\frac{1}{(\hat{\bar{v}}T)^2}\int_{\mathbb{R}\times\mathbb{R}} drds h_0\left(\frac{r}{\hat{\bar{v}}T}\right)h_0\left(\frac{r-s}{\hat{\bar{v}}T}\right)f(s) \tag{6.62}$$

Thus it is $\hat{\bar{v}}T$ that determines the variances.

The physical reason for this is that the total bandwidth of the doppler signal is proportional to $\hat{\bar{v}}$. In the time domain this implies that the correlation time of the doppler signal is inversely proportional to $\hat{\bar{v}}$. This means that the stochastical variations in the amplitude of the signal become "faster", which in a loose way may be described as having a shorter "mean periode", see Figure 7.12,as $\hat{\bar{v}}$ increases.

When the doppler signal is squared or we form $\dot{e}_2 e_1$, the short-time mean value (i.e. averaging performed over a periode $\sim \bar{f}_0^{-1}$) will see stochastical variations with "mean frequency" $\sim \hat{\bar{v}}$. Thus it is the value of the integration time relative to $\hat{\bar{v}}$ which determines the variances.

D. Effect of noise on estimator variance.

The effect of noise on the estimator performance is discussed in Section 5.2E. The electronic noise is uncorrelated with the doppler signal and has a frequency spectrum with zero mean frequency, i.e. $\langle \dot{w}_2 w_1\rangle = 0$. Thus the expectation value of the denumerator is not affected by this type of noise. However, the variance of the denumerator is increased since the finite time estimate of $\langle \dot{w}_2 w_1\rangle$ will not be identically zero.

For the numerator the expectation value is affected by this noise as discussed in Section 5.2E, and the variance will be increased as for the denumerator. Since w_2 and w_1 are fully uncorrelated, the ratio of these two expressions will see an increased variance. Due to the hard limiter in estimator II the variance of this estimator will increase more by noise than that of estimator I. However, for the estimators to be useful, it is shown in Section 5.2E that the signal to noise ratio has to be above 10 dB, and in this case the uncertainties in the estimates are determined by the stochastic nature of the signals themselves. A signal to noise ratio above this value is obtained in most cases.

6.4. Summary.

Analytical expressions for the variances of the mean velocity estimators in Chapter 5 has been given. The effect of using AGC instead of division is discussed by an example. It is indicated that the variance of an estimator with AGC is greater than of one with division when the velocity field is nearly flat in the observation region. For normal velocity fields, however, the experiments of Section 7.2B show that the difference is negligible.

Estimator type I and III are identical provided integration with uniform weight is used for averaging in estimator I.

The variances of estimator I and II are compared and it is found that the variance of estimator II is only slightly greater than that of estimator I. When AGC is used instead of division, the experiments of Section 7.2B show that the situation is reversed although the difference is negligible. The variance of estimator II will also increase more when noise is present in the signal than that of estimator I. The signal to noise ratio in practical measurements is, however, so good that this drawback has no practical implications.

The integration time, T, of the averaging filter will in most cases be so long that the filtering is strong. The variances will then be $\sim T^{-1}$. They will also be $\sim \hat{\bar{v}}^{-1}$, for constant form of the velocity profile. This implies that the uncertainty in the velocity estimate is $\sim \hat{\bar{v}}^{-\frac{1}{2}}$, which is demonstrated experimentally in Section 7.2D.

7. APPARATUS AND EXPERIMENTS

In this chapter we briefly describe the pulsed wave doppler meter which is developed. The velocity estimating capabilities of the instrument is tested in laboratory experiments both by steady and pulsatile flow. Both estimator type I and II are tested and we especially study the influence of the AGC-bandwidth on the estimator linearity and variance.

The instrument has also been tested on 18 persons for measuring aortic flow. A scanning method is used to obtain the velocity profile in the aortic arc.

7.1. PEDOF - Pulsed Echo DOppler Flow velocity meter.

A block diagram of the instrument is shown in Figure 7.1. The receiver amplifier has 70 dB gain with a 40 dB AGC capability, and a 3 dB bandwidth of 280 kHz. As discussed in Chapter 2, this will give a minimum longitudinal resolution of 3 mm. For the special application of aortic flow velocity measurement, the bandwidth could be decreased to 100 kHz, improving the signal to noise ratio with a tolerable decrease in the resolution to 7.5 mm.

The impedance of the transducer is raised to 50 Ω by a broad-band transformer. This is the characteristic impedance of the coax cable used as rf transmission line. Over 280 kHz this gives a source rms noise voltage of 0.48 μV into 50 Ω. The preamplifier has a noise figure of 2 dB which gives an equivalent rms input noise voltage of 0.6 μV into 50 Ω. For a 20 dB signal to noise ratio a rms signal input voltage of 6 μV is necessary.

The quadrature demodulator, which is described in Section 5.1, is followed by a video amplifier of 20 dB gain and a bandwidth of 200 kHz. After the sample and hold buffer, the amplitude of the signal is observed and an AGC-signal is fed back to the rf-amplifier to assure maximum amplitude at the sampling position without clipping.

The signal received from slowly moving targets is removed by the highpass filters which may be selected by a front panel control, switch B. These filters are followed by lowpass filters which remove the high frequency components introduced by the sampling. The sample filters are selected by switch A1, which is mechanically connected to switch A2, which in turn selects the repetition frequency in the generator unit, Figure 7.2. For both highpass and lowpass filters 4 pole Tchebychef response is used.

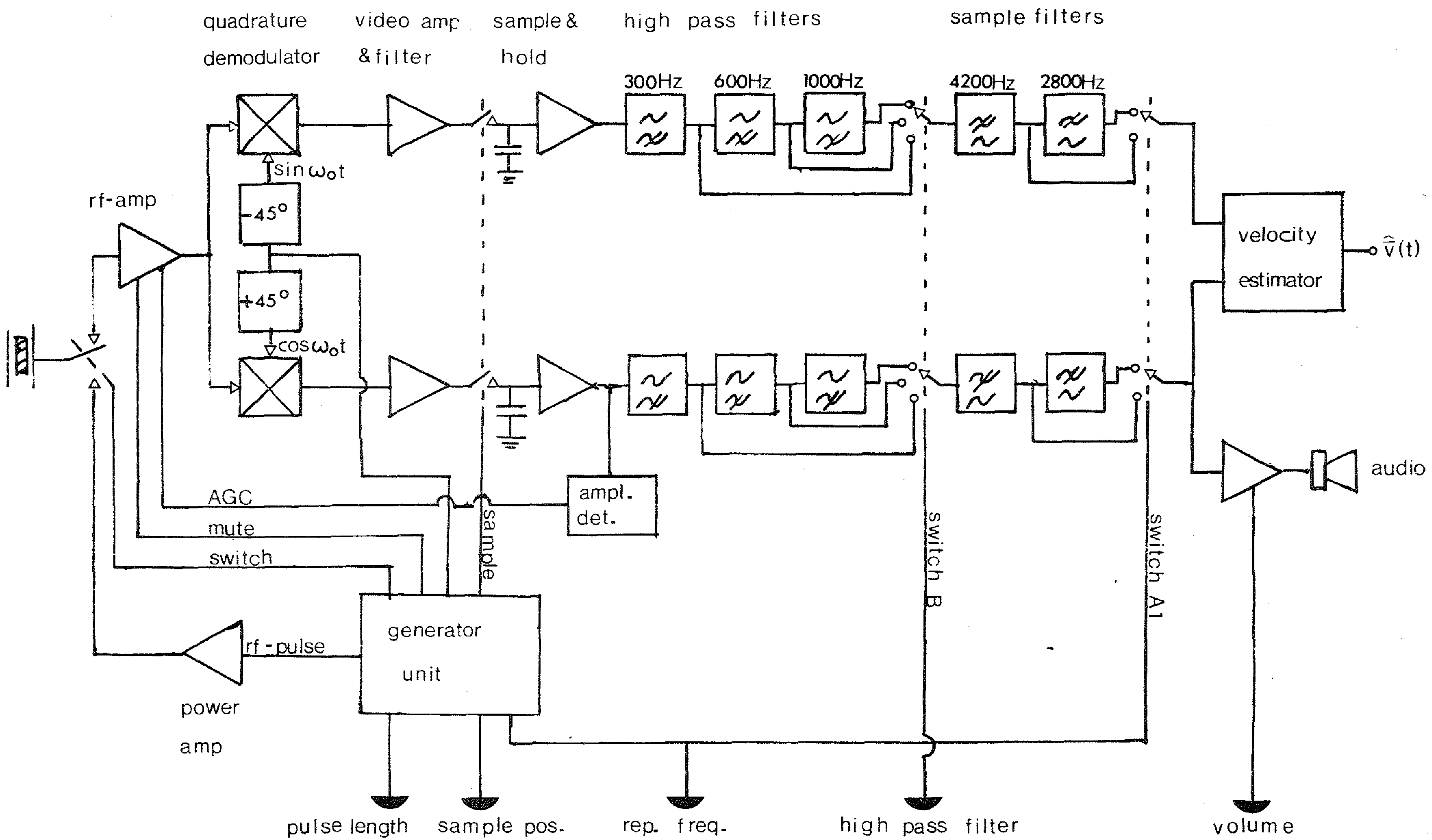

Figure 7.1. Block diagram for PEDOF.

The signal is then fed to the velocity estimator which is described in Section 5.3. Via a loudspeaker the doppler signal is made audible.

The generator unit is shown in Figure 7.2. A freerunning 1.95 MHz oscillator drives a counter which divides the frequency by 200 or 300, selected by the switch A2. This gives a repetition frequency of 9.75 kHz and 6.5 kHz which in turn gives a maximum range and maximum measurable velocity of 7.3 cm/1.7 m/s and 11 cm/1.1 m/s.

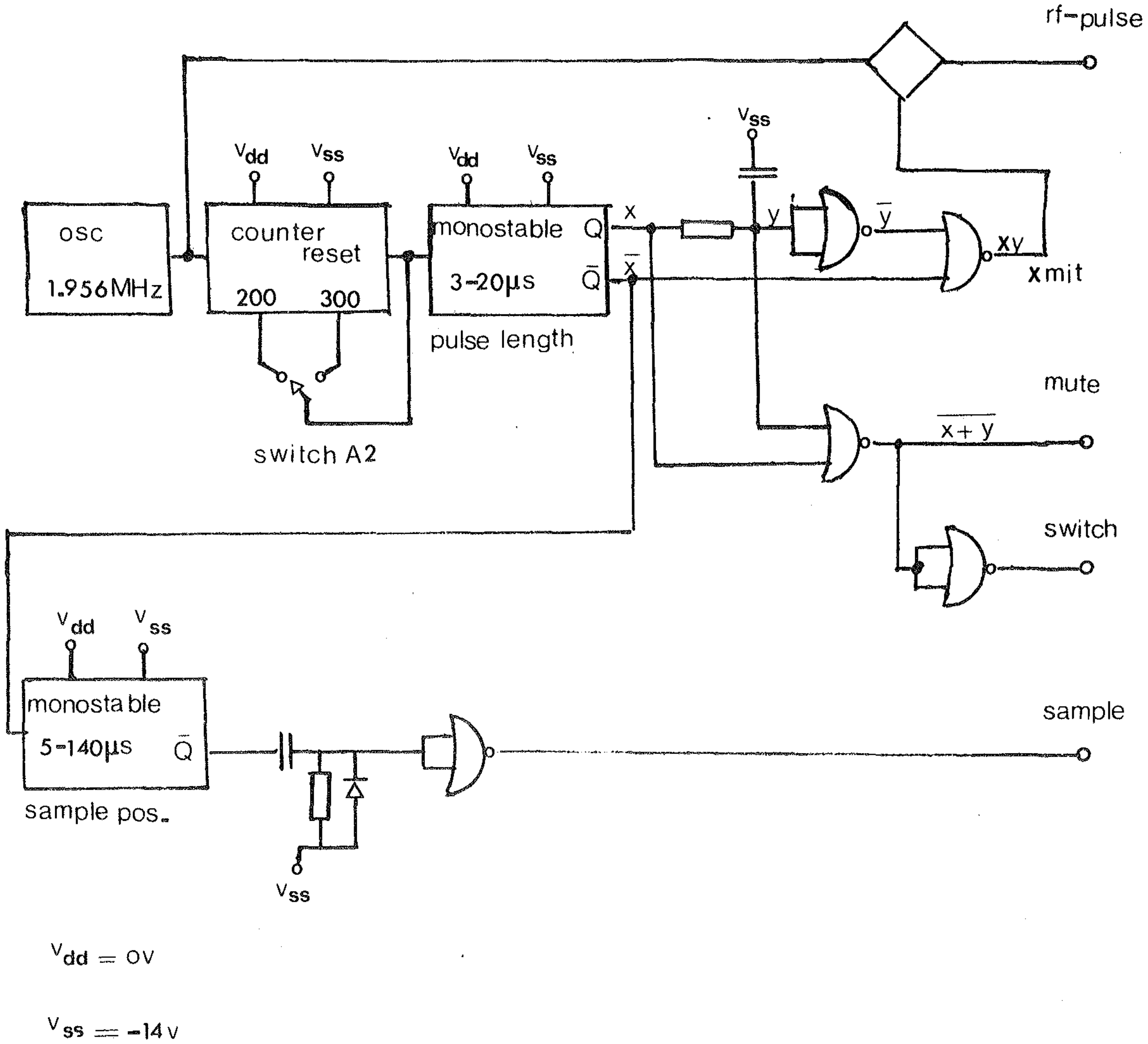

Figure 7.2. Generator unit for PEDOF.

The counter triggers a monostable multivibrator which generates the pulse x shown in Figure 7.3. The legnth of this pulse may be adjusted between 3 and 20 μs. The signal x is delayed 2 μs to give y. xmit = xy is generated and fed to a gate which generates the rf-pulse. The signal switch = x+y connects

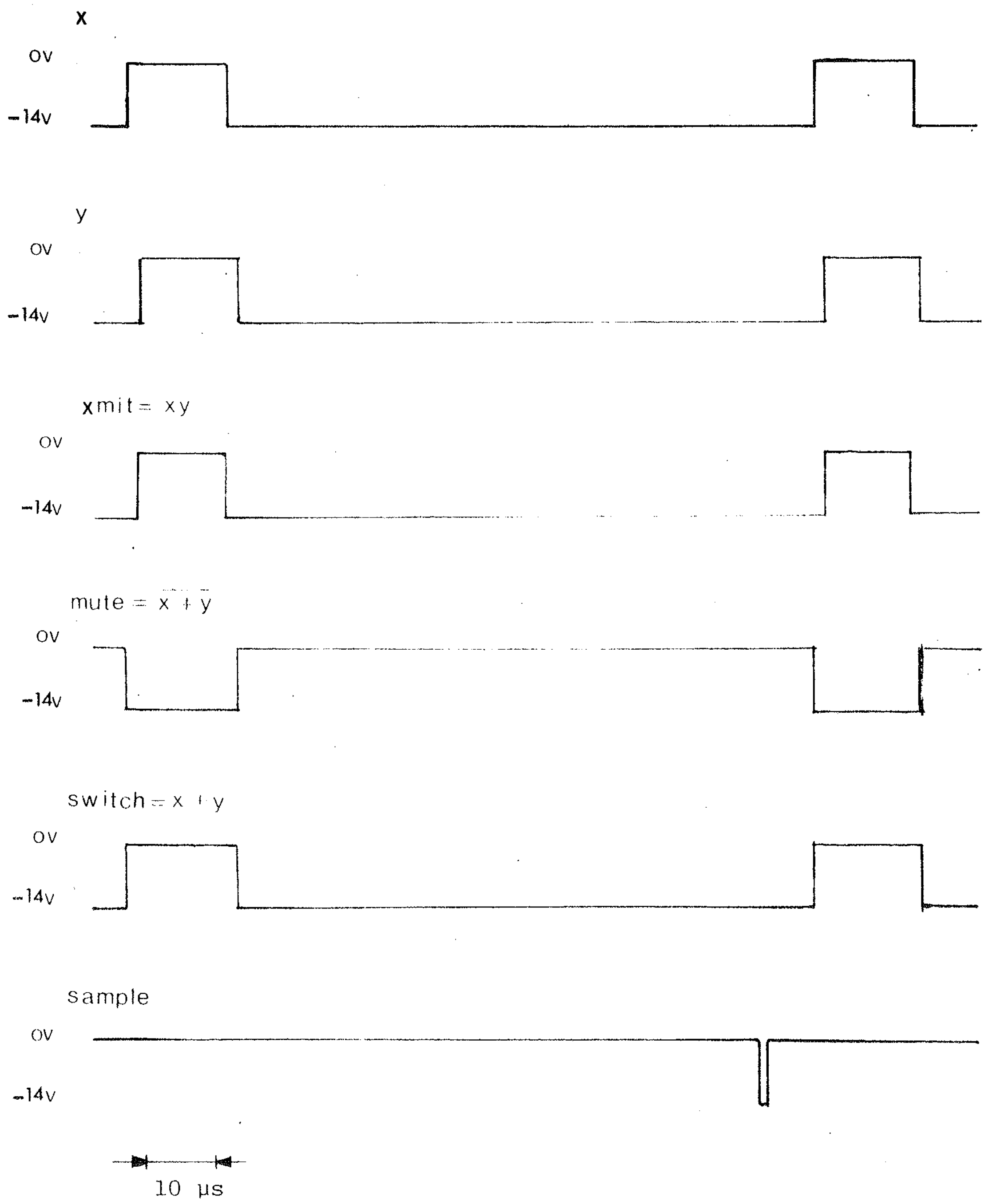

Figure 7.3. Control signals from the generator unit. The counter is in the 200 mode which gives a repetition periode of 104 μs, i.e. 9.75 kHz repetition frequency.

the transducer to the power amplifier during the transmission. The signal mute = $\overline{x+y}$ reduces the gain of the receiver rf-amplifier 40 dB to avoid saturation problems during the transmitting period.

A second monostable multivibrator which generates the sample position delay, is triggered by $\bar{x}$. Via the gate, a sample pulse of 1 µs is generated. The sample pulse delay is adjustable from 5-140 µs, giving an observation depth of 0.5 - 11 cm.

A double power supply of ±14 V is used. The generator unit is driven by the negative supply only. Logic "1" then is 0 V and logic "0" is -14 V.

The peak-to-peak amplitude of the transmitted pulse is 15 V into 50 Ω. With 60 % conversion capabilty of the transducer this gives a peak emitted acoustic power of 335 mW. A 10 µs pulse then gives an average transmitted power of 33.5 mW at 9.75 kHz repetition frequency and 22.5 mW at 6.5 kHz repetition frequency.

7.2. Experimental laboratory studies of the instrument.

A. Introduction and methods.

In these tests we have been concerned with three problems:

i) To find an optimum value of the AGC-time constant of the velocity estimator (Section 5.3). We also especially emphasize the connection between estimator variances and this time constant as discussed in Section 6.1.

ii) To study the velocity estimation capabilities of the instrument for a timesteady flow through a straight pipe.

iii) To study the instrument capabilty to estimate pulsatile flow similar to that in the human aorta.

For i) we first use a single rf-frequency input on the instrument preamplifier. This simulates the echo from a single scatterer. The deviation in frequency between this signal and the instrument local oscillator will be the doppler shift in the frequency. With this signal the linearity of the estimator is tested for various AGC time constants. We especially study the distortion of the single frequency signal through the AGC system and a comparison between this distortion and estimator nonlinearity is performed.

Echos from timesteady flow through a straight tube is also used to study the effect of the AGC.

Figure 7.4 shows the system used to obtain timesteady flow. The area of the reservoir is matched to the spring constant so that the level of the liquid surface is kept at a constant height as the liquid flows out of the reservoir. A dashpot is used to attenuate oscillations.

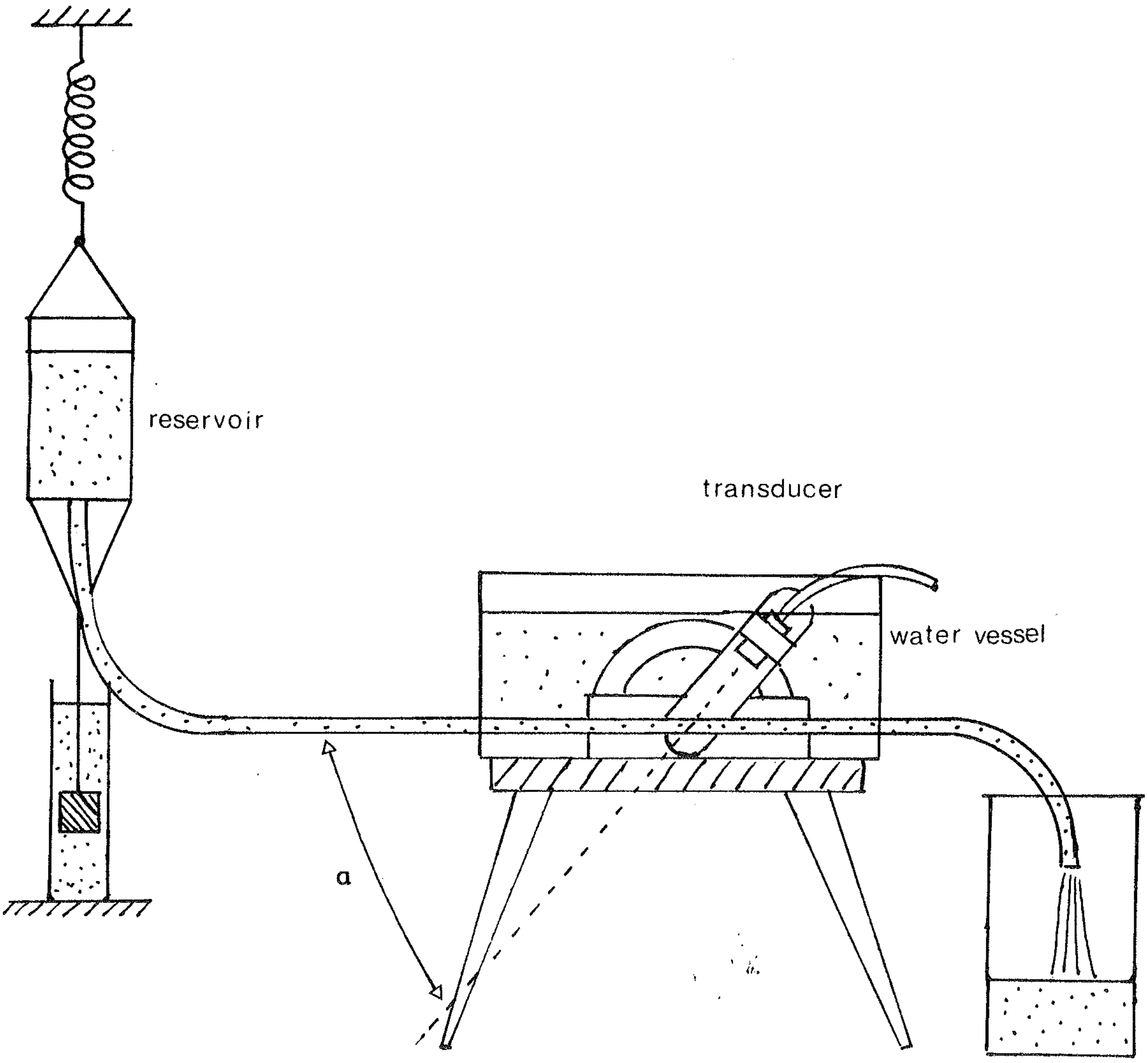

Figure 7.4. Timesteady flow system.

The transducer is mounted in a vessel of water through which the tube runs. The tube is straight for 50 diameters in front of the observation region. To control the flow velocity, the height of the outlet level of the tube is adjusted.

The mean flow velocity is calculated from the measured time, t, of outflow of a fixed volume V. The mean velocity, $\overline{v}$, will then be

$$\bar{v} = \frac{V}{t \cdot A} \tag{7.1}$$

where A is the area of the tube. The error in this measurement is less than 5 %.

The same apparatus is used to obtain calibration curve of the instrument for timesteady flow.

As discussed in Section 5.2, the velocity profile may be obtained by scanning the observation region across the vessel. To obtain the profile we have used the double layer matched transducer, described in Section 3.5, having a lense with focal length of 6 cm, described in Section 3.1. A pulse length of 5 μs is used giving a longitudinal resolution of 4 mm. The lateral resolution is determined by the lense and is approximately 4 mm (Section 2.2).

The transducer is kept at an angle of 45° with the tube and the position of the observation region is varied with a constant velocity across the tube (21 mm diameter). The estimator output is displayed versus time on a storage scope and by this the velocity profile of the timesteady flow is obtained.

To generate pulsatile flow a pump system shown in Figure 7.5 has been built. A piston pump driven by a wind shield wiper motor pumps the liquid through a tube that simulates the aorta.

The velocity of the pump may be continuously varied, thus simulating different heart rates, while the stroke volume is constant (87 ml). In the test it is the integral of the instrument velocity curve which is compared to this stroke volume. (The "aortic" diameter and angle between ultrasonic beam and velocity is known).

The liquid used for timesteady flow is cattle blood. For pulsatile flow measurements a mixture of oil in glycerin is used.

B. Effect of AGC time constant on estimator linearity and variance.

The AGC circuit is shown in Figure 7.6. Resistor R_1 and the field effect transistor form a voltage controlled attenuator in front of the Op-amp, which has a voltage gain of 200 (46 dB). The characteristic of the attenuator is given in Figure 7.7.

P_1 is adjusted do that the integrator output is clamped at the pinchoff, V_p, of the JFET when the amplitude of s_i is small. An AGC range of 40 dB is obtained for the whole range of y and a range of 30 dB is obtained when y is between -4 and -6.5 volts.

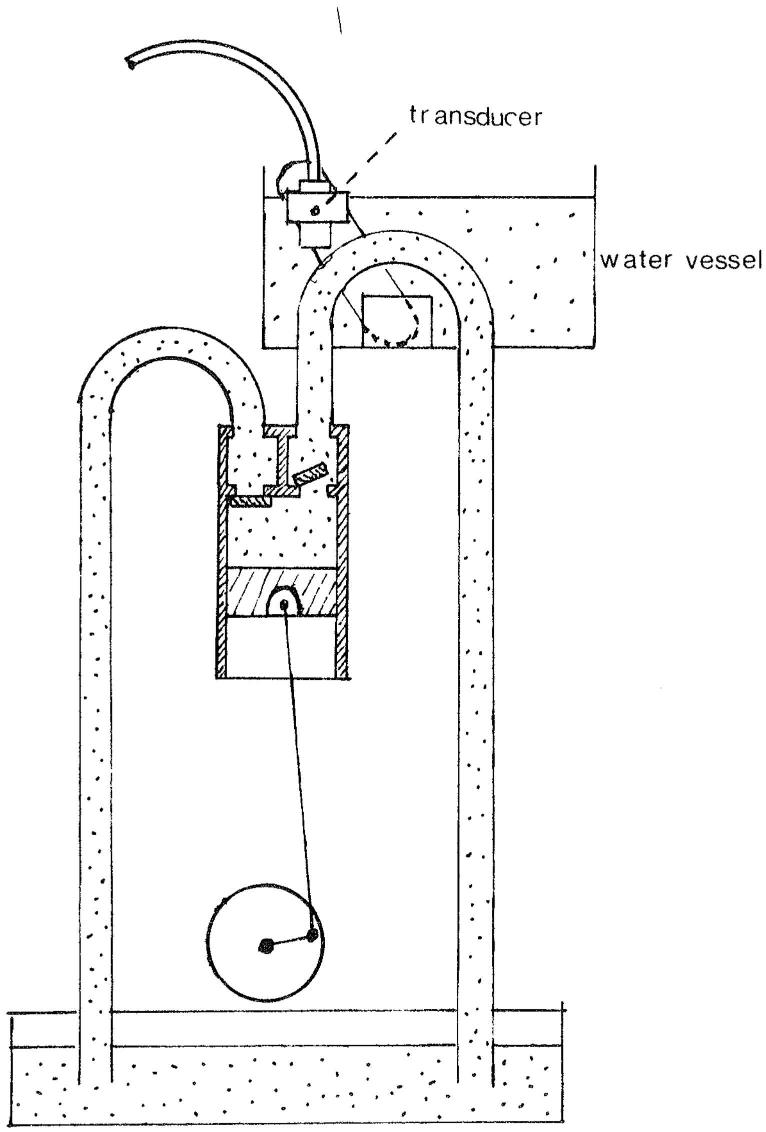

Figure 7.5. Pulsatile flow system.

The total gain of the AGC-system is

$$A(y) = A_v f(y) \tag{7.2}$$

When the integrator time constant, T = RC, is not too low, the integrator output will normally vary only near y_0 - the value which keeps the mean of $g(s_i)$ near $-v_r$. We may then linearize and obtain

$$\frac{\Delta A}{A(y_0)} = \frac{1}{f(y_0)} \frac{df}{dy} \frac{\Delta z}{T} = -K\Delta z$$
$$\Delta z = T\Delta y = T(y - y_0) \tag{7.3}$$

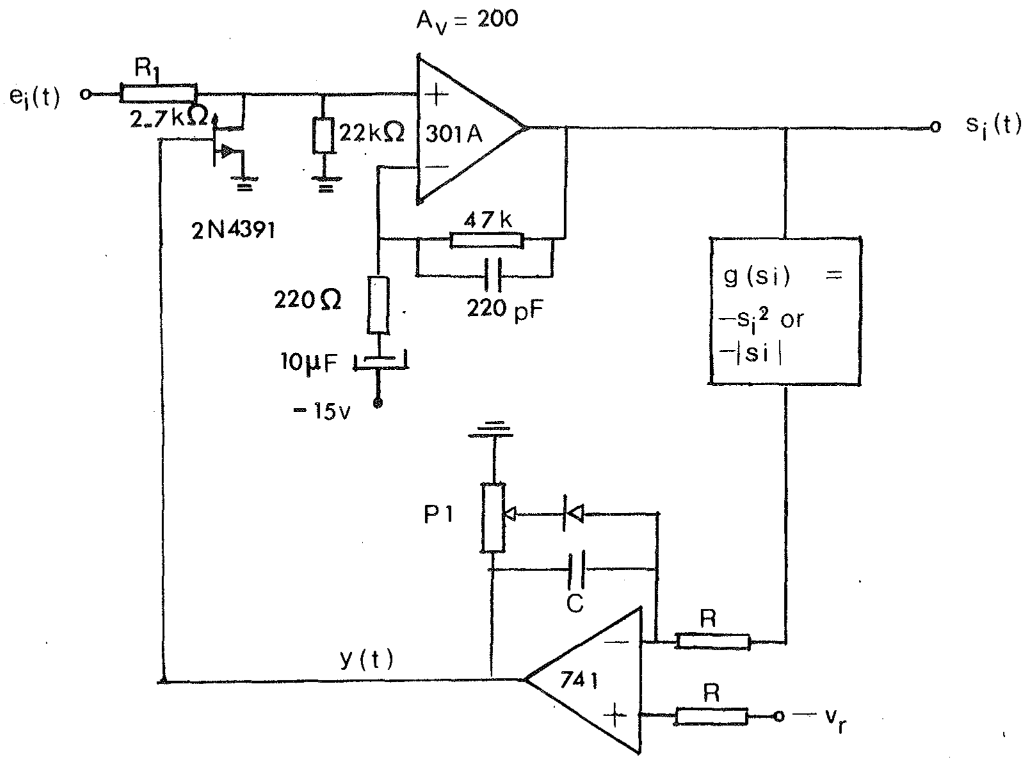

Figure 7.6. AGC-system for velocity estimator I and II.

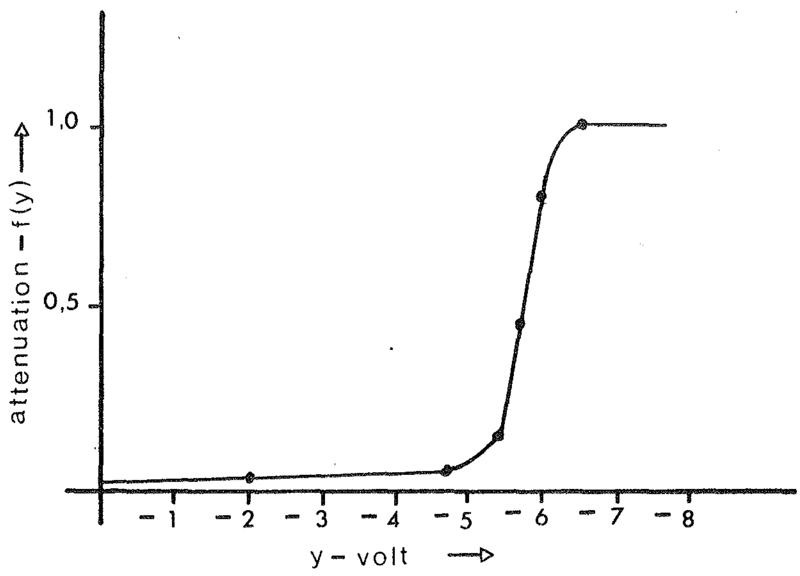

Figure 7.7. Characteristics of the AGC attenuator.

where ΔA is the change in A when y changes.

K determines the ability of the AGC-system to cancel variations in the signal amplitude. Since Δz is the integral of the difference between $g(s_i)$ and $-v_r$, a large value of K will keep this difference small. However, since Δz enters as a multiplier in the signal loop, the amount of distortion also increases with K as will be demonstrated.

Ideally K should be independent of y_0, giving differential performance of the AGC which is independent of the input signal level. From Figure 7.7 it is seen that this is not fully correct, but the variations are fully within tolerable limits. In the experiments reported in this section, the level of e_i is adjusted so that $f(y_0) \approx 0.6$, giving a one-to-one correspondence between K and T. This value of y_0 also gives about the maximum K.

Figure 7.8 gives the estimator outputs for a single frequency input to the amplifier. The output is given against the frequency deviation between the input signal and the instrument local oscillator.

Three values of integrator time constants have been studied

$$T = 0.5\text{ ms} \leftrightarrow K = 16000\ (\text{Vs})^{-1}$$

$$T = 3.3\text{ ms} \leftrightarrow K = 2500\ (\text{Vs})^{-1}$$

$$T = 8.5\text{ ms} \leftrightarrow K = 1000\ (\text{Vs})^{-1}$$

For each value the estimators are calibrated to give 5 V output at +2.5 kHz frequency.

The highest value of K shows considerable nonlinearity in the estimate, while the linearity for the other two values is quite acceptable.

The wave forms out of the AGC circuit are shown in Figure 7.9 illustrating the distortion of the signals, especially at low frequencies. The percentage ratio of the power contained in the higher harmonics to the power in the fundamental harmonic is shown in Figure 7.10 as a function of frequency.

The distortion in estimator II is greater than that in estimator I. This is reasonable since $|e_i(t)|$ contains more relative power in the higher harmonics than does $e_i^2(t)$.

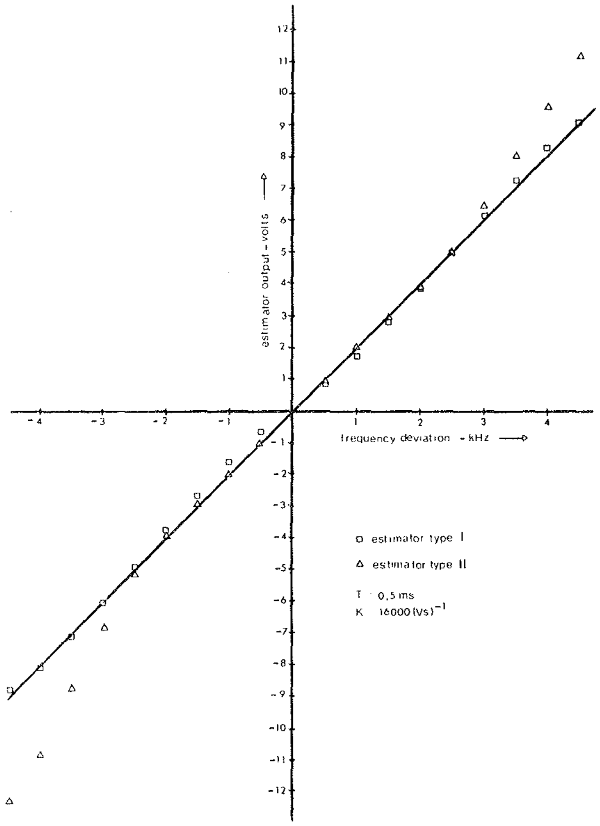

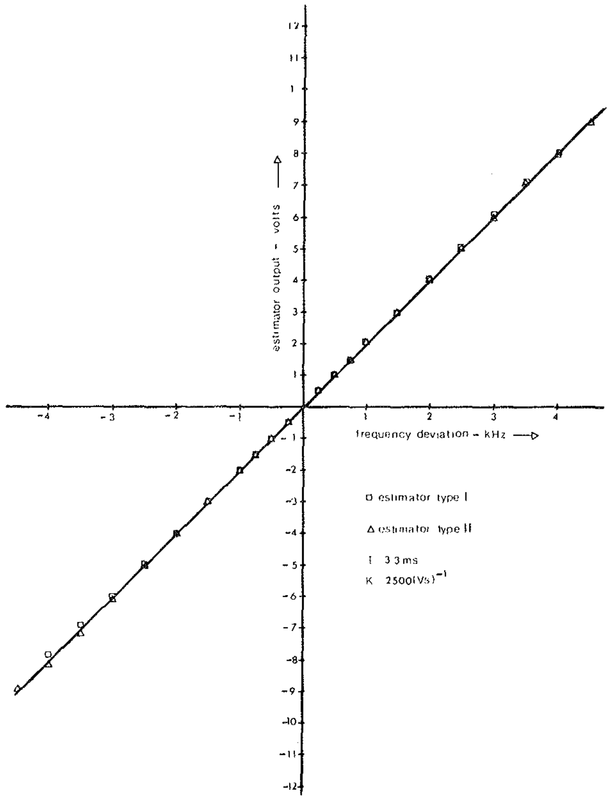

Figure 7.8. Estimator output for single frequency input.

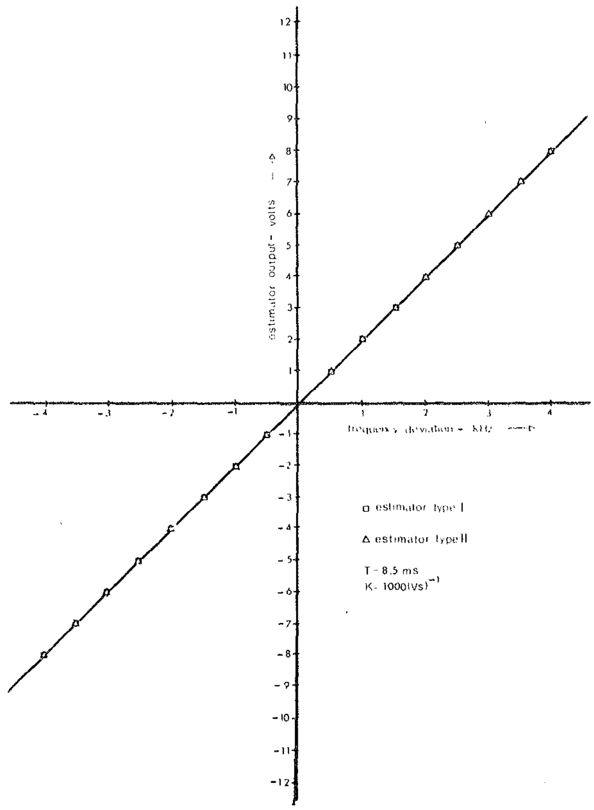

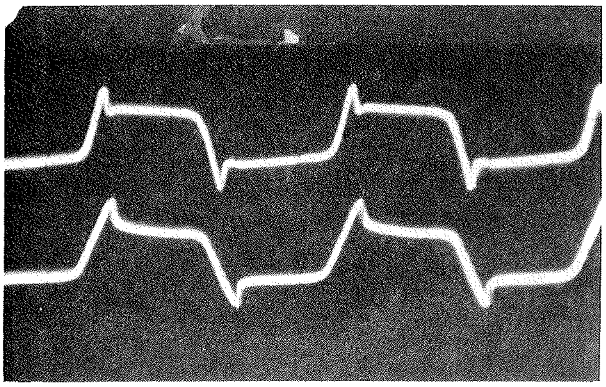

200 Hz $T = 0.5$ ms $K = 16000\ (Vs)^{-1}$

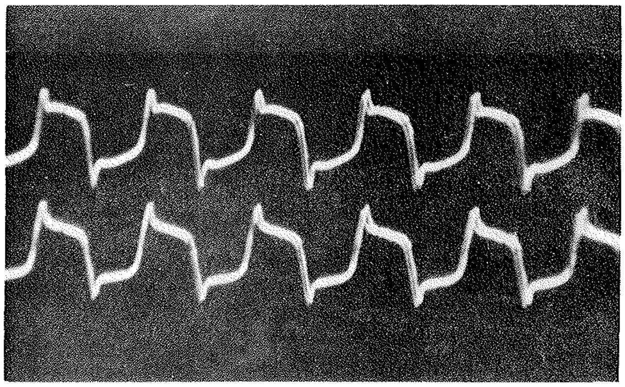

500 Hz $T = 0.5$ ms $K = 16000\ (Vs)^{-1}$

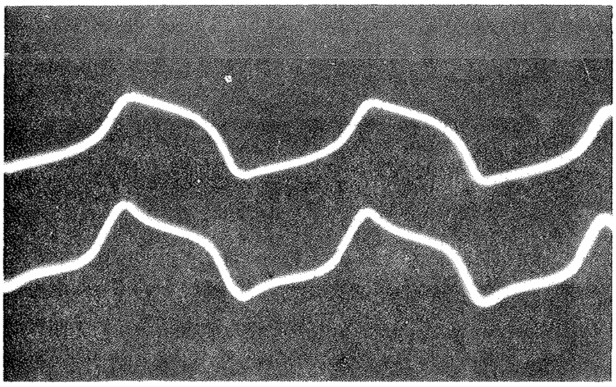

200 Hz $T = 3.3$ ms $K = 2500\ (Vs)^{-1}$

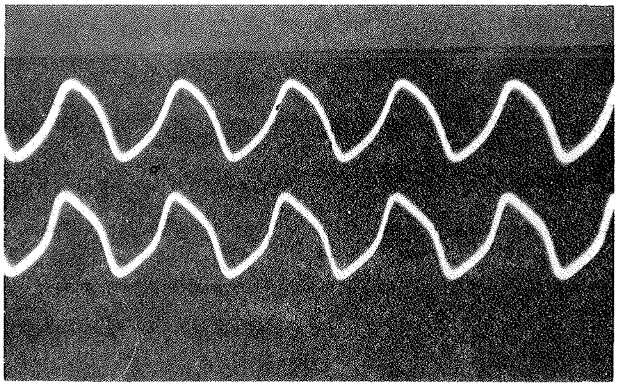

500 HZ $T = 3.3$ ms $K = 2500\ (Vs)^{-1}$

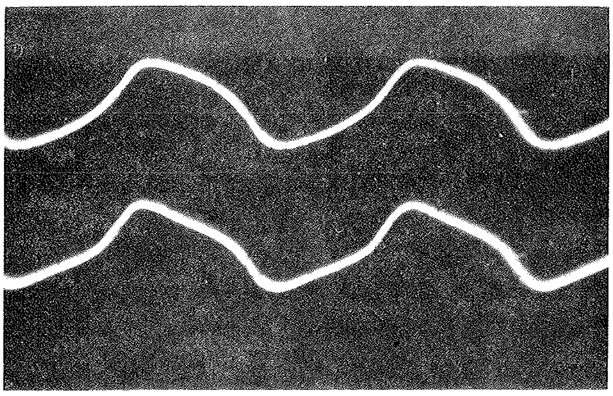

200 Hz $T = 8.5$ ms $K = 1000\ (Vs)^{-1}$

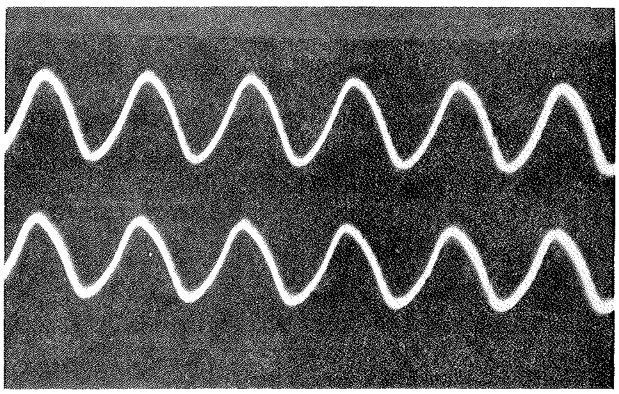

500 Hz $T = 8.5$ ms $K = 1000\ (Vs)^{-1}$

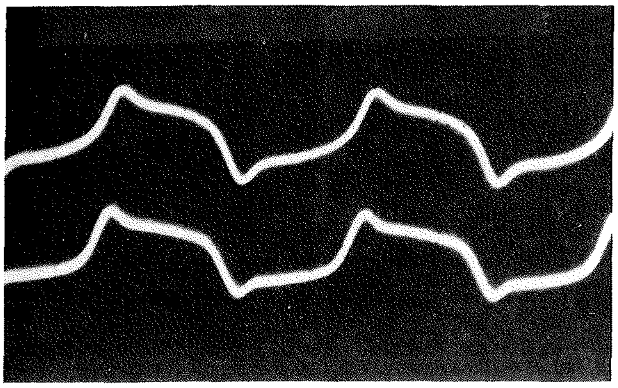

1000 Hz $T = 0.5$ ms, $K = 16000\ (Vs)^{-1}$

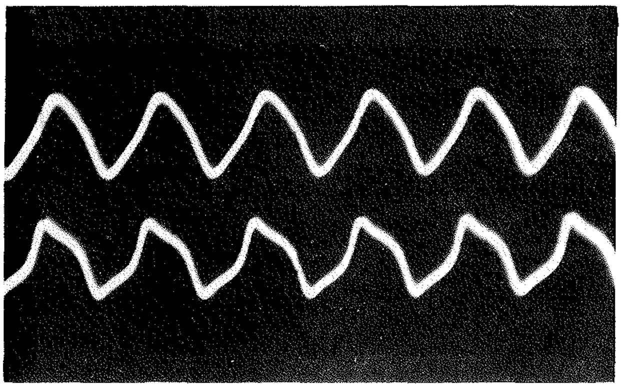

2500 Hz $T = 0.5$ ms, $K = 16000\ (Vs)^{-1}$

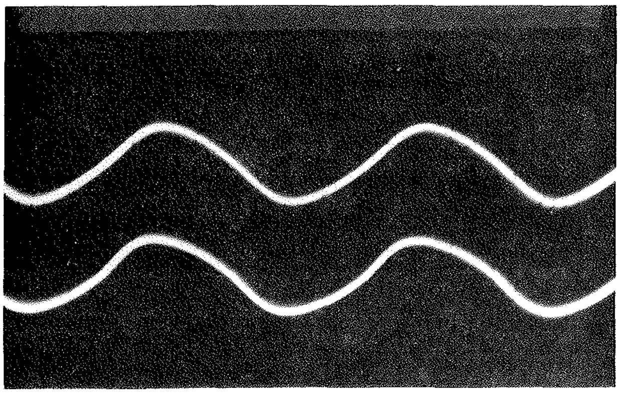

1000 Hz $T = 3.3$ ms, $K = 1000\ (Vs)^{-1}$

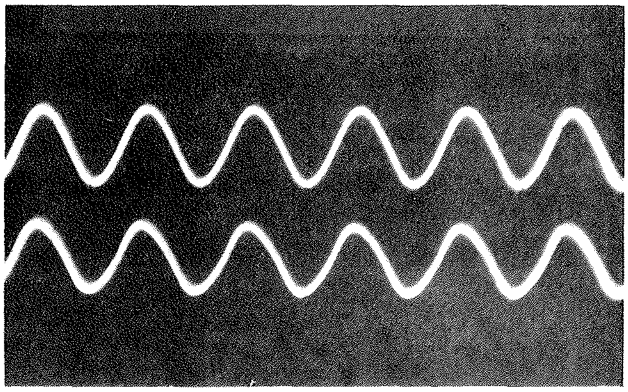

2500 Hz $T = 3.3$ ms, $K = 1000\ (Vs)^{-1}$

Figure 7.9. Waveforms out of the AGC-circuit for a single frequency input signal.
Upper trace: Estimator I
Lower trace: Estimator II.

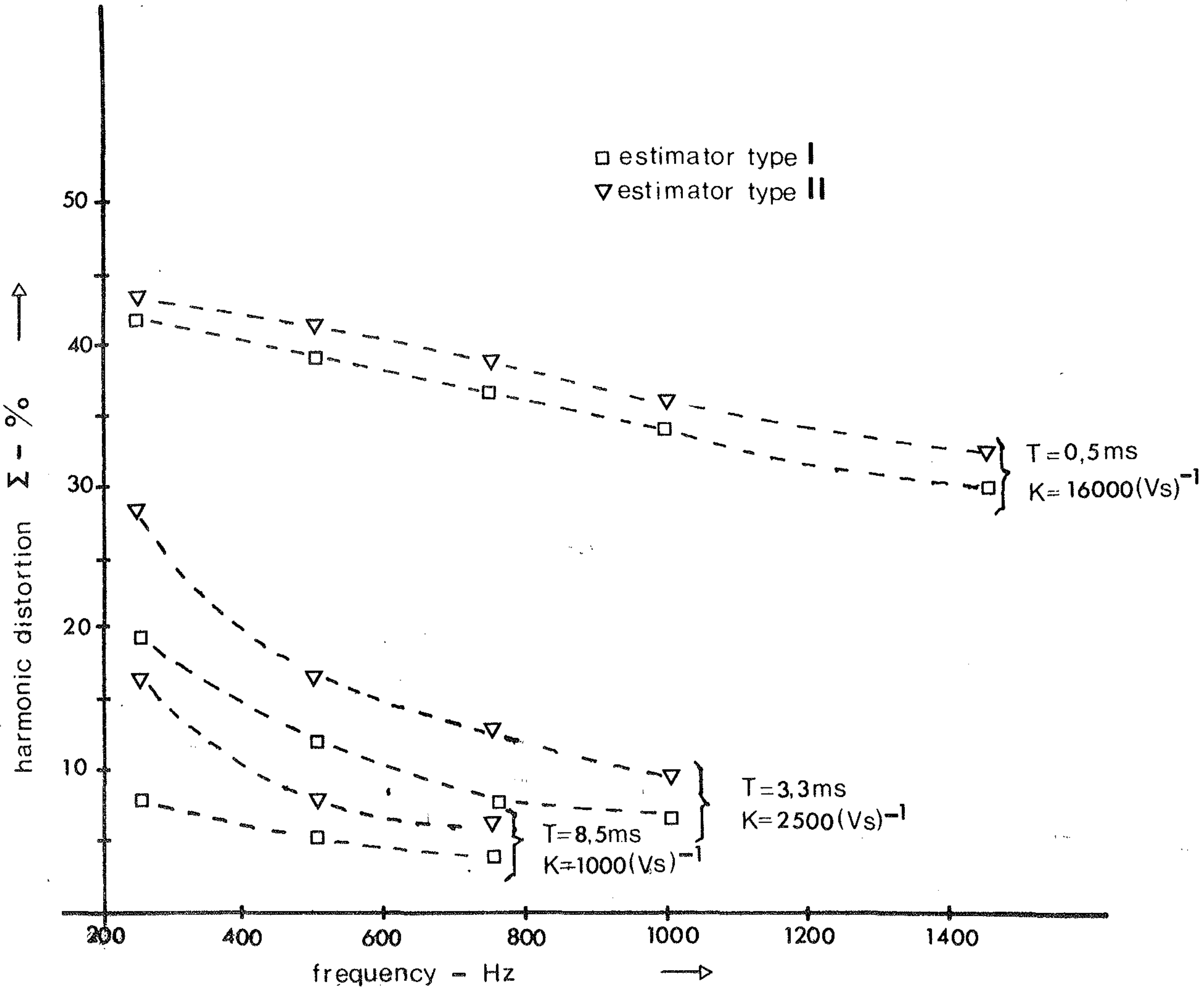

Figure 7.10. Power content in the higher harmonics out of the AGC-system relative to the power in the fundamental harmonic.

Figure 7.11. shows the estimator output from measurements of timesteady flow for various integrator time constants. The transducer (diam. 20 mm) forms an angle of 45° with the tube whose diameter is 12 mm. Thus to get the real flow velocities, the values in the figure should be divided by cos 45°.

The observation region is adjusted so that the transit length of the cells is constant across the tube. A good indication of correct adjustment is that at moderate flow velocities, where a parabolic profile should be expected, a square spectrum of the doppler signal is obtained.

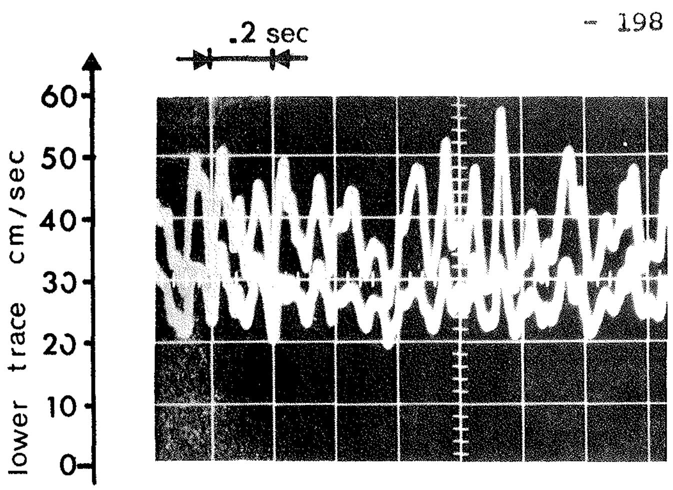

T = 2.2 s   K = 4.0 $\bar{v}$ = 27 cm/s

a)

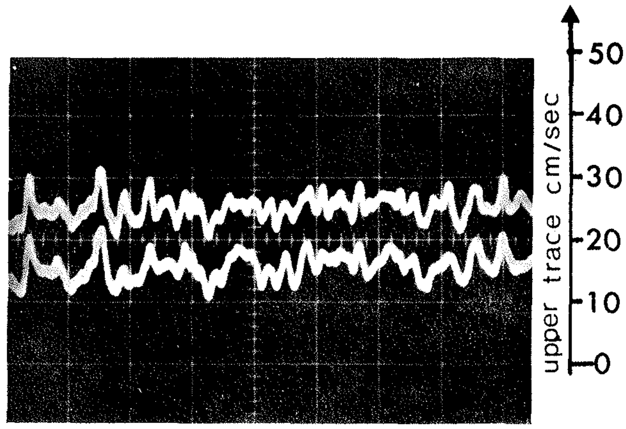

T = 22 ms   K = 400 $\bar{v}$ = 26 cm/s

b)

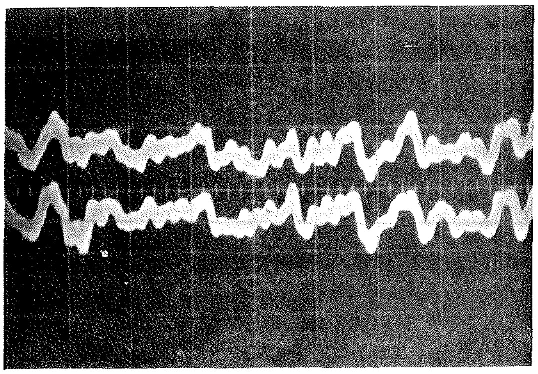

T = 3.3 ms   K = 2500 $\bar{v}$ = 26 cm/s

c)

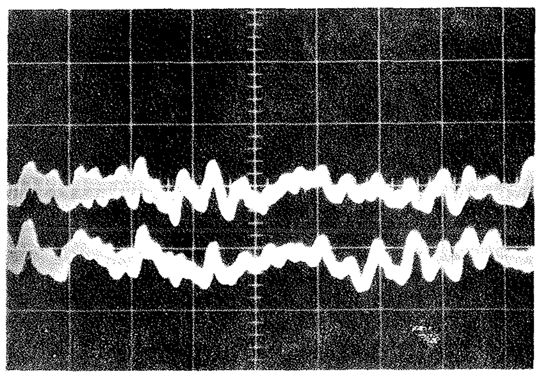

T = 0.5 ms   K = 16000 $\bar{v}$ = 27 cm/s

d)

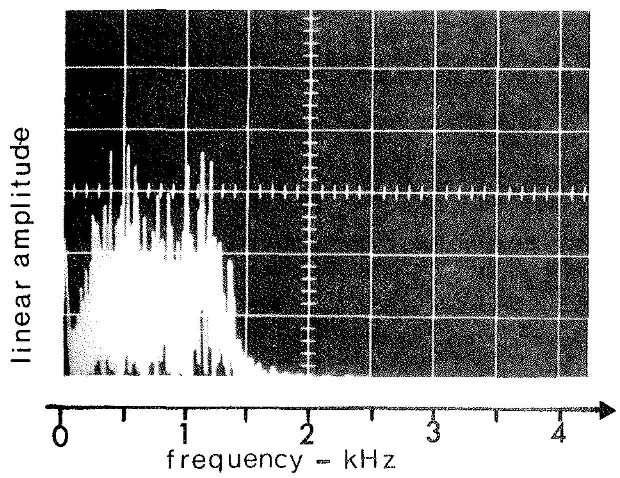

e)

Figure 7.11. *Estimator output from measurements on timesteady parabolic flow for various integrator time constants. A lowpass filter with three real poles at 20 Hz is used. The measurements are independent so that the mean velocity differs between the experiments. e) shows the amplitude spectrum from the flow analysed in b).*
Upper trace: Estimator I. Lower trace: Estimator II.

The estimator filter has three real poles at 20 Hz. A two pole highpass filter of 200 Hz is used instead of the filters shown in Figure 7.1. There is no need for better highpass filtering since the vessel walls and surroundings are not moving.

For $K = 4$ the estimate variance is higher for estimator I compared to estimator II. In this case the AGC is so slow that its effect is to divide $p(t)$ with $\langle q \rangle$ (Section 6.1). Thus the estimator variance is given by that of p. The theoretical estimate of the relative uncertainty in this estimate $\sqrt{\langle a^2 \rangle}$ is given in Example II of Section 6.3B.

The input of the averaging filters are non-Gaussian due to the correlation multiplication, the distribution for the first estimator being χ^2. When the signals are lowpass filtered, the distribution becomes more Gaussian as is indicated by Figure 7.11. However, the non-Gaussian character is especially demonstrated by the large positive peaks in the upper trace of Figure 7.11a, estimator I. No similar negative peaks exist.

Approximating the distribution by the Gaussian type we may assume that the variations of the signals are within 4σ (95 % confidence interval) giving an estimate of

$$\left.\frac{\sqrt{\langle \delta\tilde{\tilde{v}}^2 \rangle}}{\langle \tilde{\tilde{v}} \rangle}\right|_{est} = \sqrt{\langle a^2 \rangle}_{est} = 0.17 \text{ estimator I}$$

$$\left.\frac{\sqrt{\langle \delta\tilde{\tilde{v}}^2 \rangle}}{\langle \tilde{\tilde{v}} \rangle}\right|_{est} = \sqrt{\langle a^2 \rangle}_{est} = 0.11 \text{ estimator II}$$

This is in agreement with the theoretical values from Section 6.3B of 0.15 and 0.10 respectively.

An example of the doppler signal is shown in Figure 7.12. The other quadrature component is similar, shifted $\pi/2$ in phase. When differentiating an additional $\pi/2$ phase shift is obtained. The multiplication of the two signals then gives a signal with one polarity only (only one sign of doppler shifts present). The variations in the estimator output is caused by the stochastic fluctuations in the signal amplitude, as discussed in Section 6.3B.

For estimator I the amplitude variations out of the multiplier will be proportional to the square of the amplitude variations in the doppler signal. For estimator II there is a linear proportionality between these variations, and this is the reason for the greater variance of estimator I.

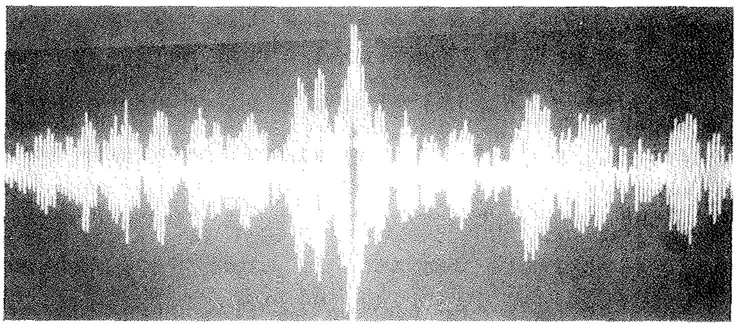

Figure 7.12. Example of one of the quadrature components of the doppler signal.

When the integrator time constant is reduced, the variations in the signal amplitude is also reduced. This is found as a reduction in the estimator uncertainty of Figure 7.11 without any other change in estimator performance. The difference in uncertainty between estimator I and II is also reduced and is negligible for $K = 2500$. Increasing K to 16000 reduces the estimator output due to distortion of the signals. Thus the maximum useful value of K is about 2500 as found in the single frequency study. To obtain minimum estimator uncertainty without destroying estimator linearity, this value of K is used in the instrument.

It is interesting to note that although considerable distortion of the signals occurs for this value of K (Figure 7.10), the estimator linearity is not markedly damaged.

The uncertainty of the velocity estimate is approximately

$$\frac{\sqrt{\langle \delta \tilde{\tilde{v}}^2 \rangle}}{\langle \tilde{\tilde{v}} \rangle}_{est} \approx 0.10$$

which is close to the theoretical value of 0.08 found in Example II of Section 6.3B for the estimator with division.

For estimator I the normalization factor is $\langle e_1{}^2 \rangle^{-1}$, while that for estimator II is $\langle |e_1| \rangle^{-1}$. The usefulnes of the gain control is that it adjusts the gain so that these values are approximately constant. Now, if $\langle e_1{}^2 \rangle$ is kept near constant, $\langle |e_1| \rangle$ will also be. Therefore, $g(\cdot)$ in estiamtor II may also be $g[e_i(t)] = -e_i{}^2(t)$. By this the amplitude variations of the integrator output will be increased and a better AGC capability is obtained without distorting the oscillations of the waveform. Since the amplitude variations in $\dot{e}_2 \text{sgn } e_1$ is proportional to the input amplitude variations while that of

$\dot{e}_2 e_1$ is proportional to the square of the input amplitude variations, the variance of estimator II will be less than that of Estimator I, even with fast AGC. This is demonstrated experimentally in Figure 7.13, where K is 300.

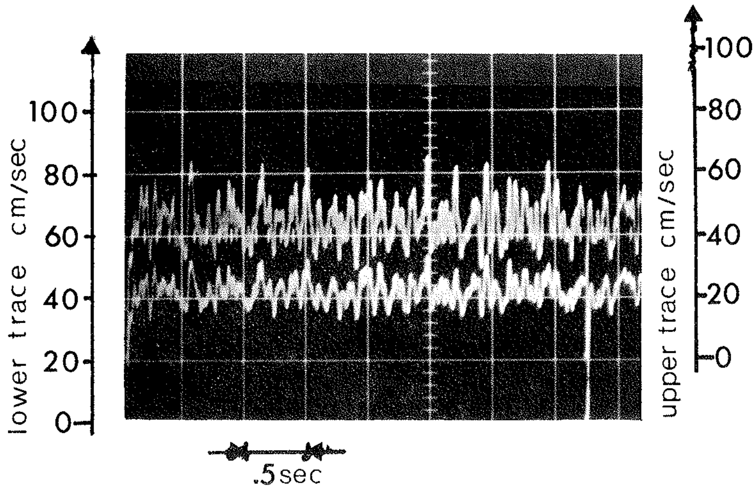

Figure 7.13.
Estimator outputs when $g[e_i(t)] = -e_i^2(t)$ for both estimator I and II.
Upper trace: Estimator I
Lower trace: Estimator II.

However, to use $|e_1|$ instead of e_1^2 simplifies the electronics so much that this form of g is used.

The amplitude spectrum of the received signal is shown in Figure 7.11e. The rectangular form indicates a parabolic profile (Section 5.1D). By inspection we see that the mean frequency of the spectrum is about 700 Hz, which corresponds to a velocity of 27 cm/s. This value is in good agreement with the estimator output of 26 cm/s.

C. Performance study with timesteady flow.

The instrument is tested for timesteady flow obtained by the system in Figure 7.4 with a tube of 12 mm diameter. The transducer beam has an inclination of 45° to the flow. It may be directed opposite to the flow direction indicated by a positive value of v, and along the flow direction indicated by negative values of v.

To obtain small variances in the estimates, an averaging filter with three real poles at 1 Hz is used. The highpass filter has two poles at 200 Hz, and the AGC time constant is 3.3 ms (K = 2500).

A plot of the instrument output against $\bar{v}$ cos 45, where $\bar{v}$ is calculated from Eq. 7.1, is shown in Figure 7.14. The two estimators resulted in such a small difference that they are both indicated by the same curve.

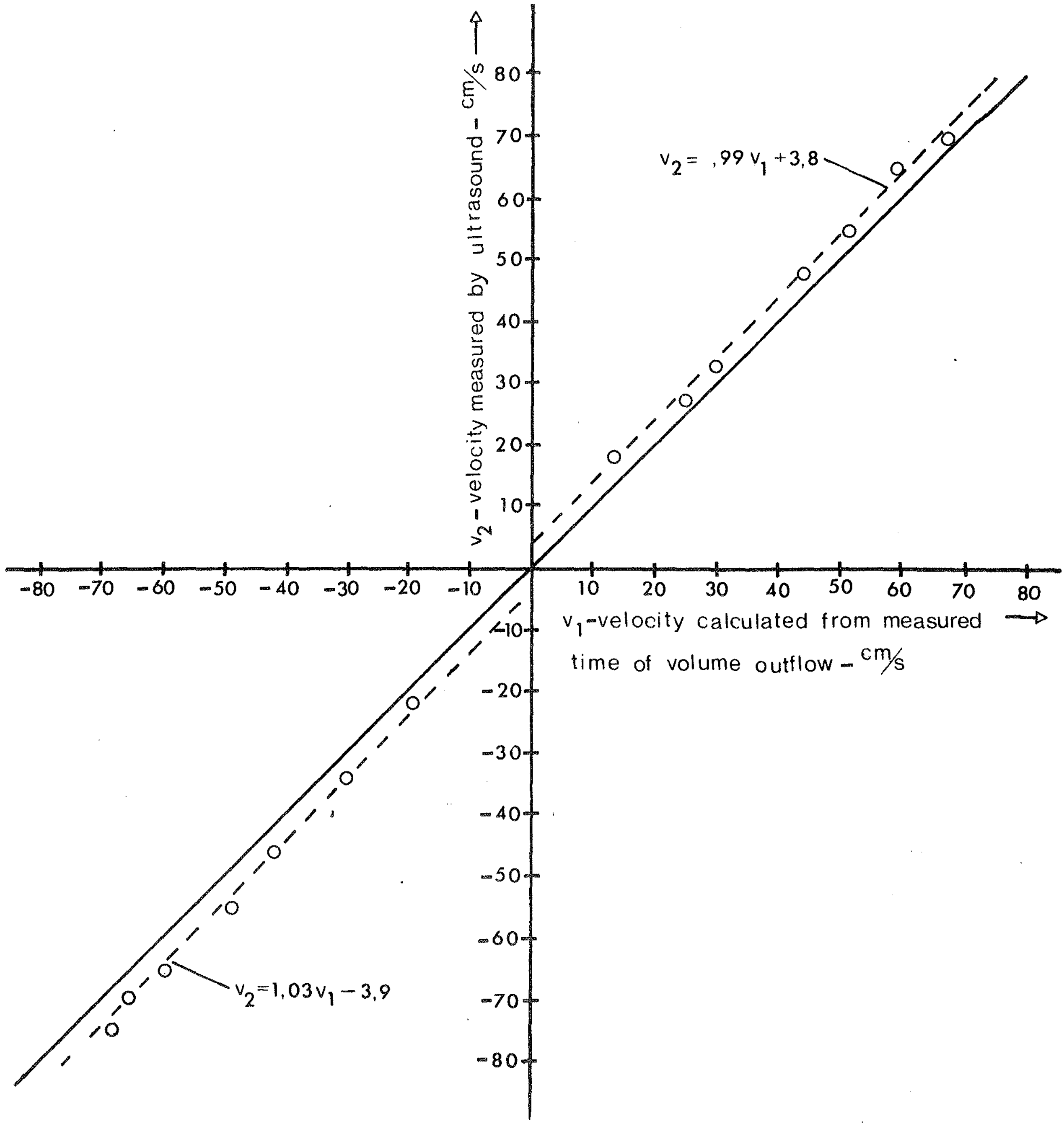

Figure 7.14. *Calibration of the doppler meter by timesteady parabolic flow. The difference between the outputs of the two estimators are so small that they are indicated by one dot.*

The two dotted lines are obtained by linear, least squares approximation to the data for positive and negative velocities separately. The offset of the lines from the line of identity stems from the highpass filters used (Section 5.2E). The theoretical value of the offset (parabolic profile) is a little less than 4 cm/s, which is in good agreement with the experimental values of 3.8 cm/s.

The velocity profile of time-steady flow in a tube of 21 mm diameter is measured as described in Section A. The result is given in Figure 7.15. An averaging filter with three real poles at 1 Hz and a highpass filter with two poles at 200 Hz is used.

For the lowest velocity the measured peak velocity is almost twice the mean velocity measured from the time of volume outflow. This is the situation for parabolic profile.

For the highest velocity the peak velocity is 54 cm/s, while the mean velocity measured from the time of the volume outflow is 32 cm/s. The measured peak velocity is, therefore, 10 cm/s less than that for parabolic flow giving the same mean velocity.

This may be caused by the finite resolution capability of the instrument. By this the measured profile will be the convolution between the observation region and the real profile [62]. In addition the profile might be flatter than a parabola due to the anomalous viscosity of blood.

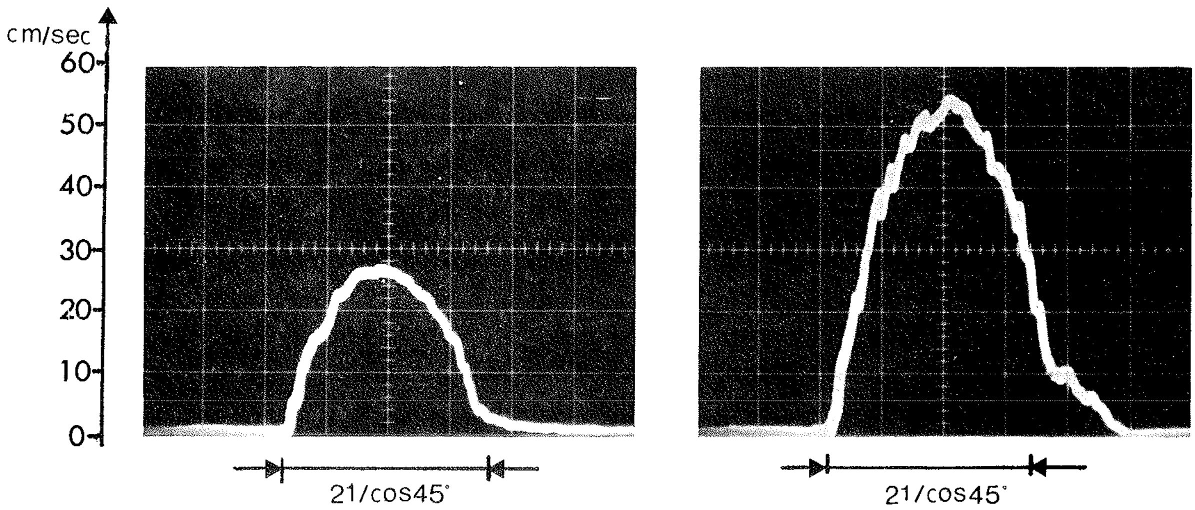

a) $\bar{v}$ *= 14 cm/s* *b)* $\bar{v}$ *= 32 cm/s*

Figure 7.15. Measurement of velocity profiles for two flow velocities.

Because of the convolution between the observation region and the profile, an output of the estimator is also observed when the front of the observation region has passed out of the tube. This is the reasons for the tails on the right side of the profiles in Figure 7.15. Knowing the form of the observation region, the real profile may be obtained from the measured values by a deconvolution process [62].

D. Relation between estimator uncertainty and the magnitude of the velocity.

This problem has been discussed theoretically in Section 6.3C. The estimator variances has been estimated for four values of $\bar{v}$ from the 4σ rule described in Section B. The result is shown in Table 7.1. The inverse square root dependency of the relative uncertainty to the velocity which is theoretically deduced, is clearly demonstrated. The bandwidth of the filter inputs ranges from 1000 to 2000 Hz for $\bar{v}$ ranging from 20 to 40 cm/s (the signals are squared). Since the averaging filter is 20 Hz only, the filtering is clearly strong.

$\bar{v}$ cm/s	19	26	30	40
$\sqrt{\langle\delta\tilde{\bar{v}}^2\rangle}$ cm/s	2.7	2.9	3.4	3.8
$\frac{\sqrt{\langle\delta\tilde{\bar{v}}^2\rangle}}{\bar{v}}$	0.14	0.10	0.11	0.095
	$\frac{0.61}{\sqrt{\bar{v}}}$	$\frac{0.51}{\sqrt{\bar{v}}}$	$\frac{0.60}{\sqrt{\bar{v}}}$	$\frac{0.60}{\sqrt{\bar{v}}}$

Table 7.1. Estimated estimator variances for various velocities.

E. Performance study with pulsatile flow.

Measurements on pulsatile flow obtained by the pump system described in Section A is shown in Figure 7.16. Estimator type II is used with an averaging filter of three poles at 20 Hz. A highpass filter with two poles at 200 Hz is used. In a) and b) a non-focussed transducer is used, so that the whole cross-section is approximately uniformly illuminated while in c) a lens with a focal length of 6 cm i placed in front of the transducer.

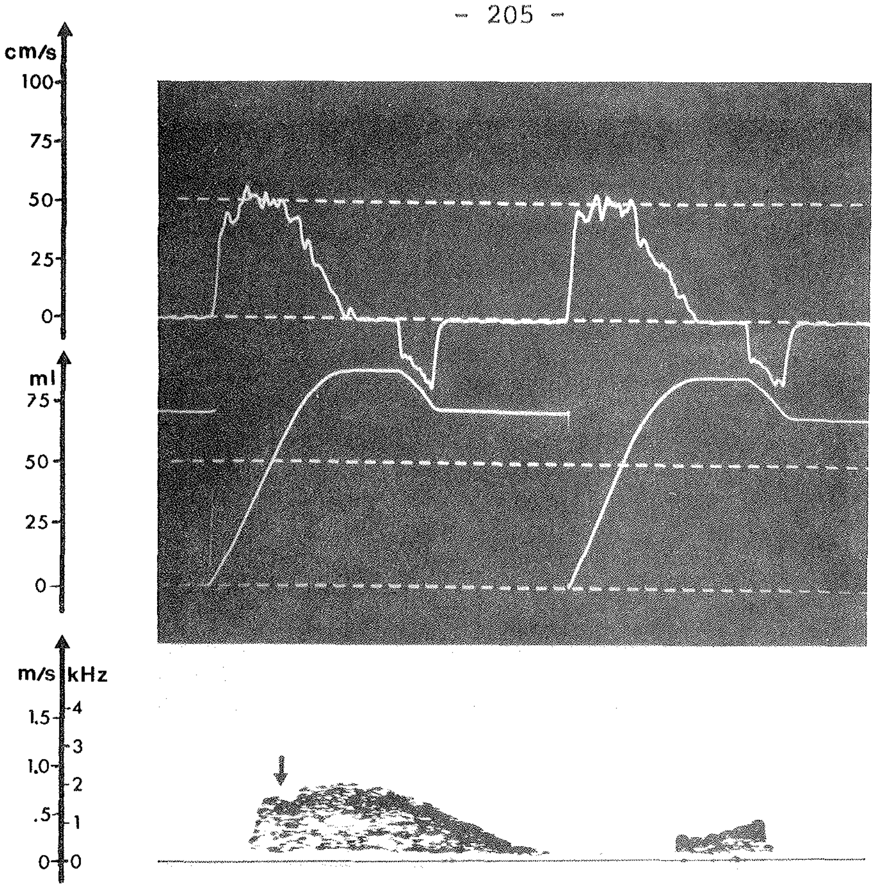
cm/s
100
75
50
25
0
ml
75
50
25
0
m/s
kHz
1.5
1.0
.5
0
4
3
2
1
0

a)

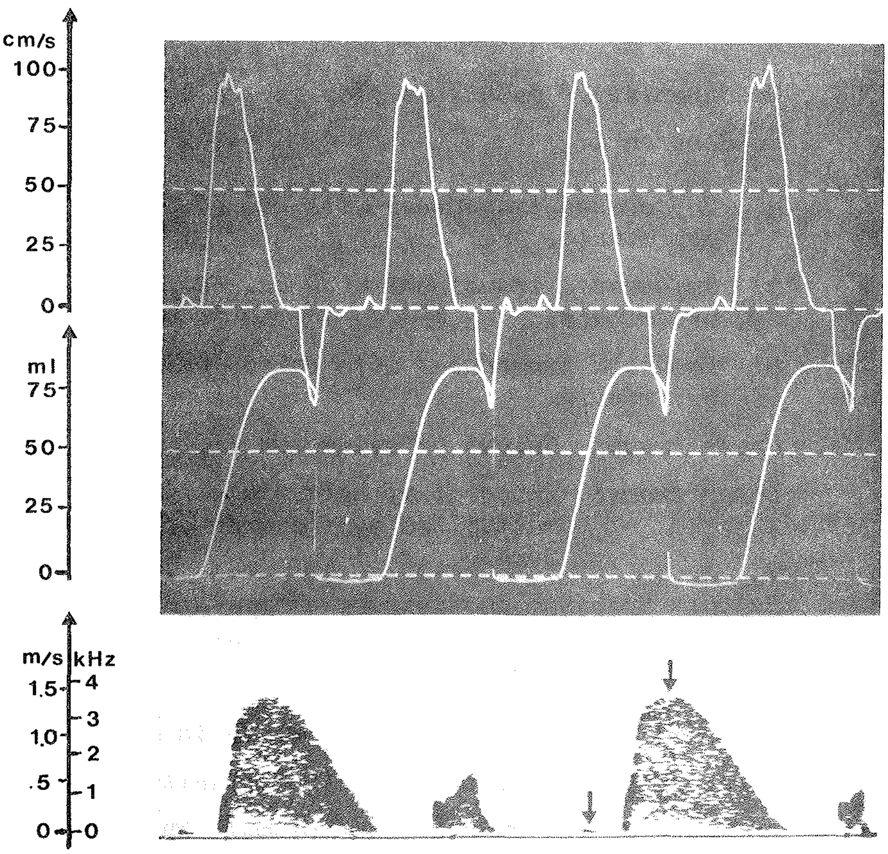
cm/s
100
75
50
25
0
ml
75
50
25
0
m/s
kHz
1.5
1.0
.5
0
4
3
2
1
0

b)

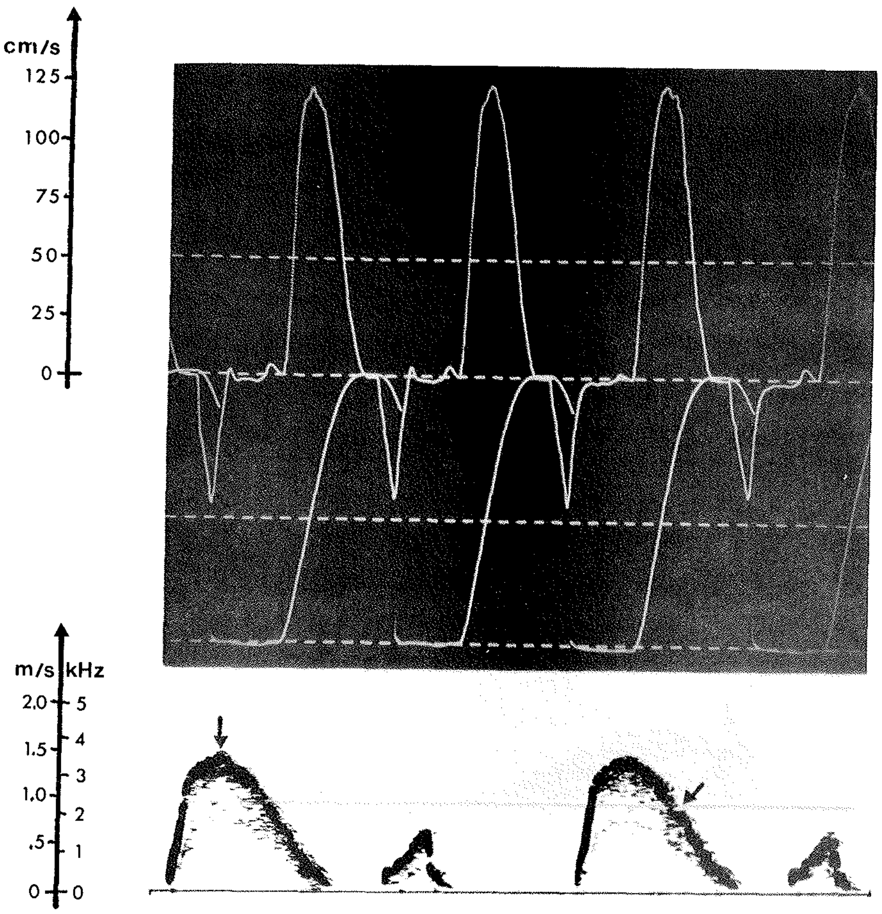

c)

Figure 7.16. *Measurement of pulsatile flow on the pump model in Section A.*

a) Unfocussed transducer with ca. 30 pulses pr. minute.

b) Unfocussed transducer with ca. 60 pulses pr. minute.

c) Focussed transducer with ca. 60 pulses pr. minute.

Upper trace: Output of estimator II.

Lower trace: Integral of velocity estimate multiplied by the area of the tube.

Below: Spectrum analysis by a Type B/65 Sonograph, Kay Elemetrics Co.

The pump frequency in a) is about 30 pr. minute, while in b) and c) it is 60 pr. minute. The integral of the velocity curve is multiplied with the area of the tube to form an estimate of the pump stroke volume. In a) and b) this gives a value of 84 ml, while the value obtained from construction data is 87 ml. It is also interesting to note that increasing the pump frequency leaves the estimated stroke volume constant (as the real is) changing only the peak velocity with a subsequent decrease in ejection time.

The integral in c) gives an overestimation of the stroke volume as the maximum instead of the mean velocity of the profile is measured.

Below the scope traces a spectrum analysis of the last flow pulse in Figure a), the two last pulses in Figure b) and the two last full pulses in Figure c) is shown. The spectrum in Figure a) shows a hump at the leading edge of the flow pulse (arrow), due to oscillations in the pump system. It is seen that this hump is faithfully reproduced by the estimator.

In Figure b) the first arrow indicates a small oscillation of the flow in the "diastole", which also is reproduced by the estimator. The second arrow indicates a dip in the frequency spectrum, which also is reproduced by the estimator (last pulse).

The first arrow in Figure c) shows a hump in the spectrum which also is found at the top of the estimator output, second pulse. The second arrow shows a dip in the descending edge of the spectrum also reproduced by the estimator, third pulse. The mean frequency in the spectrum is also well defined and in good agreement with the estimator output. Peak velocities of 125 cm/s is found in both cases.

The ratio in Figure a) and b) of the mean frequency, deduced from the estimator output, to the maximum frequency in the spectrum, at each instant of the time is 0.63 in a) and 0.65 in b). This indicates a profile flatter than a parabola. The "blunt" profile of example II, Section 5.1D gives these values for $p = 3.4$ and 4.25 respectively.

F. Discussion.

The velocity estimation capabilities of estimator I and II are approximately equal. With the optimum value of the AGC time constant found in Section B, estimator uncertainties are found. These are close to the theoretical values of 8 % found for estimators with division in Section 6.3, Example II.

This shows that the division in the estimators is successfully substituted by AGC. Especially we note that, although (discussed in Section 6.1) the estimator with division would have zero uncertainty for plug flow while the estimator with AGC would not have, the difference between the experimental uncertainty for the AGC estimator and the theoretical uncertainty of the division estimator is negligible for the parabolic profile.

The experiments of Section D also gives a very clear evidence of the inverse square root dependency of the uncertainty in the estimates to the velocity.

The experiments also clearly indicate that true mean velocity estimates are obtained both for steady and pulsatile flow. However, for the estimates to be correct it is necessary that the angle between the ultrasonic beam and the flow direction and the illumination of the tube is carefully controlled. As this is difficult to do in vivo, problems arise when measurements are performed in the human aorta.

7.3. In vivo measurements of aortic blood velocity and cardiac stroke volume.

A. Methods.

By positioning the transducer in the suprasternal notch, flow velocity in the ascending aorta as well as the aortic arc can be recorded, as indicated in Figure 1.2. By angling the beam until no velocity signal is recorded, the beam is normal to the aorta and in this position the aortic diameter can be calculated by the time lag between the echos from the anterior and posterior vessel walls.

In order to evaluate whether these velocity and diameter measurements could be used for obtaining volume flow and stroke volume, the following calculations were performed:

$$q = \frac{\pi \cdot d^2}{4} \cdot v \qquad (7.5)$$

where q is the volume flow estimate, d is the measured aortic diameter and v is the measured velocity.

$$Q = \int_{\substack{\text{heart}\\\text{cycle}}} q(t)\,dt \qquad (7.6)$$

where Q is the stroke volume estimate.

$$CO = Q \cdot HR \qquad (7.7)$$

where CO is the estimated cardiac output and HR is the heart rate.

A sector scanning system has also been built. A focussed transducer is suspended in a goniometer system as shown in Figure 7.17. By this the relative

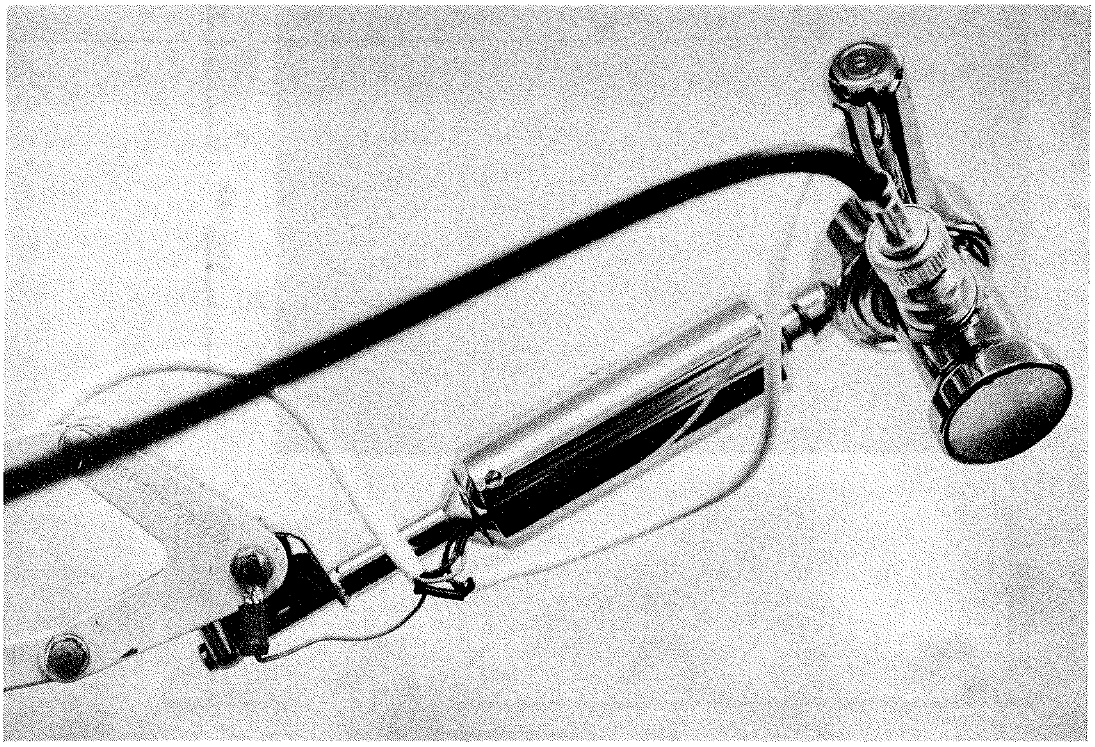

Figure 7.17. Goniometer for suspension of the transducer in sector scanning measurements.

position of the observation region (approximate cylinder of 5 mm diameter and 7 mm length) may be observed and transferred to the x-y position of the beam of a storage tube. A reference velocity is set in the instrument and every time the measured velocity exceeds this threshold, the beam lights up at the position and a mark on the storage screen is obtained.

By scanning across the vessel an area is obtained where the velocity exceeds the threshold value. The scanning has to be performed over many cycles, so that only a mean is obtained. By progressively lowering the velocity threshold, areas with velocities above defined values were obtained.

Using the radii of the areas developed in this manner, a velocity profile across the lumen was constructed by plotting the radii against the threshold velocities. This profile is the mean for many cycles, and it must also be assumed that the profile does not change during the cycle.

B. Results.

Figure 7.18 shows measurements of blood velocity in the ascending aorta from the suprasternal notch. a) and b) are obtained at two nearby directions of the unfocussed transducer at the same depth, 6-7 cm.

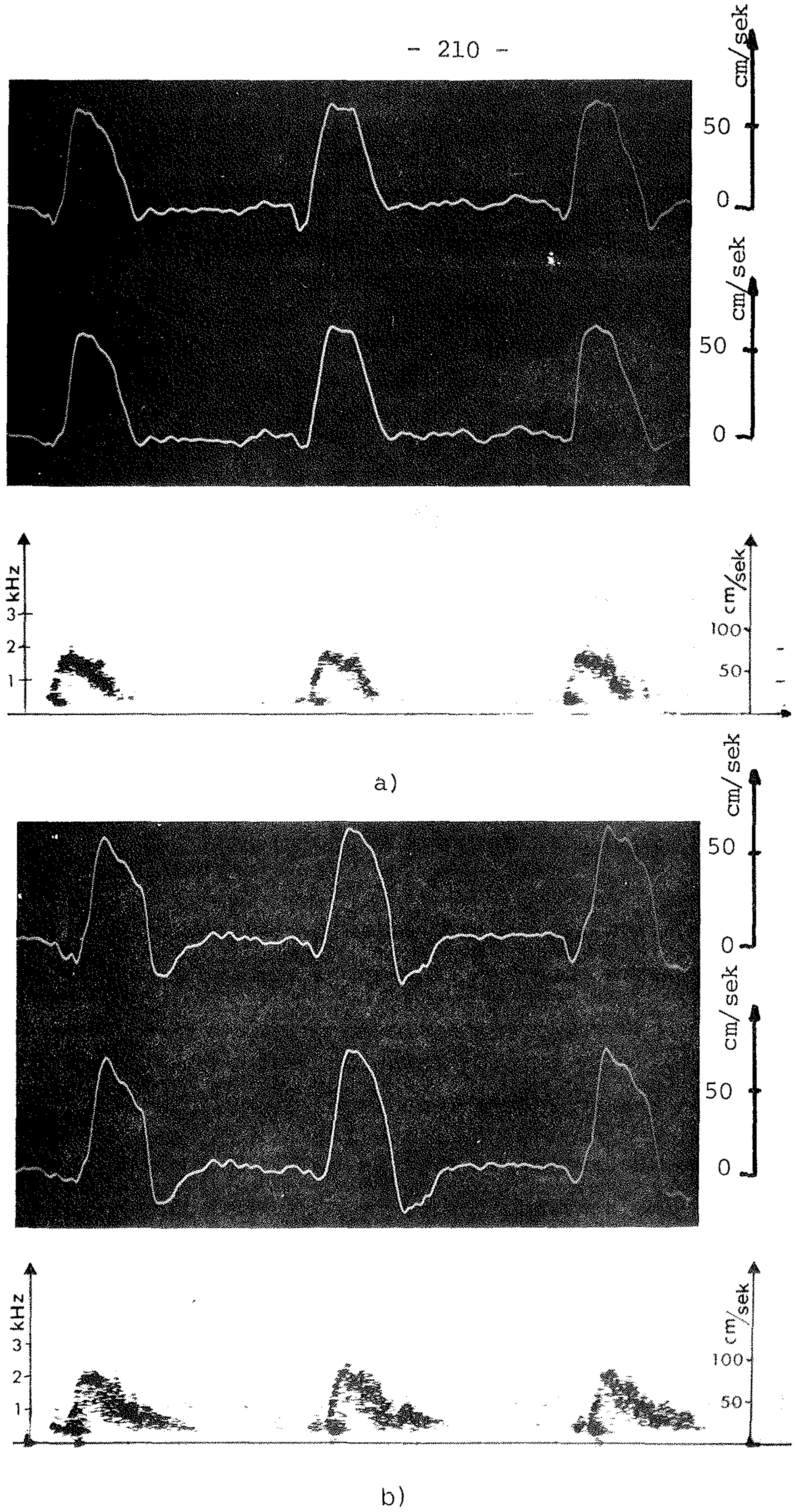

Figure 7.18. *Measurement of blood velocity in aorta ascendence from the suprasternal notch. a) and b) show the results from two nearby directions of the unfocused transducer, both depths 6-7 cm. Upper trace estimator type I, lower trace estimator type II, and below spectrum analysis by a TypeB/65 Sonograph, Kay Elemetrics Co. Note that the irregularities in the estimator outputs are also found in the spectrum.*

Comparison with the spectrum analysis indicates good velocity estimation capabilities of the estimators. The irregularities found in the estimator outputs are also found in the spectrum. This is best demonstrated by the flat top of the second pulse in a) and the small oscillations of the traces when the velocities fall from their maximum values in the first and the last pulse in b).

The downward dip in the estimator outputs seen at the beginning of some pulses stems from the motion of the tissue when the heart starts to eject (isovolumetric contraction phase). This dip is also found in the spectrum. Note that the motion is away from the transducer as would be expected from the isovolumetric contraction of the heart.

An M scan of the aorta at a position where the ultrasonic beam may be directed normal to the aorta from the suprasternal notch, is shown in Figure 7.19. Assuming a circular crossection of the aorta the estimates of the volume flow of blood and cardiac stroke volume may be calculated from Eqs. (7.5-7). This has been done for a group of 18 persons, and the result is given in Table 7.2. The measurements are performed in the ascending aorta.

An example of a sector scan in the aortic arc is shown in Figure 7.20. It can be seen that the areas are increasing as the velocity threshold is lowered. At low velocities an area blow the aorta appears, which probably represents velocity signals from the pulmonary artery, having a greater angle to the ultrasonic beam and consequently lower velocity components along the beam.

The velocity profile was constructed by plotting the radii of the areas against the measured velocities. This is shown in Figure 7.21. The point on the velocity axis was determined by the maximum velocity measured, and the point on the radius axis is half the diameter measured by the echo technique. A curve for the profile is drawn according to the discussion, giving a rather flat profile in contrast to the parabola drawn for comparison.

C. Discussions.

The estimated values of the cardiac output in Table 7.2 are 30-70 % of normal values. There are six possible error sources to the measurements:

I A highpass filter of 4 poles at 600 Hz is used to remove the signal from the tissue. This will give an overestimation of the velocity (Section 5.2E).

II Because the artery is so large compared to the transducer, it is difficult to obtain a uniform illumination of the whole crossection. With the center of the observation region in the middle of the artery, the central portion

Patient number	Aortic diameter cm	Heart rate beats/min	Peak aortic flow "velocity" cm/sec	Peak aortic "flow" ml/sec	Stroke "volume" ml	Cardiac "output" liters/min
1	2.2	88	50	206	28	2.5
2	2.4	84	55	250	40	3.4
3	2.2	60	68	280	41	2.7
4	2.5	72	44	226	39	2.8
5	2.4	52	39	200	33	1.7
6	2.7	60	52	294	53	3.2
7	2.4	64	55	257	39	2.5
8	3.3	76	55	278	34	2.6
9	2.9	84	42	280	38	3.2
10	2.4	48	64	288	47	2.3
11	2.9	60	55	363	53	3.2
12	2.9	66	42	275	41	2.7
13	2.8	96	36	220	22	2.1
14	2.6	60	43	227	59	3.5
15	2.7	72	40	227	43	3.1
16	2.4	72	46	208	32	2.3
17	2.5	80	34	166	28	2.3
18	2.1	75	64	309	22	1.7

Table 7.2.

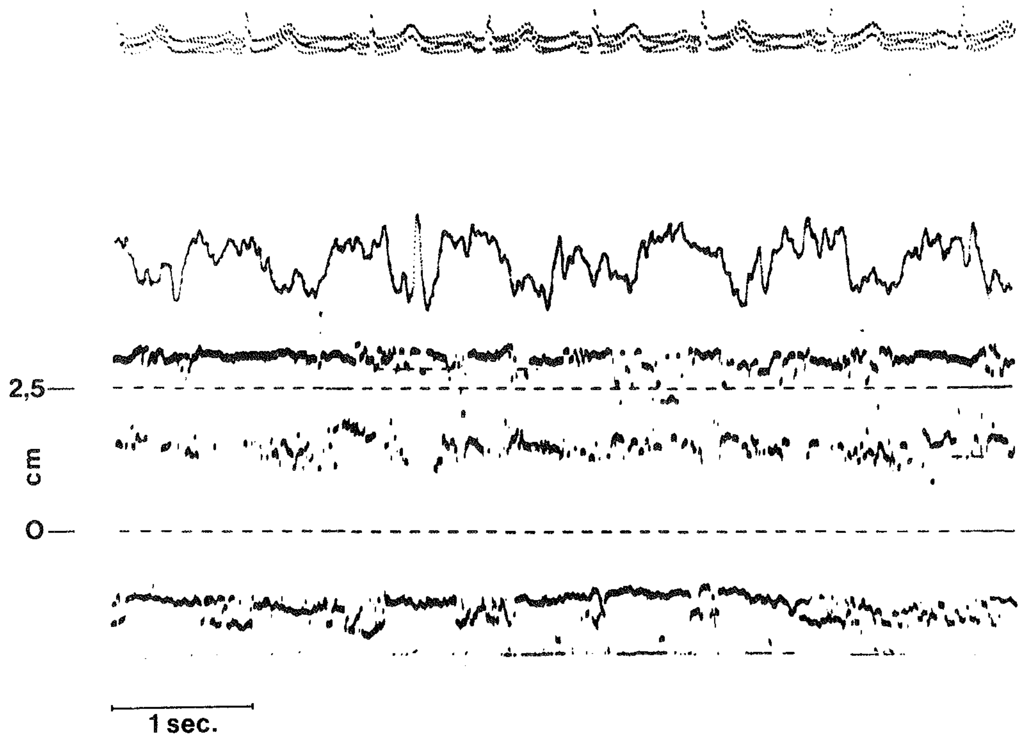

Figure 7.19. Ordinary M-scan of aorta. The two lower traces show the anterial and posterial wall of the aorta. The third trace from below is probably caused by a branching of the aorta. Upper trace is the ECG, and second upper trace is the velocity in the middle of the aorta. Zero velocity indicates that the beam is normal to the flow direction.

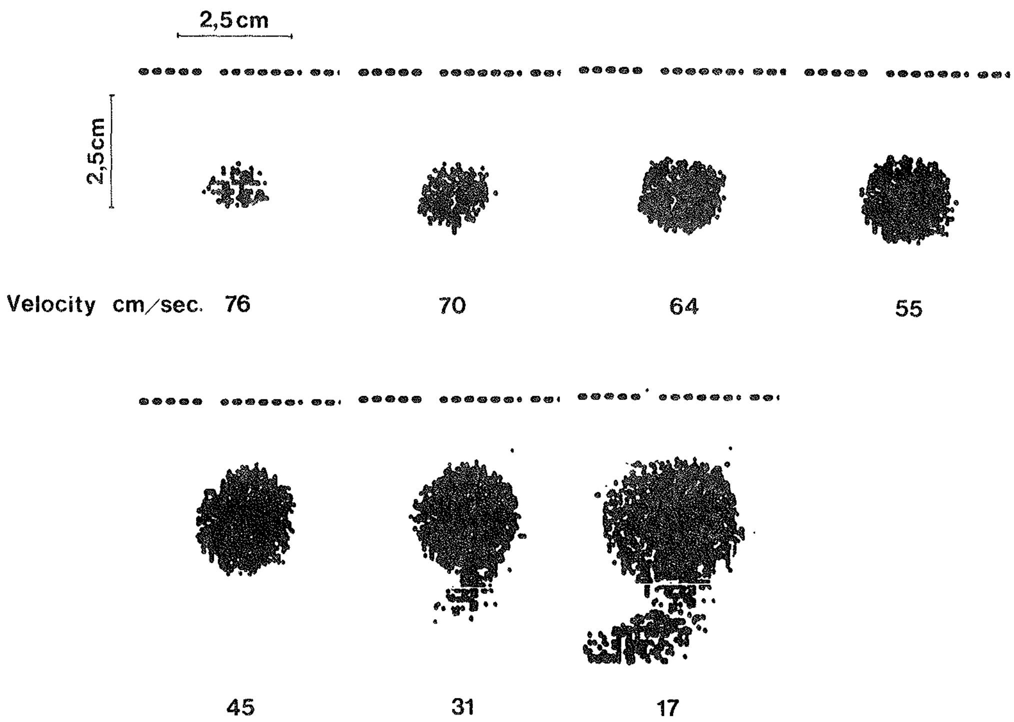

Figure 7.20. Sector scans of the aortic arc for different values of the velocity threshold.

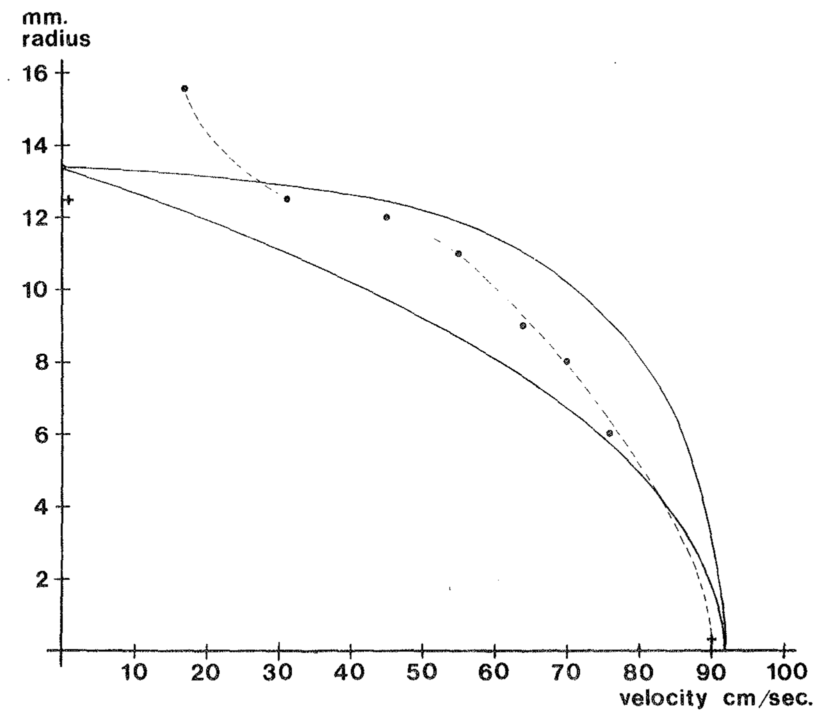

Figure 7.21. Velocity profile obtained from the sector scan in Figure 7.20. See discussion.

of the artery will be stronger illuminated than the periphery. This will give an overestimation of the velocity (Section 5.1E).

III Electronic noise in the signal. This will give an underestimation of the velocity (Section 5.2E). However, we have $S/N > 10\,dB$, which assures that this error source will not reduce the velocity estimate more than 90 %.

IV Stochastic errors in the velocity estimate due to the stochastic nature of the return signal. This is discussed in Chapter 6, and will be less than 10 %. Since this error is unbiased, the error in the integral of the velocity will be negligible.

V Errors in the diameter measurement. This will give a relative error in the flow and stroke volume estimate of

$$\frac{\Delta q}{q} = \frac{\Delta Q}{Q} = 2\,\frac{\Delta d}{d} \tag{7.8}$$

$\Delta d = 2$ mm and $d = 25$ mm gives

$$\frac{\Delta q}{q} = 2\,\frac{2}{25} = 0.16 \tag{7.9}$$

If the error in d is unbiased, this error will give an overestimation of q and Q due to the square dependency of d in Eq. (7.5).

VI A nonzero angle, θ, between the beam and the flow velocity. The estimate is proportional to $\cos\theta$ so that this error source will give an underestimation of the velocity.

Source I, II and V give overestimation of the velocity and source III and IV are negligible. We therefore conclude that the low estimates obtained are caused by a nonzero angle between the ultrasonic beam and the ascending aorta. The angle seems to range from $35^\circ - 70^\circ$ giving reductions in the estimates of 30-70 %.

Light [66] indicates that in the aortic arc the velocity is tangential to the ultrasonic beam. By scanning with the method described above, ellipsoidal forms of the areas in the aortic arc is frequently found. This indicates that the beam in most cases is not tangential to the arc. The scan presented in Figure 7.20 is, however, circular indicating no significant angle between the aorta and the beam.

By scanning the crossectional area, A', of the artery normal to the beam is obtained. This is related to the area, A, of the artery through

$$A' = A/\cos\theta \tag{7.10}$$

where θ is the angle between the beam and the artery.

By a uniform illumination of the artery, the instrument output, v', is related to the mean velocity v by

$$v' = v \cos\theta \tag{7.11}$$

Forming the product, $\cos\theta$ is cancelled, and we obtain the volume flow. This has been suggested by Aaslid [23].

However, the measured area will not be correct due to the convolution between the velocity profile and the ultrasonic beam shown in Figure 7.22. Figure 7.22a indicates the crossection of the artery with the ultrasonic beam. Let A be the region in the plane covered by the arterial crossection. Let $\chi_A(x,y)$ be the characteristic function of A, i.e.

$$\chi_A(x,y) = \begin{cases} 1 & (x,y) \in A \quad \text{(inside the artery)} \\ 0 & (x,y) \notin A \quad \text{(outside the artery)} \end{cases} \tag{7.12}$$

We also define a beam weighting function $\mathcal{B}(x-x',y-y')$ where (x,y) is the position of the center of the beam (indicated on the scope screen in our method). $\mathcal{B}$ is then the weight given to the point (x',y'). $\mathcal{B}$ may be approximated by a uniform weighting

$$\mathcal{B}(x,y) = \begin{cases} \dfrac{1}{\pi r^2} & x^2 + y^2 < r^2 \\ 0 & x^2 + y^2 > r^2 \end{cases} \tag{7.13}$$

where r is the beam radius.

Without highpass filters the measured profile will be

$$g(x,y) = \frac{\int dx'dy' v(x',y') w(x,x';y,y')}{\int dx'dy' w(x,x';y,y')} \tag{7.14}$$

where the weighting function w is given by

$$w(x,x';y,y') = \mathcal{B}(x-x',y-y')\chi_A(x',y') \tag{7.15}$$

$g(x,y)$ is thus the weighted average of the velocity field inside the beam and the artery.

When highpass filters are used, velocities below a certain limit set by the cutoff frequency of the highpass filters, v_ℓ, are not observed. The observable region of the artery, O, is those points (x,y) where $v(x,y) > v_\ell$, i.e.

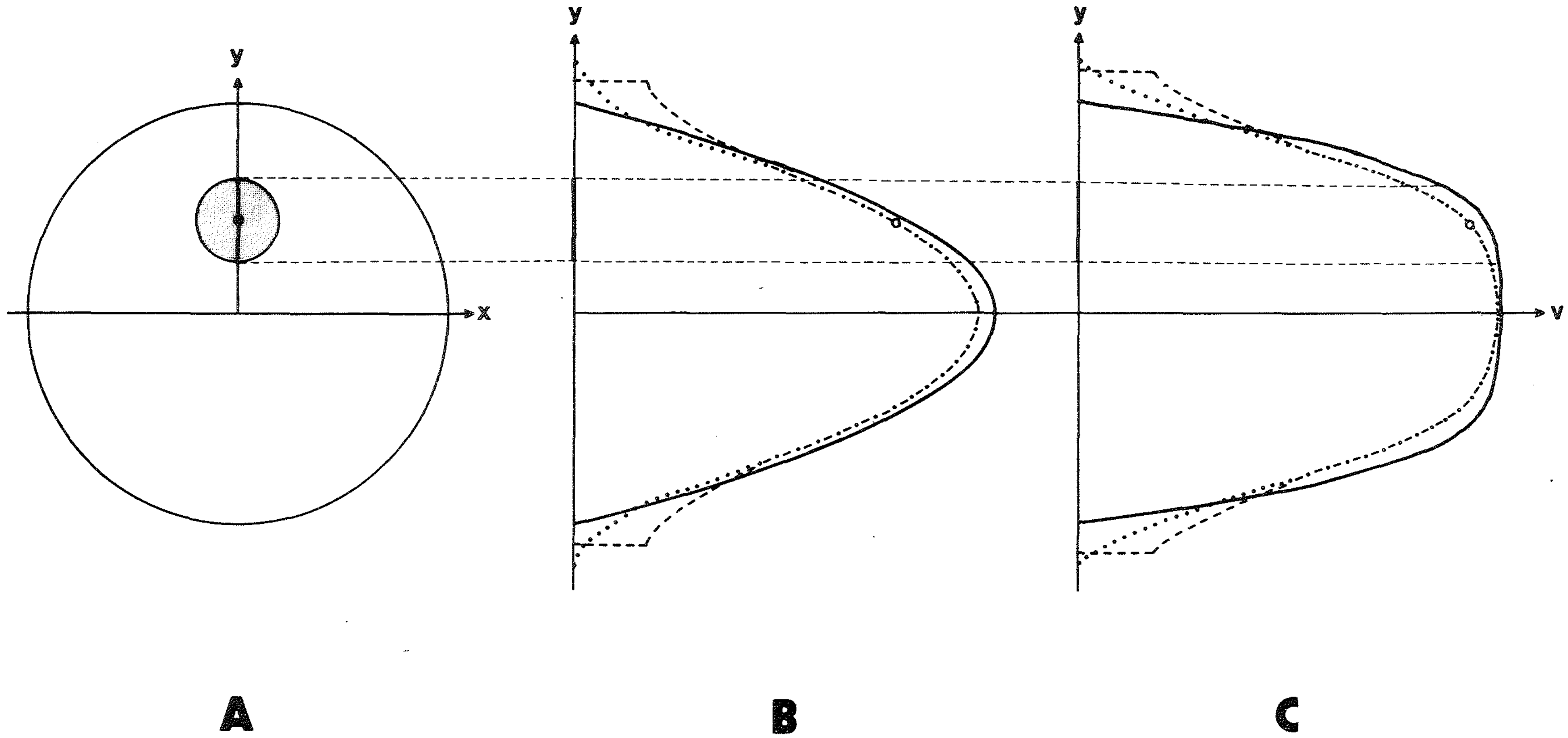

Figure 7.22. Convolution between the profile and the observation region.
a) Arterial and beam crossection. b) and c) Parabolic and blunt profile (p = 4) with modifications by the convolution. Dotted line: without highpassfilter. Stipled line: with highpassfilter, cuts off velocities below $0.2v_{max}$.

$$O = \{(x,y) | v(x,y) > v_\ell\} \tag{7.16}$$

The observable part of the velocity profile is

$$v_O(x,y) = v(x,y)\chi_O(x,y) \tag{7.17}$$

where $\chi_O(x,y)$ is the characteristic function of O. We also obtain a new weighting function $w_O(x,x';y,y')$

$$w_O(x,x';y,y') = \mathcal{B}(x-x',y-y')\chi_O(x',y') \tag{7.18}$$

With highpass filters the measured profile is

$$g_o(x,y) = \frac{\int dx'dy'v(x',y')w_O(x,x';y,y')}{\int dx'dy'w_O(x,x';y,y')} \tag{7.19}$$

For blunt profiles with p being an integer, (including the parabolic) analytical expressions may be found for g_o. Approximate evaluations of Eq. (7.19) may also be performed by expanding $v(x',y')$ in a Taylor series around (x,y) to the second order

$$\begin{aligned} v(x',y') = v(x,y) &+ \frac{\partial v}{\partial x}(x'-x) + \frac{\partial v}{\partial y}(y'-y) + \frac{1}{2}\left[\frac{\partial^2 v}{\partial x^2}(x'-x)^2\right. \\ &\left. + 2\frac{\partial^2 v}{\partial x \partial y}(x'-x)(y'-y) + \frac{\partial^2 v}{\partial y^2}(y'-y)^2\right] + \ldots\ldots \end{aligned} \tag{7.20}$$

When the beam is fully inside the observable region, we obtain

$$g_o(x,y) = v(x,y) + \frac{r^2}{8}\nabla^2 v(x,y) \tag{7.21}$$

If the second order approximation is not sufficient, we may from the mean value theorem of integrals, find a point inside the beam so that

$$g_o(x,y) = v(x,y) + \frac{r^2}{8}\nabla^2 v(x_0,y_0) \tag{7.22}$$

For a parabolic profile the second order expansion of Eq. (7.20) is exact and Eq. (7.21) is exact as long as the beam is fully inside the artery. There will be a position independent reduction in the velocity measured with the center of the beam at (x,y) by $r^2/4a^2$ from the real velocity at (x,y). a is the radius of the tube.

In general we may note the following

Profile convex outwards: $\nabla^2 v < 0$ reduction

Profile concave outwards: $\nabla^2 v > 0$ increase

We also note that the error increases monotonously with the curvature of the profile.

As the beam passes out of the observable region, the boundary conditions of the integration in Eq. (7.19) become more complicated. There will be an output of the instrument until the whole beam is outside the observable region of the artery. Then the instrument output will be zero. For an outwards convex profile the reduction in measured velocity will, therefore, decrease as the beam passes out of O and eventually result in an increase in the measured velocity.

The modified profiles for parabolic and blunt (p=4) real profile are shown in Figure 7.22b and c, both without highpass filter and with a highpass filter which cuts away velocities less than 0.2 of the maximum velocity. For a maximum velocity of 90 cm/s (2250 Hz) this corresponds to 18 cm/s (450 Hz). This is the values of the scan presented in Figures 7.20-21.

From the discussions above the estimated form of the real profile in Figure 7.21 is drawn. A parabolic profile is drawn for comparison and we see that the real profile is flatter than this as should be expected. We also note that due to the flatness of the profile the measured profile is more pointed than the real. The reason for this is that $\nabla^2 v$ increases with the distance from the artery axis.

The deconvolution of Eq. (7.17) may be mathematically performed by using the Fourier transform [25]. However, such a deconvolution is sensitive to errors in the measurement, and a better approach would probably be to model the profile as discussed in the next chapter.

A radius of aorta at the position of the scan greater than that obtained by the M-scan is indicated. This is reasonable since the M-scan is performed at a branching as shown in Figure 7.19 (same person).

Using an arterial diameter of 2.65 cm a mean flow of 4 l/min through the aortic arc is found. Taking account of 20 % to head and arms a cardiac output of 5 l/min is obtained. This is a normal value for a resting man. However, for the value to be trustworthy, two requirements are important:

I. The area estimation has to be performed with great care since it has a quadratic dependency to the linear dimensions and are thus very sensitive to errors in these as discussed above.

II. Uniform illumination of the artery is required to obtain a correct mean value estimate.

As discussed above, errors of these two types will result in an overestimation of the flow.

The illumination problem may be solved by scanning with a focused transducer across the artery and summing the contributions from different parts of the crossection.

One limitation of this method is that it is difficult to scan in the ascending aorta, due to its location. We are, therefore, left with a scan in the aortic arc and the flow to the head and the arms would be unknown.

Apart from this deficiency, the method should give an estimate of the flow in the aortic arc with an accuracy well within 20 %. Since the method is non-invasive and quick, it has several advantages to existing methods.

7.4. Phase shift counting position meter.

By counting the phase shifts of the received signal from a single reflector, as the posterior cardiac wall, the relative change in position of the reflector is estimated. From the quadrature components of the signal the direction of the motion, towards or away from the transducer, may be determined.

Figure 7.23 shows a phase shift up-down counter capable of counting changes of $\lambda/4$ in position of the reflector. The magnitude of e_1 is proportional to $\sin \varphi$ and that of e_2 is proportional to $\cos \varphi$ where φ is the phase of the reflected rf-signal. When the distance of the reflector to the transducer increases by an amount $\Delta \ell$, the increase in φ is

$$\Delta\varphi = 2\pi \frac{2\Delta\ell}{\lambda} \qquad (7.23)$$

The signals out of the two comparators are shown for constantly increasing and decreasing φ in Figure 7.24.

Suppose that φ is increasing. The position of the switches in Figure 7.23 is shown for comp II = -V. Comp I changes to -V and the upper capacitor is charged to -V. When comp. II changes to +V, the upper capacitor is switched to the integrator input and a charge $C_1 \cdot V$ is redrawn from C_2. This gives a rise in the integrator output of

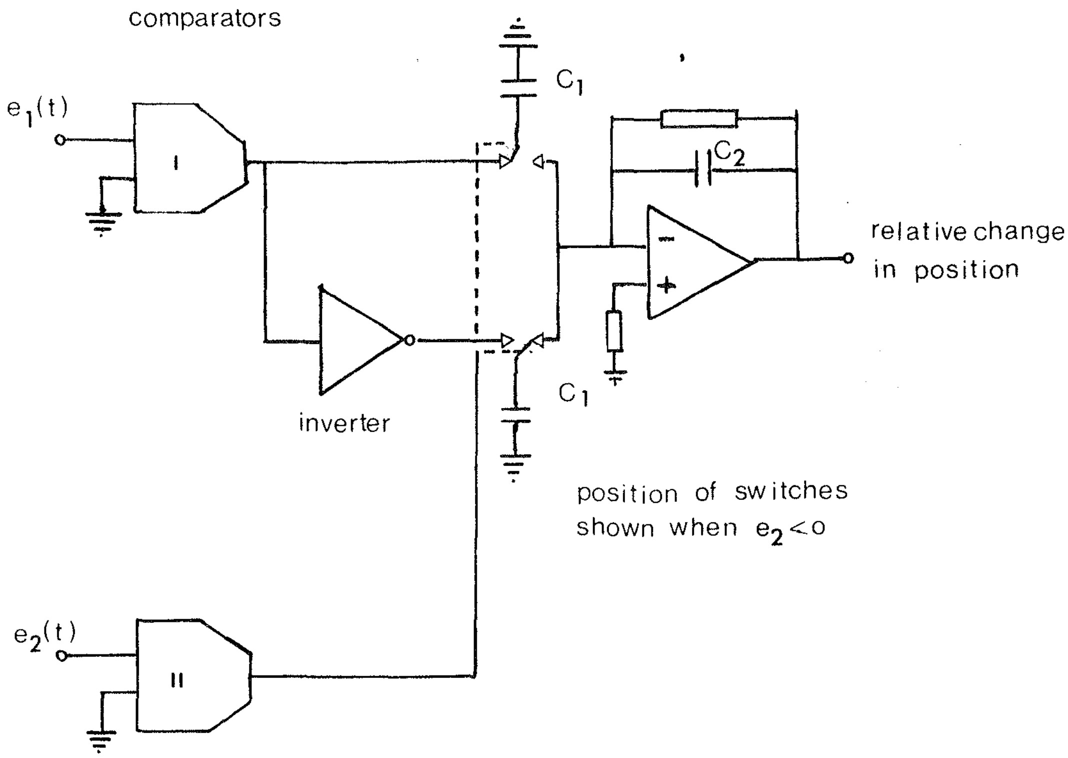

Figure 7.23. *Phase shift up-down counter for measuring relative change in position of a single reflector. The change of $\lambda/4$ in reflector position is observed.*

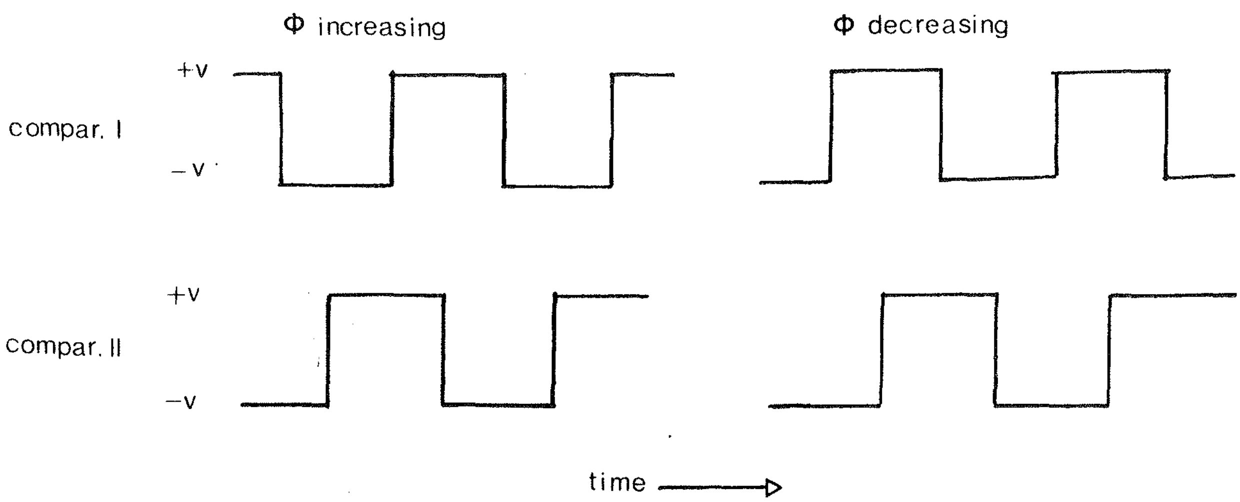

Figure 7.24. *Signals out of the comparators for constantly increasing and decreasing* φ.

$$\Delta V = \frac{C_1}{C_2} \cdot V \qquad (7.24)$$

At the same time the lower capacitor C_1 is switched to the inverter and loaded to -V before comp II goes to -V and the switches changes. By this change the lower capacitor redraws a charge $C_1 \cdot V$ from the integrator capacitor and a rise ΔV in the integrator output is obtained.

When φ is decreasing, a decrease ΔV in the integrator output is obtained for every change in the output of comparator II.

The distance in φ between the changes of the comparator outputs is π. From Eq. (7.23) we see that this corresponds to a change in distance between the transducer and the reflector.

$$\Delta \ell = \frac{\lambda}{4} \qquad (7.25)$$

Figure 7.25 shows the estimator ouptut from measurements of the posterior cardiac wall. The transducer is positioned on the chest at the fourth intracostal space.

The width of the ultrasonic beam introduces an error in the measurement. When the heart beats, the wall twists which give different changes in position of different points observed. In our measurement the transducer diameter is 10 mm. The reliability of the measurement must, therefore, be studied in future investigations.

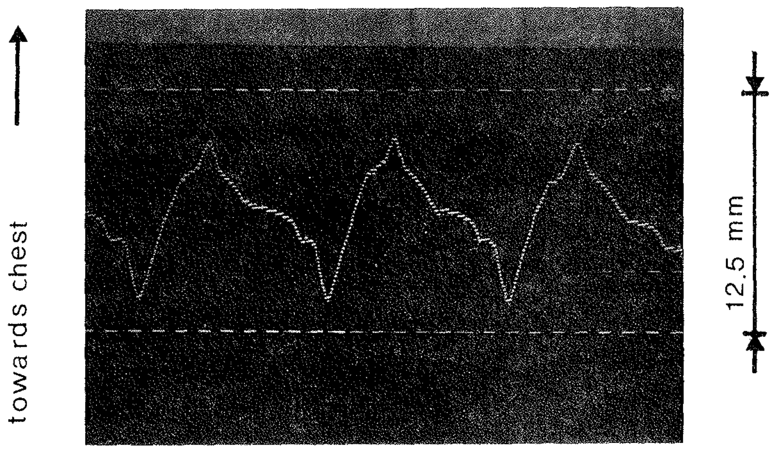

Figure 7.25. Output of phase shift counting detector from measurements on the posterior wall of the heart. Each jump represents a motion of $\lambda/4$ = 0.192 mm of the wall.

7.5. Summary.

A pulsed bidirectional ultrasonic flow velocity meter is described. It is shown that under idealized conditions in laboratory testing it gives an unbiased estimate of the mean velocity of flow. The estimate uncertainty is about 10 % at $v = 30$ cm/s. The uncertainty is inversely proportional to the square root of the velocity.

For using the instrument to measure aortic flow and cardiac output, practical problems arise. These are mainly

I. The problem of uniform illumination of the artery.

II. The unknown angle between the flow direction and the ultrasonic beam.

Both these problems may be solved using a focused transducer and scanning the observation region acorss the arterial lumen. However, it seems possible to scan only in the aortic arc. Thus the amount of flow for head and arms would be unknown.

Apart from the difficulties to obtain absolute values of the flow it seems possible to record relative changes in flow by holding the transducer in the same position and measuring at the same depth each time. Relative values are also sufficient for estimating the degree of backflow through the valves.

8. CONCLUDING REMARKS.

Our approach to the theoretical description of the doppler velocity meter may be schematically described as follows

Deterministic time dependent velocity field	$\longrightarrow$ Stochastic scattering	Doppler signal	$\longrightarrow$ Estimation	Mean velocity or velocity field estimate

Although Eq. (5.105) gives a deterministic correspondence between the velocity field and the doppler signal for a given event of $n(\vec{r},t)$, we have only stochastic knowledge of $n(\vec{r},t)$ which introduces the stochastic nature of the scattering process.

The properties of the deterministic profile are found in the stochastic properties of the doppler signal. Since the doppler signal is Gaussian (Section 5.2C), its higher order distributions may be obtained once the correlation functions, $R_{e_1e_1}(t,\tau)$ and $R_{e_1e_2}(t,\tau)$ are known (the approximations of Eq. (5.35) are assumed to be valid). Thus all the information of the velocity profile contained in the doppler signal are contained in these correlation functions. We have already seen how $R_{\dot{e}_2e_1}(t,t)/R_{e_1e_1}(t,t)$ give a vector weighted average of the instantaneous velocity field in the observation region and how the power spectrum of the doppler signal, the Fouriertransform of the correlation functions, may be used to deduce the form of the velocity field, Chapter 5.

However, since the velocity field is time dependent, the stochastic properties of the doppler signal has to be evaluated for a finite time introducing uncertainties in the estimates. This uncertainty may be reduced if we utilize apriori knowledge of the flow. Up to now we have considered our stochastic ensemble to be defined by the velocity field (unknown). Letting the velocity field be a stochastic process itself its probability law would give apriori information which could be combined with the measurement to give more accurate estimates of the velocity field.

Let the apriori expectation value of the mean velocity be $\bar{x}(t)$ with a covariance function $C_{xx}(t,\tau)$. Given a measurement

$$y(t) = x(t) + n(t) \tag{8.1}$$

where $n(t)$ is noise and $x(t)$ is the actual mean velocity, we can use a minimum variance linear filter to combine measurement and a priori knowledge (Wiener filter) [86]

$$\hat{x}(t) = \bar{x}(t) + \int_I d\tau\ h_0(t,\tau)[y(\tau) - \bar{x}(\tau)] \tag{8.2}$$

I is the interval of observation. The optimum filter response satisfies the following integral equation

$$C_{xy}(t,u) = \int_I dz\ h_0(t,z)C_{yy}(z,u) \tag{8.3}$$

Using the inverse kernel of the covariance function of y we obtain formally

$$h_0(t,\tau) = \int_I du\ C_{xy}(t,u)Q_{yy}(u,\tau) \tag{8.4}$$

where Q_{yy} is defined by [86]

$$\int_I du\ C_{yy}(z,u)Q_{yy}(u,\tau) = \delta(z - \tau) \tag{8.5}$$

The covariance function of the estimate is

$$\hat{C}_{xx}(t,\tau) = C_{xx}(t,\tau) - \int_I d\tau\ h_0(t,\tau)C_{xx}(t,\tau) \tag{8.6}$$

One way of obtaining apriori knowledge of x is to use a mathematical model of the cardiovascular system as that developed by Aaslid [69]. For cardiovascular systems that are almost periodic we can write

$$x_{k+1}(t) = x_k(t) + v_k(t) \tag{8.7}$$

with the measurement

$$y_k(t) = x_k(t) + w_k(t) \tag{8.8}$$

where the index refers to the number of the periodic and the zero reference of time is at the beginning of each period. The above equation expresses that the velocity of one period is the velocity of the preceding period plus a noise term v_k which we assume has zero mean and is uncorrelated to x. The covariance function is $C^k_{vv}(t,\tau)$. We also assume that $w_k(t)$ has zero mean and is uncorrelated to x and v_k with the covariance function $C^k_{ww}(t,\tau)$.

We are now to obtain the optimum estimate of $x_{k+1}(t)$ given the measurement set $\{y_1(t), y_2(t), \ldots, y_{k+1}(t)\}$. The expectation value of $x_{k+1}(t)$ apriori to the measurement $y_{k+1}(t)$ is obtained from Eq. (8.7)

$$\bar{x}_{k+1}(t) = E\{x_{k+1}(t)\,|y_1(t)\ldots y_k(t)\} = E\{x_k(t)\,|y_1(t)\ldots y_k(t)\} = \hat{x}_k(t) \tag{8.9}$$

Similarly the apriori covariance function is

$$C_{xx}^{k+1}(t,\tau) = \hat{C}_{xx}^{k}(t,\tau) + C_{vv}^{k}(t,\tau) \tag{8.10}$$

where $\hat{C}_{xx}^{k}(t,\tau)$ is the covariance function of $x_k(t)$ given the measurements $\{y_1(t)\ldots.y_k(t)\}$. The covariance function of $y_{k+1}(t)$ is

$$C_{yy}^{k+1}(t,\tau) = C_{xx}^{k+1}(t,\tau) + C_{ww}^{k+1}(t,\tau) \tag{8.11}$$

We now have the following iterative estimation scheme

$$\begin{aligned}
\hat{x}_{k+1}(t) &= \hat{x}_k(t) + \int_I d\tau\, h_0^{k+1}(t,\tau)[y_{k+1}(\tau) - \hat{x}_k(\tau)] \\
h_0^{k+1}(t,\tau) &= \int_I du\, C_{xx}^{k+1}(t,u)Q_{yy}^{k+1}(u,\tau) \\
\hat{C}_{xx}^{k+1}(t,\tau) &= C_{xx}^{k+1}(t,\tau) - \int_I d\tau\, h_0^{k+1}(t,\tau)C_{xx}^{k+1}(t,\tau)
\end{aligned} \tag{8.12}$$

C_{xx}^{k+1} and C_{yy}^{k+1} are given in Eqs. (8.10-11).

The covariance function of w is obtained by extending the calculations of Chapter 6 to non-zero lag. The stochastic properties of v must, however, be estimated from observations. It will systematically be affected by a number of factors such as the breath and changes in conditions of work. This introduces difficulties in applying the above scheme.

The filter given by Eq. (8.4) is the unrealizable one. We might also use the realizable Wiener filter. If x could be given a state space representation excited by white noise a Kalman filter might be used.

However, as the theory of Chapter 6 and the experiments of Chapter 7 show, the uncertainties in the estimates with the averaging periode so short that the parameters may be considered constant, is about 10 %. For measurement of aortic flow and cardiac output the unknown angle and the problem of uniform illumination of the artery introduces more severe limitations of the method.

The scanning method suggested in Section 7.3 seems a useful way to go to obtain absolute values for the flow in the aortic arc. However, the deconvolution which is necessary is sensitive to noise and according to Hottinger & al [25] it is difficult to perform in more than one dimension.

A less noise sensitive approach may be to use a parametric model of the profile, $v'(x,y,t;\vec{\alpha}(t))$ and adjust $\vec{\alpha}$ so as to get the best representation of the measurements by the convoluted version of this profile (Section 7.3C)

$$g_0'[x,y,t;\vec{\alpha}(t)] = \frac{\int dx'dy'v'[x',y',t;\vec{\alpha}(t)]w_0(x,x';y,y')}{\int dx'dy'w_0(x,x';y,y')} \tag{8.13}$$

A useful measure of the degree of approximation of g_0 by g_0' could be

$$J_c = \int_I dt\, dxdy[g_0(x,y,t) - g_0'(x,y,t;\vec{\alpha}(t))]^2 \tag{8.14}$$

The measurements will be given for discrete values of (x,y) as a function of time. If we discretize in time, we could form the set of vectors

$$\{h_{ik}\} = \{g_0'[x_i,y_i,t_k;\vec{\alpha}(t_k)]\} + \{w_{ik}\} \tag{8.15}$$

or in the vector notation

$$\underline{h}_k = \underline{g}_k'(\vec{\alpha}_k) + \underline{w}_k \tag{8.16}$$

$\underline{w}_k$ are error vectors.

In analogy with Eq. (8.14) we could minimize the following functional

$$J_d(\alpha) = \sum_{k=1}^{N} [\underline{h}_k - g_k'(\vec{\alpha}_k)]^T S_k [\underline{h}_k - g_k'(\vec{\alpha}_k)] \tag{8.17}$$

where S_k are positive definite weight matrices. They have to be chosen from the spacing of the points (x_i,y_i) if a discrete representation of Eq. (8.14) is wanted. An even distribution of points in space and time then gives $S_k = I$.

The usefulnes of a model is demonstrated by the following. Let v' be given by

$$\begin{aligned} v'(x,y;\vec{\alpha}) &= \alpha_1 + u(x,y;\vec{\alpha}') \\ \vec{\alpha}' &= (\alpha_2,\ldots\ldots,\alpha_n) \end{aligned} \tag{8.18}$$

Then the vector $\vec{\alpha}_0$ that minimizes

$$J(\vec{\alpha}) = \int dxdy[v(x,y) - v'(x,y;\vec{\alpha})]^2 \tag{8.19}$$

is such that

$$\int dxdy\ v(x,y) = \int dxdy\ v(x,y;\vec{\alpha}_0) \tag{8.20}$$

i.e. the flow determined by the approximate profile is identical to the actual flow. This is seen by differentiating Eq. (8.19) with respect to α_1.

When the profiles are convoluted, the minimization of Eq. (8.14) or (8.17) will not in general give the minimum of Eq. (8.19). When the beam diameter is small compared to the radius of curvature of the velocity profile, the deviation between these values of $\vec{\alpha}$ will not be great.

If the model is a good representation of the real profile, measurements in a few positions only would be necessary to obtain a good value of $\vec{\alpha}_0$. Thus this method would be much faster than a deconvolution. The scan in Section 7.3 indicates that the following elliptical form of the blunt profile may be used as a model.

$$v(x,y;\vec{\alpha}) = \alpha_1 + v_0\left\{1 - \left[\frac{x^2}{a^2} + \frac{y^2}{b^2}\right]^{p/2}\right\} \tag{8.21}$$

where the parameter vector $\vec{\alpha}$ is

$$\vec{\alpha} = [\alpha_1, v_0, a, b, p]$$

Actually v_0 will be a function of time in Eq. (8.14) or k in Eq. (8.17)

APPENDIX I

Acoustic Lens Materials.

Four types of acoustic lens materials have been studied.

I Plexiglass.

II Araldite Casting Resin D and Hardener 951, Ciba, composition 9:1.

III Araldite Casting Resin D and Polyamid Hardener 846, Ciba, composition 55:45.

IV Hard PVC.

Data for the materials are given in Table I.1. The focal length of a plane concave lens with radius of curvature of the concave face of 2.3 cm is given.

Material	I	II	III	IV
Wave vel. m/s	3450	2420	2250	2060
Density g/cm^3	1.2	1.28	1.19	1.35
Impedance 10^6 kg/cm^2	4.15	3.1	2.68	2.78
Focal length cm	4	6	7	8.5

Table I-1. Data for lens materials.

Reflection losses in the lenses increase with increasing characteristic impedance of the materials which increases the losses for the lower focal lengths.

APPENDIX II

Measurement of Blood Velocity.

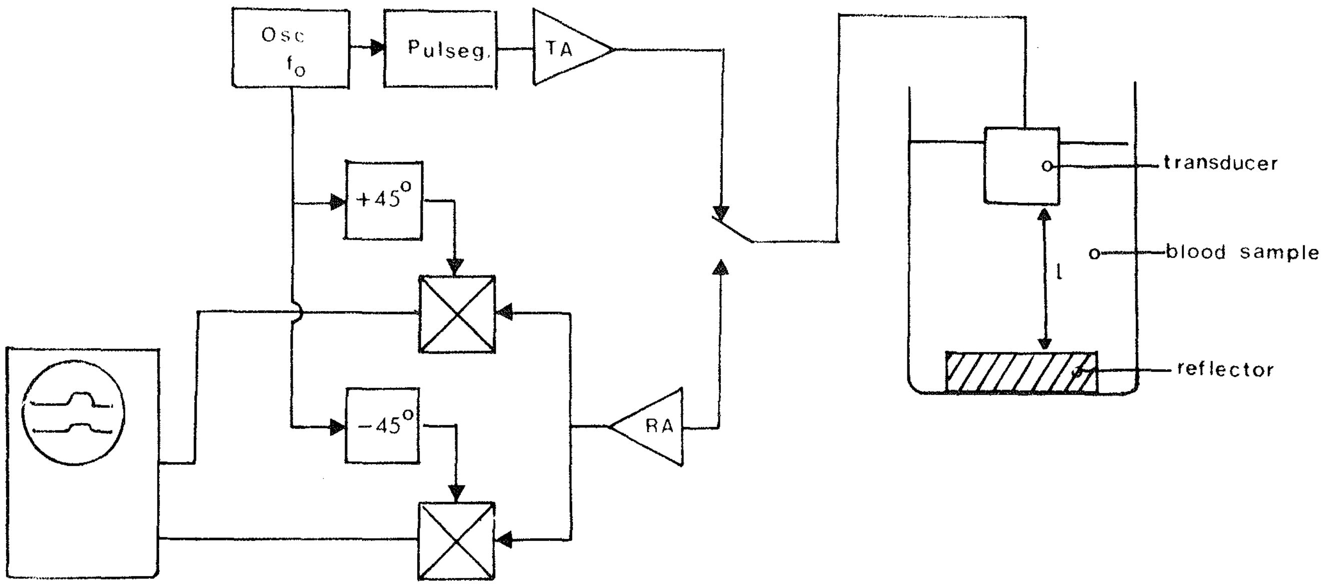

Figure II.1. Apparatus for measuring blood velocity.

The apparatus for measuring the blood velocity is similar to the pulsed doppler flowmeter. Coherent ultrasonic pulses are transmitted into the blood sample and reflected by a polished block of brass. The received signal is split into two channels and phase demodulated by two signals 90° out of phase and synchronous to the local oscillator. Two channels are used to increase the accuracy of the measurement.

The demodulated signals are observed on an y/time scope so that the phase of the received pulse may be compared to the reference signals. When the distance between the transducer and the reflector changes, the demodulated pulses oscillate. One cycle of oscillation for each channel corresponds to a change of $\lambda/2$ in ℓ. The zero crossings of the oscillations measure $\lambda/4$ changes in ℓ. Since the oscillations of the two demodulated signals are 90° out of phase, $\lambda/8$ changes in ℓ may be observed by counting the zero crossings of both channels.

The length ℓ between the transducer and the reflector is changed by an amount $\Delta\ell$ and the zero crossings of both channels are counted to be n. The transmitted frequency is f_0. We than have

$$n \cdot \lambda/8 = \Delta\ell \tag{II.1}$$

Using the relation $\lambda = c/f_0$ gives

$$c = \frac{8f_0 \cdot \Delta\ell}{n} \tag{II.2}$$

Since only the zero crossings of the phase are counted there will be a quantification error in c

$$\Delta c_1 = 8f_0 \cdot \Delta\ell \left(\frac{1}{n} - \frac{1}{n+1}\right) \tag{II.3}$$

$$\frac{\Delta c_1}{c} = \frac{1}{n+1} \tag{II.4}$$

To minimize this error n and thereby $\Delta\ell$ should be made large.

We use a micrometer screw to position the transducer. Maximum $\Delta\ell = 16$ mm which gives $n \sim 170$. The uncertainty in the measurement of $\Delta\ell$ is .02 mm. A frequency of 2 MHz is used.

The quantification error of c is

$$\frac{\Delta c_1}{c} = .6\ \% \tag{II.5}$$

while the error introduced by the uncertainty in $\Delta\ell$ is

$$\frac{\Delta c_2}{c} = .2\ \% \tag{II.6}$$

Since $c \approx 1500$ m/s, the maximum error in the measurement of c is

$$12 \text{ m/s} \tag{II.7}$$

Outdated human blood from the bank was carefully centrifuged and cells and plasma were mixed to get samples with different cell content. Each sample was measured two times subsequently. If these values differed, a third measurement was performed.

APPENDIX III

Proof of the Reciprocity Relation for Transducers.

We approximate the transducer by a radiating piston with a specified normal velocity at the surface [54]. The field at a position $\vec{r}$ will be

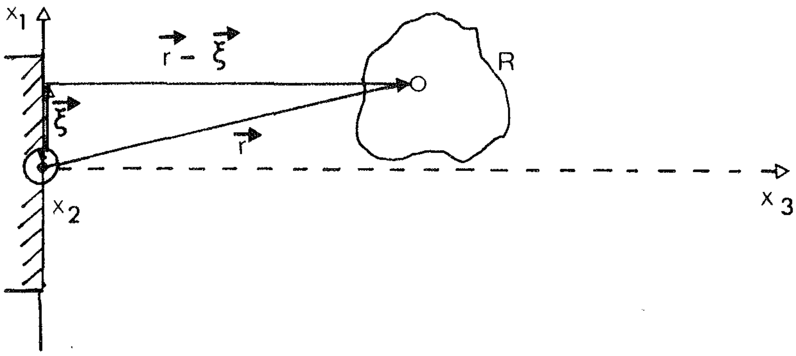

Figure III.1. Proof of the reciprocity relation.

$$p_R(\vec{r},t) \sim \int_S d^2\xi \, \frac{e^{-i(k|\vec{r}-\vec{\xi}|-\omega t)}}{|\vec{r} - \vec{\xi}|} \tag{III.1}$$

where S is the surface of the transducer and $\vec{\xi}$ is the position vector on S.

Let a monopole source distribution, $m(\vec{r},t)$, be located in a region R. The radiated field from this distribution at a position $\vec{\xi}$ will be

$$p(\vec{\xi},t) \sim \int_R d^3r \, \frac{e^{-i(k|\vec{\xi}-\vec{r}|-\omega t)}}{|\vec{\xi} - \vec{r}|} \, m(\vec{r},t) \tag{III.2}$$

The waves will hit the transducer and excite an electric voltage at the output. This voltage will be proportional to the integral of the complex pressure amplitude over the transducer.

$$e_m(t) \sim e^{i\omega t} \int_S d^2\xi \int_R d^3r \, \frac{e^{-ik|\vec{\xi}-\vec{r}|}}{|\vec{\xi} - \vec{r}|} \, m(\vec{r},t) \tag{III.3}$$

Interchanging the integration we see that the surface integral is proportional to $\hat{p}_R(\vec{r})$. We, therefore, have

$$e_m(t) \sim e^{i\omega t}\int_R d^3r \cdot m(\vec{r},t)\,\hat{p}_R(\vec{r}) \qquad \text{(III.4)}$$

This completes the proof for the monopole source density.

The dipole density $\vec{d}(\vec{r},t)$ is represented by two monopole densities q and $-q$ equal in magnitude and opposite in sign, and displaced a small distance ℓ relative to eachother, i.e.

$$\vec{d}(\vec{r},t) = \lim_{\substack{\vec{\ell}\to 0 \\ q\to\infty}} \vec{\ell}\; q(\vec{r},t) \qquad \text{(III.5)}$$

We then have for the output from the transducer, using $-\alpha$ for the proportionality factor in Eq. (III.4)

$$e_d(t) = -\alpha e^{i\omega t}\int d^3r \lim \vec{\ell}\,(q(\vec{r},t) - q(\vec{r}+\vec{\ell},t))\,\hat{p}_r(\vec{r})$$

$$= -\alpha e^{i\omega t}\int d^3r \lim \vec{\ell}\cdot\nabla q(\vec{r},t)\,\hat{p}_r(\vec{r})$$

Integrating the last expression by parts, we get

$$e_d(t) = \alpha e^{i\omega t}\int d^3r \lim \vec{\ell}\cdot q(\vec{r},t)\,\nabla\hat{p}_r(\vec{r})$$

or at last

$$e_d(t) = \alpha e^{i\omega t}\int d^3r\; \vec{d}(\vec{r},t)\,\nabla\hat{p}_r(\vec{r}) \qquad \text{(III.6)}$$

This completes the proof for the dipole source distribution.

APPENDIX IV

Evaluation of Eq. (5.48).

We change the variables of integration in Eq. (5.47)

$$p_2 = \omega - \vec{q}\,\vec{v}\,(\vec{\sigma}) \tag{IV.1}$$

p_2 = const. defines a curve or family of curves in the $\vec{\sigma}$-plane, $\{\Gamma_i(\omega,p_2)\}$. Let us first assume that p_2 = const. defines a single curve Γ as shown in Figure IV.1. This curve has a parametric representation

$$\vec{\sigma}(\omega,p_2\ ;\ p_1) \tag{IV.2}$$

where p_1 is the arc length parameter of Γ oriented so that $\nabla(\vec{q}\,\vec{v}) \times \partial\vec{\sigma}/\partial p_1$ points out of the plane.

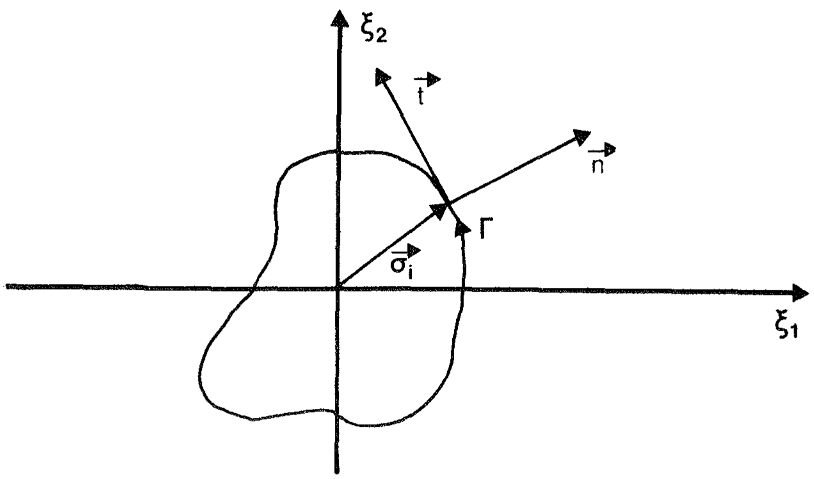

Figure IV.1. The curve $\Gamma(\omega,p_2)$ *of Eq. (IV.2).*

The unit tangent vector, $\vec{t}$, along Γ is

$$\vec{t} = \frac{\partial\vec{\sigma}}{\partial p_1} = \frac{1}{|\nabla\vec{q}\,\vec{v}|}\left[\frac{\partial\,\vec{q}\,\vec{v}}{\partial\xi_2}\,\vec{e}_1 - \frac{\partial\,\vec{q}\,\vec{v}}{\partial\xi_1}\,\vec{e}_2\right] \tag{IV.3}$$

From Eq. (IV.1) we obtain

$$dp_2 = -\frac{\partial\,\vec{q}\,\vec{v}}{\partial\xi_1}\,d\xi_1 - \frac{\partial\,\vec{q}\,\vec{v}}{\partial\xi_2}\,d\xi_2 \tag{IV.4}$$

On the other hand we generally have

$$\begin{bmatrix} d\xi_1 \\ \\ d\xi_2 \end{bmatrix} = \begin{bmatrix} \dfrac{\partial\xi_1}{\partial p_1} & \dfrac{\partial\xi_1}{\partial p_2} \\ \\ \dfrac{\partial\xi_2}{\partial p_1} & \dfrac{\partial\xi_2}{\partial p_2} \end{bmatrix} \begin{bmatrix} dp_1 \\ \\ dp_2 \end{bmatrix} \tag{IV.5}$$

$$\begin{bmatrix} dp_1 \\ \\ dp_2 \end{bmatrix} = \frac{1}{J} \begin{bmatrix} \dfrac{\partial\xi_2}{\partial p_2} & -\dfrac{\partial\xi_1}{\partial p_2} \\ \\ -\dfrac{\partial\xi_2}{\partial p_1} & \dfrac{\partial\xi_1}{\partial p_1} \end{bmatrix} \begin{bmatrix} d\xi_1 \\ \\ d\xi_2 \end{bmatrix} \tag{IV.6}$$

where J is the Jacobian of the transformation $(\xi_1,\xi_2) \rightarrow (p_1,p_2)$. Comparing (IV.3), (IV.4) and (IV.6) we see that the following relation holds

$$\frac{\partial p_2}{\partial \xi_1} = -\frac{\partial \vec{q}\,\vec{v}}{\partial \xi_1} = -\frac{1}{J}\frac{\partial \xi_2}{\partial p_1} = \frac{1}{J}\frac{1}{|\vec{\nabla q}\;\vec{v}|}\frac{\partial \vec{q}\,\vec{v}}{\partial \xi_1}$$

By comparing the second and the last term the Jacobian of the transformation is obtained

$$J = -\frac{1}{|\vec{\nabla q}\;\vec{v}(\vec{\sigma})|} \tag{IV.7}$$

Eq. (5.47) may now be written

$$G_{\hat{e}\hat{e}}(\omega) = 2\pi|\alpha|^2 \int dp_1 dp_2 \frac{L[\vec{\sigma}(p_1,p_2)]\langle n^2[\vec{\sigma}(p_1,p_2)]\rangle \delta(p_2)}{|\vec{\nabla q}\;\vec{v}[\vec{\sigma}(p_1,p_2)]|} \tag{IV.8}$$

Performing the integration over p_2 we may express the power spectrum by the following curve integral

$$G_{\hat{e}\hat{e}}(\omega) = 2\pi|\alpha|^2 \int_{\Gamma(\omega)} dp_1 \frac{L(\vec{\sigma})\langle n^2(\vec{\sigma})\rangle}{|\vec{\nabla q}\;\vec{v}(\vec{\sigma})|} \tag{IV.9}$$

where $\Gamma(\omega)$ is the curve $\Gamma(\omega,0)$.

If the relation $p_2 = 0$ holds for a family of curves $\{\Gamma_i(\omega)\}$ in the $\vec{\sigma}$-plane, the result will still be given by Eq. (IV.9) if we extend $\Gamma(\omega)$ to be

$$\Gamma(\omega) = \bigcup_i \Gamma_i(\omega) \qquad \text{(IV.10)}$$

APPENDIX V

Filtering and Spectral Estimation of Stochastic Processes.

The correlation function between two real stochastic processes x and y is defined by

$$R_{xy}(t_1,t_2) = \langle x(t_1)y(t_2)\rangle \tag{V.1}$$

Similarly the covariance function between the same processes is defined by

$$\begin{aligned} C_{xy}(t_1,t_2) &= \langle [x(t_1) - \langle x(t_1)\rangle][y(t_2) - \langle y(t_2)\rangle]\rangle \\ &= R_{xy}(t_1,t_2) - \langle x(t_1)\rangle\langle y(t_2)\rangle \end{aligned} \tag{V.2}$$

Suppose that the processes x and y pass through two linear filters with impulse responses h_p and h_q to give $p(t)$ and $q(t)$. We then have [75]

$$\begin{aligned} &p(t) = \int_{\mathbb{R}} d\tau h_p(t,\tau)x(\tau) \qquad q(t) = \int_{\mathbb{R}} d\tau h_q(t,\tau)y(\tau) \\ &\langle p(t)\rangle = \int_{\mathbb{R}} d\tau h_p(t,\tau)\langle x(\tau)\rangle \qquad \langle q(t)\rangle = \int_{\mathbb{R}} d\tau h_q(t,\tau)\langle y(\tau)\rangle \\ &R_{pq}(t_1,t_2) = \int_{\mathbb{R}} d\tau_1 d\tau_2 h_p(t_1,\tau_1)h_q(t_2,\tau_2)R_{xy}(\tau_1,\tau_2) \\ &C_{pq}(t_1,t_2) = \int_{\mathbb{R}\times\mathbb{R}} d\tau_1 d\tau_2 h_p(t_1,\tau_1)h_q(t_2,\tau_2)C_{xy}(\tau_1,\tau_2) \\ &\mathbb{R} = (-\infty,\infty) \end{aligned} \tag{V.3}$$

In the special case of wide sense stationary processes and time independent filters we have

$$\begin{aligned} &p(t) = \int_{\mathbb{R}} d\tau h_p(t-\tau)x(\tau) \qquad q(t) = \int_{\mathbb{R}} d\tau h_q(t-\tau)y(\tau) \\ &\langle p\rangle = \langle x\rangle\int_{\mathbb{R}} d\tau h_p(\tau) \qquad \langle q\rangle = \langle y\rangle\int_{\mathbb{R}} d\tau h_q(\tau) \\ &R_{pq}(\tau) = \int_{\mathbb{R}\times\mathbb{R}} d\tau_1 d\tau_2 h_p(\tau_1)h_q(\tau_1 - \tau_2)R_{xy}(\tau + \tau_2) \\ &C_{pq}(\tau) = \int_{\mathbb{R}\times\mathbb{R}} d\tau_1 d\tau_2 h_p(\tau_1)h_q(\tau_1 - \tau_2)C_{xy}(\tau + \tau_2) \end{aligned} \tag{V.4}$$

Especially we obtain for the covariance between p and q

$$\langle \delta p \, \delta q \rangle = \langle [p(t) - \langle p(t) \rangle][q(t) - \langle q(t) \rangle] \rangle = C_{pq}(0) \tag{V.5}$$

In the discussion of estimator type I and II we shall assume that the dc-gain of the filters is normalized to unity, i.e.

$$\int_{\mathbb{R}} d\tau \, h(\tau) = 1 \tag{V.6}$$

We also consider the case of timesteady fields only.

In the case of strong filtering the bandwidth of the filters are much smaller than that of C_{xy}. The variation of the filter responses over the range where C_{xy} is appreciably different from zero may, therefore, be neglected, and we may use the following approximation

$$C_{pq}(\tau) = \int_{\mathbb{R}} d\tau_1 h_p(\tau_1) h_q(\tau_1 + \tau) \int_{\mathbb{R}} d\tau_2 C_{xy}(\tau_2) \tag{V.7}$$

or especially for zero lag

$$C_{pq}(0) = \int_{\mathbb{R}} d\tau_1 h_p(\tau_1) h_q(\tau_1) \int_{\mathbb{R}} d\tau_2 C_{xy}(\tau_2) \tag{V.8}$$

Suppose that our filters are obtained by time scaling of a standard filter, h_0, (e.g. unit bandwidth). The normalization of Eq. (V.6) is used. We then have

$$h(\tau) = \frac{1}{T} h_0(\frac{\tau}{T}) \tag{V.9}$$

In this case we get

$$\boxed{C_{pq}(0) = \frac{1}{T} \int_{\mathbb{R}} d\tau_1 h_{0p}(\tau_1) h_{0q}(\tau_1) \int_{\mathbb{R}} d\tau_2 C_{xy}(\tau_2)} \tag{V.10}$$

This means that in the case of strong filtering, the output covariance is inversely proportional to the integration time.

Methods of power spectrum estimation are described in [71], [72], [78]. An estimate of the crosscorrelation spectrum of two real processes x(t) and y(t) may be obtained by multiplication of the finite time Fourier transforms of the processes

$$\hat{G}_{xy}(\omega) = \frac{1}{T} X^*_T(\omega) Y_T(\omega) = \frac{1}{T} \int_{-T/2}^{T/2} dt x(t) e^{i\omega t} \int_{-T/2}^{T/2} dt y(t) e^{-i\omega t} \tag{V.11}$$

The expectation value of this estimator is [78]

$$<\hat{G}_{xy}(\omega)> = G_{xy}(\omega) * T\left(\frac{\sin \frac{\omega T}{2}}{\frac{\omega T}{2}}\right)^2 \tag{V.12}$$

The variance of this estimate will, however, not tend to zero when $T \to \infty$, [72], and the estimate is, therefore, convolved with a suitable spectral window $W(\omega)$

$$\tilde{G}_{xy}(\omega) = \hat{G}_{xy}(\omega) * W(\omega) \tag{V.13}$$

The variance of this smoothned estimate will tend to zero as $T \to \infty$. The Fourier transform of the spectral window $W(\omega)$ is called the data window, $w(\tau)$

$$w(\tau) \leftrightarrow W(\omega) \tag{V.14}$$

The windows are normalized so that

$$w(0) = \frac{1}{2\pi} \int_{\mathbb{R}} d\omega W(\omega) = 1 \tag{V.15}$$

The Fourier transform of $\hat{G}_{xy}(\omega)$ is often used as an estimate of the crosscorrelation function between x and y [78]

$$\hat{R}_{xy}(\tau) = \begin{cases} \frac{1}{T} \int_{(-T+|\tau|)/2}^{(T-|\tau|)/2} dt\, x[t+\tau/2]y[t-\tau/2] & |\tau| < T \\ 0 & \text{else} \end{cases} \tag{V.16}$$

The expectation value of this estimator is, Eq. (V.12)

$$<\hat{R}_{xy}(\tau)> = \begin{cases} [1 - \frac{|\tau|}{T}]R_{xy}(\tau) & |\tau| < T \\ 0 & \text{else} \end{cases} \tag{V.17}$$

Similarly we obtain for the expectation value of the Fourier transform of $\tilde{G}_{xy}(\omega)$, $\tilde{R}_{xy}(\tau)$ from Eq. (V.13)

$$\langle \tilde{R}_{xy}(\tau) \rangle = \begin{cases} [1 - \frac{|\tau|}{T}]\, w(\tau) R_{xy}(\tau) & |\tau| < T \\ 0 & \text{else} \end{cases} \tag{V.18}$$

The zeroth and first moment of $\tilde{G}_{xy}(\omega)$ are defined by

$$\boxed{q = \int_{\mathbb{R}} d\omega\ \tilde{G}_{xy}(\omega)} \tag{V.19}$$

$$\boxed{p = \int_{\mathbb{R}} d\omega\ i\omega\ \tilde{G}_{xy}(\omega)} \tag{V.20}$$

Inserting $\tilde{G}_{xy}$ from Eqs. (V.11-13) we obtain

$$q = \frac{1}{2\pi T} \int_{\mathbb{R}} d\omega \int_{\mathbb{R}} dw \int_{-T/2}^{T/2} dt_1 \int_{-T/2}^{T/2} dt_2 x(t_1) y(t_2) e^{i(\omega - w)(t_1 - t_2)} W(w) \tag{V.21}$$

The integration over ω may be performed straight and we obtain

$$\int_{\mathbb{R}} d\omega\ e^{i\omega(t_1 - t_2)} = 2\pi\delta(t_1 - t_2) \tag{V.22}$$

The integration over t_2 is now easily performed and the integration over w is obtained from Eq. (V.15). The result is

$$\boxed{q = \frac{2\pi}{T} \int_{-T/2}^{T/2} dt\ x(t) y(t)} \tag{V.23}$$

For the second moment we use the following relation

$$\int_{\mathbb{R}} d\omega\ i\omega\ e^{i\omega(t_1 - t_2)} = 2\pi\delta'(t_1 - t_2) \tag{V.24}$$

where δ' is the derivative of the δ-function. By performing partial integration over t_2 and assuming $W(w)$ to be symmetric so that

$$\int_{\mathbb{R}} dw\ w\ W(w) = 0 \tag{V.25}$$

we obtain

$$\boxed{p = \frac{2\pi}{T} \int_{-T/2}^{T/2} dt\ x(t) \dot{y}(t) - \frac{\pi}{T} [x(T/2) - x(-T/2) y(-T/2)]} \tag{V.26}$$

We thus see that the moments are independent of the spectral windows used. If we are interested in these only and not the entire spectrum, the convolution in Eq. (V.13) is not necessary to perform.

APPENDIX VI

Correlation Functions and Power Spectra for the Derivative of a Stochastic Process.

Given the mean square differentiable complex processes x and y. Then [79]

$$R_{x\dot{y}}(t_1,t_2) = \langle x^*(t_1)\dot{y}(t_2)\rangle = \frac{\partial}{\partial t_2} R_{xy}(t_1,t_2)$$

$$R_{\dot{x}y}(t_1,t_2) = \langle \dot{x}^*(t_1)y(t_2)\rangle = \frac{\partial}{\partial t_1} R_{xy}(t_1,t_2) \tag{VI.1}$$

For wide sence stationary processes we immediately obtain from these equations with $\tau = t_2-t_1$

$$R_{x\dot{y}}(\tau) = R_{x\dot{y}}(t_2 - t_1) = \langle x^*(t_1)\dot{y}(t_2)\rangle = \frac{\partial}{\partial t_2} R_{xy}(t_2 - t_1) = \dot{R}_{xy}(\tau)$$

$$R_{\dot{x}y}(\tau) = R_{\dot{x}y}(t_2 - t_1) = \langle \dot{x}^*(t_1)y(t_2)\rangle = \frac{\partial}{\partial t_1} R_{xy}(t_2 - t_1) = -\dot{R}_{xy}(\tau) \tag{VI.2}$$

From these equations it directly follows

$$R_{\dot{x}\dot{y}}(t_1,t_2) = \frac{\partial^2}{\partial t_1 \partial t_2} R_{xy}(t_1,t_2)$$

$$R_{\dot{x}\dot{y}}(\tau) = -\ddot{R}_{xy}(\tau) \tag{VI.3}$$

For the cross power spectra we obtain

$$G_{x\dot{y}}(\omega) = \mathcal{F}\{R_{x\dot{y}}(\tau)\} = \mathcal{F}\{\dot{R}_{xy}(\tau)\} = i\omega G_{xy}(\omega)$$

$$G_{\dot{x}y}(\omega) = \mathcal{F}\{R_{\dot{x}y}(\tau)\} = -\mathcal{F}\{\dot{R}_{xy}(\tau)\} = -i\omega G_{xy}(\omega) \tag{VI.4}$$

APPENDIX VII

Derivation of Covariance Functions for Estimator Type II.

Theorem. Let x and y be two Gaussian random vectors with zero mean $\dim(\vec{x}) = \dim(\vec{y}) = 2$, i.e.

$$\vec{x} = \begin{bmatrix} x_1 \\ x_2 \end{bmatrix} \qquad \vec{y} = \begin{bmatrix} y_1 \\ y_2 \end{bmatrix}$$

Then

$$\langle x_1 x_2 \operatorname{sgn} y_1 \operatorname{sgn} y_2 \rangle = \frac{2}{\pi} \Bigg\{ \langle x_1 x_2 \rangle \arcsin \rho_{y_1 y_2}$$

$$+ \frac{\langle x_1 \tilde{y}_1 \rangle \langle x_2 \tilde{y}_2 \rangle + \langle x_1 \tilde{y}_2 \rangle \langle x_2 \tilde{y}_1 \rangle - \rho_{y_1 y_2} [\langle x_1 \tilde{y}_1 \rangle \langle x_2 \tilde{y}_1 \rangle + \langle x_1 \tilde{y}_2 \rangle \langle x_2 \tilde{y}_2 \rangle]}{\sqrt{1 - \rho^2_{y_1 y_2}}} \Bigg\} \qquad \text{(VII.1)}$$

where we have defined

$$\tilde{y}_i = \frac{y_i}{\sqrt{\langle y_i^2 \rangle}} \qquad i = 1,2$$

$$\rho_{y_1 y_2} = \langle \tilde{y}_1 \tilde{y}_2 \rangle$$

Note: The normalized variables $\tilde{y}_i$ enters since it is only the sign of y_1 and y_2 which determine the value of the product.

Proof.

$$\langle x_1 x_2 \operatorname{sgn} y_1 \operatorname{sgn} y_2 \rangle = \int_{R+} d^2 y E\{x_1 x_2 | \vec{y}\} p(\vec{y}) - \int_{R-} d^2 y E\{x_1 x_2 | \vec{y}\} p(\vec{y}) \qquad \text{(VII.2)}$$

where R+ is the first and third quadrant of the y_1-y_2 plane while R- is the second and fourth quadrant as shown in Figure VII.1.

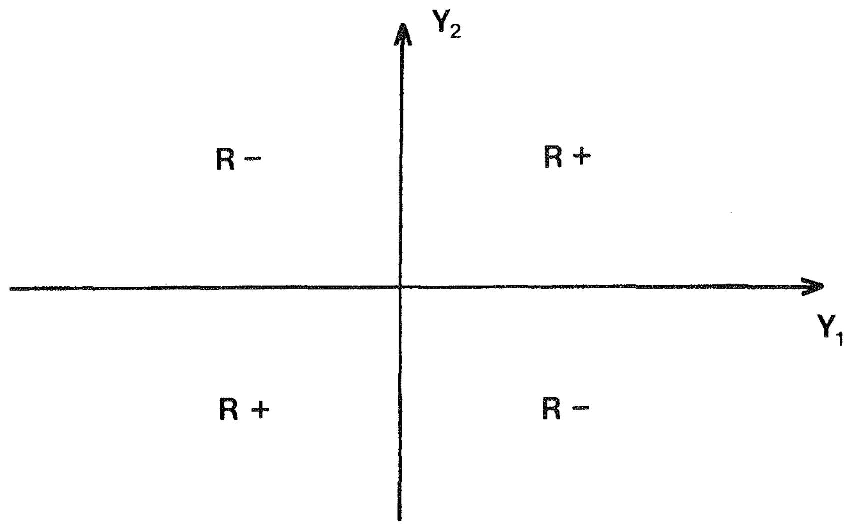

Figure VII.1. Definition of R+ and R-.

Now [79]

$$E\{\vec{x}\vec{x}^T|\vec{y}\} = X - PY^{-1}P^T + \vec{m}\vec{m}^T \tag{VII.3}$$

where

$$X = \langle\vec{x}\vec{x}^T\rangle \qquad Y = \langle\vec{y}\vec{y}^T\rangle \qquad P = \langle\vec{x}\vec{y}^T\rangle$$
$$\vec{m} = E\{\vec{x}|\vec{y}\} = PY^{-1}\vec{y} \tag{VII.4}$$

From this equation we directly write

$$E\{x_1x_2|\vec{y}\} = \langle x_1x_2\rangle - (PY^{-1}P^T)_{12} + m_1m_2$$
$$= \langle x_1x_2\rangle - (PY^{-1}P^T)_{12} + \alpha y_1^2 + \gamma y_1y_2 + \beta y_2^2 \tag{VII.5}$$

Direct calculation gives

$$(PY^{-1}P^T)_{12} = \frac{\langle x_1y_1\rangle\langle x_2y_1\rangle\langle y_2^2\rangle - \langle x_1y_1\rangle\langle x_2y_2\rangle\langle y_1y_2\rangle}{D}$$
$$+ \frac{-\langle x_1y_2\rangle\langle x_2y_1\rangle\langle y_1y_2\rangle + \langle x_1y_2\rangle\langle x_2y_2\rangle\langle y_1^2\rangle}{D}$$

$$\alpha = \frac{\langle x_1y_1\rangle\langle x_2y_1\rangle\langle y_2^2\rangle^2 - \langle x_1y_2\rangle\langle x_2y_1\rangle\langle y_2^2\rangle\langle y_1y_2\rangle}{D^2}$$

$$+ \frac{-\langle x_1y_1\rangle\langle x_2y_2\rangle\langle y_2^2\rangle\langle y_1y_2\rangle + \langle x_1y_2\rangle\langle x_2y_2\rangle\langle y_1y_2\rangle^2}{D^2}$$

$$\beta = \frac{\langle x_1y_2\rangle\langle x_2y_2\rangle\langle y_1^2\rangle^2 - \langle x_1y_1\rangle\langle x_2y_2\rangle\langle y_1^2\rangle\langle y_1y_2\rangle}{D^2}$$

$$+ \frac{-\langle x_1y_2\rangle\langle x_2y_1\rangle\langle y_1^2\rangle\langle y_1y_2\rangle + \langle x_1y_1\rangle\langle x_2y_1\rangle\langle y_1y_2\rangle^2}{D^2}$$

$$\gamma = \frac{\langle x_1y_1\rangle\langle x_2y_2\rangle\langle y_1^2\rangle\langle y_2^2\rangle - \langle x_1y_2\rangle\langle x_2y_2\rangle\langle y_1^2\rangle\langle y_1y_2\rangle}{D^2}$$

$$+ \frac{-\langle x_1y_1\rangle\langle x_2y_1\rangle\langle y_2^2\rangle\langle y_1y_2\rangle + \langle x_1y_2\rangle\langle x_2y_1\rangle\langle y_1y_2\rangle^2}{D^2}$$

$$+ \frac{\langle x_1y_2\rangle\langle x_2y_1\rangle\langle y_1^2\rangle\langle y_2^2\rangle - \langle x_1y_1\rangle\langle x_2y_1\rangle\langle y_2^2\rangle\langle y_1y_2\rangle}{D^2}$$

$$+ \frac{-\langle x_1y_2\rangle\langle x_2y_2\rangle\langle y_1^2\rangle\langle y_1y_2\rangle + \langle x_1y_1\rangle\langle x_2y_2\rangle\langle y_1y_2\rangle^2}{D^2} \tag{VII.6}$$

$$D = \langle y_1^2\rangle\langle y_2^2\rangle - \langle y_1y_2\rangle^2$$

The marginal distribution of $\vec{y}$ is

$$p(\vec{y}) = \frac{1}{2\pi\sigma_1\sigma_2\sqrt{1-\rho^2}}\, e^{-\frac{\sigma_2^2y_1^2 + \sigma_1^2y_2^2 - 2\rho\sigma_1\sigma_2y_1y_2}{2\sigma_1^2\sigma_2^2(1-\rho^2)}} \tag{VII.7}$$

where we have used the shorthand notation

$$\sigma_1^2 = \langle y_1^2\rangle \qquad \sigma_2^2 = \langle y_2^2\rangle$$

$$\rho = \rho_{y_1y_2}$$

From Eqs. (VII.2) and (VII.5) we see that we have to evaluate the following integrals

$$I_1 = \int_{R+} d^2y p(\vec{y}) - \int_{R-} d^2y p(\vec{y}) = 2\int_0^\infty dy_1 \int_0^\infty dy_2 p(y_1,y_2) - 2\int_{-\infty}^0 dy_1 \int_0^\infty dy_2 p(y_1,y_2)$$

where we have used the even symmetry of $p, p(-\vec{y}) = p(\vec{y})$. This expression may be further evaluated to

$$\boxed{I_1 = 2\int_0^\infty dy_1 \int_0^\infty dy_2 \{p(y_1,y_2) - p(-y_1,y_2)\}} \tag{VII.8}$$

Similarly we obtain

$$I_2 = \int_{R+} d^2y y_1^2 p(\vec{y}) - \int_{R-} d^2y y_1^2 p(\vec{y})$$

$$\boxed{I_2 = 2\int_0^\infty dy_1 \int_0^\infty dy_2 y_1^2 \{p(y_1,y_2) - p(-y_1,y_2)\}} \tag{VII.9}$$

$$I_3 = \int_{R+} d^2y y_2^2 p(\vec{y}) - \int_{R-} d^2y y_2^2 p(\vec{y})$$

$$\boxed{I_3 = 2\int_0^\infty dy_1 \int_0^\infty dy_2 y_2^2 \{p(y_1,y_2) - p(-y_1,y_2)\}} \tag{VII.10}$$

$$I_4 = \int_{R+} d^2y y_1 y_2 p(\vec{y}) - \int_{R-} d^2y y_1 y_2 p(\vec{y})$$

$$\boxed{I_4 = 2\int_0^\infty dy_1 \int_0^\infty dy_2 y_1 y_2 \{p(y_1,y_2) + p(-y_1,y_2)\}} \tag{VII.11}$$

To evaluate the integrals we use the following transformation for I_1, I_2 and I_4

$$y_1 = r\cos\theta \qquad y_2 = r\sin\theta \tag{VII.12}$$

and for I_3

$$y_1 = r\sin\theta \qquad y_2 = r\cos\theta \tag{VII.13}$$

$$I_1 = \frac{1}{\pi\sigma_1\sigma_2\sqrt{1-\rho^2}} \int_0^{\frac{\pi}{2}} d\theta \int_0^{\infty} dr\, r \left\{ e^{-r^2 \frac{\sigma_2^2\cos^2\theta + \sigma_1^2\sin^2\theta - \rho\sigma_1\sigma_2\sin 2\theta}{2\sigma_1^2\sigma_2^2(1-\rho^2)}} - e^{-r^2 \frac{\sigma_2^2\cos^2\theta + \sigma_1^2\sin^2\theta + \rho\sigma_1\sigma_2\sin 2\theta}{2\sigma_1^2\sigma_2^2(1-\rho^2)}} \right\}$$

The integration over r may be performed straight and we obtain

$$I_1 = \frac{\sigma_1\sigma_2\sqrt{1-\rho^2}}{\pi} \int_0^{\frac{\pi}{2}} d\theta \left\{ \frac{1}{\sigma_2^2\cos^2\theta + \sigma_1^2\sin^2\theta - \rho\sigma_1\sigma_2\sin 2\theta} - \frac{1}{\sigma_2^2\cos^2\theta + \sigma_1^2\sin^2\theta + \rho\sigma_1\sigma_2\sin 2\theta} \right\}$$

Changing variable of integration to

$$z = \frac{\sigma_1}{\sigma_2}\tan t \tag{VII.14}$$

we obtain

$$I_1 = \frac{\sqrt{1-\rho^2}}{\pi} \int_0^{\infty} dz \left\{ \frac{1}{z^2 - 2\rho z + 1} - \frac{1}{z^2 + 2\rho z + 1} \right\} \tag{VII.15}$$

For I_2 we get

$$I_2 = \frac{1}{\pi\sigma_1\sigma_2\sqrt{1-\rho^2}} \int_0^{\frac{\pi}{2}} d\theta \int_0^{\infty} dr\, r^3\cos^2\theta \left\{ e^{-r^2 \frac{\sigma_2^2\cos^2\theta + \sigma_1^2\sin^2\theta - \rho\sigma_1\sigma_2\sin 2\theta}{2\sigma_1^2\sigma_2^2(1-\rho^2)}} - e^{-r^2 \frac{\sigma_2^2\cos^2\theta + \sigma_1^2\sin^2\theta - \rho\sigma_1\sigma_2\sin 2\theta}{2\sigma_1^2\sigma_2^2(1-\rho^2)}} \right\}$$

Here too the integration over r may be performed straight and we obtain

$$I_2 = \frac{2\sigma_1^3\sigma_2^3(1-\rho^2)^{3/2}}{\pi}\int_0^{\frac{\pi}{2}} d\theta\cos^2\theta\left\{\frac{1}{(\sigma_2^2\cos^2\theta + \sigma_1^2\sin^2\theta - \rho\sigma_1\sigma_2\sin 2\theta)^2} - \frac{1}{(\sigma_2^2\cos^2\theta + \sigma_1^2\sin^2\theta + \rho\sigma_1\sigma_2\sin 2\theta)^2}\right\}$$

Using the transformation in Eq. (VII.14) we eventually obtain

$$I_2 = \frac{2}{\pi}(1-\rho^2)^{3/2}\sigma_1^2\int_0^\infty dz\left\{\frac{1}{(z^2-2\rho z+1)^2} - \frac{1}{(z^2+2\rho z+1)^2}\right\} \qquad \text{(VII.16)}$$

For I_3 we use the transformation in Eq. (VII.13) instead of that in Eq. (VII.12). I_3 will therefore, be equal to I_2 when we interchange σ_1 and σ_2

$$I_3 = \frac{2}{\pi}(1-\rho^2)^{3/2}\sigma_2^2\int_0^\infty dz\left\{\frac{1}{(z^2-2\rho z+1)^2} - \frac{1}{(z^2+2\rho z+1)^2}\right\} \qquad \text{(VII.17)}$$

By the same calculation as above we obtain for I_4

$$I_4 = \frac{2}{\pi}(1-\rho^2)^{3/2}\sigma_1\sigma_2\int_0^\infty dz\,z\left\{\frac{1}{(z^2-2\rho z+1)^2} + \frac{1}{(z^2+2\rho z+1)^2}\right\} \qquad \text{(VII.18)}$$

The following formulas for the indefinite integrals hold

$$\int\frac{dz}{z^2\pm 2\rho z+1} = \frac{1}{\sqrt{1-\rho^2}}\arctan\frac{z\pm\rho}{\sqrt{1-\rho^2}} + C$$

$$\int\frac{dz}{(z^2\pm 2\rho z+1)^2} = \frac{z\pm\rho}{2(1-\rho^2)(z^2\pm 2\rho z+1)} + \frac{1}{2(1-\rho^2)^{3/2}}\arctan\frac{z\pm\rho}{\sqrt{1-\rho^2}} + C \qquad \text{(VII.19)}$$

$$\int \frac{zdz}{(z^2 \pm 2\rho z + 1)^2} = -\frac{1 \pm \rho z}{2(1-\rho^2)(z^2 \pm 2\rho z + 1)}$$

$$\mp \frac{\rho}{2(1-\rho^2)^{3/2}} \arctan \frac{z \pm \rho}{\sqrt{1-\rho^2}} + C \qquad \text{(VII.19)}$$

By using these formulas we finally obtain for the integrals

$$\boxed{\begin{aligned} I_1 &= \frac{2}{\pi} \arcsin \rho \\ I_2 &= \frac{2}{\pi} \sigma_1^2 \{\rho\sqrt{1-\rho^2} + \arcsin \rho\} \\ I_3 &= \frac{2}{\pi} \sigma_2^2 \{\rho\sqrt{1-\rho^2} + \arcsin \rho\} \\ I_4 &= \frac{2}{\pi} \sigma_1\sigma_2 \{\sqrt{1-\rho^2} + \rho \arcsin \rho\} \end{aligned}} \qquad \text{(VII.20)}$$

Our expectation value may now be written as, Eqs. (VII.2), (VII.5), (VII.8-11) and (VII.20)

$$\langle x_1x_2 \mathrm{sgn}y_1 \mathrm{sgn}y_2\rangle = \frac{2}{\pi}\left\{\langle x_1x_2\rangle - (PY^{-1}P^T)_{12} + \alpha\langle y_1^2\rangle + \beta\langle y_2^2\rangle + \gamma\langle y_1y_2\rangle\right\}\arcsin \rho_{y_1y_2}$$

$$\frac{2}{\pi}\left\{\alpha\langle y_1^2\rangle + \beta\langle y_2^2\rangle + \gamma\frac{\langle y_1^2\rangle\langle y_2^2\rangle}{\langle y_1y_2\rangle}\right\}\rho_{y_1y_2}\sqrt{1-\rho_{y_1y_2}^2} \qquad \text{(VII.21)}$$

From Eq. (VII.6) we obtain by direct calculation

$$\alpha\langle y_1^2\rangle + \beta\langle y_2^2\rangle + \gamma\langle y_1y_2\rangle = (PY^{-1}P^T)_{12}$$

$$\alpha\langle y_1^2\rangle + \beta\langle y_2^2\rangle + \gamma\frac{\langle y_1^2\rangle\langle y_2^2\rangle}{\langle y_1y_2\rangle}$$

$$= \frac{\langle x_1y_1\rangle\langle x_2y_2\rangle + \langle x_1y_2\rangle\langle x_2y_1\rangle - \dfrac{\langle x_1y_1\rangle\langle x_2y_1\rangle\langle y_1y_2\rangle}{\langle y_1^2\rangle} - \dfrac{\langle x_1y_2\rangle\langle x_2y_2\rangle\langle y_1y_2\rangle}{\langle y_2^2\rangle}}{\langle y_1y_2\rangle\left[1 - \dfrac{\langle y_1y_2\rangle^2}{\langle y_1^2\rangle\langle y_2^2\rangle}\right]} \qquad \text{(VII.22)}$$

Inserting these expressions into Eq. (VII.21), Eq. (VII.1) is obtained q.e.d.

Application I $x_1 = y_1 = e_1(t), \quad x_2 = y_2 = e_1(t+\tau)$.

Stationarity is assumed. We then have

$$R_{e_1 \operatorname{sgn} e_1, e_1 \operatorname{sgn} e_1}(\tau) = \langle e_1(t) e_1(t+\tau) \operatorname{sgn} e_1(t) \operatorname{sgn} e_1(t+\tau) \rangle$$

$$= \frac{2}{\pi} \{ R_{e_1 e_1}(\tau) \arcsin \rho_{e_1 e_1}(\tau) + \sqrt{R^2_{e_1 e_1}(0) - R^2_{e_1 e_1}(\tau)} \} \quad \text{(VII.23)}$$

The normalized correlation function corresponding to the covariance function of Eq. (6.28) will be

$$\rho_{e_1 \operatorname{sgn} e_1, e_1 \operatorname{sgn} e_1}(\tau) = \frac{R_{e_1 \operatorname{sgn} e_1, e_1 \operatorname{sgn} e_1}(\tau)}{R^2_{e_1 \operatorname{sgn} e_1}(0)}$$

$$= \rho_{e_1 e_1}(\tau) \arcsin \rho_{e_1 e_1}(\tau) + \sqrt{1 - \rho^2_{e_1 e_1}(\tau)} \quad \text{(VII.24)}$$

where $\rho_{e_1 e_1}$ is defined in Eq. (6.21).

The normalized covariance function is obtained by subtracting

$$\frac{\langle e_1 \operatorname{sgn} e_1 \rangle^2}{R^2_{e_1 \operatorname{sgn} e_1}(0)} = 1$$

Thus

$$\boxed{\zeta_{|e_1|,|e_1|}(\tau) = \rho_{e_1 e_1}(\tau) \arcsin \rho_{e_1 e_1}(\tau) + \sqrt{1 - \rho^2_{e_1 e_1}(\tau)} - 1} \quad \text{(VII.25)}$$

This covariance function is obtained in a simpler way [81] from Price's theorem [80]. To use Price's theorem to calculate the other correlation functions of estimator type II seems to be more complicated than to prove the general theorem of ours.

Application II $x_1 = \dot{e}_2(t), \quad y_1 = e_1(t), \quad x_2 = y_2 = e_1(t+\tau)$.

By direct insertion into Eq. (VII.1) we obtain (stationary case)

$$R_{\dot{e}_2 \mathrm{sgn}\, e_1, |e_1|}(\tau) = \langle \dot{e}_2(t)\,\mathrm{sgn}\, e_1(t) e_1(t+\tau)\,\mathrm{sgn}\, e_1(t+\tau)\rangle$$

$$= \frac{2}{\pi}\{R_{\dot{e}_2 e_1}(\tau)\arcsin \rho_{e_1 e_1}(\tau) + R_{\dot{e}_2 e_1}(0)\sqrt{1-\rho^2_{e_1 e_1}(\tau)}\} \qquad \text{(VII.26)}$$

The normalized correlation function corresponding to the covariance function in Eq. (6.28) will be

$$\rho_{\dot{e}_2 \mathrm{sgn}\, e_1, |e_1|}(\tau) = \frac{R_{\dot{e}_2 \mathrm{sgn}\, e_1, |e_1|}(\tau)}{R_{\dot{e}_2 \mathrm{sgn}\, e_1}(0) R_{e_1 \mathrm{sgn}\, e_1}(0)}$$

$$= \rho_{\dot{e}_2 e_1}(\tau)\arcsin \rho_{e_1 e_1}(\tau) + \sqrt{1-\rho^2_{e_1 e_1}(\tau)} \qquad \text{(VII.27)}$$

where $\rho_{\dot{e}_2 e_1}$ and $\rho_{e_1 e_1}$ are defined in Eq. (6.21).

The normalized covariance function of Eq. (6.28) is obtained by subtracting

$$\frac{\langle \dot{e}_2 \mathrm{sgn}\, e_1\rangle\langle e_1 \mathrm{sgn}\, e_1\rangle}{R_{\dot{e}_2 \mathrm{sgn}\, e_1}(0) R_{e_1 \mathrm{sgn}\, e_1}(0)} = 1$$

Thus

$$\boxed{\zeta_{\dot{e}_2 \mathrm{sgn}\, e_1, |e_1|}(\tau) = \rho_{\dot{e}_2 e_1}(\tau)\arcsin \rho_{e_1 e_1}(\tau) + \sqrt{1-\rho^2_{e_1 e_1}(\tau)} - 1} \qquad \text{(VII.28)}$$

<u>Application III $\quad x_1 = \dot{e}_2(t),\ \ y_1 = e_1(t),\ \ x_2 = \dot{e}_2(t+\tau),\ \ y_2 = e_1(t+\tau).$</u>

By direct insertion into Eq. (VII.1) we obtain (stationary case)

$$R_{\dot{e}_2 \mathrm{sgn}\, e_1, \dot{e}_2 \mathrm{sgn}\, e_1}(\tau) = \langle \dot{e}_2(t)\,\mathrm{sgn}\, e_1(t)\dot{e}_2(t+\tau)\,\mathrm{sgn}\, e_1(t+\tau)\rangle$$

$$= \frac{2}{\pi}\Bigg\{R_{\dot{e}_2 \dot{e}_2}(\tau)\arcsin \rho_{e_1 e_1}(\tau)$$

$$+ \frac{R^2_{\dot{e}_2 e_1}(0) + R_{\dot{e}_2 e_1}(\tau) R_{e_1 \dot{e}_2}(\tau) - [R_{\dot{e}_2 e_1}(\tau) + R_{e_1 \dot{e}_2}(\tau)] R_{\dot{e}_2 e_1}(0)\rho_{e_1 e_1}(\tau)}{R_{e_1 e_1}(0)\sqrt{1-\rho^2_{e_1 e_1}(\tau)}}\Bigg\} \qquad \text{(VII.29)}$$

We shall assume that Eq. (5.12) holds, which, together with the formulas of Appendix VI imply

$$R_{\dot{e}_2 e_1}(\tau) = -\dot{R}_{e_2 e_1}(\tau) = \dot{R}_{e_1 e_2}(\tau) = R_{e_1 \dot{e}_2}(\tau) \qquad \text{(VII.30)}$$

The normalized correlation function corresponding to the covariance function of Eq. (6.28) will be

$$\rho_{\dot{e}_2 \operatorname{sgn} e_1, \dot{e}_2 \operatorname{sgn} e_1}(\tau) = \frac{R_{\dot{e}_2 \operatorname{sgn} e_1, \dot{e}_2 \operatorname{sgn} e_1}(\tau)}{R^2_{\dot{e}_2 \operatorname{sgn} e_1}(0)}$$

$$= \rho_{\dot{e}_2 \dot{e}_2}(\tau) \arcsin \rho_{e_1 e_1}(\tau) + \frac{1 + \rho^2_{\dot{e}_2 e_1}(\tau) - 2\rho_{\dot{e}_2 e_1}(\tau)\rho_{e_1 e_1}(\tau)}{\sqrt{1 - \rho^2_{e_1 e_1}(\tau)}} \qquad \text{(VII.31)}$$

where $\rho_{\dot{e}_2\dot{e}_2}$, $\rho_{\dot{e}_2 e_1}$, and $\rho_{e_1 e_1}$ are defined in Eq. (6.21). The normalized covariance function of Eq. (6.28) is obtained by subtracting

$$\frac{\langle \dot{e}_2 \operatorname{sgn} e_1 \rangle^2}{R^2_{\dot{e}_2 \operatorname{sgn} e_1}(0)} = 1$$

Thus

$$\boxed{\zeta_{\dot{e}_2 \operatorname{sgn} e_1, \dot{e}_2 \operatorname{sgn} e_1}(\tau) = \rho_{\dot{e}_2 \dot{e}_2}(\tau) \arcsin \rho_{e_1 e_1}(\tau) + \frac{1 + \rho^2_{\dot{e}_2 e_1}(\tau) - 2\rho_{\dot{e}_2 e_1}(\tau)\rho_{e_1 e_1}(\tau)}{\sqrt{1 - \rho^2_{e_1 e_1}(\tau)}} - 1} \qquad \text{(VII.32)}$$

Low signal to noise ratio.

This is the case studied by Yerbury. Let $x(t)$ and $y(t)$ be the correlator inputs and let $x_1 = x(t)$, $y_1 = y(t)$, $x_2 = x(t + \tau)$, $y_2 = y(t + \tau)$. When the noise processes on the two channels are uncorrelated and the signal to noise ratios are small, we may approximate

$$\langle x_1 y_1 \rangle = \langle x_1 y_2 \rangle = \langle x_2 y_1 \rangle = \langle x_2 y_2 \rangle = 0$$

which gives

$$\langle x(t) \operatorname{sgn} y(t) x(t+\tau) \operatorname{sgn} y(t+\tau) \rangle = \frac{2}{\pi} R_{xx}(\tau) \arcsin \rho_{yy}(\tau) \qquad \text{(VII.33)}$$

This may directly be obtained by approximating the expectation value by

$$\langle x(t) x(t+\tau) \rangle \langle \operatorname{sgn} y(t) \operatorname{sgn} y(t+\tau) \rangle$$

since $x(t)$ and $y(t)$ are uncorrelated Gaussian and thereby independent.

APPENDIX VIII

Bussgang's relation for non Gaussian signals.

We here discuss conditions for the extension of Bussgang's relation to non Gaussian signals. The discussion is an extension of the work of Barret and Lampard [85] to get the weakest conditions on the non-linearity and the process obtainable by their method, for the relation to hold. Barret and Lampard used an expansion of the second order probability density function $p_{x_1x_2}(x_1,x_2)$ in a series of polynomials $\{\theta_n\}$ and $\{\psi_n\}$ which were orthogonal with respect to the marginal distributions $p_{x_1}(x_1)$ and $p_{x_2}(x_2)$ respectively.

i.e.

$$p_{x_1x_2}(x_1,x_2) = p_{x_1}(x_1)p_{x_2}(x_2)\sum_{m=0}^{\infty}\sum_{n=0}^{\infty} a_{mn}\theta_m(x_1)\psi_n(x_2)$$

where

$$\int_{-\infty}^{\infty} dx_1\ p_{x_1}(x_1)\theta_m(x_1)\psi_n(x_1) = \delta_{mn}$$

$$\int_{-\infty}^{\infty} dx_2\ p_{x_2}(x_2)\psi_m(x_2)\theta_n(x_2) = \delta_{mn}$$

(VIII.1)

$$p_{x_1}(x_1) = \int_{-\infty}^{\infty} dx_2\ p_{x_1x_2}(x_1,x_2)$$

$$p_{x_2}(x_2) = \int_{-\infty}^{\infty} dx_1\ p_{x_1x_2}(x_1,x_2)$$

The requirement on $p_{x_1x_2}$ for this to hold is that

i) $$\frac{p_{x_1x_2}(x_1,x_2)}{\sqrt{p_{x_1}(x_1)p_{x_2}(x_2)}}$$ is square integrable .

ii) All moments of p_{x_1} and p_{x_2} are finite.

The first requirement assures that $p_{x_1x_2}/\sqrt{p_{x_1x_2}}$ belongs to a Hilbert space of square integrable functions defined on $\mathbb{R}^2$ with inner product

$$(f,g) = \int_{-\infty}^{\infty} dx_1 \int_{-\infty}^{\infty} dx_2 f(x_1,x_2)g(x_1,x_2) \qquad \text{(VIII.2)}$$

This Hilbert space is separable, i.e. functions with finite norm may be expressed by an infinite series of an orthonormal basis of the form $\{h_{mn}(x_1,x_2)\} = \{u_m(x_1)v_n(x_2)\}$. The orthonormality requirement may be written

$$
\begin{aligned}
(h_{mn},h_{pq}) &= \int_{-\infty}^{\infty} dx_1 \int_{-\infty}^{\infty} dx_2\, h_{mn}(x_1,x_2)h_{pq}(x_1,x_2) \\
&= \int_{-\infty}^{\infty} dx_1 u_m(x_1)u_p(x_1) \int_{-\infty}^{\infty} dx_2 v_n(x_2)v_q(x_2) \\
&= \delta_{mp}\delta_{nq} \qquad \text{(VIII.3)}
\end{aligned}
$$

Thus $\{u_m\}$ and $\{v_n\}$ forms orthonormal basises of square integrable functions defined on $\mathbb{R}$.

The first requirement may also be expressed as

$$\int_{-\infty}^{\infty} dx_1 \int_{-\infty}^{\infty} dx_2 p(x_1|x_2)p(x_1|x_2) < \infty$$

The second requirement assures that u_m and v_n of the form

$$
\begin{aligned}
u_m(x_1) &= \sqrt{p_{x_1}(x_1)}\;\theta_m(x_1) \\
v_n(x_2) &= \sqrt{p_{x_2}(x_2)}\;\psi_n(x_2)
\end{aligned} \qquad \text{(VIII.4)}
$$

where θ_m and ψ_n are polynomials of degree m and n will have finite norm. This is established since their norms will be of the form

$$\|u_m(x_1)\|^2 = \int_{-\infty}^{\infty} dx_1 p_{x_1}(x_1)\theta^2{}_m(x_1)$$

$$\|v_n(x_2)\|^2 = \int_{-\infty}^{\infty} dx_2 p_{x_2}(x_2)\psi^2{}_n(x_2)$$

which are linear combinations of moments of degree up to 2m of p_{x_1} for u_m and 2n of p_{x_2} for v_n.

The orthonormality of $\{u_m\}$ and $\{v_n\}$ implies that $\{\theta_m\}$ and $\{\psi_n\}$ are orthonormal with the weight functions p_{x_1} and p_{x_2} respectively, Eq. (VIII.3).

$$
\begin{aligned}
(u_m,u_n) &= \int_{-\infty}^{\infty} dx\; p_{x_1}(x)\theta_m(x)\theta_n(x) = \delta_{mn} \\
(v_m,v_n) &= \int_{-\infty}^{\infty} dx\; p_{x_2}(x)\psi_m(x)\psi_n(x) = \delta_{mn}
\end{aligned} \qquad \text{(VIII.5)}
$$

From the above follows that

$$\frac{p_{x_1x_2}(x_1,x_2)}{\sqrt{p_{x_1}(x_1)p_{x_2}(x_2)}} = \sum_{m=0}^{\infty}\sum_{n=0}^{\infty} a_{mn}u_m(x_1)v_n(x_2)$$

$$= \sqrt{p_{x_1}(x_1)p_{x_2}(x_2)} \sum_{m=0}^{\infty}\sum_{n=0}^{\infty} a_{mn}\theta_m(x_1)\psi_n(x_2) \qquad \text{(VIII.6)}$$

This is the same as Eq. (VIII.1). The coefficient a_{pq} may be obtained by multiplying both sides with $u_p v_q$, integrating, and using the orthonormality relation, Eq. (VIII.5) which gives

$$a_{pq} = \int_{-\infty}^{\infty} dx_1 \int_{-\infty}^{\infty} dx_2 p_{x_1x_2}(x_1,x_2)\theta_m(x_1)\psi_n(x_2) \qquad \text{(VIII.7)}$$

The polynomials may be constructed from $\{1,x,x^2,\ldots.\}$ by using the Gram-Schmidt orthogonalization procedure and the orthonormality requirement, Eq. (VIII.5). Chosing $\theta_0 = \psi_0 = 1$, $\theta_1 = a_1x_1 + b_1$, $\psi_1 = a_2x_2 + b_2$, we obtain [85]

$$\theta_0(x_1) = 1 \qquad \psi_0(x_2) = 1$$

$$\theta_1(x_1) = \frac{x_1 - \langle x_1\rangle}{\sigma_1} \qquad \psi_1(x_2) = \frac{x_2 - \langle x_2\rangle}{\sigma_2} \qquad \text{(VIII.8)}$$

$$\sigma_1^2 = \langle[x_1 - \langle x_1\rangle]^2\rangle \qquad \sigma_2^2 = \langle[x_2 - \langle x_2\rangle]^2\rangle$$

Barrett and Lampard further specializes to the class of distributions where $\{a_{mn}\}$ is diagonal. Suppose that a nonlinear function may be expressed by the following series

$$g(x_2) = \sum_{n=0}^{\infty} c_n\psi_n(x_2) \qquad \text{(VIII.9)}$$

From the orthonormality condition Eq. (VIII.5) we obtain

$$c_n = \int_{-\infty}^{\infty} dx_2 p_{x_2}(x_2)g(x_2)\psi_n(x_2) \qquad \text{(VIII.10)}$$

which specially gives

$$c_0 = \int_{-\infty}^{\infty} dx_2 p_{x_2}(x_2) g(x_2) = \langle g(x_2) \rangle$$

$$c_1 = \int_{-\infty}^{\infty} dx_2 p_{x_2}(x_2) g(x_2) \left(\frac{x_2 - \langle x_2 \rangle}{\sigma_2} \right) = \frac{\langle g(x_2)[x_2 - \langle x_2 \rangle] \rangle}{\sigma_2} \tag{VIII.11}$$

For the covariance between x_1 and $g(x_2)$ we obtain

$$\langle [x_1 - \langle x_1 \rangle][g(x_2) - \langle g(x_2) \rangle] \rangle$$

$$= \langle \sigma_1 \theta_1(x_1) \cdot \sum_{n=1}^{\infty} c_n \psi_n(x_2) \rangle$$

$$= \sigma_1 \sum_{n=1}^{\infty} c_n \int_{-\infty}^{\infty} dx_1 \int_{-\infty}^{\infty} dx_2 p_{x_1 x_2}(x_1, x_2) \theta_1(x_1) \psi_n(x_2)$$

$$= \sigma_1 \sum_{n=1}^{\infty} c_n a_{1n}$$

But since we have assumed $\{a_{mn}\}$ diagonal, we obtain

$$= \sigma_1 c_1 a_{11}$$

From Eq. (VIII.7) we have

$$a_{11} = \int_{-\infty}^{\infty} dx_1 \int_{-\infty}^{\infty} dx_2 p_{x_1 x_2}(x_1, x_2) \frac{[x_1 - \langle x_1 \rangle]}{\sigma_1} \frac{[x_2 - \langle x_2 \rangle]}{\sigma_2}$$

$$= \frac{\langle [x_1 - \langle x_1 \rangle][x_2 - \langle x_2 \rangle] \rangle}{\sigma_1 \sigma_2} \tag{VIII.12}$$

Thus we finally obtain

$$\boxed{\langle [x_1 - \langle x_1 \rangle][g(x_2) - \langle g(x_2) \rangle] \rangle = \frac{\langle [x_1 - \langle x_1 \rangle][x_2 - \langle x_2 \rangle] \rangle \langle g(x_2)[x_2 - \langle x_2 \rangle] \rangle}{\langle [x_2 - \langle x_2 \rangle]^2 \rangle}} \tag{VIII.13}$$

In the proof we only need θ_1, ψ_1, and ψ_0 to be of the form given in Eq. (VIII.8). Thus the rest of the basis functions need not to be expressed by polynomials as given by Eq.(VIII.4). $\|v_0\|$ will always be finite since

$$\|v_0\|^2 = \int_{-\infty}^{\infty} dx \, p_{x_2}(x)$$

For $\|u_1\|^2$ and $\|v_1\|^2$ to be finite $<x_1{}^2>$ and $<x_2{}^2>$ must be finite (this implies $<x_1>$, $<x_2>$, finite) which is the physical requirement of the finite power in the signals.

The requirement for Eq.(VIII.9) to hold is that $g(x_2)\sqrt{p_{x_2}(x_2)}$ is square integrable, i.e.

$$<g^2(x_2)> = \int_{-\infty}^{\infty} dx_2 p_{x_2}(x_2) g^2(x_2) < \infty \qquad \text{(VIII.14)}$$

This implies that

$$g(x_2)\sqrt{p_{x_2}(x_2)} = \sum_{n=0}^{\infty} c_n v_n(x_2) \qquad \text{(VIII.15)}$$

which with the special form of v_n given in Eq.(VIII.4) is identical to Eq. (VIII.9).

For the sgn function we obtain

$$<\text{sgn}\ x_2{}^2> = \int_{-\infty}^{\infty} dx_2 p_{x_2}(x_2) = 1$$

which implies that the theorem holds in our case. The validity of the estimator equations are therefore also proved for a class of non Gaussian signals, namely those signals where

a) the condition i) holds and $\{a_{mn}\}$ is diagonal

b) $<x_1{}^2>$ and $<x_2{}^2>$ have finite energy.

Brown [77] has extended the result to hold for a wider class of distributions where $\{a_{mn}\}$ is nondiagonal. Requiring that the form of u_n and v_n in Eq. (VIII.4) exists (all moments finite) he shows.

Theorem.

$$<[x_1 - <x_1>][g(x_2) - <g(x_2)>]> = K<[x_1 - <x_1>][x_2 - <x_2>]> \qquad \text{(VIII.16)}$$

if, and only if, there exists a sequence of real constants $\{d_m\}$ with $d_m = 1$ so that $a_{1m} = d_m a_{11}$ $\quad m = 1,2,\ldots\ldots$ $\quad (K = \frac{1}{\sigma_2} \sum_{m=1}^{\infty} c_m d_m)$

Thus the validity of estimator type II is shown to hold for a wide class of signals including the Gaussian type. In Chapter 7 we shall obtain experimental evidence for the usefulness of the estimator.

REFERENCES

[1] Bom, N., Lancée, Ch.T., van Zwieten, G., Kloster, F.E., Roelandt, J.: "Multiscan echo cardiography. I. Technical description". Circulation, XLVIII (Nov. 1973) 1066-1074.

[2] Kloster, F.E., Roelandt, J., Folkert, J.T.C., Bom, N., Hugenholtz, P.G.: "Multiscan echocardiography. II. Technique and initial clinical results". Circulation XLVIII (Nov. 1973) 1075-1084.

[3] Fish, P.: "Visualising blood vessels by ultrasound". In Roberts, C. (ed): "Blood flow measurement", Sector Publ. Ltd. (London 1972) 29-32.

[4] Hottinger, C.F., Meindl, J.D.: "An ultrasonic scanning system for arterial imaging". IEEE Ultrasonics Symposium (Nov. 1973) 86-87.

[5] Waag, R.C., Myklebust, J.B., Rhoads, W.L., Gramiak, R.: "Instrumentation for nonivasive cardiac chamber flow rate measurement". IEEE Ultrasonics Symposium (Nov. 1972) 74-77.

[6] Ohtsuki, S., Okujima, M.: "Ultrasonic doppler velocity meter by double M-sequence modulation method". 2nd World Congress on Ultrasonics in Medincine, Rotterdam, Abstract (June 1973) 51.

[7] Newhouse, V.L., Bendick, Ph.J.: "Analysis of random signal blood flow measurement". IEEE Ultrasonics Symposium (Nov. 1973) 94-97.

[8] Somer, J.C., Oosterbaan, W.A., Freund, H.J.: "Ultrasonic tomographic imaging of the brain with an elctronic sector scanning system". IEEE Ultrasonics Symposium (Nov. 1973) 43-48.

[9] Bom, N., Lancée, C.T., Roelandt, J., van Egmond, F.C.: "Two multi-element systems for real time cross-sectional analysis of the heart". IEEE Ultrasonics Symposium (Nov. 1973) 1-3.

[10] Maginess, M.G., Plummer, J.O., Meindl, J.D., Susal, A.L.: "A cardic dynamics visualization system". IEEE Ultrasonics Symposium (Nov. 1973) 4-6.

[11] Havlice, J.F., Kino, G.S., Quate, C.F.: "A new acoustic imaging device". IEEE Ultrasonic Symposium (Nov. 1973) 13-17.

[12] Wells, P.N.T.: "Physical principles of ultrasonic diagnoses". Academic Press (London 1969).

[13] Franklin, D.L., Baker, D.W., Rushmer, R.F.: "Pulsed ultrasonic transit time flowmeter". IRE Trans. Bio. Med. Electron, 9, (1962) 44-49.

[14] Satomura, S.: "Study of the flow patterns in ateries by ultrasonics". J. Acoust. Soc. Jap., 15 (1959) 151-158.

[15] Perronneau, P., Deloche, A., Bui-Mong-Hung, Hinglais, J.: "Débitmétrie ultrasonore p Développements et applications expérimentales". Europ. Surg. Res. 1 (1969) 147-156.

[16] Baker, D.W.: "Pulsed ultrasonic doppler blood-flow sensing". IEEE Trans. on S. and U.S., SU-17, 3 (July 1970) 170-185.

[17] Franklin, D.L., Schlegal, W.A., Rushmer, R.F.: "Blood flow measured by doppler frequency shift of backscattered ultrasound". Science, 132 (1961) 564-565.

[18] Baker, D.W., Watkins, D.W.: "A phase coherent pulse doppler system for cardiovascular measurements". Proc. 20th Ann. Conf. on Engng. in Med. and Biol., 27 (1967) 2.

[19] Bernstine, R.L., Litt, B.D.: "Doppler ultrasound studies of the fetal animal". In Rand, E. (ed): "Recent advances in diagnostic ultrasound". Thomas (Springfield, Ill., 1971) 133-142.

[20] Rice, S.O.: "Mathematical analysis of random noise". Bell System Tech. Jour., 23 (1944) 282-332.

[21] Johnson, S.L., Baker, D.W., Lute, R.A., Dodge, H.T.: "Doppler echocardiography. The localization of cardiac murmurs". Circulation, XLVIII (Oct. 1973) 810-822.

[22] Gill, R.W., Meindl, J.D.: "Optimal system design of the pulsed ultrasonic blood flowmeter". IEEE Ultrasonics Symposium (Nov. 1973) 88-93.

[23] Aaslid, R.: Private communication.

[25] Jorgensen, J.E., Campau, D.N., Baker, D.W.: "Physical characteristics and mathematical modelling of the pulsed ultrasonic flowmeter". Med. Biol. Engng., 11 (July 1973) 404-421.

[26] Baker, D.W., Yates, W.G.: "Technique for studying the sample volume of ultrasonic doppler devices". Med. Biol. Engng., 11 (Nov. 1973) 766-770.

[27[Jaffe, H., Berlincourt, D.A.: "Piezoelectric transducer materials". Proc. of the IEEE, 53, (Oct. 1965) 1372-1386.

[28] Kossoff, G.: "The effects of backing and matching on the performance of piezoelectric ceramic transducers". IEEE Trans on S and US, SU-13, 1 (March 1966) 20-30.

[29] Zemanek, J.: "Beam behaviour in the near field of a vibrating piston". J. Acoust. Soc. Am., 49 (1971) 181-191.

[30] Gooberman, G.L.: "Ultrasonics. Theory and application". The English Universities Press Ltd. (London 1968).

[31] "American Institute of Physics Handbook". 3rd ed. McGraw Hill (N.Y. 1972).

[32] Lees, S., Gilmore, R.S., Kranz, P.R.: "Acoustic properties of tungsten-vinyl composites". IEEE Trans on S and US, SU-20, 1 (Jan. 1973) 1-2.

[33] Kossoff, G., Robinson, D.E., Garret, W.J.: "Ultrasonic two-dimensional visualization for medical diagnoses". J. Acoust. Soc. Am., 44 (1968) 1310-1318.

[34] Fung, Y.C.: "Theoretical considerations of the elasticity of red cells and small blood vessels". Federation Proceedings, 25, (Nov/Dec. 1966) 1761-1772.

[35] Burton, A.C.: "Physiology and biophysics of the circulation". Year Book Medical Publishers (N.Y. 1965).

[36] Brånemark, P.I., Lindström, J.: "Shape of circulating blood corpuscles". Biorheology, 1 (1963) 139-142.

[37] Fung, Y.C.: "Biomechanics: A survey of the blood flow problem". Adv. in Appl. Mech, 11 (1971) 65-130.

[38] Charm, S.E., Kurland, G.S.: "Blood Rheology". In Bergel, D.H. (ed): "Cardiovascular fluid dynamics, vol. 2". Academic Press (London 1972)

[39] Cokelet, G.R., Merill, E.W., Gilliand, E.R., Shin, H., Britten, A., Wells, R.E.: "Rheology of human blood: Measurement near and at zero shear rate". Trans. Soc. Rheol., 7 (1963) 303-317.

[40] Fåhraeus, R., Lindquist, R.: "Viscocity of blood in narrow capillary tubes". Amer. J. Physiol., 96, (1931) 562-568.

[41] Dix, F.S., Scott-Blair, G.W.: "On the flow of suspensions through narrow tubes". J. Appl. Physics, 2, (1940) 575-581.

[42] Mayer, G.A.: "Anomalous viscocity of human blood". Am. J. Physiol., 208 (1965) 1267-1269.

[43] Merill, E.W., Benis, A.M., Gilliand, E.R., Sherwood, R.K., Salzmann, E.W.: "Pressure flow relations of human blood in hollow fibers at flow rates". J. Appl. Physiol., 20 (1965) 954,960.

[44] Reid, J.M., Sigelmann, R.A., Nasser, M.G., Baker, D.W.: "The scattering of ultrasound by human blood". Proc. 8th ICOMBE (1969), 10-7.

[45] Brody, W.R.: "Theoretical analysis of the ultrasonic blood flow meter". Ph.D. Thesis and technical report, Stanford Electronics Laboratories, Stanford University, California (1971). Report No. 4958-1.

[46] von Smolukowski, M.: "Molekular-kinetische Theorie der Opaleszens von Gasen im kritischen Zustand, sowie einiger verwandter Erscheinungen" Ann. d. Phys., 25 (1908) 205-226.

[47] Einstein, A.: "Theorie der Opaleszenz von homogenen Flüssigkeiten und Flüssigkeitsgemischen in der Nähe des kritischen Zustandes". Ann. d. Physik, 33 (1910), 1275-1298.

[48] Flax, S.W., Webster, J.G., Updike, S.J.: "Statistical evaluation of the doppler ultrasonic blood flowmeter". Biomed. Sci. Inst., 7, (1970) 201-222.

[49] Achenbach, J.D.: "Wave propagation in elastic solids". North-Holland Publishing Company (Amsterdam 1973).

[50] Landau, L.D., Lifschits, E.M.: "Fluid Mechanics. A course of theoretical physics, Vol 6". Pergamon Press (London 1963).

[51 Chandrasekhar, S.: "Stochastic problems in physics and astronomy". Rev. Mod. Phys., 15, (Jan. 1943) 3-92.

[52] Uhlenbeck, G.E., Ornstein, L.S.: "On the theory of the brownian motion". Phys. Rev., 36 (Sept. 1930) 823-841.

[53] Cokelet, G.R.: "Comments on the Fåhraeus-Lindquist effect". Biorheology, 4, (1967) 123-126.

[54] Morse, P.M., Ingard, K.U.: "Theoretical Acoustics". McGraw-Hill, (N.Y. 1968).

[55] Mayer, G.A.: "Anomalous viscocity of human blood". Amer. J. Physiol., 208 (1965) 1267-1269.

[56] Newhouse, V.L.' "A theorem relating doppler system ouptut spectra to the transmitted spectrum". Report, School of Electrical Engng. Purdue University, West Lafayette, Indiana, (July 1973), Rep. No. 8/31/73.

[57] Landau, L.D., Lifschitz, E.M.: "Statistical physics. A course of theoretical physics. Vol. 5". Pergamon Press (London 1963).

[58] Stakgold, I.: "Boundary value problems of mathematical physics". Vol. II. MacMillan (N.Y. 1968).

[59] Ornstein, L.S., Zernike, F.: "Accidental deviations of density and opalescence at the critical point of a single substance". Proc. Koningkl. Akad. Wetenschap, 17 (1914) 793-806.

[60] Komarov, L.I., Fischer, I.Z.: "Theory of Rayleigh scattering of light in liquids". Sov. Phys. JETP, 16 (1963) 1358-1361.

[61] Papoulis, A.: "Probability, random variables and stochastic processes". McGraw-Hill (N.Y. 1965).

[62] Jorgensen, J.E., Campau, D.N., Garbini, J.L., Baker, D.W.: "Analytical modelling of the ultrasonic doppler flowmeter". Proc. 25th ACEMB (Oct. 1972) 35.

[63] Haase, W.C., Foletta, N.S., Meindl, J.D.: "A directional ultrasonic blood flow meter". IEEE Ultrasonics Symp. (Nov. 1973) 81-84.

[64] Histand, M.B., Miller, Ch.W., McLeod, F.D. Jr.: "Transcutaneous measurement of blood velocity profiles and flow". Cardiovascular Res., 7, (1973) 703-712.

[65] MacKay, R.S.: "Non-invasive cardiac output measurement". Cardiovascular Res., 4 (1972) 438-452.

[66] Light, L.H., Cross, G.: "Cardiovascular data by transcutaneous aorta-velography". In Roberts, C. (ed): "Blood flow measruement". Sector Publishing Limited (London 1972).

[69] Aaslid, R.: "Simulation of the individual cardiovascular system - A pilot study". Report. The Norwegian Institute of Technology, Division of Engineering Cybernetics (1974) Rep. No. 74-51-W. Thesis.

[70] Arts, M.G.J., Roevros, J.M.J.G.:"On the instantaneous measurement of blood flow by ultrasonic means". Med. & Biol. Engng. 10 (1972) 23-34.

[71] Blackman, R.B., Tukey, J.W.: "The measurement of power spectra". Dover Publ. Inc. (N.Y. 1958).

[72] Jenkins, G.M., Watts, D.G.: "Spectral Analysis". Holden Day (London 1969).

[73] "Field-Effect transistors". Mullard Ltd. (London 1972).

[74] Bom, M., Wolf, E.: "Principles of Optics". Pergamon Press (London 1965) 370-449.

[75] Thomas, J.B.: "An introduction to statistical communication theory". John Wiley & Sons, Inc. (N.Y. 1968).

[76] Bussgang, J.J.: "Crosscorrelation functions of amplitude distorted gaussian signals". Techn. Rep. Mass.-Inst. Techn. Res.Lab. Electronics, Cambridge, Mass. (March 1952). Rep. No. 216.

[77] Brown, J.L. Jr.: "On a corsscorrelation property for stationary random processes". IRE Trans. Inf. Theor., IT-3 (March 1957) 28-31.

[78] Papoulis, A.: "Minimum-Bias windows for high resolution spectral estimates". IEEE Trans. Inf. Theor., IT-19, (No. 1 Jan 1973) 9-12.

[79] Jazwinski, A.H.: "Stochastic processes and filtering theory". Academic Press (London 1970).

[80] Price, R.: "A useful theorem for nonlinear devices having gaussian inputs". IRE Trans. Inf. Theor., IT-4 (June 1958) 69-72.

[81] Hagen, J.B.: "A hybrid autocorrelator and its application to high altitude incoherent scatter". National Astronomy and Ionosphere Center, Arecibo Puerto Rico (1972) Report No. NAIC 18.

[82] Yerbury, M.J.: "Amplitude Limiting applied to a sensitive correlation detector". The Radio and Electronic Engineer, 34 (July 1967) 5-14.

[83] Farley, D.T.: "Incoherent scatter correlation function measurements". Radio Science, 4, (No. 10 Oct. 1969) 935-953.

[84] Hagen, J.B., Farley, D.T.: "Digital correlation techniques in radio science". Radio Science, 8, (No. 8,9 Aug.-Sept. 1973) 775-784.

[85] Barret, J.F., Lampard, D.G.: "An expansion for some second-order probability distributions and its application to noise problems". IRE Trans. Inf. Theor., IT-1 (March 1955) 10-15.

[86] van Trees, H.L.: "Detection estimation and modulation theory, Part I". John Wiley & Sons, Inc. (N.Y. 1968).